Characterization of the Diffuse Astrophysical All-Flavour Neutrino Spectrum using IceCube Events With Contained Vertices

By

Vedant Basu

A dissertation submitted in partial fulfillment of

the requirements for the degree of

Doctor of Philosophy

(Physics)

at the

UNIVERSITY OF WISCONSIN-MADISON

2025

Date of final oral examination: 03/12/2025

The dissertation is approved by the following members of the Final Oral Committee:

Albrecht Karle, Professor, Physics

Lu Lu, Assistant Professor, Physics

Ke Fang, Assistant Professor, Physics

Sebastian Heinz, Professor, Astronomy

Abstract

A century on from the discovery of cosmic rays, the dynamics of cosmic accelerators and their distribution in the Universe remain under active investigation. The field of multi-messenger astronomy studies cosmic rays using complementary probes, such as gamma rays and neutrinos. Neutrinos are uniquely suited to this purpose, as they are both neutral and weakly interacting. They therefore travel unimpeded over cosmic distances, pointing directly to their sources. Analyzing the spectrum of cosmic neutrinos sheds light on the mechanisms powering their sources.

The IceCube Neutrino Observatory is a gigaton-scale neutrino telescope at the South Pole. It uses Cherenkov radiation, emitted by charged particles from interactions of neutrinos with ice nucleons, to reconstruct neutrino events. Since IceCube's observation of astrophysical neutrinos in 2013, the neutrino spectrum has been studied with numerous event classes. This thesis presents a new analysis of the neutrino spectrum at energies ranging from 5 TeV to 10 PeV, using 11.4 years of IceCube data. For this purpose we have developed a selection of 'starting events', with interaction vertices inside the detector volume. This sample combines all neutrino flavours from the entire sky, boosting IceCube's sensitivity at energies below 60 TeV. A refined treatment of systematic uncertainties, notably the atmospheric self-veto effect, has also contributed to the enhanced sensitivity of this measurement. For the first time, we reject the single power law astrophysical flux hypothesis by $> 4\ \sigma$ in favour of structure in the spectrum below ~ 30 TeV. Our preferred model is a broken power law, with parameters $\Phi_{\mathrm{Astro}}^{\mathrm{per-flavour}} = 2.28^{+0.22}_{-0.20}$, $\gamma_1 = 1.72^{+0.26}_{-0.35}$, $\gamma_2 = 2.839^{+0.11}_{-0.091}$, and $\log_{10}(\frac{\mathrm{E_{break}}}{\mathrm{GeV}}) = 4.524^{+0.097}_{-0.087}$, rejecting the single power law by $4.7\ \sigma$. We also report the detection of a muon neutrino with an energy of $11.4^{+2.46}_{-2.53}$ PeV, the highest energy neutrino observed by IceCube to date.

Acknowledgements

My time at the University of Wisconsin-Madison has been an immensely rewarding journey, through which I have been supported by many incredible people.

First, I would like to thank my adviser, Prof. Albrecht Karle, for guiding me through my doctoral studies. His profoundly valuable encouragement and insights have driven a great deal of my scientific development. I am very grateful to Prof. Lu Lu, who has always been ready with advice and inspiration. I have been extremely fortunate to work with Aswathi Balagopal V., an incredibly supportive colleague and friend.

I am also indebted to the scientists and engineers at the Wisconsin IceCube Particle Astrophysics Center (WIPAC) and the Physical Sciences Laboratory (PSL), notably Christopher Wendt, Delia Tosi, Yuya Makino, Sean Griffin, Tianlu Yuan, John Hardin, Dmitry Chirkin, Jeffrey Cherwinka, Brian Landerud, Andrew Arbuckle, and Samuel Wolcott, for their guidance through our numerous challenges. I would also like to thank Claudio Kopper and Christian Haack, for their support.

I am deeply grateful for the friendships I've built, particularly with Manuel Silva, Sarah Mancina, and Pierpaolo Savina, from whom I learned an immense amount. I would like to thank Hannah Erpenbeck, Marjon Moulai, Rogan Clark, Jesse Osborn, Delaney Butterfield, MJ Romfoe, Zoë Rechav, and my other colleagues for making IceCube such a welcoming collaboration.

Madison has become a second home to me, thanks to the close-knit community I found with Marcel Granetzny, Sarah Ferguson, Jill Peery, Julie Crowns, Laura Boisten, William Knox, and the Hoofer Sailing Club.

Finally, I am grateful everyday to my parents, Aradhana and Avijit Basu, for their unwavering love and steadfast support every day along this journey. I could not imagine doing any of this without you.

Contents

List of figures

List of tables

Chapter 1

Introduction

The field of Particle Astrophysics can be said to have originated with the discovery of Cosmic Rays in 1911-12. Prior to that, it was believed that environmental radioactivity was largely due to the existence of unstable isotopes in the Earth. Victor Hess put this to experimental test, by ascending in a balloon and studying the ambient radiation at high altitudes. If radiation was primarily terrestrial in origin, the ionization rate measured would have decreased with altitude. However, Hess discovered that the ionization rate in fact increased at high altitudes. After ruling out the Sun as a possible source of ionizing radiation, Hess was forced to conclude that highly energetic radiation is incident into the atmosphere from the cosmos. What we refer to today as Cosmic Rays are charged particles created in some of the most extreme environments in the Universe, accelerated to orders of magnitude higher energy than achievable by terrestrial particle accelerators such as the Large Hadron Collider.

Victor Hess conducted high altitude experiments by balloon.

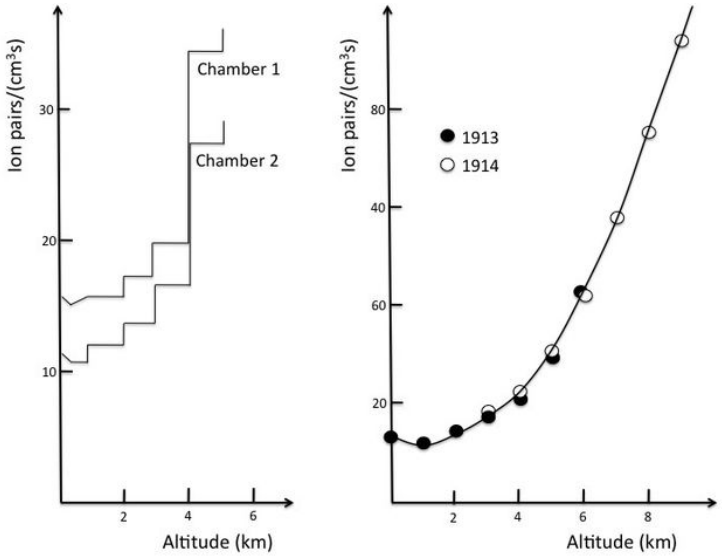

The increase in ionization rate with altitude measured by Hess, and later confirmed by Werner Kolhörster

Figure 1.1: Illustrations of the first experimental verifications of the existence of ionizing radiation from space, leading to the birth of the field of Cosmic Ray physics

1.1 Neutrinos

This thesis deals with the study of astrophysical phenomena using neutrinos at the IceCube Neutrino Observatory at the South Pole. Neutrinos are nearly-massless spin-1/2 particles (fermions) [1]. As neutral leptons, they interact primarily via the weak interaction [2]. The neutrino was first theorized by Wolfgang Pauli to explain the problem of the electron energy spectrum in neutron beta decay. Hypothesized to be a 2-body decay, the beta decay of a neutron into a proton and an electron should yield electrons of a fixed energy, instead of the continuous spectrum observed by experiments. Pauli postulated that a third particle must also be released during the decay, to account for the energy distribution of beta decay. The beta decay actually

emits what we now know to be *anti*neutrinos, and proceeds as

$$n \rightarrow p^{+} + e^{-} + \bar{\nu} \tag{1.1}$$

Subsequent measurements of the energy spectrum for products from muon and pion decay also served as compelling theoretical motivation for the existence of neutrinos. Directly detecting them, however, proved a more difficult challenge, and had to wait until 1956, when Cowan and Reines used a water detector at the Savannah River nuclear reactor to confirm the existence of the neutrino.

Each flavour of charged lepton, the electron, the muon and the tau, is associated with a specific flavour of neutrino. The three generations of leptons and their antiparticles can therefore be listed as

$$\begin{pmatrix} e^{-} \\ \nu_e \end{pmatrix}, \begin{pmatrix} \mu^{-} \\ \nu_\mu \end{pmatrix}, \begin{pmatrix} \tau^{-} \\ \nu_\tau \end{pmatrix}$$

$$\begin{pmatrix} e^{+} \\ \bar{\nu}_e \end{pmatrix}, \begin{pmatrix} \mu^{+} \\ \bar{\nu}_\mu \end{pmatrix}, \begin{pmatrix} \tau^{+} \\ \bar{\nu}_\tau \end{pmatrix}$$

The antineutrino in the beta decay, therefore, is more specifically an electron antineutrino, constrained by the conservation of lepton number, and the conservation of charge. The conservation of the specific flavour of the lepton in each reaction is not an absolute conservation law, as the neutrino flavour and mass eigenstates are different, and the mass eigenstates superpose into different flavour eigenstates during propagation. This means that the probability for measuring the flavour of a neutrino varies as it travels, first observed by Ray Davis' Homestake experiment as a deficit in the observed flux of solar neutrinos compared to theory. Larger detectors such as IMB and Kamiokande-II also observed this effect in atmospheric neutrinos, which was later experimentally confirmed by Super-Kamiokande and the Sudbury Neutrino

Observatory (SNO). The oscillation of neutrinos across different flavour eigenstates is governed by the mass difference between the mass eigenstates, as well as the energy and oscillation baseline length. Flavour conservation in the charged lepton sector is an active area of research, with experiments like Mu2e at Fermilab [3] and COMET at J-PARC [4] studying neutrinoless muon to electron conversion. As an undergraduate, I worked on event reconstructions and data acquisition (DAQ) with COMET collaboration members at KEK and Osaka University.

Other open questions deal with the relationship between neutrinos and antineutrinos. In the Dirac picture, neutrinos have the spin-state $s_z = -1/2\hbar$, while antineutrinos have spin $s_z = 1/2\hbar$ [1]. All observed neutrinos therefore have left-handed helicities and all antineutrinos have right-handed helicities, in the massless limit. Neutrinos and antineutrinos with reversed helicities, if they exist, are theorized to be very heavy, of the order of unification scales $\approx 10^{15}$ GeV, or simply inert to the weak interaction, as sterile neutrinos. The finite mass of a neutrino means that chirality is not conserved, however, but the very small mixing amplitude of a neutrino/antineutrino with reversed chirality means that an infinitesimally small fraction would exist. Experimental limits on the mass of the neutrino eigenstates are set both by direct measurement (by the KATRIN experiment [5] in 2022), and by cosmological measurements of the Cosmic Microwave Background by the Planck satellite and terrestrial instruments such as the Atacama Cosmology Telescope and the South Pole Telescope [6]

As neutral particles, however, it is also possible for neutrinos and antineutrinos to be the same particle, which may help explain why they are so much lighter than other elementary particles. In this Majorana picture, neutrinos have a spin-up and a spin-down state which are realized as neutrinos and antineutrinos in the Dirac view. Many experiments are underway to differentiate between these, including searches for neutrino-less double beta decay with experiments such as CUORE and KamLAND-

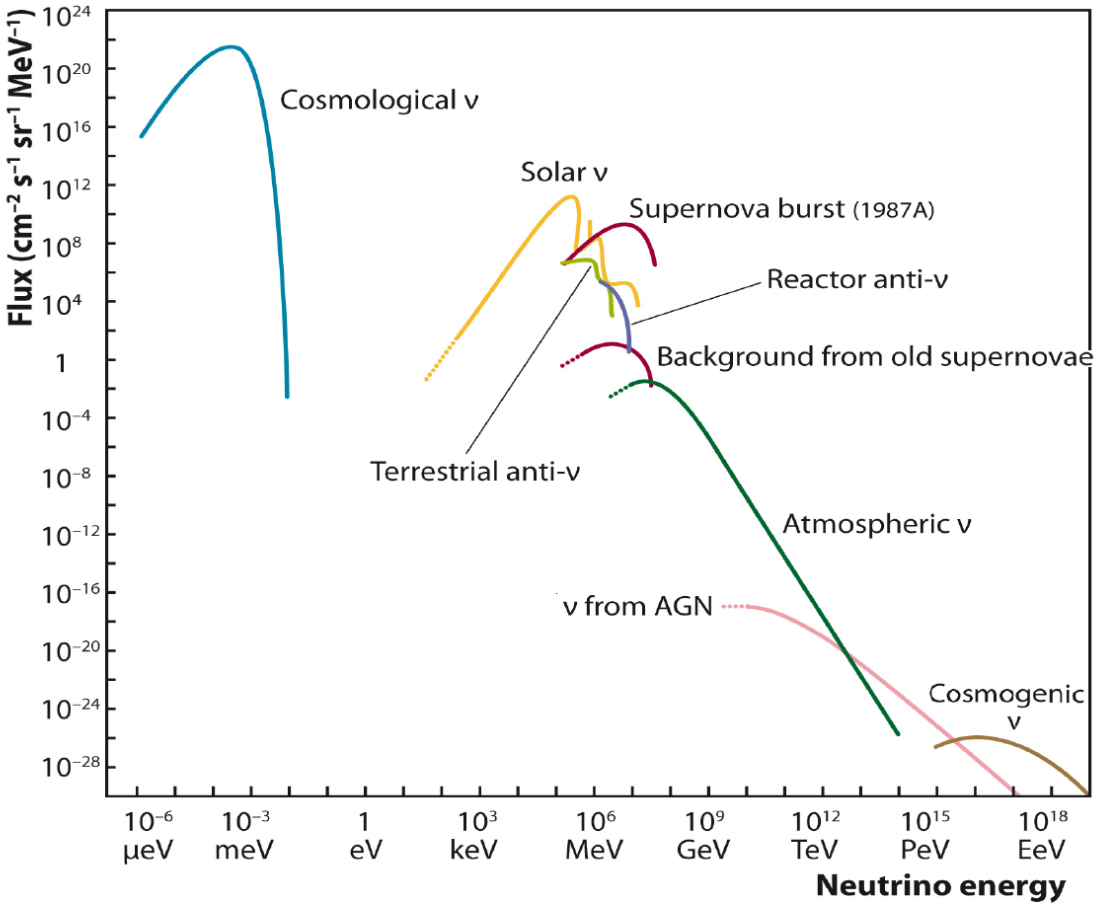

Figure 1.2: The various sources of neutrinos and their fluxes measured at the Earth [7]

Zen.

1.1.1 Where do neutrinos come from?

Neutrinos are produced in many environments across the cosmos, across almost 25 orders of magnitude in energy, as illustrated in Fig. 1.2. At the lowest energies around 1μeV-1 meV are cosmological or relic neutrinos, which decoupled from matter 1 s after the Big Bang [8], before electron and positron annihilation. With a temperature of 1.95 K and number density of ≈ 340 cm^{-3}, the Cosmic Neutrino Background (CNB) makes neutrinos the second most common particle in the cosmos, after pho-

tons from the Cosmic Microwave Background (CMB). The effects of the CNB on the CMB anisotropies have been measured by the Planck satellite, making a strong case for the existence of the CNB and verifying a prediction of Big Bang cosmology.

At the next energy scale, from keV to MeV, we find the solar neutrino flux dominant, along with neutrinos from supernovae and nuclear reactors. The 'solar neutrino puzzle', or the apparent deficit in the flux of solar neutrinos, was one of the observations which led to the postulation of neutrino oscillations. Other MeV neutrino sources include supernovae, such as SN1987A, which was observed by three neutrino detectors, Kamiokande-II (Japan), IMB (US) and Baksan (Russia). Neutrinos from radioactive decays within the Earth (geo-neutrinos) and the diffuse supernova neutrino background from past core-collapse supernovae are also in this energy range.

At higher energies upto 100 TeV, the primary source of neutrinos at the Earth are created in cosmic ray interactions with nuclei in the atmosphere, and are known as atmospheric neutrinos, first discovered in the Kolar Gold Fields in India. The high energy cosmic rays incident on the Earth from cosmic accelerators, which interact with nuclei in the atmosphere producing showers of short-lived mesons, like pions and kaons. The decay of charged pions and kaons creates neutrinos following

$$
\begin{aligned}
p^+ + \text{nucleus} &\rightarrow \pi^\pm + X \\
p^+ + \text{nucleus} &\rightarrow K^\pm + X \\
K^\pm &\rightarrow \pi^\pm, \mu^\pm, \pi^0, e^\pm, \nu_{e,\mu}, \bar{\nu}_{e,\mu} \\
\pi^+ &\rightarrow \mu^+ + \bar{\nu}_\mu \\
\pi^- &\rightarrow \mu^- + \nu_\mu \\
\mu^- &\rightarrow e^- + \bar{\nu}_e + \nu_\mu \\
\mu^+ &\rightarrow e^+ + \nu_e + \bar{\nu}_\mu
\end{aligned}
\tag{1.2}
$$

These decays result in a flux of high energy muons and neutrinos at Earth, and have been studied by large underground Cherenkov detectors such as Super-Kamiokande. At the TeV energy scale and above, we begin to see astrophysical neutrinos from extragalactic sources, such as Active Galactic Nuclei (AGNs). These cosmic accelerators create beams of high energy charged particles, which interact with the surrounding medium creating various hadrons, including pions. As illustrated above (Eq. 1.2), the decay of charged pions creates a flux of high energy neutrinos, accompanied by gamma ray photons from neutral pion decay. As a coda to our study of the sources of neutrinos, at even higher energies we find a theoretical flux of neutrinos from the interaction of cosmic rays with CMB photons, known as the cosmogenic neutrino flux.

1.1.2 Astrophysical Neutrinos

Astrophysical neutrinos offer an entirely new window to the high energy universe. Unaffected by intergalactic magnetic fields, neutrinos propagate along straight paths leading back towards their sources, unlike charged cosmic rays. As they only interact weakly, unlike gamma-ray photons, they are not absorbed or attenuated on their journey through the Universe. Their disinclination to interact has its downsides, however, and makes them extremely difficult to detect. The detection of neutrinos at TeV scales and higher requires an extremely large instrumented volume, to capture the Cherenkov radiation emitted by charged secondaries during neutrino interactions. This is the operating principle behind the IceCube Neutrino Observatory, which in 2013 reported the first detection of high energy astrophysical neutrinos [9]. The high energies of the detected neutrinos (> 100 TeV) indicated that these neutrinos originated from extragalactic sources, as the magnetic field of the galaxy would not be able to confine a progenitor charged particle accelerated to sufficient energies (the

Hillas criterion, discussed in sec. 2.1.1). Further significant detections from the blazar TXS0506+056 [10] and the Seyfert galaxy NGC1068 [11], demonstrate the importance of neutrino telescopes to the burgeoning field of multi-messenger astronomy.

1.1.3 The Medium Energy Starting Events sample

In this thesis, we will explore a new technique for selecting these astrophysical neutrinos with the IceCube Neutrino Observatory, and report a measurement of the flux of diffuse astrophysical neutrinos from 1 TeV upto 10 PeV using 11.4 years of data. The Medium Energy Starting Event selection (MESE) using neutrino events with the vertices contained within the detector (starting events), which yield sensitivity to neutrinos of all flavours and from the entire sky. Inheriting techniques from the prior High Energy Starting Event sample [12] and 2-yr MESE selection [13], we update the background rejection cuts used and the treatment of systematics to gain sensitivity to the astrophysical flux down to ≈ 5 TeV. We find that a Broken Power Law fits the energy spectrum best, with a low energy spectral index of 1.72, a high energy spectral index of 2.84, and the change in spectral index occurring at 33.11 TeV. In addition, we report the detection of the highest energy muon neutrino detected by IceCube to date, at 11.4 PeV, in the MESE event selection. As MESE is sensitive to neutrinos of all flavours, it is possible to measure the composition of astrophysical neutrinos as they arrive at Earth. After accounting for oscillations as they propagate through the cosmos, we can study the flavour composition at sources. Using the Taupede classification algorithm to identify double cascade events, a signature of tau neutrino interactions, an analysis by Aswathi Balagopal, using the MESE dataset, has for the first time rejected the hypothesis of no tau neutrinos in the diffuse flux upto 68% confidence [14].

We aim to publish the results of the MESE diffuse analysis along with a similar

result from an independent combined analysis of IceCube through-going tracks and cascades in a joint submission to Physical Review Letters [15] and Physical Review D [16], along with an independent publication of the result from the flavour composition analysis [14].

Chapter 2

On The Origin of Astrophysical Neutrinos

2.1 Cosmic Rays

The primary source of ionizing radiation in the Earth's atmosphere arises from charged particles from deep space, known as cosmic rays. These are atomic nuclei which span several orders of magnitude in energy, upto 10^{18} eV, and propagate to Earth from their sources. However, as these are charged particles, they are deflected from a linear trajectory by cosmic magnetic fields, and do not trace back to their points of origin. The mechanisms for how charged particles are accelerated to such high energies are still unknown, and are under active investigation. Studies of the processes powering such cosmic accelerators require identification and probing of their sources. Among the probes of cosmic ray sources, neutrinos and photons, as neutral particles, are undeviated during their journeys from their origin, and thus allow one to map the sites of cosmic ray acceleration. In particular, neutrinos are uniquely suited to the study of cosmic accelerators, as they interact extremely rarely

via the weak interaction, and are thus able to pass through cosmological distance scales, unlike photons, which are greatly attenuated beyond 10^5 GeV. The combination of information from astrophysical neutrinos along with gamma ray photons and cosmic rays has spurred the growth of the field of multi-messenger astrophysics.

Further investigation of the cosmic ray spectral features may provide clues as to the acceleration mechanism underpinning it. These include the *knee*, a spectral softening (steepening) observed at 3 PeV. A further steepening is observed at around 100 PeV, known as the *second knee*, followed by a hardening around 10 EeV termed the *ankle*. These features are hypothesized to be caused by a composition dependent energy cutoff in the spectrum of galactic cosmic rays in the PeV regime, followed by a transition to cosmic rays of primarily extragalactic origin in the EeV range. For a given particle charge and mass, a particle accelerated in the galactic magnetic field can only reach a certain energy before its gyroradius exceeds the size of the galaxy, allowing it to escape into the cosmos. Above $\sim 50\ EeV$, the flux of charged particles is suppressed due to resonant interactions with cosmic microwave background (CMB) photons (the GZK cutoff) following

$$\begin{aligned} p^+ + \gamma \rightarrow \Delta^+ &\rightarrow \pi^+ + n \\ &\rightarrow \pi^0 + p \end{aligned} \tag{2.1}$$

2.1.1 Cosmic Ray Acceleration Mechanisms

One of the driving questions behind the investigation of cosmic ray acceleration is the source of power for the accelerator. An order of magnitude estimate of the power required to supply galactic cosmic rays may be obtained following the derivation in Gaisser [18]. The distribution of cosmic ray energy density, ρ_{E} is assumed to be roughly constant throughout the galaxy, at a value of $\sim$ 1 eV/cm^3. We also

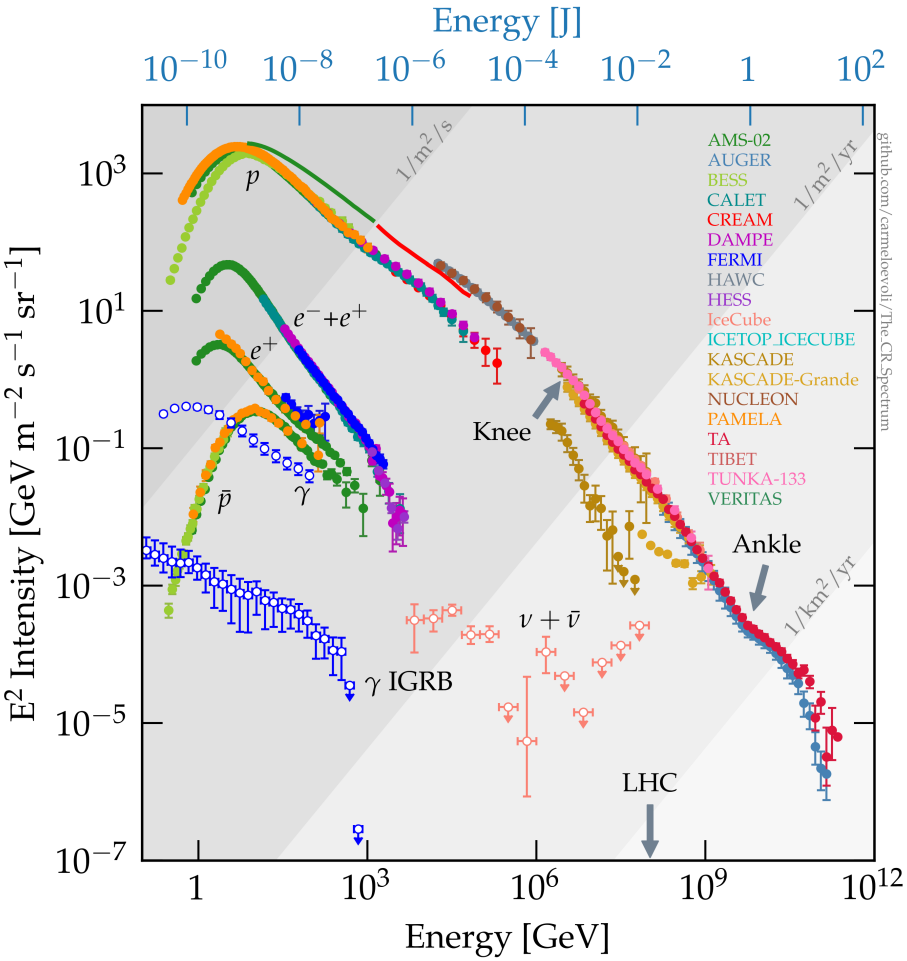

Figure 2.1: The high energy cosmic ray spectrum as a function of energy, multiplied with a factor of E^2 to better illustrate features beyond a power law. Plot from ref. [17]

require a calculation of the time τ_R during which cosmic rays are confined within the source volume, assumed here to be the galactic disk, with volume $V_d = \pi R^2 d = \pi(15 \text{ kpc})^2(200\ pc) = 4 \times 10^{66}$ cm^3. Following a diffusion model for the confinement of cosmic rays, τ_R evaluates to $\sim 6 \times 10^6$ yrs. With these quantities, we calculate the power of galactic cosmic rays $L_{\rm CR}$ to be

$$L_{\rm CR} = \frac{V_d \rho_{\rm E}}{\tau_R} \sim 5 \times 10^{40} \text{ erg/s} \tag{2.2}$$

Various mechanisms have been proposed for how charged particles are accelerated to high energies, under the influence of electric and magnetic fields. In 1949, Enrico Fermi elucidated a method of particle acceleration which could explain the characteristic power law shape observed in the cosmic ray spectrum [18]. In his initial theory, Fermi postulated that charged particles 'scattered' off inhomogeneities in moving clouds of plasma. The result of this diffusion inside the gas cloud is that on average after multiple scatterings, the particle moves with the cloud and gains energy. This can be observed following the derivation in Gaisser, where a particle with energy E_1, when boosted to the rest frame of the gas, gives

$$E_1^{'} = \gamma E_1(1 - \beta cos\theta_1) \tag{2.3}$$

The collisionless 'scattering' process is elastic in the frame of the gas, and therefore the energy of the particle before it escapes $E_2^{'} = E_1^{'}$. Converting back to the laboratory frame,

$$E_2 = \gamma E_2^{'}(1 + \beta cos\theta_2^{'}) \tag{2.4}$$

Upon substituting Eq. 2.3 in Eq. 2.4, we get the change in energy for a single encounter in terms of the angles $\theta_1^{'}$ and $\theta_2^{'}$

$$\frac{\Delta E}{E_1} = \frac{1 - \beta cos\theta_1 + \beta cos\theta_2^{'} - \beta^2 cos\theta_1 cos\theta_2^{'}}{1 - \beta^2} - 1 \tag{2.5}$$

Calculating the energy loss averaged across the appropriate angular distributions, we have, for the case of moving plasma clouds

$$\frac{\Delta E}{E_1} = \frac{1 + 1/3\beta^2}{1 - \beta^2} - 1 \sim 4/3\beta^2 \tag{2.6}$$

This is the original Fermi result, now termed a 'second order' acceleration, as the change in energy is proportional to β^2. Particles can either gain or lose energy in a single encounter, but after multiple scatterings, there is an overall gain. Eq. 2.5 also

applies to another interesting scenario, one of a planar shockwave passing through a medium. Particles therefore can diffuse across this shock front, akin to a tennis ball bouncing off a moving wall. Assuming β in this context to be the relative velocity of the shocked gas to the unshocked gas, and reevaluating the integral, we now have

$$\frac{\Delta E}{E_1} = \frac{1 + 4/3\beta + 4/9\beta^2}{1 - \beta^2} - 1 \sim 4/3\beta \tag{2.7}$$

This 'first order' acceleration always results in an energy gain for a particle. To see how this acceleration mechanism results in a power law spectrum, we consider a repeated acceleration process where a particle of energy E_0 increases its energy by $\Delta E = \epsilon E$ per cycle. After n cycles, we have

$$E_n = E_0(1 + \epsilon)^n \tag{2.8}$$

Assuming that in each cycle, the particle has a probability of escape from the acceleration region $P_{\rm esc}$, the probability that the particle is still undergoing acceleration after n cycles is

$$P_{\rm acc} = (1 - P_{\rm esc})^n \tag{2.9}$$

The proportion of particles accelerated to energies beyond E_n is therefore

$$N(> E_n) \propto \sum_{m=n}^{\infty} (1 - P_{\rm esc})^n = \frac{(1 - P_{\rm esc})^n}{P_{\rm esc}} \tag{2.10}$$

Substituting the value of n from Eq. 2.8 in Eq. 2.10, we obtain

$$\begin{aligned} N(> E_n) &\propto \frac{(1 - P_{\rm esc})^{ln(\frac{E_n}{E_0})/ln(1+\epsilon)}}{P_{\rm esc}} \\ &= \frac{1}{P_{\rm esc}} (\frac{E_n}{E_0})^{ln(1-P_{\rm esc})/ln(1+\epsilon)} \\ &\sim \frac{1}{P_{\rm esc}} (\frac{E_n}{E_0})^{-\frac{P_{\rm esc}}{\epsilon}} \end{aligned} \tag{2.11}$$

If we define the escape probability in terms of the characteristic periods of the acceleration and escape phenomena, $T_{\rm acc}$ and $T_{\rm esc}$, we may define $P_{\rm esc} = \frac{T_{\rm acc}}{T_{\rm esc}}$. This illustrates

that higher energy particles must remain in the acceleration zone for longer periods of time, and an accelerator with a certain characteristic acceleration time must have an upper bound on the energy to which it can accelerate particles. This also implies a maximum confinement area for particles from a given accelerator. This condition is evaluated by requiring that the maximum gyro radius of a particle in the accelerator's magnetic field is the radius of the accelerator, known as the Hillas criterion. A particle with higher energy than the Hillas limit will escape confinement from its source environment. To reach ultra high energies, therefore, an accelerator must either be very large or have a very strong magnetic field

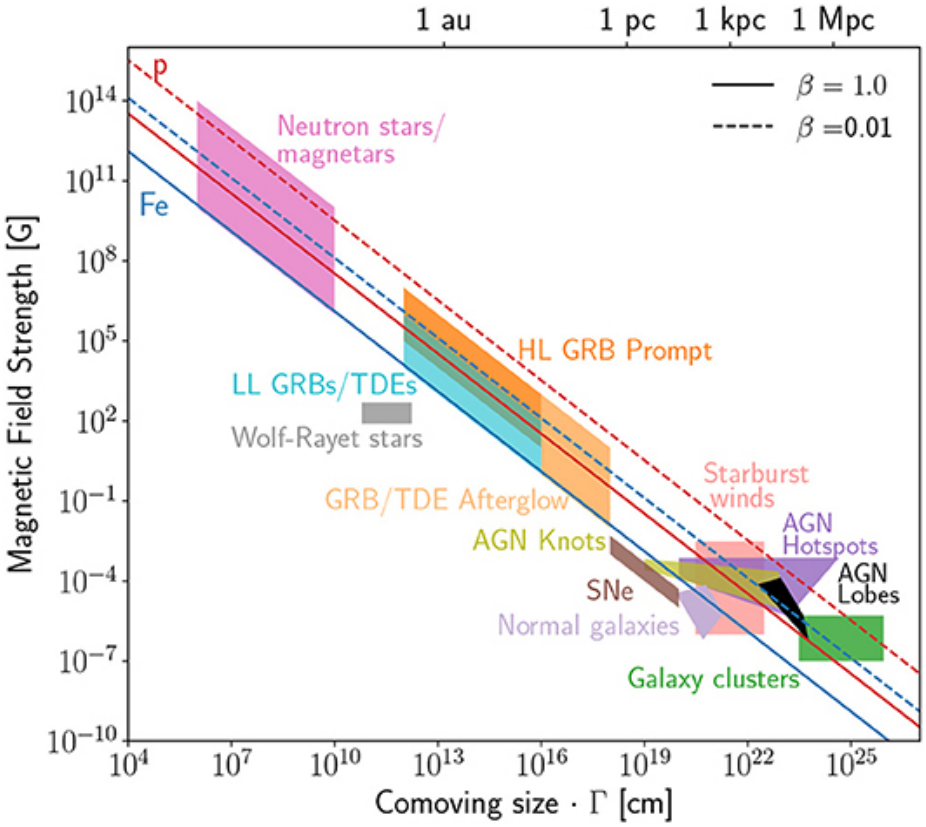

Figure 2.2: A Hillas plot of sources in terms of their sizes and magnetic fields. The fields B are evaluated in the comoving source frame, while the x-axis is a plot of the radius from the central engine times the Lorentz factor of the flow Γ. Plot from ref. [19]

2.1.2 Source Candidates

The observation of high energy cosmic rays at the Earth does not directly indicate their sources, as they may have been deflected from their original trajectories by cosmic magnetic fields. If, however, cosmic rays from an accelerator encounter a 'beam dump', interacting with matter or radiation during their journey, they may produce gamma rays or neutrinos. As neutral particles, these are unaffected by magnetic fields over cosmological distances, and trace back a path to their points of origin. Searches for sources of gamma rays or neutrinos, therefore, are fruitful avenues to explore the phenomena of cosmic ray acceleration. In particular, these studies help elucidate whether the mechanism of acceleration involves protons (hadronic acceleration), or electrons and positrons (leptonic acceleration). Both hadronic acceleration and leptonic acceleration produce gamma rays, however, either by the decay of neutral pions in the hadronic case, or by synchrotron emission and inverse Compton scattering in the leptonic scenario. Another caveat of gamma ray astronomy is that the Universe is opaque to the highest energy gamma rays, due to pair production interactions with background photons. As neutrinos only interact weakly, this disadvantage does not apply to them, and they can traverse vast distances unimpeded. The observation of neutrino emission is also a characteristic signature of proton acceleration, and can thus differentiate between the two acceleration mechanisms.

The identification of neutrino sources may be performed by correlating reconstructed neutrino arrival directions with catalogs of known astrophysical sources taken one at a time, or with all the sources of a catalog stacked simultaneously [20]. When searching for individual sources of high significance, care must be taken to correct for the number of trials performed, which can weaken the statistical significance of observations. Stacking catalog searches, however, are more sensitive to a signal from

several weak sources, but greatly depend on the weighting scheme used. Some potential source classes are described here, which may account for both neutrino emission from within the galaxy as well as from extragalactic regions.

2.1.2.1 Galactic Sources

These are the closest sites of particle acceleration, and according to the Hillas criterion, cannot accelerate the highest energy cosmic rays observed at Earth. Their proximity does mean that they are some of the most luminous sources, however. Some of these sources include

- **Supernova Remnants** are created during the deaths of massive stars, between 8-40 solar masses, which explode violently emitting a large amount of energy ($\sim 10^{51}$ erg) as MeV neutrinos. In addition, core collapse supernovae also create a rapidly advancing shock front during their gravitational collapse, creating a suitable environment for diffusive shock acceleration. Supernova remnants are primary candidates for the sources of galactic cosmic rays, and are also bright in gamma rays. The eruption of stellar material into the environment surrounding a supernova indicate suitable beam dumps for the production of TeV and sub-TeV neutrinos from supernovae. Supernova progenitors below 20 solar masses compress into neutron stars after the explosion. These classes of supernova remnants may contain **Pulsar Wind Nebulae**, created by rotating neutron stars which have a magnetic field misaligned with their rotation axes. This results in the emission of electromagnetic pulses. The magnetic field is dragged through the surrounding interstellar medium creating a strong shock where the wind decelerates to sub relativistic speeds. This provides an acceleration site which may also create neutrinos.

- **Binary Systems** of two stars in orbit around each other may also power cosmic accelerators via the process of accretion from one star onto another. Shock acceleration may occur as matter accelerates in the gravitational potential of one compact object. The mergers of compact objects such as neutron stars and black holes, known to generate gravitational wave signals, are also believed to be sites of cosmic ray acceleration.

2.1.2.2 Extragalactic Sources

Some of the highest energy particles detected at the Earth must originate outside the Milky Way, to satisfy the Hillas criterion. Some of the most promising source candidates are

- **Active Galactic Nuclei** are among the most promising sources of high energy cosmic rays. These are generally supermassive black holes of masses $10^6 - 10^9$ solar masses. Accretion of interstellar matter into a disk around the black hole powers radiation from the disk and its corona. A relativistic axial jet is also driven by the angular momentum of the rotating black hole and the accretion disk. The term blazar is used for AGNs with a jet aligned towards the Earth, with a higher luminosity due to the beaming effect. A variety of similar classifications exist depending on the orientation of the AGN, along with its radio emissivity. Most AGN are radio-quiet, typically classified as Seyfert galaxies.

- **Tidal Disruption Events** occur when stars are ripped apart in the Roche limit of a supermassive black hole. This is a violent transient event, ejecting almost half the mass of the star while accreting the remainder in the black hole accretion disk.

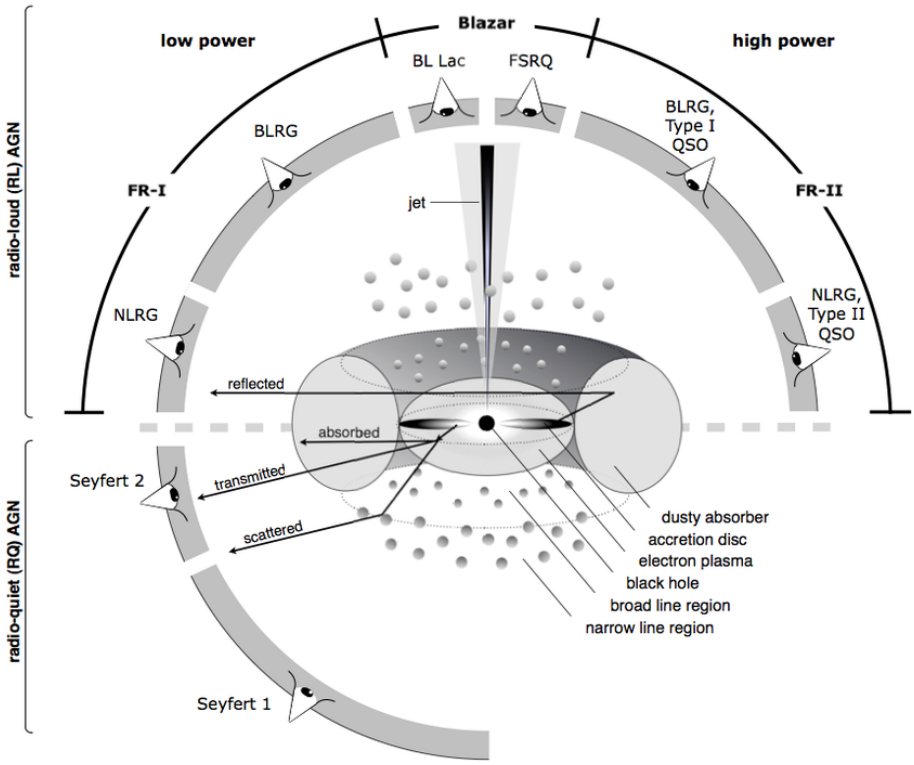

Figure 2.3: A schematic diagram of our classification of various observed active galactic nuclei. When an AGN jet is directed directly at the observer, the increase in luminosity due to beaming leads to classification as a blazar. If radio emissions have been observed from the AGN, they are classified as Fanaroff-Riley Type I or II depending on the radio luminosity, with Type I galaxies fainter at the edges of their lobes, while Type II galaxies are more luminous with hotspots at the edges of their lobes. Based on the viewing angle, these may also be narrow line radio galaxies (NLRG) or broad line radio galaxies (BLRG). Extremely luminous radio AGNs are termed quasi-stellar objects, or quasars (QSOs). Plot from ref. [21]

- **Gamma Ray Bursts** (GRBs) are some of the most luminous explosions in the Universe. They are classified into short duration GRBs, of the order of two seconds, and long GRBs, lasting for 10-1000 s. Short GRBs are believed to originate from binary neutron star mergers, supported by the association of GW170817 with the GRB 170817A. Long duration GRBs on the other hand are believed to be associated with core collapse supernovae. In a gamma ray burst, particle acceleration is driven by shock fronts created by the ejection of matter

in multiple shells, where protons are accelerated to very high energies while electrons lose energy to synchrotron radiation, visible as prompt gamma-ray emission.

- **Cosmic Ray Reservoirs** are magnetized regions of space which serve to confine cosmic rays emitted from accelerators, providing opportunities for high energy nucleons to interact with interstellar matter and produce high energy neutrinos and gamma rays. These include galaxy clusters, which are known to have μG magnetic fields capable of confining cosmic rays for long timescales. Cosmic rays above PeV scales accelerated by AGNs in galaxy clusters would be able to escape confinement, while lower energy particles would lose energy during confinement. This would explain the hard spectrum of high energy neutrinos below a few PeV, while simultaneously accounting for the origin non-blazar diffuse gamma-ray background as well. This mechanism has interesting implications for the observation of the similar energy densities of the cosmic messengers, which implies a relation between their origins. Galaxies with a very high rate of star formation are termed starburst galaxies, with high matter densities and magnetic fields on the order of mG. This causes cosmic rays to lose the bulk of their energy via collisions with matter or adiabatic cooling in a vacuum before they can escape. These collisions result in the emission of neutrinos and gamma rays.

2.1.3 Cosmic Ray Air Showers

Cosmic rays interact with nuclei in the upper atmosphere upon their arrival to Earth, and emit showers of secondary particles known as air showers. These undergo further interactions in the atmosphere resulting in a cascade of various particles at the Earth.

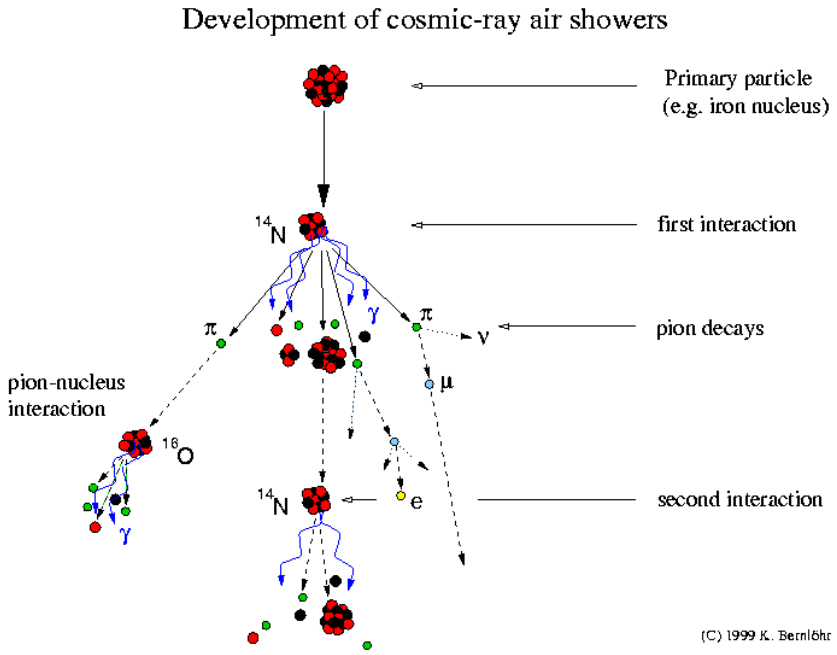

Figure 2.4: A schematic of a cosmic ray air shower. Plot from ref. [22]

These include hadrons such as pions and kaons, gamma ray photons and charged leptons such as electrons, positrons and muons. The decay of charged pions and kaons via the weak interaction, elaborated upon further in sec. 2.2, also generates a flux of neutrinos, known as atmospheric neutrinos. Gamma rays from the cosmos or from neutral pion decay also create electromagnetic cascades of electrons and positrons through Bethe-Heitler pair production. Neutrinos may also be produced through the decay of heavier charmed mesons at higher energies. Their short lifetimes mean that their decay occurs before they have a chance to interact, and they are therefore known as 'prompt neutrinos'.

For neutrinos from the decay of charged pions and kaons, typically we perform a Monte Carlo simulation of the full air shower, or solve coupled cascade equations to arrive at the flux. Insights can still be obtained from a simplified analytical expression

from ref. [18], however-

$$\phi_\nu(E,\theta) = \phi_{\mathrm{CR}}(E,\theta)\left[\frac{A_{\pi\nu}}{1+\frac{B_{\pi\nu}E\cos(\theta)}{\epsilon_\pi}} + \frac{A_{K\nu}}{1+\frac{B_{K\nu}E\cos(\theta)}{\epsilon_K}} + \frac{A_{\mathrm{charm},\nu}}{1+\frac{B_{\mathrm{charm},\nu}E\cos(\theta)}{\epsilon_{\mathrm{charm}}}}\right] \tag{2.12}$$

The coefficients $A_{\pi\nu}, B_{\pi\nu}, A_{K\nu}$, and $B_{K\nu}$ determine the ratio of neutrinos generated

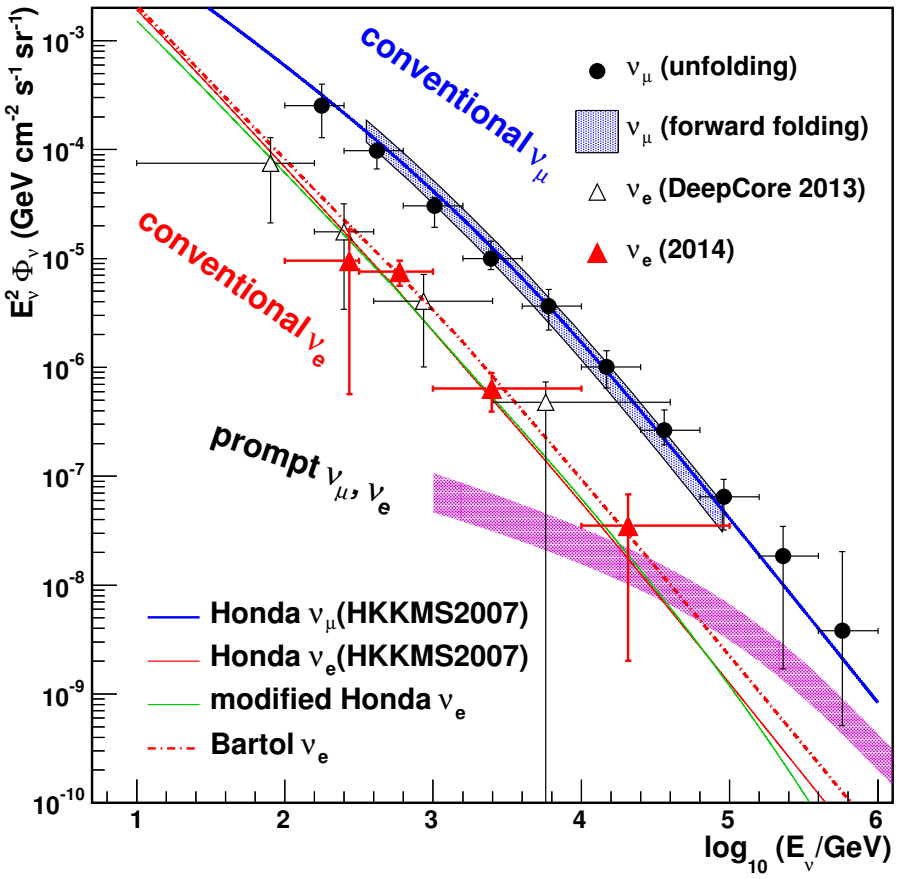

Figure 2.5: An unfolded energy spectrum of atmospheric electron and muon neutrinos. The depicted prompt flux has not yet been observed, and is a theoretical prediction. We expect the flux of atmospheric tau neutrinos to be purely from charm mesons, as it is kinematically impossible for pions or kaons to decay into tau leptons. Plot from ref. [22]

from pions and kaons respectively, and are either derived from simulation or from fits to experimental data. The terms ϵ_π and ϵ_K denote the energies where the decay and interaction lengths are equal, and are 115 GeV and 850 GeV for pions and kaons respectively. We observe that, at neutrino energies $E << \epsilon_{\pi,K}$, the atmospheric

neutrino spectrum follows the primary spectrum, with the pions and kaons decaying before they can lose energy from interactions. In the intermediate neutrino energy regime, where $\epsilon_\pi < E < \epsilon_K$, we find that kaons contribute an increasing fraction of atmospheric neutrinos. In the higher TeV energy ranges relevant to the analysis presented in this thesis, however, where $\epsilon_{\pi,K} << E$, meson interactions dominate over decays. As both scale as 1/E, we find that the atmospheric neutrino spectral index is one unit softer than the cosmic ray primary spectrum. The angular distribution of atmospheric neutrinos is symmetric in the upgoing and downgoing directions, and peaked at the horizon reflecting the higher probability of meson decay. The remaining terms $A_{\text{charm},\nu}$ and $B_{\text{charm},\nu}$ govern prompt neutrino production from the decay of charmed mesons. Due to the short lifetime ($\sim 10^{-12}$ s) of charmed mesons, prompt neutrinos closely follow the spectrum of cosmic ray primaries, and do not show a particular angular dependence, as there is no impact of interactions.

Atmospheric muons are also created during cosmic ray air showers, and due to

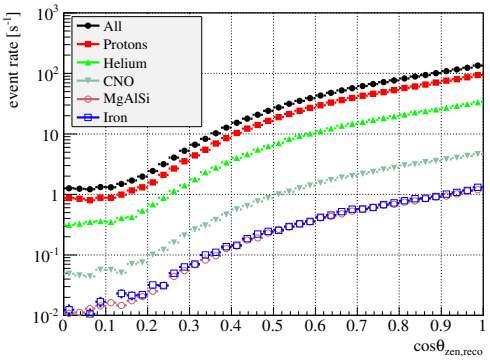

Figure 2.6: A plot of the expected muon rate at IceCube as a function of cosine zenith, with cosine zenith 0 corresponding to events from the horizon, and cosine zenith 1 corresponding to vertically downgoing events. Plot from ref. [23]

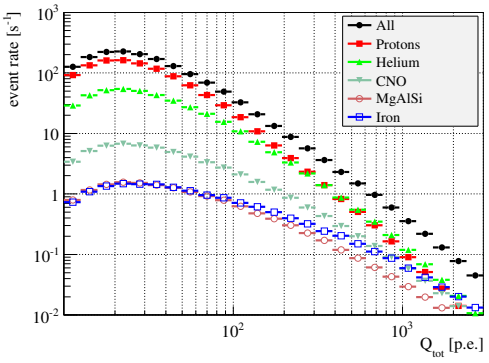

Figure 2.7: A plot of the expected muon rate at IceCube as a function of deposited charge, which is a proxy for the energy of the event. Plot from ref. [23]

their relativistic energies, survive until they reach the Earth's surface before decay-

ing. Figures 2.6 and 2.7 show the expected muon flux at IceCube as a function of cosine zenith, and deposited charge (a proxy for the energy of the muon). We expect to detect 3000 muons every second. The primary products of cosmic ray air showers which are relevant to neutrino astronomy at IceCube are the aforementioned atmospheric neutrinos and muons. These act as backgrounds in searches for cosmic neutrinos, and it is therefore extremely important to have an accurate model for their fluxes. This involves an estimate of the composition of primary cosmic rays, along with a model of their interactions in the atmosphere. The mass composition model of primary cosmic rays is constructed by fitting aggregated cosmic ray spectral data from multiple experiments, assuming that the cosmic ray flux can be broken down into a finite number of component nuclides. Another important aspect of modelling the atmospheric background from air showers is the hadronic interaction model governing the collisions of cosmic rays with atmospheric nucleons, along with the energy distributions of the daughter particles. The different hadronic interaction models are constructed using fits to collider data and then extrapolated to the higher centre of mass energies of interest to neutrino astronomy.

2.2 Production Mechanisms of High Energy Neutrinos

The flux of neutrinos created by the interactions of the cosmic rays at their sources depends on the column density of the target nuclei or photons. However, in an extremely dense environment, most cosmic rays would be unable to escape the source, and therefore for efficient cosmic ray production at very high energies, the sources must be thin to the accelerated nuclei. An upper bound can be set on the neutrino flux created by cosmic rays from a thin source, by requiring that all the cosmic rays

accelerated undergo interactions. This limit, known as the Waxman Bahcall bound, can be understood as a calorimetric bound on the neutrino flux to avoid saturating the observed cosmic ray flux. The major channels through which neutrinos are produced at cosmic accelerators are through the weak decays of pions and kaons, following [18]

$$\begin{aligned} \pi^{\pm} &\rightarrow \mu^{\pm} + \nu_{\mu}(\bar{\nu}_{\mu})(\ 100\%) \\ K^{\pm} &\rightarrow \mu^{\pm} + \nu_{\mu}(\bar{\nu}_{\mu})(\ 63.5\%) \\ K_L &\rightarrow \pi^{\pm} + e^{\pm} + \nu_e(\bar{\nu}_e)(\ 38.7\%) \\ \mu^{\pm} &\rightarrow e^{\pm} + \nu_e(\bar{\nu}_e) + \bar{\nu}_{\mu}(\nu_{\mu}) \end{aligned} \tag{2.13}$$

The leptonic decay products carry on average 25% of the energy of the initial parent pion. This translates to roughly 5 percent of the energy of the initial proton [24]. The energy of the gamma photon in the case of neutral pion decay is a factor 2 higher, i.e 10% of the parent proton energy. These pions are created during the interactions of protons with either photons in a radiation field, known as the p-γ interaction, or with other protons in a gaseous environment, commonly referred to as p-p interactions. In p-p interactions, pion production is possible down to GeV proton energies, and at higher center of mass energies, multi-pion production plays a major role. As the target protons are at rest relative to the accelerated cosmic rays, neutrinos from p-p scenarios therefore inherit the power law spectrum of their parent cosmic rays. Nuclei heavier than protons can be modelled as an aggregate of A protons each with an equal fraction of the total energy. The neutrinos observed by IceCube in the 1 TeV-10 PeV range are thus implied to correspond to cosmic ray primaries with energies below the EeV scale, and are not necessarily from UHECR sources. In addition, when the p-γ interaction is considered, the production cross section of pions has a sharp resonance at the Δ^+ mass of 1232 MeV. Assuming that each of the 3 daughter neutrinos inherit 5% of the primary energy, for neutrinos of $\sim$ 100 TeV energy, we require an intense target field of photons in the keV (X-ray) energy range to efficiently produce

neutrinos which are detectable by IceCube [25]. In addition to the main Δ resonance channel, the p-γ interaction also produces pions through non-resonant direct π^+ exchange, and at higher center of mass energies through multi-pion processes. These processes modify the neutrino production spectrum depending on the proton and photon energies, and require a threshold proton energy of 70 (E_γ/keV) TeV. In general, however, the steep target photon spectrum means that in the p-γ scenario, the Δ channel is relevant even to very high primary energies. This lends a bump-like feature in the neutrino spectrum from p-γ interactions [26], around the characteristic neutrino energy $E_{\nu,\mathrm{bump}} \approx 0.01\ \mathrm{GeV}^2/E_\gamma$. This bump may be modelled in many ways, including a log-parabolic form which is studied further in this thesis.

As a signature of hadronic acceleration is the production of both neutral and charged pions, which decay into gamma rays and neutrinos respectively, we can examine the link between their emission spectra and the dynamics of the parent accelerator. Considering the decay of charged pions, the neutrino energy rate is the product of the neutrino energy in the cosmic frame ϵ_ν and number flux $\mathcal{Q}_\nu$, following the notation used in [27],

$$\epsilon_\nu \mathcal{Q}_\nu = \frac{3\mathrm{K}}{4(1+\mathrm{K})} f_{pp,p\gamma} \epsilon_p \mathcal{Q}_p \tag{2.14}$$

where the factor 3/4 accounts for the fact that three of the four leptons created during the decay of a charged pion are neutrinos. The term K denotes the average ratio of charged to neutral pions created, with $\mathrm{K} \approx 1$ for p-γ interactions and $\mathrm{K} \approx 2$ for p-p interactions. The term $f_{pp,p\gamma}$ accounts for the energy dependent efficency of cosmic ray interactions in the sources environments. This yields the diffuse neutrino flux to be

$$\mathrm{E}_\nu^2 \Phi_\nu = \frac{c}{4\pi} \int \frac{dz}{(1+z)^2 H(z)} [\epsilon_\nu \mathcal{Q}_\nu]_{\epsilon_\nu = (1+z)\mathrm{E}_\nu} \tag{2.15}$$

where E_ν is the observed neutrino energy, and H(z) is the redshift dependent Hubble parameter. The flux of gamma rays from π^0 can be related to the neutrino flux using

the relation that each π^0 decays into two gamma ray photons.

$$E_\nu^2 \Phi_\nu = \frac{3K}{4} E_\gamma^2 \Phi_\gamma \tag{2.16}$$

2.2.1 Gamma Rays

The energy relation between photon and neutrino power fluxes as observed in Eq. 2.16 indicates a connection between the fluxes of the three cosmic messengers, cosmic rays, neutrinos and gamma rays. We see from Fig. 2.8 that the energy densities are very similar across these messengers, which may hint at a relationship among their origins. This would be consistent with a model in which source candidates such as AGN jets embedded within large scale structures [28] accelerate cosmic rays, which then interact with the surrounding environment to generate neutrinos and photons. The gamma ray flux in Fig. 2.8 is derived from the measurement of the isotropic diffuse gamma ray background (IGRB) from the Large Area Telescope instrument aboard the Fermi Gamma-Ray Space Telescope (*Fermi*-LAT). This flux is the superposition of all unresolved extragalactic gamma ray sources, after having subtracted the flux of resolved sources from the total extragalactic gamma ray background (EGB). Both the IGRB and the EGB show a suppression in the flux above 100 GeV, predicted to be because of Bethe-Heitler pair-production with cosmic photon fields, known as the extragalactic background light (EBL). Measurements of the IGRB spectrum by *Fermi*-LAT find it well-described by a power law with an exponential cutoff, with a spectral index of 2.32 ± 0.02, and a break energy of 279 ± 52 GeV [29]

Naively, in the case of hadronic acceleration, we would expect both neutrinos and gamma rays to be emitted from the same sites. The flux of neutrinos is indeed broadly consistent with an origin in pion decays, which could also model the IGRB observed by Fermi. However, in the p-γ scenario, as the accelerated protons need to interact

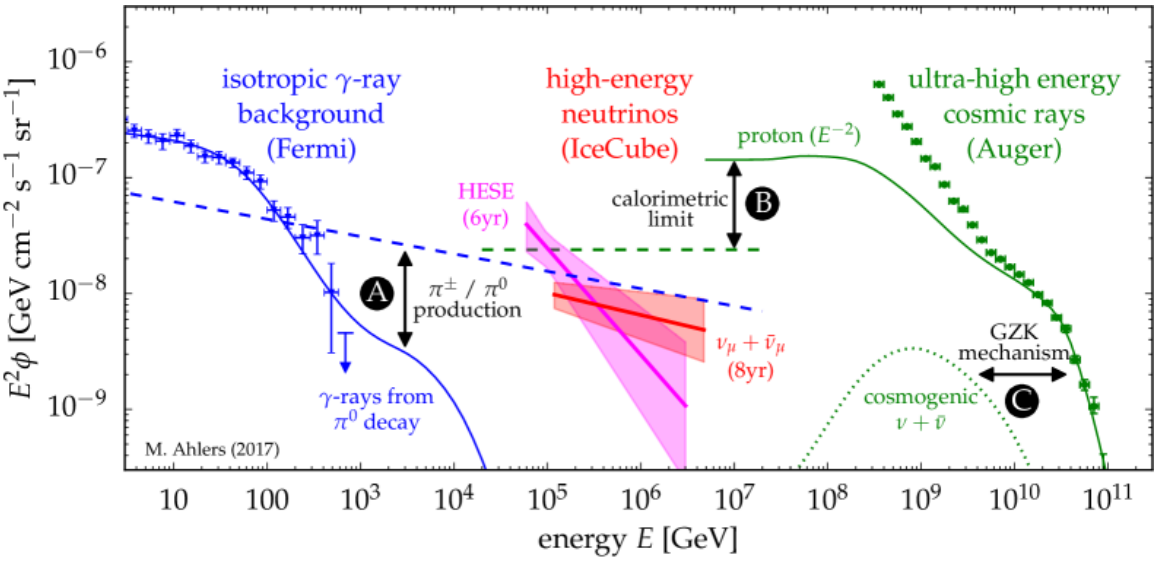

Figure 2.8: The energy densities of cosmic rays, neutrinos and gamma rays [30]. The spectrum of neutrinos is derived from historical IceCube measurements using samples of upgoing tracks and high energy starting events. The gamma ray spectrum has been obtained by subtracting resolved sources from the total extragalactic gamma ray light measured by *Fermi*-LAT, while the cosmic ray spectrum is obtained from measurements at the Pierre Auger Observatory. The blue dashed line indicates the neutrino flux extrapolated from the gamma ray spectrum assuming both messengers arise from pion decay. The green dashed line indicates the Waxman-Bahcall calorimetric bound on the neutrinos produced from cosmic rays, while the dotted line indicates a theoretical flux of neutrinos from interactions of UHECRs with cosmic microwave background (CMB) photons, which is predicted to suppress the flux of cosmic rays from the distant cosmos above a threshold proton energy of 50EeV (known as the Greisen–Zatsepin–Kuzmin (GZK) limit).

with a keV X-ray photon field to produce the TeV neutrino flux detected by IceCube, we may expect a correlation between neutrino emitters and X-ray sources as opposed to gamma ray sources. In addition, the link between neutrinos and gamma rays may be more tenuous if the gamma ray photons produced from π^0 decay undergo pair production with EBL photons, suppressing the TeV-PeV flux.

2.3 Constraints on Cosmic Accelerators using Neutrino Observations

As most astrophysical neutrinos detected to date are predominantly of extragalactic origin, and the few sources identified are not luminous enough to account for a significant fraction of the total flux, we may expect the bulk of neutrinos to be emitted from numerous sources of low luminosity. Following the treatment of [27], we compare the fluxes of gamma rays and neutrinos in both the p-p and p-γ cases to constrain the environment around cosmic ray accelerators. Tackling the p-p case, we assume a power law model for both the neutrino and gamma ray fluxes, with a break energy $\mathrm{E_{break}}$ in the neutrino spectrum necessary to avoid overshooting the IGRB flux. The neutrino spectrum is modelled as

$$\epsilon_\nu \mathcal{Q}_\nu \propto \begin{cases} \epsilon_\nu^{2-\gamma_1} \,, (\epsilon_\nu < E_{\mathrm{break}}) \\ \epsilon_\nu^{2-\gamma_2} \,, (\epsilon_\nu > E_{\mathrm{break}}) \end{cases} \tag{2.17}$$

Similarly, the gamma ray spectrum can be modelled by a power law below 1 TeV

$$\epsilon_\gamma \mathcal{Q}_\gamma \propto \epsilon_\gamma^{2-\gamma_1} \tag{2.18}$$

A limit on $\gamma_1 \leq 2.1 - 2.2$ is required to account for p-p scenarios which explain the $\geq$ 100 TeV neutrino data. The resulting flux is shown as dotted lines in Fig. 2.9. Below 100 TeV, the extrapolated flux in the p-p scenario saturates the IGRB when $\gamma_1 \geq 2$, and is therefore in tension with the *Fermi*-LAT results. We then consider the p-γ scenario, where both the neutrino and gamma ray spectra depend on the ambient photon fields around the proton accelerator. In general, the photo-pion interaction cross section increases with proton energy, which would predict that the neutrino spectrum should be harder than the parent primary spectrum. From [18], however,

we observe that the neutrino spectrum from pion decay cannot be too hard, with the low energy spectrum following $\epsilon_\nu \mathcal{Q}_\nu \propto \epsilon_\nu^2$. Considering, therefore a minimal p-γ

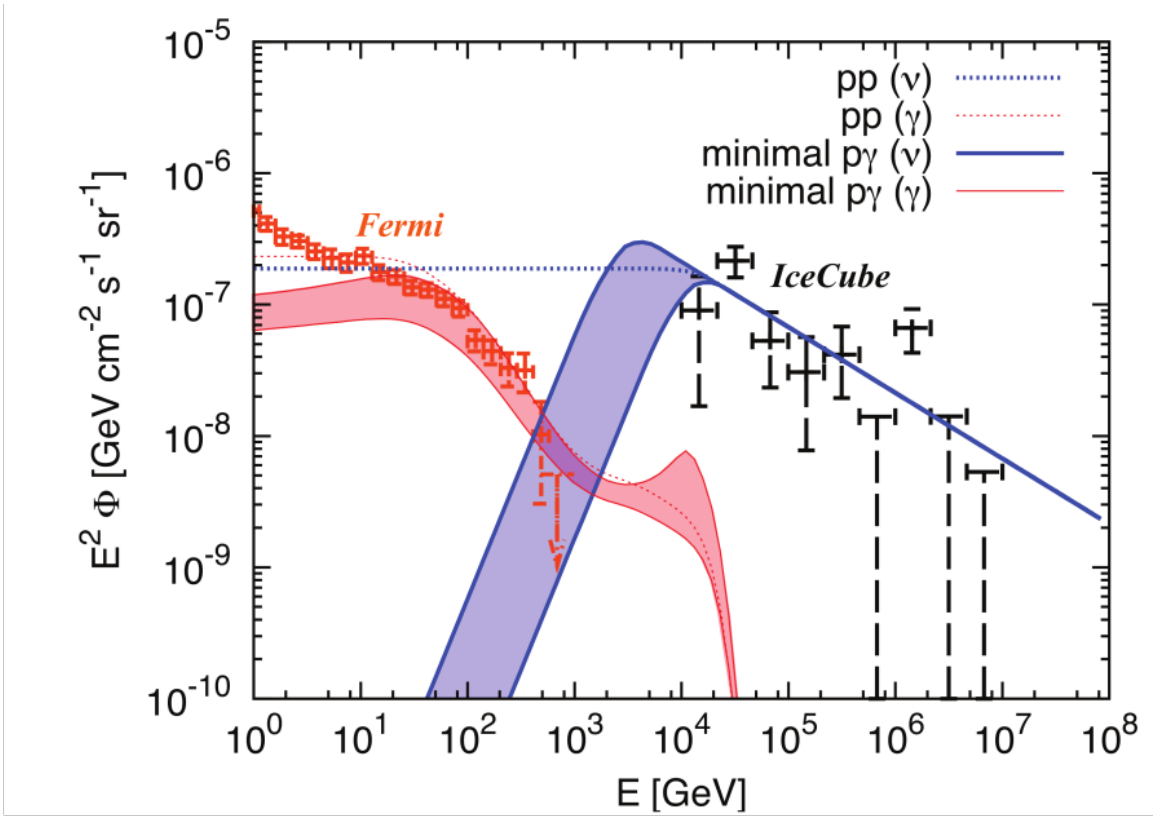

Figure 2.9: The fluxes of neutrinos and gamma rays in the p-p and p-γ scenarios [27]. The flux models are tuned to account for historical IceCube TeV data, as well as *Fermi*-LAT measurements of the IGRB, assuming that the sources are transparent to gamma rays. The neutrino spectral indices following Eq. 2.17 are $\gamma_1 = 2$; $\gamma_2 = 2.5$. For the p-γ case, the solid lines are evaluated for $E_{\rm break}$ between 6-25 TeV.

scenario, where $\gamma_1 = 0$, we have

$$\epsilon_\nu \mathcal{Q}_\nu \propto \begin{cases} \epsilon_\nu^2 \,, (\epsilon_\nu < E_{\rm break}) \\ \epsilon_\nu^{2-\gamma_2} \,, (\epsilon_\nu > E_{\rm break}) \end{cases} \tag{2.19}$$

This weakens the tension with the IGRB measurement, but will still saturate the gamma ray flux for a low $E_{\rm break}$. This is despite the conservative assumptions [31] about the source, namely neglecting the effects of meson and muon cooling, and additional production of gamma rays from pair production or synchrotron emission,

independent of hadronic processes. This minimal model leads to tension with the *Fermi*-LAT IGRB and EGB measurements, and must lead us to reconsider our fundamental assumption that neutrino sources are transparent to gamma rays. This is unlikely, not least because the intense photon field necessary for efficient neutrino production would also cause gamma ray photons to undergo energy losses via Bethe-Heitler pair production. Such opaque or 'hidden' sources such as choked GRBs or AGN cores are promising candidates for IceCube's TeV neutrino observations [32], and merit further study. It must be noted that these sources are opaque to merely high energy gamma rays, at GeV scales, and these photons may be reprocessed down to MeV and keV scales.

In summary, we see that studies of the neutrino flux may reveal details about the source environment inaccessible to gamma ray measurements alone, and may in fact hint at large populations of gamma-opaque neutrino emitters. Features of the observed neutrino spectrum may also enable distinction between the p-p and p-γ models for hadronic acceleration. In particular, the analysis of lower energy ($\mathcal{O}$(10 TeV)) neutrinos would require ambient photon fields with proportionally higher energies, potentially upto the X-ray regime. Assuming that sources are obscured in gamma rays, improving measurements of the neutrino spectrum and pushing the energy threshold lower will provide model-independent constraints about the radiation fields in the environments of cosmic ray accelerators. Such an analysis of the neutrino spectrum is the main subject of this thesis.

Chapter 3

The IceCube Neutrino Observatory

3.1 Particle Interactions

3.1.1 Neutrinos

As near-massless neutral leptons [33], neutrinos interact only via the weak interaction. This is why neutrinos have a very low interaction cross-section, and therefore serve as excellent cosmic messengers, while also being very difficult to detect. Via the exchange of W-bosons and Z-bosons, and the conservation of lepton number and charge one can illustrate the various interactions neutrinos undergo with nucleons, our primary detection mechanism. Interactions mediated by the Z-boson are termed neutral-current (NC) interactions, where a neutrino scatters off a nucleon creating a shower of charged particles, and an outgoing neutrino of the same flavour as the primary. In the charged-current (CC) interaction, an incoming neutrino exchanges a virtual W-boson with a nucleon, to convert to an outgoing charged lepton of the same flavour as the neutrino.

At the energies of interest at IceCube, the dominant interaction is deep inelastic

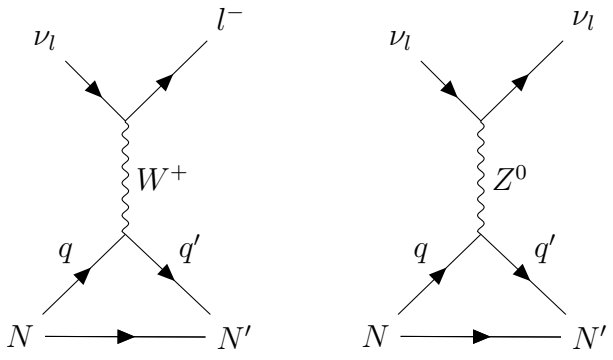

(a) Charged Current (b) Neutral Current

Figure 3.1: Neutrino-nucleon Deep Inelastic Scattering interactions.

scattering [34, 35]. The cross-section model primarily used in this analysis is the Cooper-Sarkar-Mertsch-Sarkar (CSMS) model [36] for the neutrino-nucleon cross-sections. At the energy ranges studied, the uncertainty in the cross section is within 5% but rapidly rises above 10 PeV. A measurement of the cross-section between 60 TeV and 10 PeV was performed on a sample using 7.5 years of IceCube data [37] and found that the predictions from CSMS were consistent with observations. At PeV energies, one may also encounter a particular interaction known as the Glashow resonance, which occurs when electron anti-neutrinos interact with electrons in bulk matter to produce a W^- boson, which then creates a shower of particles. As the electrons are at rest, we find that an anti-neutrino energy of 6.3 PeV is required to initiate this reaction, which is much higher than the centre-of-mass energies obtained at terrestrial collider facilities, but can be attained at cosmic particle accelerators. In 2021, IceCube announced the successful detection of a Glashow resonance candidate event using 4.6 years of data [38].

In this thesis, we focus on neutrinos of energies above 1 TeV, where the dominant interaction processes are CC and NC Deep Inelastic Scattering.(Figs. 3.1 and 3.2)

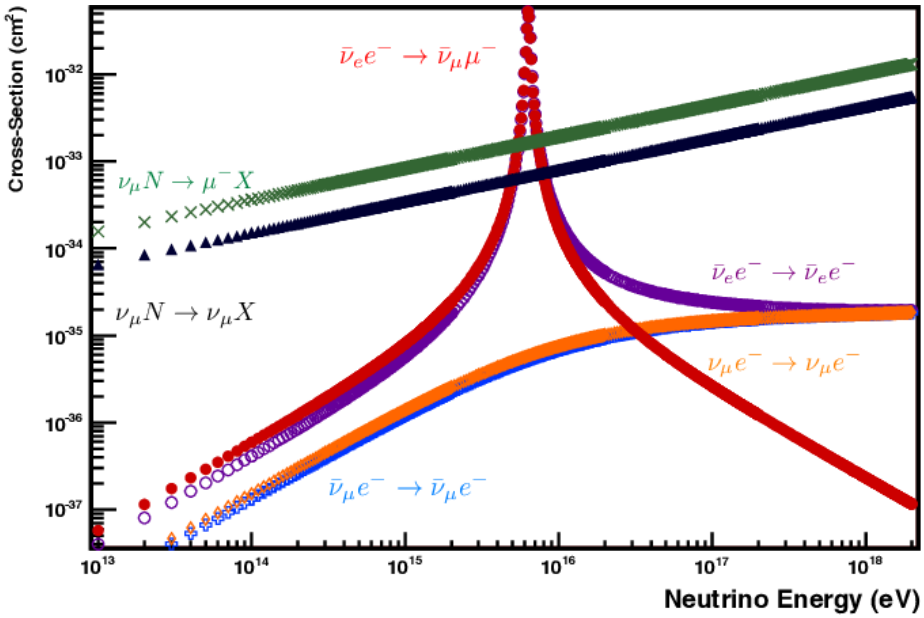

Figure 3.2: Deep Inelastic Scattering cross-sections for TeV-scale neutrinos [34]. The peak observed is known as the Glashow Resonance [39, 38], a resonant interaction of electrons with electron antineutrinos at ~ 6.3 PeV to produce W^- bosons, which can decay into multiple channels

3.1.2 Muon Interactions

At the energies of interest, the main processes by which muons interact are pair production, bremsstrahlung, photonuclear interaction, ionization, and decay. Assuming a typical muon rate of energy loss while travelling in ice of 2-3 MeV/cm, we see that a 100 GeV muon will travel a maximum of ~ 500 m, while a 1 TeV muon can travel around 3-5 kilometers. The energy loss rate becomes more stochastic above 1 TeV, however, and the survival probability at a certain depth is now a distribution instead of a discrete value.

3.1.3 Electron Interactions

Electron energy loss is dominated by bremsstrahlung and pair production, to a larger extent than heavier charged leptons. The various interactions are illustrated in Fig.

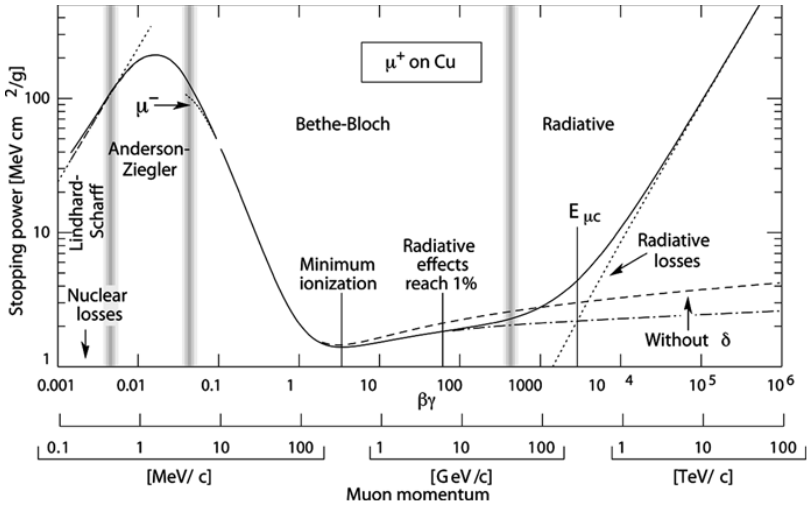

Figure 3.3: A plot of the different mechanisms of energy losses for muons travelling through matter [33]. IceCube is sensitive to muons of energies above 100 MeV, from the minimum ionizing regime to the radiative regime

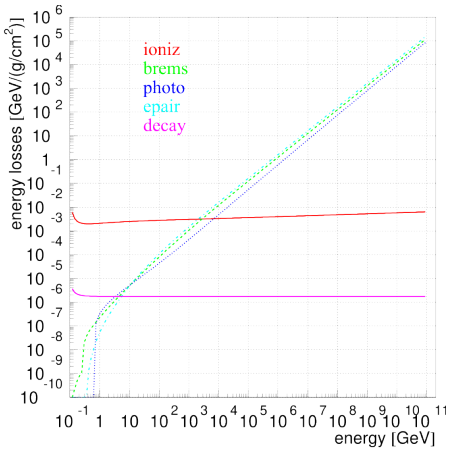

Figure 3.4: The different energy loss mechanisms in muons as a function of energy. Above 1 TeV, muon energy losses are stochastic, leading to a distribution in their energies after traversing through to the detector. Plot from ref. [40]

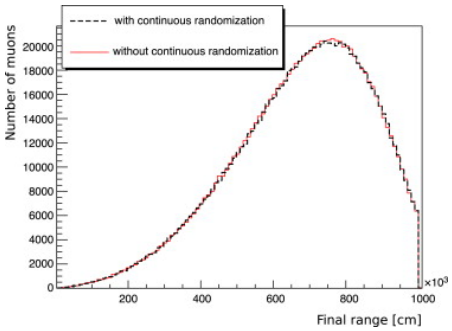

Figure 3.5: The range distribution for muons with energy 9 TeV propagated through 10 km of water. We find a wide variation in the range of individual muons, and that a sizable fraction survive the passage. Plot from ref. [40]

3.6.

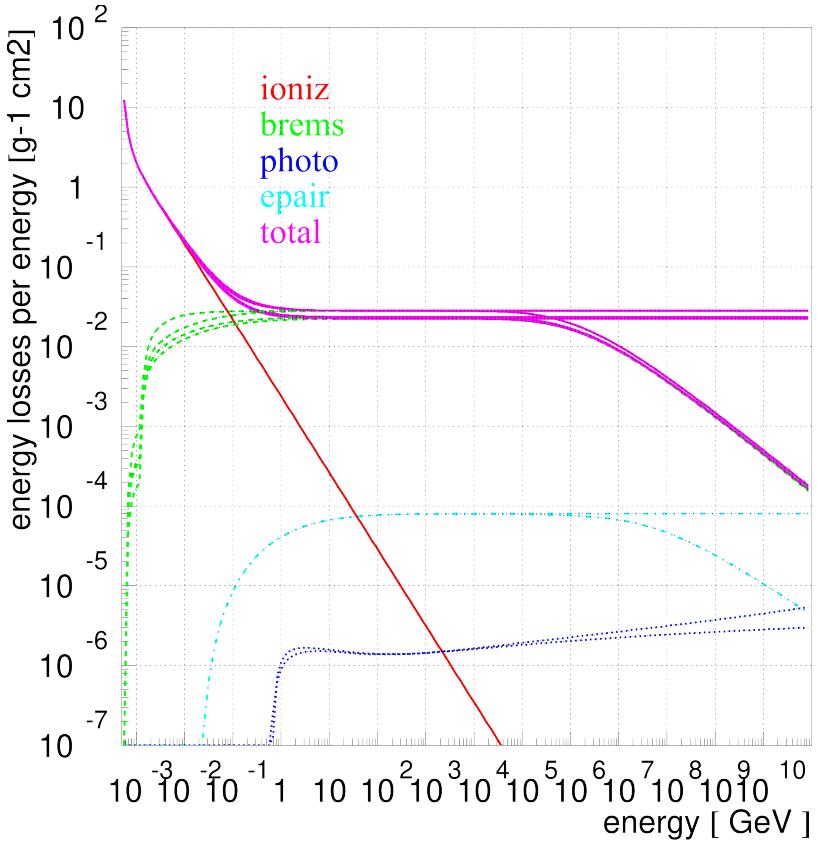

Figure 3.6: The different energy loss mechanisms in electrons as a function of energy, assuming passage through ice. Plot from ref. [41]

3.1.4 Tau Interactions

Due to their short lifetimes at the energies of interest, tau leptons are likely to decay before interacting. These decay channels are listed in [42]. Of particular interest are the decays of taus into hadrons or electrons, which initiate showers in the detector at the site of tau decays. This appears in IceCube as the Double Cascade event morphology, discussed further in sec. 3.4.3

3.2 Detection Principle

The DIS interactions create a shower of charged hadrons, along with an outgoing charged lepton in the case of CC interactions. When high energy charged particles traverse an optical medium faster than the phase velocity of light, they emit electromagnetic radiation known as Cherenkov radiation. This occurs due to the polarization of the material during the passage of a moving charge, akin to a ripple in a pond. The angle of emission of Cherenkov photons $cos(\Theta_c)$ can be calculated to be [43]

$$cos(\Theta_c) = \frac{1}{n_{med}\beta}. \tag{3.1}$$

where n_{med} is the refractive index of the optical medium, and β is the velocity of the particle relative to the speed of light in a vacuum (c). For ice, with a refractive index of ~ 1.31, Θ_c is around 40.2°. Cherenkov photons emitted during a charged particle's passage through a medium allow for the observation of the trajectory. As neutrinos have no charge, they do not emit Cherenkov radiation themselves. However, upon Deep Inelastic Scattering off nucleons in the ice, showers of charged hadrons may be generated, along with a charged lepton in case of charged-current (CC) interactions. The number of Cherenkov photons emitted are a proxy for the energy deposited in the neutrino interaction, with about 10^{-4} of the shower energy converted to photons. In addition to direct Cherenkov energy losses, the charged particle also loses energy due to inelastic collisions with bulk-ice electrons and excitation of atoms. The net energy loss of a charged particle travelling through bulk matter is provided by the Bethe-Bloch equation [43]

$$-\frac{dE}{dx} = 2\pi N_a m_e r_e^2 c^2 \rho \frac{Z}{A}\frac{z^2}{\beta^2}\left[ln(\frac{2m_e\gamma^2 v^2 W_{\max}}{I^2} - 2\beta^2 - \delta - 2\frac{C}{Z}\right]. \tag{3.2}$$

where

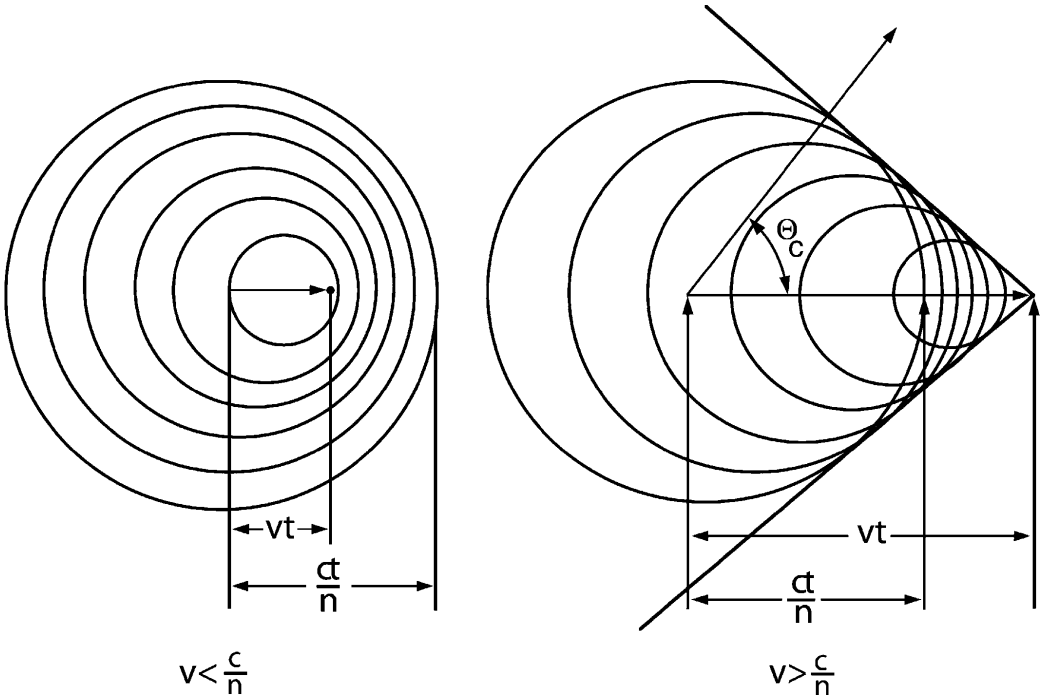

Figure 3.7: A diagram illustrating the Cherenkov radiation emitted by a particle when it travels faster than the speed of light in an optical medium, and the Cherenkov angle made by the wavefront to the direction of propagation [33].

- m_e, r_e : the electron mass and classical radius (2.82×10^{-15} m)
- N_a : Avogadro's constant
- I : mean excitation potential
- Z, A, ρ : Atomic number, atomic weight, and density of bulk material
- C : shell correction
- β, γ : $\frac{v}{c}$ and Lorentz factor of incident particle.
- δ : density correction
- z : charge of incident particle in units of e
- $W_{\max}$: maximum energy transfer in a head-on collision

which is approximately

$$-\frac{dE}{dx} = \rho(2\,\text{MeV cm}^2/g)\frac{Z^2}{\beta^2}. \tag{3.3}$$

At higher energies, the ionization losses of charged particles measured by the Bethe-

Bloch equation become subdominant to the loss of energy via radiative processes. These include bremsstrahlung, the radiation emitted when a charged particle deviates from its trajectory due to a nuclear collision, and pair production, where a charged particle emits virtual photons which create an electron-positron pair in the vicinity of a nucleus. The radiative energy losses are stochastic in nature, and the averaged energy loss per unit length traversed in a medium is usually linear in the energy of the incident particle

$$\langle \frac{dE}{dx} \rangle = -\frac{E}{X_0}. \tag{3.4}$$

where X_0 is a quantity known as the radiation length. In ice, the radiation length is 0.39 m. Above $\mathcal{O}(10$ TeV), the muon energy losses via radiative processes become quite stochastic, and lead to poor energy resolution due to fluctuations in the energy deposited in the detector.

3.3 IceCube

The IceCube Neutrino Observatory [45] is located at the South Pole, atop the Antarctic plateau. The extremely low interaction cross-section of neutrinos requires a large detection volume of clear matter, and the vast volume of ice with very long optical attenuation lengths, along with the logistical facilities operated by the National Science Foundation make the Pole an ideal site.

When neutrinos interact with nucleons in the ice, they produce a shower of charged particles which emit Cherenkov radiation. These Cherenkov photons are picked up by optical sensors called Digital Optical Modules (DOMs). These DOMs collect Cherenkov light from interactions in the ice, and convert the optical signal to an electrical one using Photomultiplier Tubes. The number of photons seen is a proxy of how much energy was deposited inside the detector by the initial primary neu-

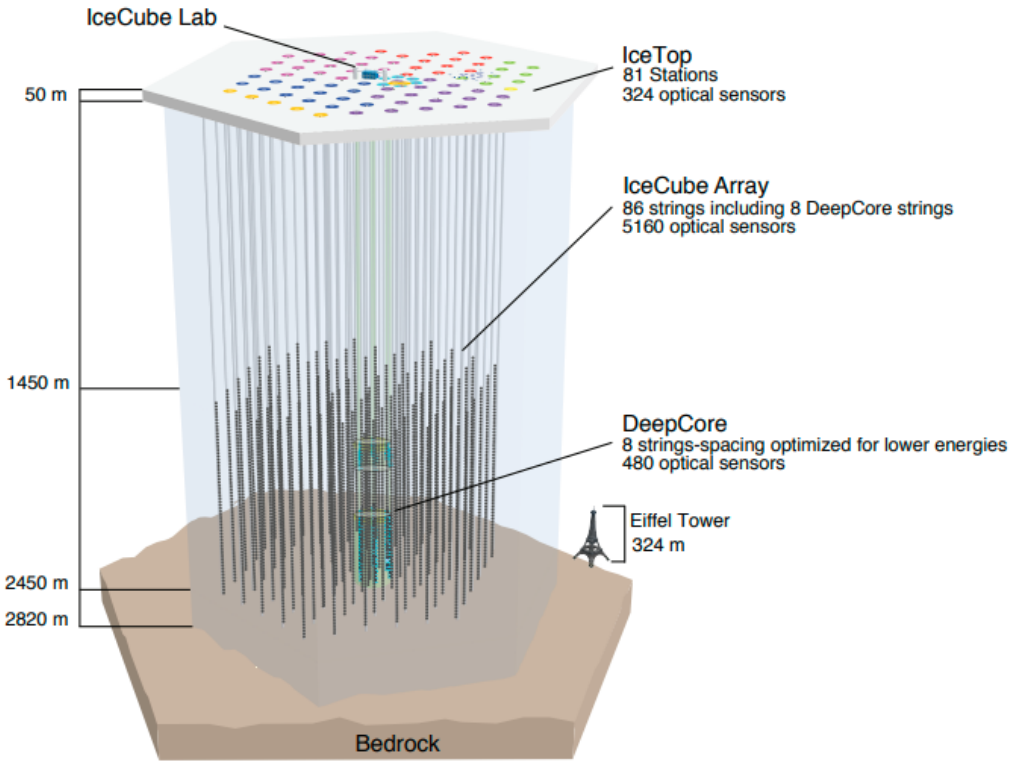

Figure 3.8: A scale diagram of the IceCube detector array [44]

trino, and in general, the higher the primary neutrino energy, the more light visible within the detector. The signal is amplified and processed before being transmitted up the cables to the surface. The information from the DOMs is used to reconstruct the initial particle interaction, most importantly the deposited energy and the initial trajectory. Specifically designed for reliability, after 10 years of operation, less than 1% of the installed DOMs have failed [46].

The IceCube detector uses a right-handed coordinate system [47], with the y-axis aligned along the Prime (Greenwich) Meridian, and the x-axis along 90°E, so the positive z-axis is vertically upwards, towards the Southern Sky. The origin of the IceCube Coordinate System is close to the centre of the array, at a depth of 1948.07 m below the surface of the ice. Fig 3.9 illustrates the orientation of the coordinate system, along with the definitions of the zenith (θ) and azimuth (ϕ) directions. In IceCube,

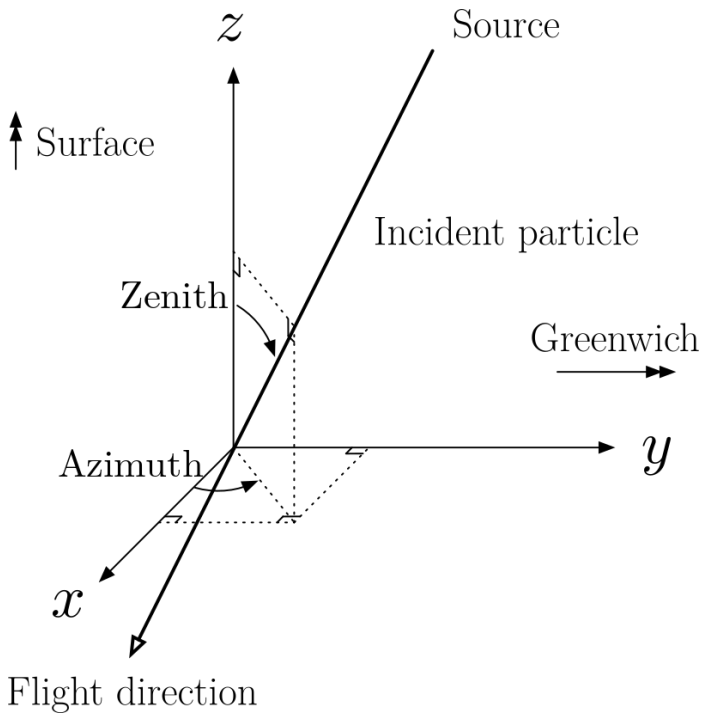

Figure 3.9: An illustration of the Coordinate System used in IceCube

the angle of incidence is often measured in detector coordinates, as both signal and background rates are strongly correlated to to the incident zenith angle. This is often evaluated as the cosine zenith, and therefore a downgoing particle, from the Southern Sky, would have a positive cosine zenith.

3.3.1 Digital Optical Modules

The primary sensor used in the IceCube array is the Digital Optical Module (DOM). The DOM consists of a 10" diameter Hamamatsu Photomultiplier Tube (PMT) [48], inside a 13" diameter glass pressure vessel. This pressure vessel protects the PMT and internal electronics from the pressure exerted by the ice during hole refreezing (around 70 kPa), and during operations over longer terms. The PMT captures photons at the photocathode, converting the photon signal to electrons via photoelectric emission. The electrons generated at the photocathode are accelerated and multi-

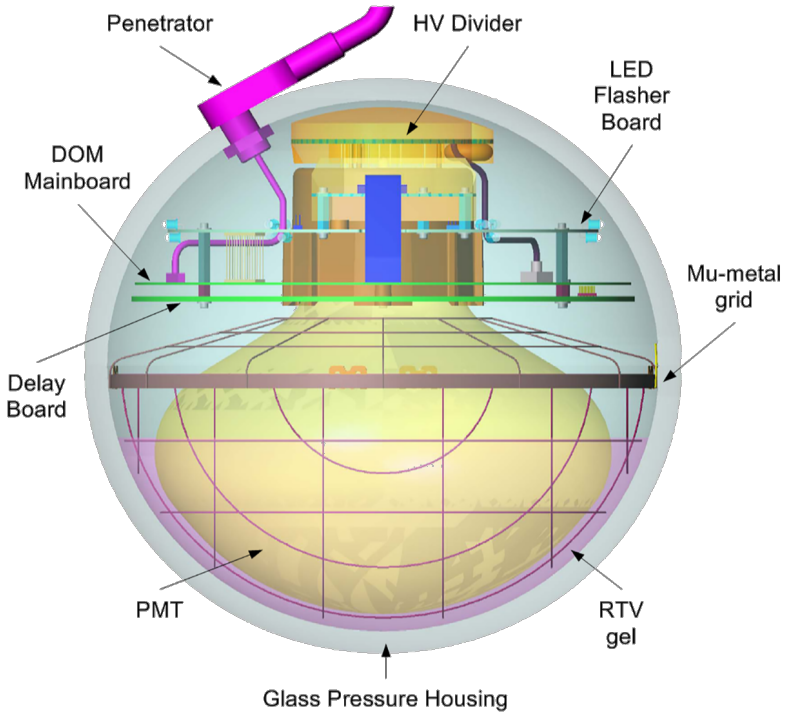

Figure 3.10: A diagram of the Digital Optical Modules

plied via secondary emission at a series of electrodes of increasing voltage, known as dynodes. The PMT used in the DOM is the Hamamatsu R7081-02, with peak quantum efficiency (QE) around 25% at 390 nm, and a sensitive wavelength range of 300 nm-650 nm. The DeepCore DOMs use a variant with 34% QE instead. There is also a layer of transparent silicone gel between the PMT glass and the pressure vessel, which prevents the loss of photons from reflection at the interface, while also holding the PMT in place.

The main electronics board (mainboard) is responsible for controlling all devices within the DOM, and communication with the surface through the Penetrator cable. The high voltage required to bias the PMTs to their operational gain is generated within the module, from a High Voltage Control Board connected to the Mainboard, and a resistive divider on the PMT base. The PMT waveforms are amplified and compared to a threshold value. Crossing this threshold triggers the digitization. Each

DOM has two Analog Transient Waveform Digitizer (ATWD) chips, each of which have varying gains to for a large dynamic range. To record the waveform prior to the threshold crossing, a delay of 75 ns is added through the Delay Board. The ATWD chips sample the waveform at 300 MHz, and record for 427 ns. For longer duration signals, a fast Analog Digital Converter (fADC) is programmed to save an interval of 6.4 μs after the threshold crossing. Calibration of the module array local clocks relative to the surface Master Clock is performed using the Reciprocal Active Pulsing calibration (RAPcal) technique [45].

The amount of information captured also depends on whether neighbouring modules see a coincidence signal too. This local coincidence capability allows for the suppression of noise hits while retaining physics information. If a hit occurs, a DOM opens a time window of upto 1 μs, during which a neighboring DOM can send or receive a local coincidence (LC) 'tag' signal [45]. In the baseline operating mode of IceCube, known as soft local coincidence (SLC), only a hit accompanied by an LC tag receives both PMT ADC and ATWD waveform data, while an isolated hit only contains PMT ADC information. If no coincidence is seen, the digitization halts after sending a timestamp and charge information, whereas if a nearest or next-nearest DOM also sees a signal within 1 μs, the full waveform is transmitted. If only hits with LC tags are selected, the operating mode is known as hard local coincidence (HLC). As isolated hits are more likely to be PMT noise, avoiding ATWD digitization both reduces deadtime and saves bandwidth for data transmission. It is also possible for an isolated hit to contain ATWD waveform information if the PMT sees a signal much larger than a regular single photoelectron (SPE) event, known as a Self-LC event.

In baseline operation, the deadtime is restricted to within individual DOMs, without correlation across other modules. Deadtime is not incurred during waveform capture, but may occur if digitization is subsequently initiated. If digitization is aborted (for

example, if no LC tag is received in time) then the DOM is ready to retrigger in 50 ns. The incorporation of dual ATWDs enables digitization by an alternate if the DOM retriggers while one ATWD is already digitizing a signal, acting like a ping-pong buffer, to minimize deadtime. It is estimated that the total dead time fraction does not exceed 10^{-4} [45].

A Flasher Board with LEDs allows for in-ice calibration of the different DOMs. The ability of the module to accurately capture the time at which photons arrive at the PMT cathode is vital to the performance of reconstruction algorithms, and the flasher LEDs provide the ability to measure this resolution in-situ, with flashes from neighbouring DOM providing a calibrated light source. The time resolution has been determined by this method to be $\mathcal{O}(1$ ns) [45].

The DOM PMTs nominally operate at a gain of 10^7, allowing one to translate the charge measured from the waveform into the total number of photons observed. This measurement is conditional on the PMT responding linearly to varying signal brightnesses. This dynamic range has been measured to be 250 photoelectrons (PE) /15 ns, with a 10% deviation from linearity at 400 PE/15 ns. The IceCube detector can be further subdivided into the In-Ice Array and the IceTop Air Shower Array

3.3.2 In-Ice Array

The IceCube In-Ice Array consists of 86 vertical strings, each of which contain 60 DOMs spaced at 17 m intervals. These strings lie in holes 2460 m deep and 60 cm wide, drilled into the ice with high-pressure hot water. As the ice closest to the surface has a high scattering coefficient due to trapped air, the shallowest DOMs are located at depths close to 1450 m, for a total instrumented volume is 1 km^3. A layer of ice of reduced attenuation length, referred to as the dust-layer, is present at depths from 2000 m-2100 m. The primary array consists of 78 strings in a hexagonal pattern

with 125 m spacing between strings, designed to detect astrophysical neutrinos with energies in the TeV range and above. In addition, there are 8 strings of DOMs deployed deeper than 1750 m and more densely spaced, to boost sensitivity to lower energy events. These strings are referred to as the DeepCore array, with the inter-string spacing from 41 m -105 m. The DeepCore sub-array inter-DOM spacing is also reduced, with DOMs beneath the dust-layer 7 m apart, and 10 DOMs above the dust-layer at a spacing of 10 m, acting as a 'veto cap'. The DeepCore DOMs also use PMTs of higher quantum efficiency for additional sensitivity at lower energies. The DeepCore array is designed to detect neutrinos of energies from 10 GeV-100 GeV, allowing for the study of neutrino oscillations and the detection of supernovae.

3.3.3 IceTop Array

The IceTop array is a cosmic-ray (CR) air shower detector at the surface of the ice. It consists of 162 ice-filled tanks which contain two DOMs each, one with a higher gain of 5×10^6 and one with a reduced gain of 10^5, to be able to study both high and low energy events with a wide dynamic range. CR air showers are usually spread over multiple stations, with the amount of Cherenkov light deposited by charged particles visible at the stations serving as a proxy for the energy of the CR primary. The IceTop array is sensitive to CRs with energies ranging from PeV to EeV, with a lower energy sub-array known as the 'infill' which is sensitive to TeV scales. This energy range allows IceTop to cover the 'knee' transition from galactic to extragalactic sources in the CR spectrum. In addition, IceTop can serve as a partial veto for atmospheric muons for IceCube.

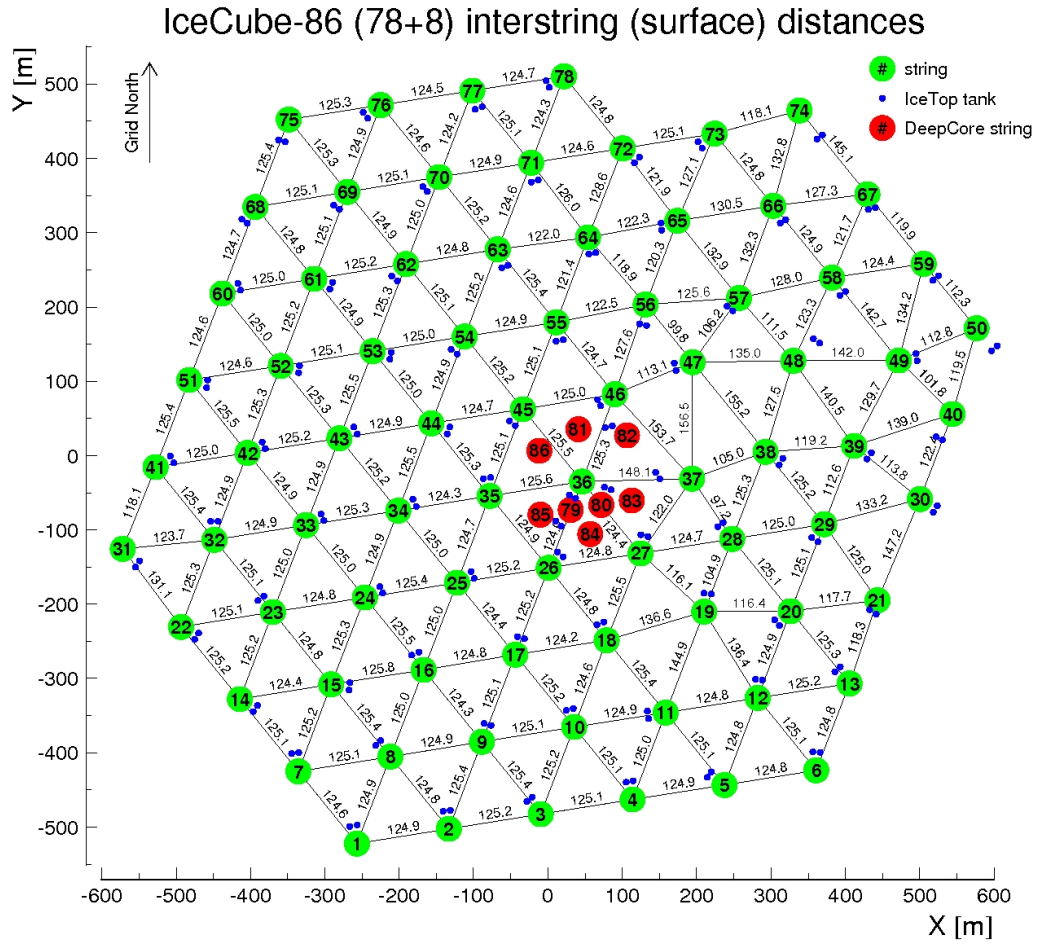

Figure 3.11: A diagram of the layout of the IceCube Array. The top right corner departs from the hexagonal symmetry of the array to avoid the restricted area around the Old South Pole Station. The DeepCore strings are highlighted in the centre of the array

3.4 IceCube Event Morphologies

The different neutrino interactions illustrated in sections 3.1.1 and 3.2 have characteristic patterns of charge deposition within the detector, when viewed chronologically in time. These may be broadly categorized into "cascade" events and "track" events. A third class of events is the "double cascade" events, characteristic of tau neutrino interactions at high energies [49]. In the event selection developed for this analysis,

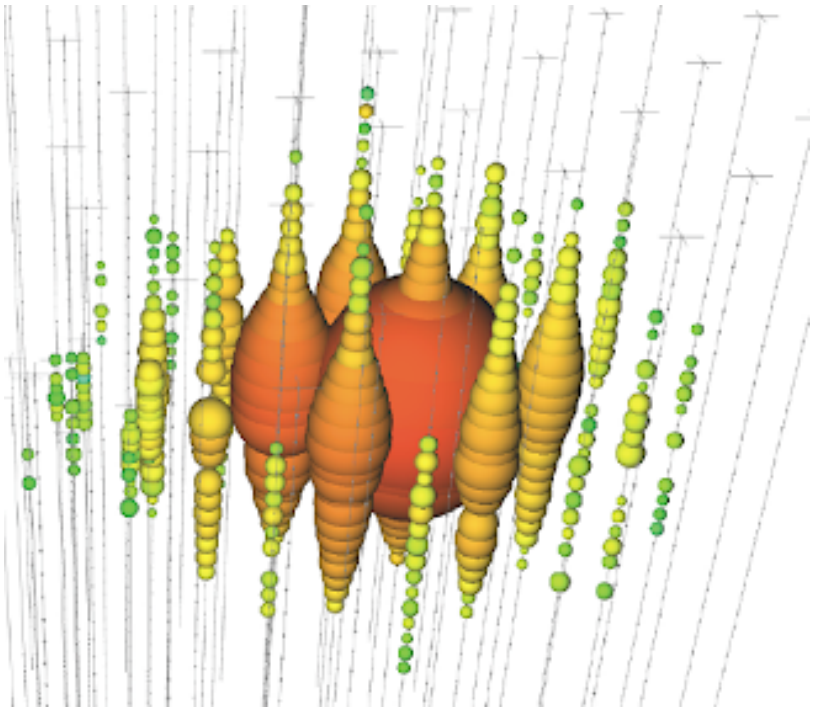

Figure 3.12: An event display of cascade-like events within IceCube, using the data event "Bert" [51] of reconstructed energy 1.1 PeV. The spheres represent DOMs which see light, with the size correlating to the amount of light seen by a particular DOM. The early pulses are in red, while later pulses are first in green, then yellow and finally blue

elaborated upon in chapter 4, a Deep Neural Net (DNN) is used to classify events into the different morphology categories [50].

3.4.1 Cascades

When an electron neutrino (anti-neutrino) undergoes a charged current interaction, an outgoing high energy electron (positron) is created which causes a compact electromagnetic shower within the ice. Another class of events which yield cascade-like signatures are neutral current interactions of neutrinos with in-ice nucleons, where a portion of the neutrino energy is transferred to the nucleon, leading to a hadronic shower, creating charged particles like pions. These particles deposit Cherenkov light

during their propagation and decay. Due to the high energies of the primary particle in both electromagnetic and hadronic showers, these charged particles are created with momentum aligned along the shower axis. The Cherenkov photons emitted along the tracks of these charged particles scatter through the bulk ice. This results in an isotropic distribution of photons, which is captured by the DOMs as a spherical pattern.

Cascade events may be further classified into contained and uncontained events, based on the location of the neutrino interaction vertex. If the vertex is located in the detector volume far enough that most of the light deposited is captured by the DOMs, the event is classified as contained. If the interaction vertex is closer to the detector boundary or outside the detector, it is termed a partially-contained or uncontained event, and is harder to reconstruct. For this reason, in the event selection developed for our analysis, we solely select contained events. However, a recent analysis using deep neural nets was able to use contained and uncontained cascade events to isolate a neutrino signal from the galactic plane [52].

As the bulk of the energy deposited by contained cascades is contained within the detector volume, contained events have good energy resolution (8% at 100 TeV) [53]. They are more difficult to reconstruct directionally, however, due to their spherical geometry. Median angular errors of 8° were obtained with advanced neural net-based reconstructions [54]. A better understanding of the anisotropy, due to birefringence of polycrystalline ice, has improved the situation with more refined models of South Pole ice [55]. These updated models improve the median angular resolution to around 4° at 100 TeV.

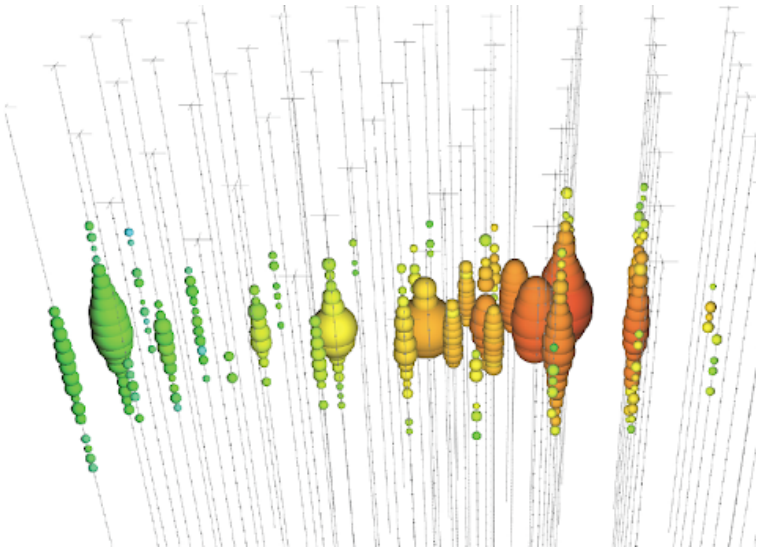

Figure 3.13: An event display of track events within IceCube, using the starting track data event "Dr. Strangepork" [51] of reconstructed energy 74 TeV.

3.4.2 Tracks

Tracks occur when high energy muon neutrinos undergo a Charged Current interaction and create an outgoing high energy muon. At TeV energies, the muon generally travels a distance large enough to resolve as a straight line with the IceCube array. Various subclasses of track events are

- **Starting Tracks**: Tracks with the initial ν_μ CC interaction vertex contained within the detector, and the outgoing muon visible as a track exiting the detector.

- **Throughgoing Tracks**: Tracks with the initial ν_μ CC interaction vertex outside the detector volume, so the muon track spans the entire detector volume.

- **Skimming Tracks**: Tracks with the initial ν_μ CC interaction vertex outside the detector volume, where the muon track passes close to the detector boundary without ever entering.

- **Stopping Tracks**: Tracks where the muon decays inside the detector volume after losing all its energy.

The large lever-arm afforded by the track on its passage through the detector allows one to accurately reconstruct the direction of incidence, with angular resolution of the order of $0.3^\circ - 0.6^\circ$. This allows selections focusing on track events to be more suited for searches for neutrino sources in the sky. However, the poor confinement of the deposited energy of the initial neutrino, along with the fact that only a part of the light deposited by the muon track is visible to the detector, means that the energy reconstruction of tracks suffers. At TeV energies, we see from Fig. 3.3 that the $\frac{\mathrm{d}E}{\mathrm{d}x}$ and the muon energy follow a roughly linear relationship, and therefore estimating the average $\frac{\mathrm{d}E}{\mathrm{d}x}$ from the stochastic energy deposits within the detector. This serves as a lower bound on the initial energy, based on the total length of the track contained within the detector.

Starting tracks, however, have improved energy resolution compared to throughgoing tracks, as the neutrino interaction vertex is contained within the detector volume. The hadronic shower created at the interaction vertex is largely contained and provides a useful handle on the neutrino energy, as defined by the differential cross-section. The fraction of the primary neutrino energy in the hadronic shower varies with energy, ranging from an average 45% at 1 TeV, to 30% at 1 PeV [36]. This makes it possible to lower the median neutrino energy resolution to within 25% at 100 TeV. The outgoing muon track, meanwhile, ensures that the angular direction can be resolved to 1.5° [56, 57].

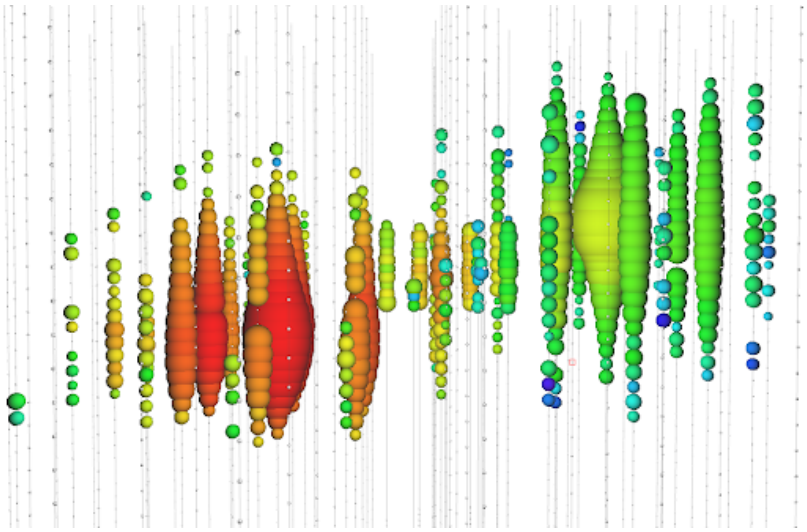

Figure 3.14: An event display of Double Cascade events within IceCube, obtained from simulations.

3.4.3 Double Cascades

When tau neutrinos undergo a charged current interaction, a tau lepton is created. The short lifetime of the tau means that the tau lepton may decay within the boundaries of the detector, with both interaction and decay vertices contained inside the detector. Depending on the energy of the tau interaction, the separation between the vertices is visible, with a separation of the order of 50 m for a 1 PeV interaction. Other kinds of tau neutrino event morphologies are listed in ref [49], depending on the relative positions of the interaction and decay vertices. A study of the flavour composition of astrophysical neutrinos [58] using the MESE sample has been performed using double cascade events. It relies on a further classification of events into the double cascade channel using the Taupede reconstruction algorithm [59, 60].

Chapter 4

MESE: The Medium Energy Starting Event Sample

4.1 Motivation

The IceCube Neutrino Observatory sees a very large flux of atmospheric muons from cosmic ray air showers in the Southern sky, triggering the detector at 3 kHz before the application of any background rejection cuts. These muons are created from the decay of charged pions, and constitute the dominant background in searches for astrophysical neutrinos. Historically, IceCube has conducted analyses selecting specific event morphologies to minimize the background. These analyses can broadly be classified into two categories, Upgoing Track Samples and Starting Event samples.

4.1.1 Upgoing Tracks

As atmospheric muon tracks primarily originate in the Southern sky, if one cuts out the downgoing direction completely and instead selects tracks which originate in the Northern sky, and thus are upgoing with respect to the IceCube coordinate system,

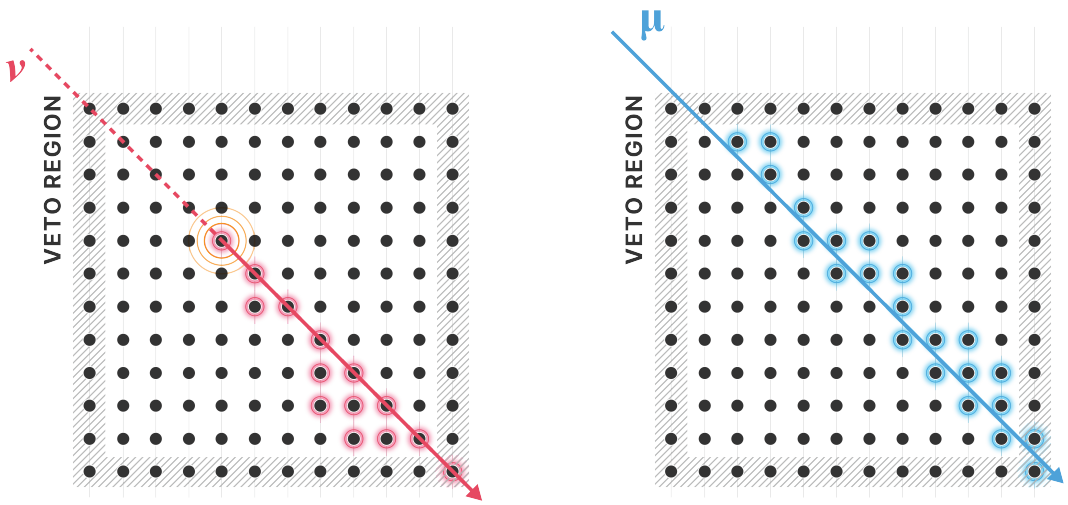

(a) A diagram illustrating a neutrino starting event. The neutrino, as a neutral particle, does not trigger the veto while entering the detector. Upon interaction with the ice, however, a shower of charged particles are created, which create Cherenkov radiation and are visible to the DOMs

(b) A diagram illustrating a muon track. An atmospheric muon leaves Cherenkov light deposits along its trajectory, and triggers the veto as it enters the detector.

Figure 4.1: Veto-based event selections

it is possible to greatly suppress the muon background. This is because muons are unlikely to penetrate far through the Earth, and are thus filtered out, while neutrinos are able to traverse the Earth without a significant reduction in flux. This yields a high statistics sample of muon neutrinos, from both astrophysical and atmospheric sources. A sample of upgoing tracks is also useful for point source analyses, as tracks have superior angular reconstruction and are thus able to point back towards their sources.

4.1.2 Starting Events

An alternative approach is to study starting events, where the neutrino-nucleon in-ice interaction vertex lies within the detector volume. It is possible to define a veto region at the periphery of the detector, to reject atmospheric muons which begin

outside the detector and leave deposit charge in the veto region as they traverse the detector. This enables them to be rejected by the selection. Neutrino events, on the other hand, do not deposit charge as they enter the detector, and the first deposit of Cherenkov light occurs at the interaction vertex, which for a starting event would be contained in the interior of the fiducial volume.

There are many advantages to using starting events, one of which is sensitivity to all flavours of neutrinos. Neutral current interactions from all flavours have a characteristic starting cascade morphology, additionally shared by electron neutrino charged current interactions. In addition, muon and tau neutrino charged current interactions, which appear as starting track morphologies are also included. This allows for measurements of the flavour composition of astrophysical neutrinos with samples of starting events.

Another important benefit when selecting starting events is that there is no restriction on direction, and events from the entire sky are included. The veto and subsequent selection stages suppress the atmospheric muon background, opening up sensitivity to events from the Southern sky. The atmospheric neutrino self-veto effect yields greater sensitivity to astrophysical neutrinos at lower energies from the Southern sky, by suppressing the flux of atmospheric neutrinos, which get vetoed due to accompanying muons.

IceCube first discovered astrophysical neutrinos in a study of Starting Events in 2 years of data [9], known as the High Energy Starting Event (HESE) sample. HESE looked for neutrinos at higher energies(above tens of TeV) to suppress the atmospheric muon background, which falls with energy more rapidly than the spectrum of cosmic neutrinos. The high energy threshold, however, reduces the number of events in the sample, and therefore the statistical power of the analysis to constrain the spectrum of astrophysical neutrinos. The spectrum was found to fit a single power

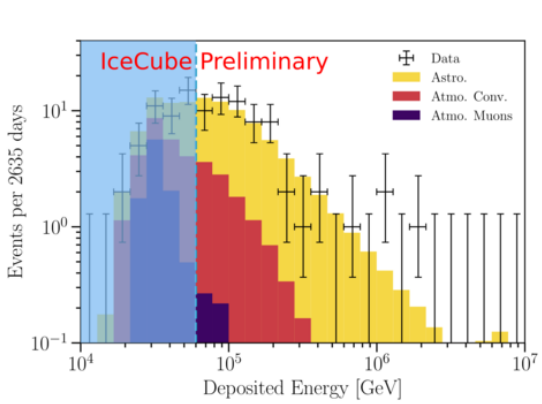

(a) The energy spectrum obtained from the HESE analysis fitting to 7.5 years of IceCube data. Events with reconstructed energies below 60 TeV have been masked from the fit

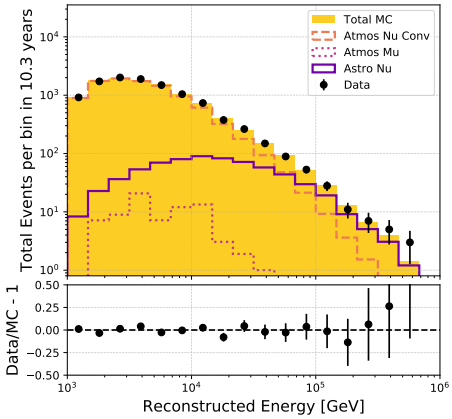

(b) The energy spectrum obtained from the ESTES analysis fitting to 10.3 years of IceCube data.

Figure 4.2: Energy spectra from published analyses focusing on IceCube Starting Events

law flux above 60 TeV. A subsequent follow-up analysis was performed with 7.5 years of IceCube data [12] confirmed the HESE results, with increased statistics. A recently published analysis focusing on starting tracks, known as the Enhanced Starting Track Event Selection (ESTES) also found the spectrum of astrophysical neutrinos followed a single power law [57], down to neutrinos of energy 5 TeV.

The motivation behind the Medium Energy Starting Event sample (MESE) was to extend the energy threshold of a spectral fit using starting events from the 60 TeV threshold set by HESE down to $\mathcal{O}$(1 TeV). Lowering the threshold vastly increases the event statistics, allowing better constraints on the measured flux. This is performed by loosening the HESE veto to allow events of lower brightness [1]. Reducing the energy threshold does, however, also increase the number of background atmospheric muons and neutrinos in the sample, which become dominant at the lowest energies. Suppressing this background at lower energies necessitates the use of addi-

[1]The number of Cherenkov photons deposited during interactions in the detector is a reasonable proxy for neutrino energy.

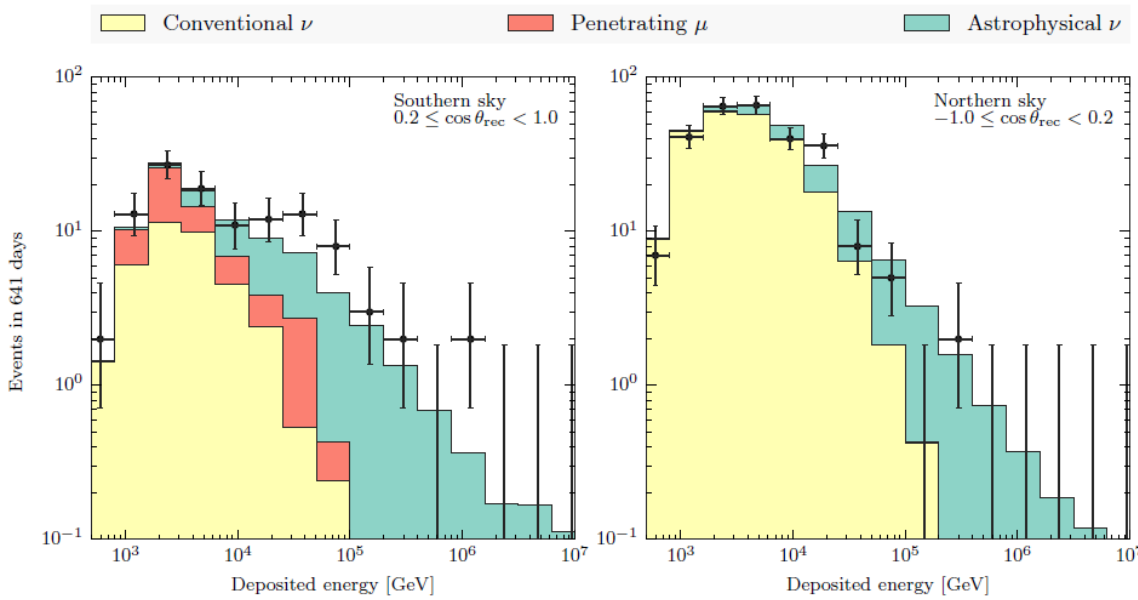

Figure 4.3: Energy spectra from the 2-year MESE analysis [13], with an excess at 30 TeV in the Southern sky

tional selection cuts. As high energy background muons are effectively suppressed by the veto layer cut, the bulk of background events which pass the veto are dim events, and therefore the cuts are tuned to focus on dim events which do not deposit as much charge as HESE events, which are retained to final level.

The MESE analysis was first created by Jakob van Santen [61], using 2 years of IceCube data. This analysis focused primarily on starting cascades, with a smaller proportion of starting tracks. The analysis was later extended by Nancy Wandkowsky with additional years of data, incorporation of starting tracks and updated simulations. Although unblinded, issues regarding the modelling of detector systematics prevented the results from being published. In this thesis, we present the latest version of the MESE event selection, with 11.4 years of IceCube data and an updated event selection. The detector systematics are handled using the SnowStorm method citeSnowStorm, unifying the sample with other contemporary diffuse analyses within IceCube.

4.2 Overview of Event Selection

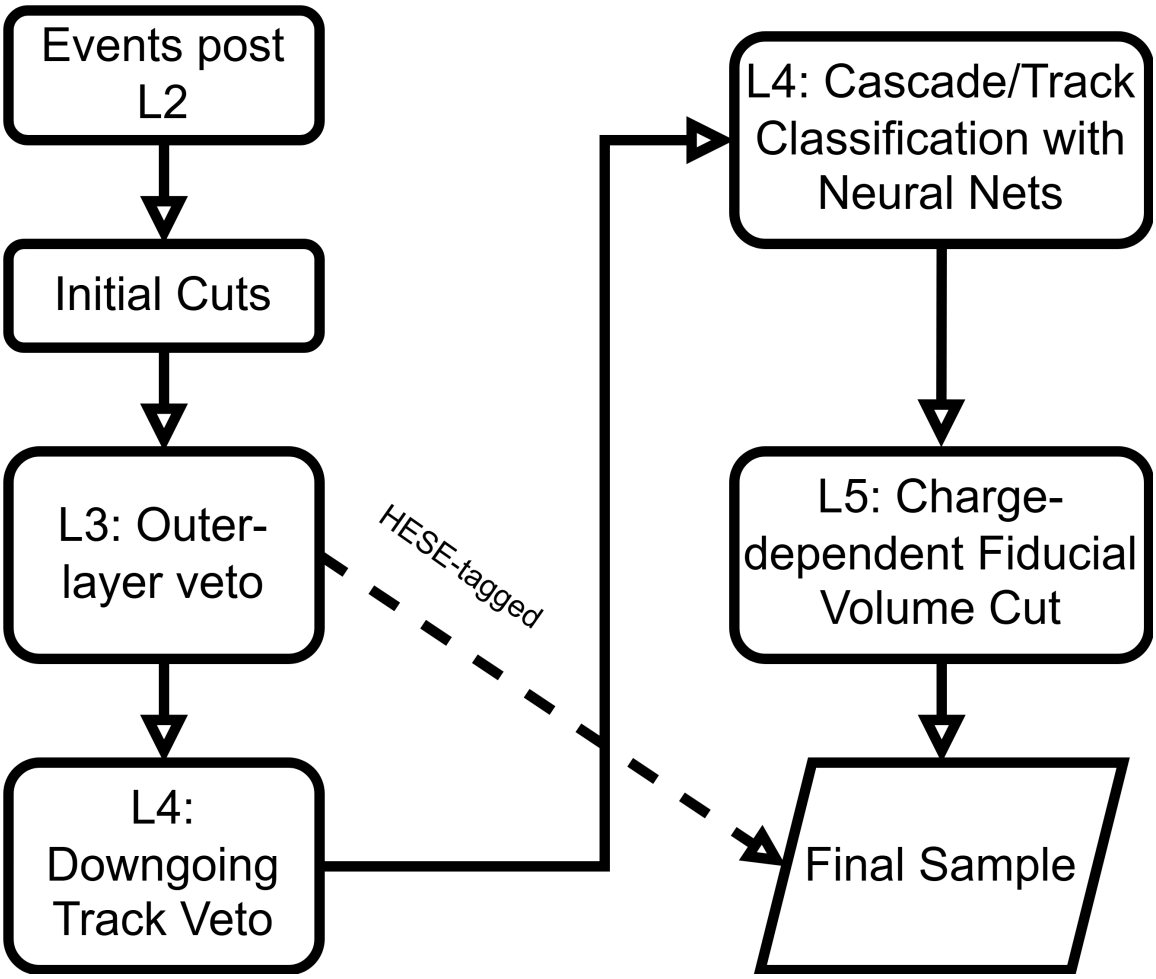

Figure 4.4: An overview of the steps of the MESE Event Selection. The events which act as an input to MESE have passed through IceCube Level2 reconstructions and filters.

4.3 IceCube Filtering: From Raw Data to Filtered Events

The IceCube filtering chain begins with the online Processing and Filtering system, or 'PnF', which processes all triggered events collected by the Data Acquisition (DAQ) framework, and reduces the raw data rates from 1000 GB/day to $\sim$ 75 GB/day. This corresponds to a reduction in the event rate from $\sim$ 2.7 kHz at the array trigger level to $\sim$ 300 Hz passing the online filters, also known as the 'L1' filtering. This includes the characterization and calibration of events, the generation of alerts in realtime for events interesting to the astrophysical community, and the creation of data files and information [45]. At L1, all events are saved to hard drive arrays, while selected interesting events are transmitted North over the Tracking and Data Relay Satellite System (TDRS) for further processing.

The data then undergoes offline filtering, at the 'L2' stage. This consists of a combination of additional cuts, along with higher level reconstructions. These reconstructions are often too computationally intensive to run online at the L1 stage. It is the events which pass IceCube's L2 stage filters which we use as the input to MESE, as illustrated in Fig. 4.4.

4.4 Initial Cuts

The initial cuts are applied to remove very dim events, which are difficult to reconstruct, and to eliminate potential background coincidences. The following conditions are required for an event to pass the initial cuts-

- Charge Cut: A quantity known as the "homogenized total charge" (Homoge-

nizedQTot) is calculated from the charge deposited in the detector. The homogenized total charge is the sum of all HLC pulses detected on non-DeepCore DOMs, which do not add up to more than 50% of the total. This is less affected by stochastic fluctuations than the raw summed charge, and is evaluated using the VHESelfVeto package. If an event has less than 100 photoelectrons (PE) HomogenizedQTot, the event is removed.

- String cut: If the number of strings which see hits is below 3, the event is removed.
- Filter Cuts: Events must pass one of the following filters
  - CascadeFilter_13
  - HighQFilter_17
  - EHEAlertFilter_15
  - MuonFilter_13
  - MESEFilter_15
  - HESEFilter_15

,In addition, we apply the Topological Trigger Splitter Algorithm [62] to split potentially coincident events, which can now be recovered into the data-sample instead of being rejected. This improves the effective area of the event selection, with more statistics at lower energies.

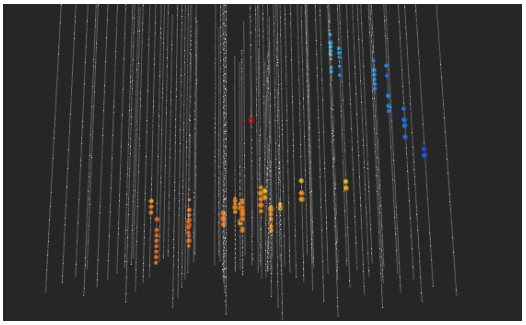

(a) An upgoing neutrino track (signal) coincident with a downgoing muon (background)

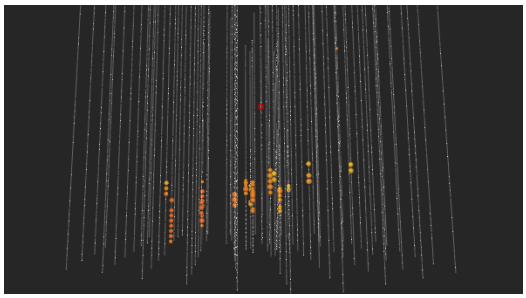

(b) The cleaned upgoing track after running the splitter to eliminate coincident background

Figure 4.5: Running the Topological Trigger Splitter allows for the retaining of re-split coincident events, which would previously have been cut from the sample

4.5 L3: Outer Layer Veto

The Outer Layer Veto aims to reject events which start outside the detector. The geometry of the veto layer is inspired by the veto cut used in the HESE analysis, with some differences. Hits seen in the veto layer (Fig. 4.6) within a 3 μs window at the beginning of the event are known as veto hits. The start of the event is defined when the total event charge crosses a threshold value. The calculation of the threshold charge (Q_{thresh}) for the event start time depends on how much charge was deposited inside the detector. For a bright HESE event, depositing at least 6000 PE, a constant cut of 250 PE was appropriate. For dimmer events, however, such a cut absorbs more and more of the total charge (QTot), and therefore we use a scaled charge cut, following

$$Q_{\text{thresh}} = \begin{cases} 3 \text{ PE}, & \text{if QTot} < 72 \text{ PE} \\ \frac{\text{QTot}}{24}, & \text{if } 72 \text{ PE} < \text{QTot} < 6000 \text{ PE} \\ 250 \text{ PE}, & \text{if QTot} > 6000 \text{ PE} \end{cases} \tag{4.1}$$

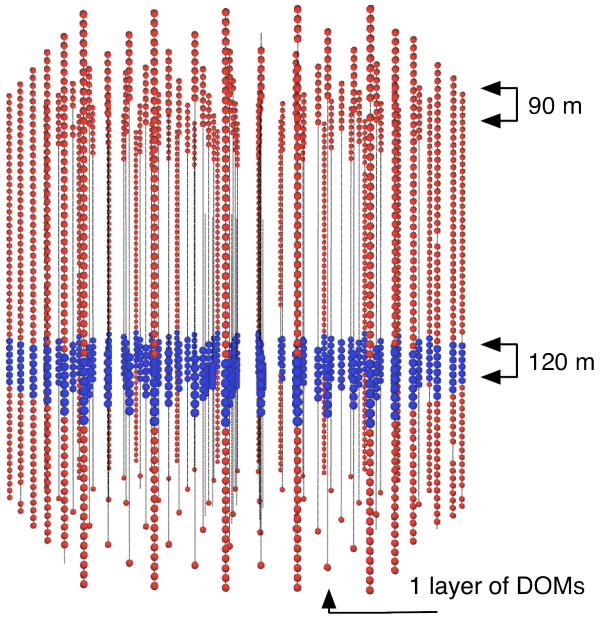

Figure 4.6: A diagram of the veto layer used by MESE at the L3 stage. The veto layer is composed of a 90 m thick band of DOMs at the top of the detector, the dust layer veto and the bottom using the deepest active DOM on each string. The dust layer veto extends from z-coordinate -100 m to -220 m, and is designed to reject down-going muons which attempt to sneak in through the dust before appearing in the clear ice.

The veto window is therefore defined as a 3 μs window which slides until the charge encompassed within exceeds the threshold. Events which deposit at least 6000 PE in total in the detector are tagged as HESE events, and are only vetoed if they have more than 3 PE of veto hits. The threshold charge is set to 250 PE for HESE events. For dimmer events, which deposit less than 6000 PE, we must apply more stringent cuts, and we require zero veto hits for these events. Events which pass this criterion are referred to as MESE-tagged events.

4.6 L4: Downgoing Track Veto

The outer layer veto gets less efficient for dimmer background events. The bulk of the muon background which sneaks through the outer layer veto is predominantly single muon events. These stochastically deposit an isolated energy loss in the interior of the detector, without triggering the L3 veto. These dim muons may not leave any

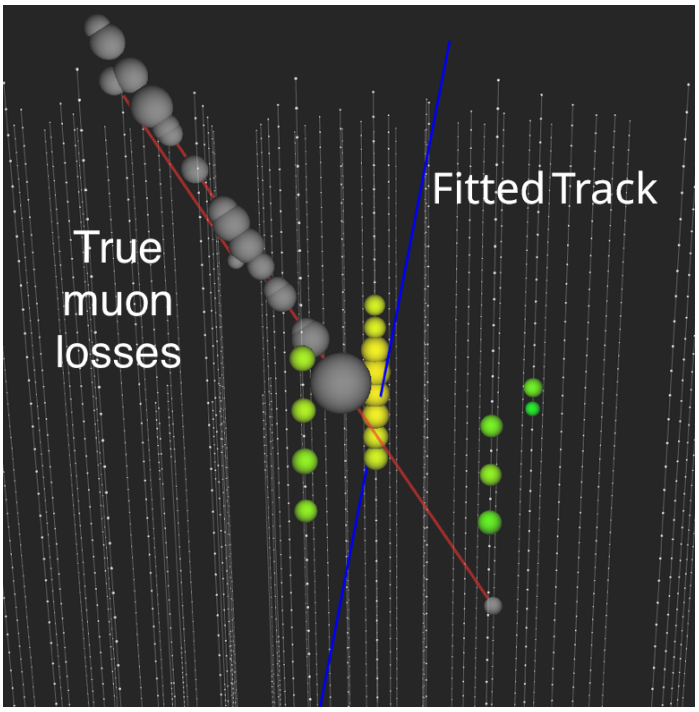

Figure 4.7: An event display of a simulated dim muon which passes the outer layer veto. There are no cleaned veto hits, and the isolated deposit within the detector, which has been misreconstructed. Using a track hypothesis and searching for single hits, one can find traces of the true muon track

HLC cleaned veto hits, but may show up as single SLC hits. These SLC hits must occur prior to the internal reconstructed vertex to maintain causality. By looking back from the vertex, one can test various track direction hypotheses to see if there is any charge in the veto layer causally associated with them, which may indicate a muon track. We search for hits within a cylinder of radius 100 m centred along the

track hypothesis, and sum up any veto hits we see.

As we are not yet sure of whether a given event is a track or a cascade, we run both reconstructions on all events. We run a cascade vertex fit using the Monopod reconstruction [63], requiring that the vertex lies in the interior of the detector. Using the reconstructed vertex, for each hypothesis, if we find more than 0.5 PE associated veto charge deposits for events depositing a total below 1000 PE, we reject the event. For brighter events, above a total charge deposit of 1000 PE, we require greater than 2 PE to reject the event. The reconstruction of tracks is somewhat more involved. We first run a series of fits on cleaned split pulses for the track direction.

- LineFit: A first-guess algorithm which has a closed-form solution, but simplifies the Cherenkov emission pattern as a plane wave moving through the detector. [64]
- Single Pandel Fit [65], using LineFit as a seed. This reconstruction is able to account for the geometry of photon emission, and also the effects of optical scattering in the South Pole ice. The distribution of time delays from optical scattering is modelled by a family of analytic approximations which are called the 'Pandel' functions. We refer to this reconstruction as the SPEFitSingle.
- 4 iterations of an Iterative Pandel Fitter, using the previous stage as a seed. We refer to this as SPEFit4
- A single pandel fit using the Multi Photoelectron (MPE) Pandel Likelihood functions, with the previous stages as seeds
- SplineMPE fit [66], again using the previous fits as seeds for the fitter

If the final stage of the fit fails for any reason, the previous valid stage is used for reconstruction of the track direction. The track energy is reconstructed by running

the Millipede algorithm [67].

In addition, if we see clear upgoing track events, which are a signature of muon neutrino charged current interactions, we tag those events at L4. We require a more stringent cut, however, requiring at least 10 PE of charge associated with either the Cascade Monopod vertex, or the Track Millipede vertex.

In addition, several cuts on coincident events are performed beginning at L4. We first compute a charge weighted distance for each DOM from the reconstructed event. If the hits in the detector are from two coincident events, this charge weighted distance would be quite large, compared to causally connected hits from a single event. We therefore cut events with a charge weighted distance greater than both 150 m for the cascade reconstructed vertex and 110 m for the track reconstruction. The next cut applied checks the opening angles between different track fits applied to the event. If the opening angle is greater than 30°, this is likely a coincident event and is also removed. Lastly, we apply a cut based on the reduced log-likelihood of the SPEFit4 reconstruction. This is a check on the quality of the reconstruction, which would be worse for a coincident event, resulting in a greater value of the reduced log-likelihood. We cut events with an SPEFit4 reduced log-likelihood above 8.5.

4.7 L4: Cascade/Track Classification

We run the deep neural net (DNN) based 'i3deepice' [68] classifier to separate our events into track and cascade morphologies. The DNN [50] takes a pulse series as an input, and generates a probability that the event is one of five categories, from

- Cascades: Usually well-contained within the detector volume.
- Starting Tracks: Track with the interaction vertex contained within the detector

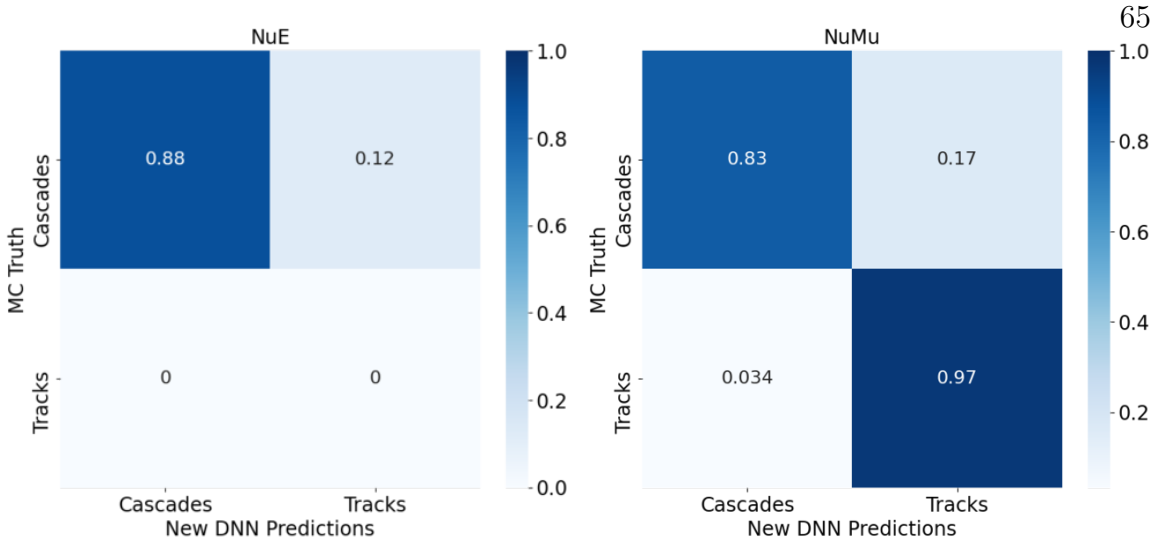

(a) ν_e (b) ν_μ

Figure 4.8: Confusion Matrices of the DNN Classification cut, derived from MC. These show the rate of correctly classified and misclassified events for each flavor

- Throughgoing Tracks: Track with the interaction vertex outside the detector volume, which goes through the detector without a secondary decay from the muon.

- Stopping Tracks: Events where the muon track ends inside the detector volume, mostly low energy minimum ionizing events entering the detector.

- Skimming Events: Events with little to no energy deposition in the detector, such as a cascade with its primary vertex outside the detector (uncontained) or a track which passes by the detector without entering

In MESE, the input to the DNN is the "TWTSInIcePulses" pulse series, which is the result of "InIcePulses" having undergone TimeWindow(TW) and TopoSplitter(TS) cleaning. We require

$$(\mathcal{P}_{\text{Cascade}} > 0.6)\&(\mathcal{P}_{\text{StartingTrack}} < 0.1)\&(\mathcal{P}_{\text{StoppingTrack}} < 0.1)\&(\mathcal{P}_{\text{ThroughGoingTrack}} < 0.1) \tag{4.2}$$

for an event to be classified as a cascade, with all other events failing this cut being classified as tracks. These cuts were obtained from checks on Monte Carlo simulations, with their relative performances illustrated in Fig. 4.8

4.8 L5: Charge-dependent Fiducial Volume Cut

The downgoing track veto becomes less efficient for dimmer events, with incoming muons at this stage having lower energy. A cut based on scaling the fiducial volume depending on the magnitude of the deposited charge is more efficient at eliminating muon tracks. This is because any potential incoming muon track has a greater chance of depositing hits further inside the detector, in effect a thicker veto region.

In the earlier 2-year analysis [69], the Fiducial Volume for each event was scaled solely by deposited charge. A major update in this analysis has been adding zenith and morphology dependence, retaining more events to boost low energy sensitivity. Given the inclusion of a large number of tracks, this analysis considers that the reconstructed monopod vertex may not align with the track's initial energy loss. Consequently, the fiducial volume cut is applied to the monopod vertex for cascade-classified events and to the Millipede first loss position for track-classified events. The zenith dependence takes into account the fact that most of our background is downgoing muons, which is where we need the strictest cuts, whereas we do not need very thick margins in the upgoing direction.

We recalculate the optimal cuts on the distance of the vertex from the top (VetoMargin_Top) and the side of the detector (VetoMargin_Side) to optimise the ratio of atmospheric neutrinos to atmospheric muon background for each charge and zenith bin. For events in the more vertical bins, we first evaluate the top margin, and then decide on the side margin cut for events which pass the top margin cut for each charge

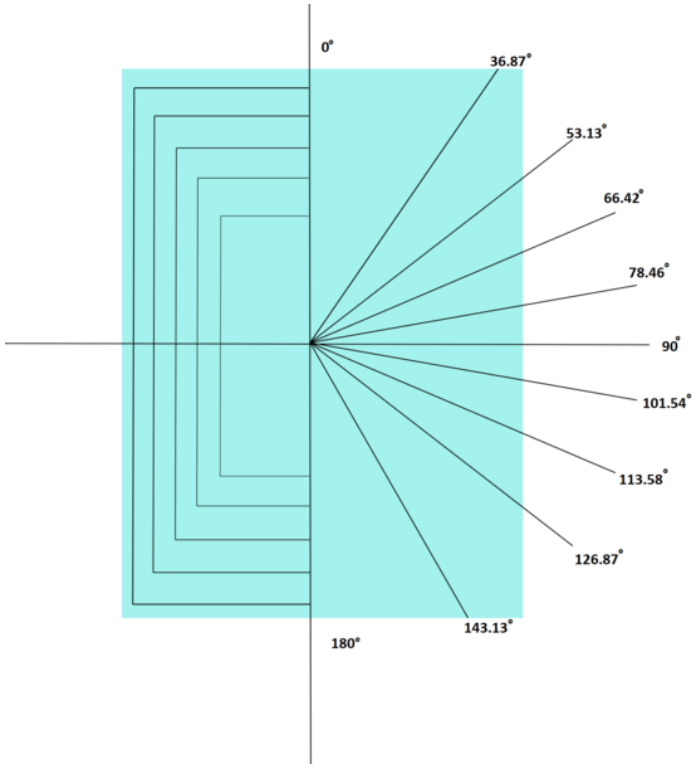

Figure 4.9: The new zenith binning for the Fiducial Volume Cut. We use thicker veto margins in the downgoing regions where we expect the bulk of our muon background. The bin edges correspond to the 10 evenly spaced cosine zenith binning used in the diffuse analysis, elaborated upon in chapter 7

bin. On the other hand, we decide the side margin cut first for the horizontal events, followed by the top margin.

4.9 Event Rates

We evaluate the expected event rates at each stage of MESE to ascertain the efficiency of our cuts and our expected signal rates. These studies are performed with MC simulations

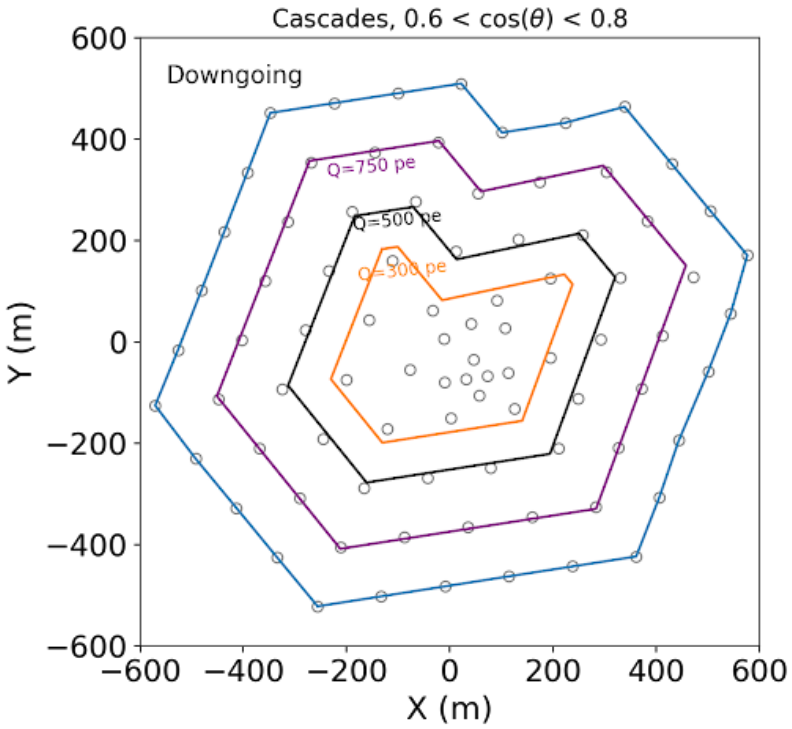

(a) Top view

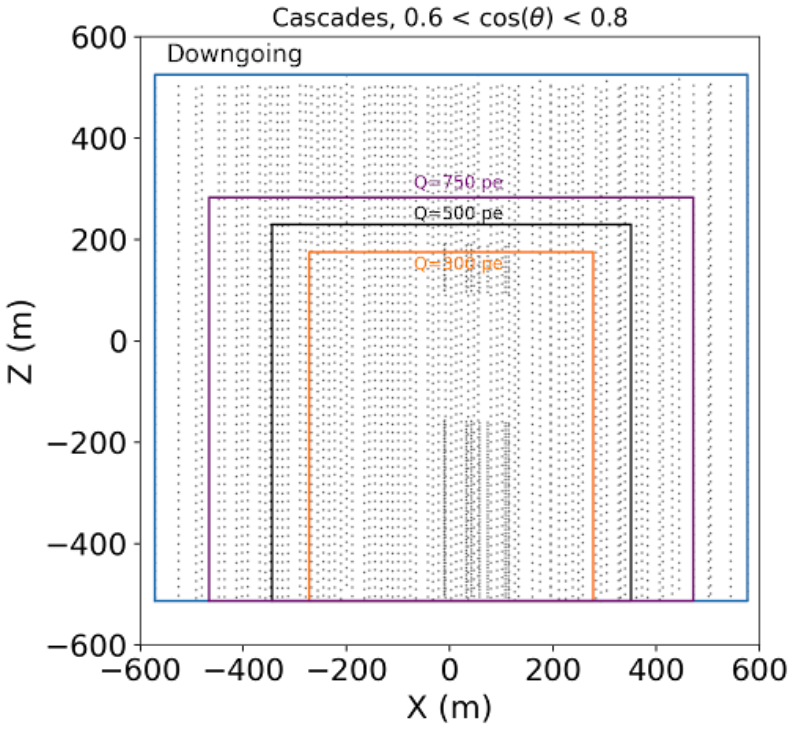

(b) Side view

Figure 4.10: An illustration of the scaling of fiducial volume with deposited charge for a specific zenith bin (cosine zenith $\in (0.6, 0.8)$) for cascades

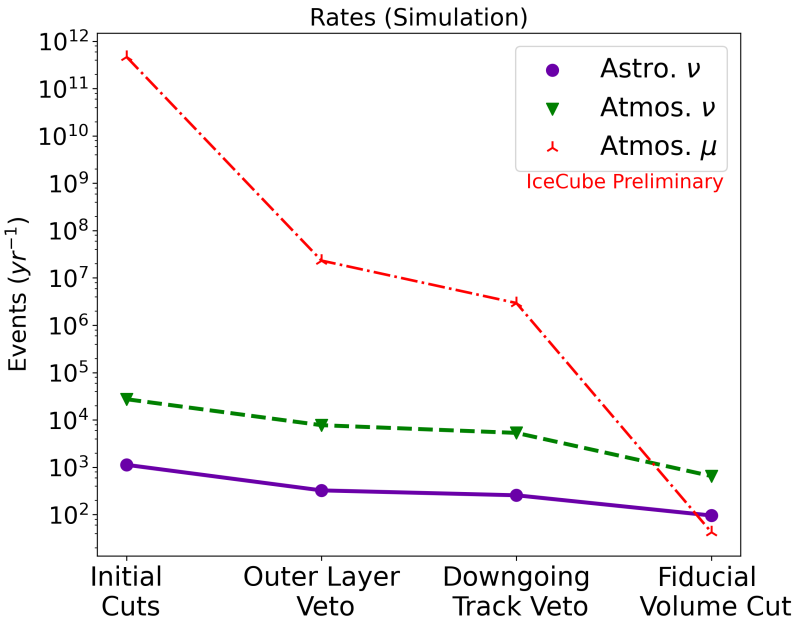

Figure 4.11: The expected rates of signal astrophysical neutrinos compared to background atmospheric neutrinos and muons at each stage. To evaluate the per-flavour flux of astrophysical neutrinos, we assume here that $(\Phi_{\text{astro}}(10^{-18}/\text{GeV}/\text{cm}^2/\text{s}/\text{sr}), \gamma_{\text{astro}}) = (2.06, 2.46)$(from the 2-year MESE analysis). For the atmospheric flux prediction, we use the *H4a* cosmic ray nuclear composition model [70] and the *SIBYLL2.3c* hadronic interaction model [71]. The cuts reduce the background muon flux by ten orders of magnitude at the final level, while preserving a significant proportion of signal events.

Chapter 5

The Atmospheric Neutrino Flux and the Self-Veto Effect

The atmospheric neutrino self-veto effect is the suppression in the atmospheric neutrino flux due to an accompanying muon from the same air shower arriving at the detector at the same time. This scenario is illustrated in Fig. 5.1. The muon causes the entire event to be vetoed, including the neutrino. This effect is primarily observed in the Southern Sky, due to the Earth acting as a filter for atmospheric muons from the Northern Sky, as illustrated in Fig. 5.2. Due to computational limitations, the signal neutrino flux and atmospheric background are not simulated together. This is because an efficient background rejection algorithm would reject the bulk of the simulated air shower flux, resulting in a very low simulation efficiency and correspondingly large simulation livetime requirements.

The p_{light} is the likelihood that a muon will get rejected by the event selection. It can be understood as the complement of the fraction of muons which pass the event selection i.e $1 - \frac{N_{\mu,\text{pass}}}{N_{\mu,\text{total}}}$.

The approach taken to model the self-veto suppression follows the method outlined in [73], where the muon rejection efficiency is parameterized as the p_{light}, a function of

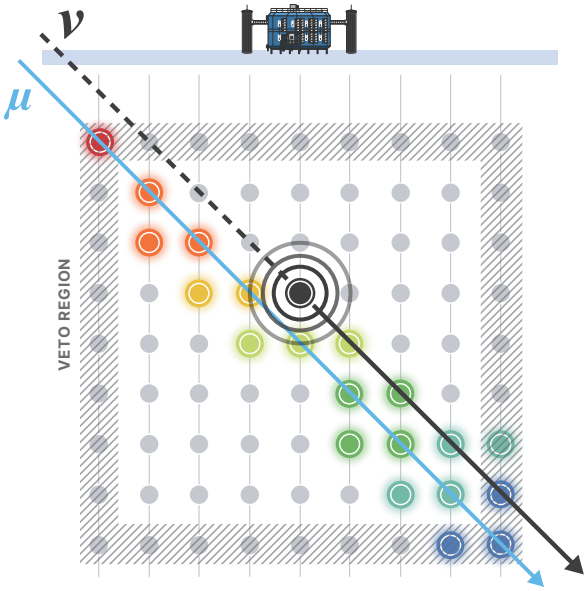

Figure 5.1: Cosmic ray showers in the atmosphere can produce a flux of both neutrinos and muons. Due to the relativistic energy of the primary cosmic ray, these are produced along trajectories almost parallel to the parent particle, and may arrive at the detector together. The veto may detect the incoming muon, and reject the entire event. [72]

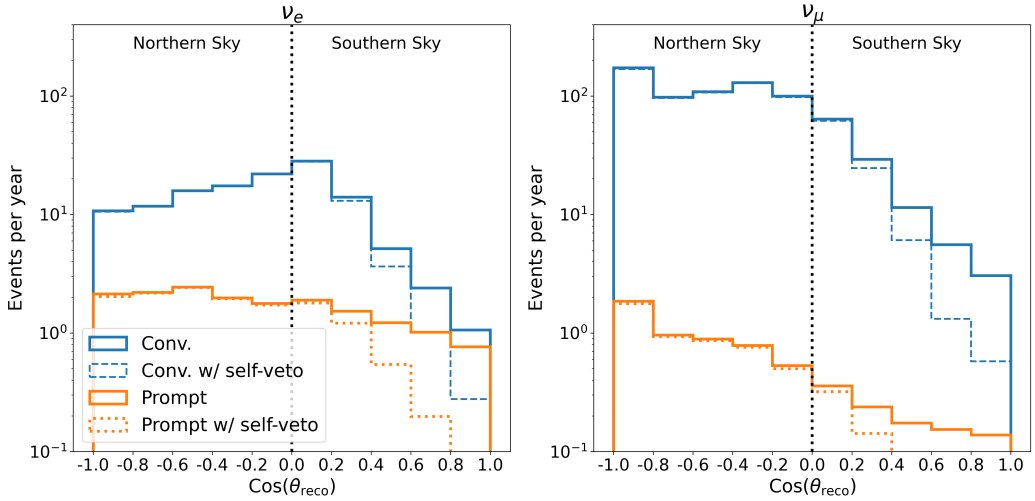

Figure 5.2: An illustration of the suppression in atmospheric neutrino flux due to the self-veto effect, compared to the flux when the self-veto is ignored. It is evident that an inaccurate model of the self-veto will result in biasing of the astrophysical neutrino measurement at lower energies where the atmospheric flux is dominant

the muon energy, cosine of the incident zenith angle, and the depth of the interaction. The nuVeto package [74] uses the p_{light} as an input to calculate passing fractions for the neutrino flux, which is the fraction of atmospheric neutrino events which are not rejected due to accompanying muons, and survive into the final sample. nuVeto uses the MCEq [75] cascade matrix shower along with muon range tables to evaluate the passing fractions. The effects of the analysis therefore affect the calculation when evaluating the p_{light} The p_{light} can be calculated in many ways. The simplest approach is to model the p_{light} as a step function, as done in the ESTES [57] and Cascades [76] analyses. Passing fraction tables are created for a few specific transition energies, and these are interpolated using a fit parameter. A more sophisticated modelling of the event selection response was carried out by the HESE analysis [12], which used MuonGun MC simulation of single muons. The fraction of muons which passed the event selection provided a smooth continuous functional form for the p_{light}, and as the HESE analysis focused on brighter events, the assumption of the muon flux primarily consisting of single muons is valid. When analyses push towards sensitivity at lower energies, however, one must account for muon bundles. As the event selection cuts are more stringent, it is also difficult to obtain sufficient MuonGun MC statistics to adopt the method used by the HESE analysis.

The approach taken in MESE is to inject muon bundles into signal neutrino events which are known to have survived the selection cuts. One is thus able to evaluate the p_{light} directly from the fraction of these events which survive the event selection when combined with muons. As the bundles are injected only into signal events at final level, we know that all of these neutrino events would have survived the event selection if not for the additional muons. Another advantage of this method is that it can be extended to other high purity event samples.

The muon bundle must be carefully constructed to account for correlations between

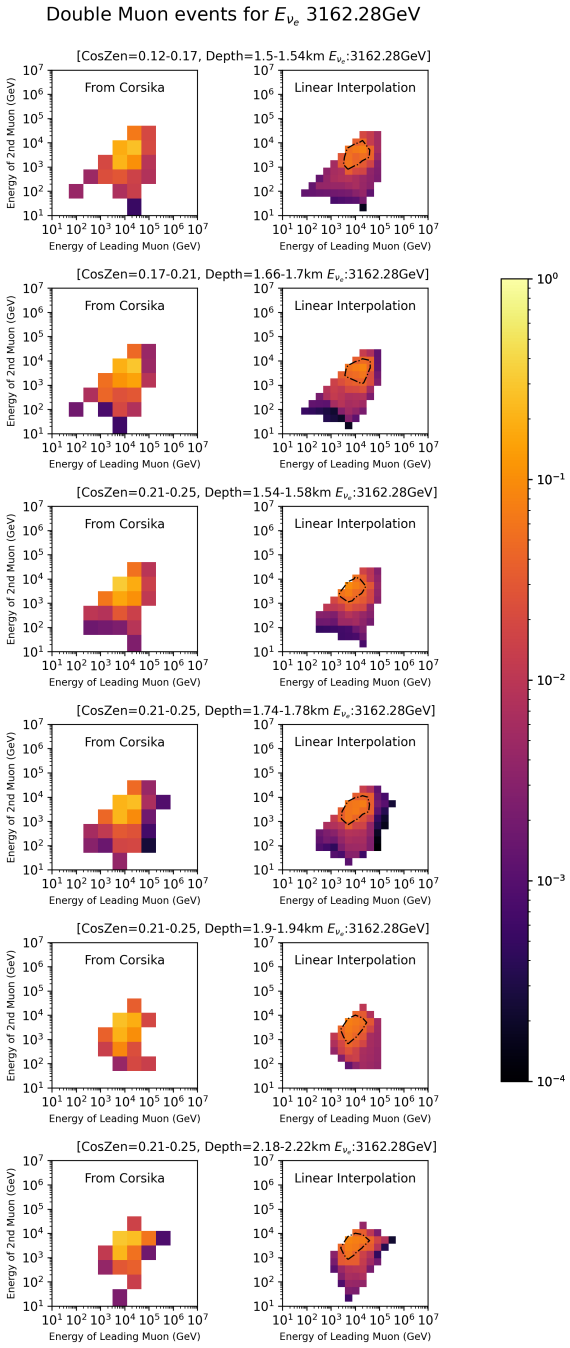

Figure 5.3: An illustration of the muon tables created from CORSIKA. These histograms represent muon energies for events with multiplicity two accompanying an electron neutrino of energy 3.16 TeV. The leading muon energy is on the x-axis, while the subleading muon energy is on the y-axis. The right hand side plots are linear interpolations of the CORSIKA histograms, which are statistics limited. The contours on the interpolated plots show the region of probability summing to 50%

the atmospheric neutrinos and muons from the same bundle. We use CORSIKA [77] air shower simulations to characterize these correlations, by building tables of muon multiplicities and energies accompanying neutrinos of specific flavours and energies, incident from a particular zenith angle. We also bin our tables based on whether the interaction vertex was below, above, or in the dust layer. The first stage in the process is identifying the most likely multiplicity for the accompanying muon bundle. CORSIKA gives us a distribution of these multiplicities for each neutrino bin. Removing muons below 10 MeV, we linearly interpolate the statistics-limited CORSIKA results to obtain smooth distributions, normalized by neutrino energy to obtain PDFs. We then sample the histograms to obtain the most likely multiplicity of the muon bundle. As illustrated in Fig. 5.3, for each multiplicity n, we have n-dimensional distributions of the muon energies in descending order. For computational ease, we restrict our multiplicities to n$\leq$4, although we have verified that extending multiplicities to greater values does not significantly affect whether an event is retained or rejected. Once the multiplicity is selected, the energies of the muons in the bundled is sampled from the n-dimensional template. This template is obtained by splining the histograms created from CORSIKA, to obtain a smoothly varying distribution. As we are limited by the statistics of our CORSIKA MC, for some bins too sparsely populated to generate individual splines, we inject a single muon with the summed energy of the entire muon bundle. After injecting the muon bundle into the neutrino event, we reprocess the combined event through the different stages of simulation and analysis, incorporating the SnowStorm propagation technique, detector simulation, and preliminary L1 and L2 cuts followed by the MESE event selection. Using the ratio of fluxes from L2 (pre-MESE) and L5 (post-MESE), we evaluate $p_{\text{light}} = 1 - \frac{\Phi_{\text{L5}}}{\Phi_{\text{L2}}}$, as illustrated in Fig.5.4. We fit the p_{light} using the sum of a sigmoid and a Gaussian

function, as defined by

$$\mathcal{F}_{E_{mu}} = \frac{1}{1. + e^{-b(log(E_{mu})-log(a))}} + c * e^{-\frac{(log(E_{mu})-log(x1))^2}{k1}} \tag{5.1}$$

We use the statistical error on the fit function parameters to create an envelope of

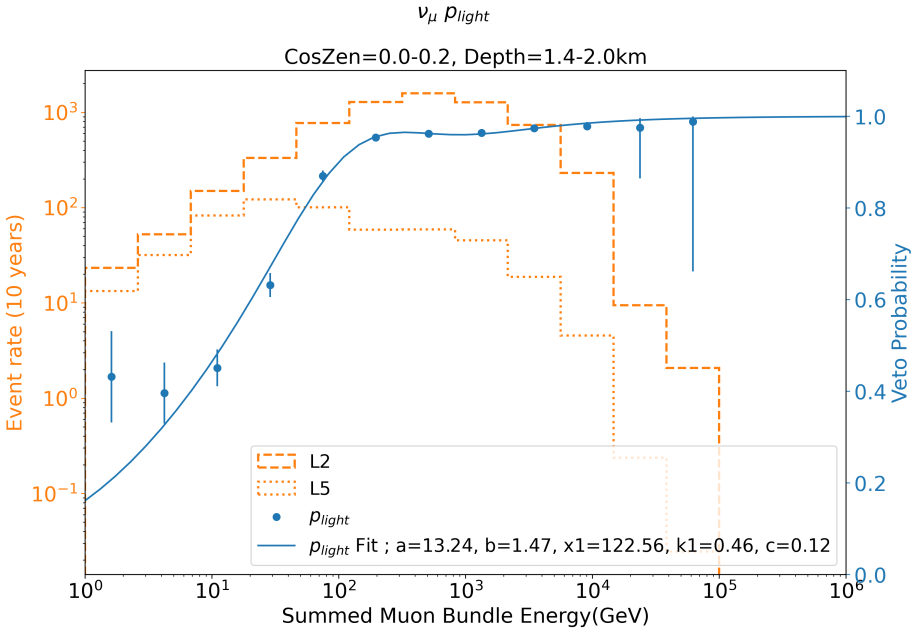

Figure 5.4: The calculation of p_{light} for a particular cosine zenith-interaction depth bin for muon neutrinos. The error bars are calculated using the PyIK package [78] to evaluate the 68% confidence intervals using the Wilson score method [79]

p_{light} around the baseline fit, which allows for variation in the self veto to accommodate the fit to data. This is done by evaluating the p_{light} with the location parameters for the sigmoid and the Gaussian (a and x1) shifted by $^{+10}_{-3}$ sigma from the best fit values, creating the envelopes illustrated in Fig. 5.5. Intermediate values using shifts of $^{+3}_{-1}$ sigma shifts from the best fit values are also evaluated We use the nuVeto package [74] to evaluate the neutrino passing fractions as a function of neutrino energy, binned by neutrino cosine zenith and interaction depth, as shown in Fig. 5.8. The binning in cosine zenith mirrors the binning used in the analysis, with five equal bins from (0.0-1.0), while the binning in the interaction depth splits the detector into deep (beneath

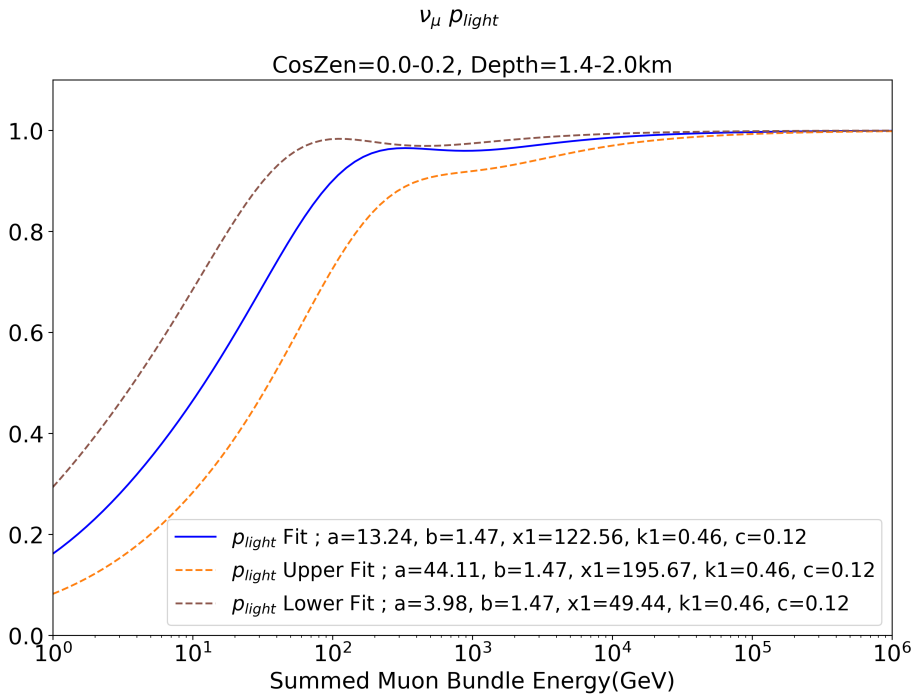

Figure 5.5: The upper and lower bound p_{light} envelopes for muon neutrinos in a specific cosine zenith and depth bin, along with the best fit p_{light}.

the dust layer, with interaction depths from 2.1-2.5 km), and shallow (above the dust layer, with interaction depths from 1.4-2.0 km) events, along with a separate classification for events with their interaction depth inside the dust layer from 2.0-2.1 km. The **effective_veto** ($\eta_{\mathrm{Self-Veto}}$) nuisance parameter is used to parametrize the variation in the passing fractions, interpolating between the bounds to obtain the best fit to data. For each event, the five passing fractions generated from the baseline p_{light} and the shifted values are fitted by a χ^2 Cumulative Distribution Function given by

$$PF(\epsilon) = \frac{1}{\Gamma(\mathrm{df}/2)}(\gamma(\mathrm{df}/2, \frac{x - \mathrm{loc}}{2 * \mathrm{scale}})) \tag{5.2}$$

in the nuisance parameter (Fig. 5.7). A CDF was used to parametrize the passing fraction to ensure that the value would be asymptotically capped at 1. For each event, we obtain a fitted value of the *df*, *loc*, and *scale*, as a function of the nuisance

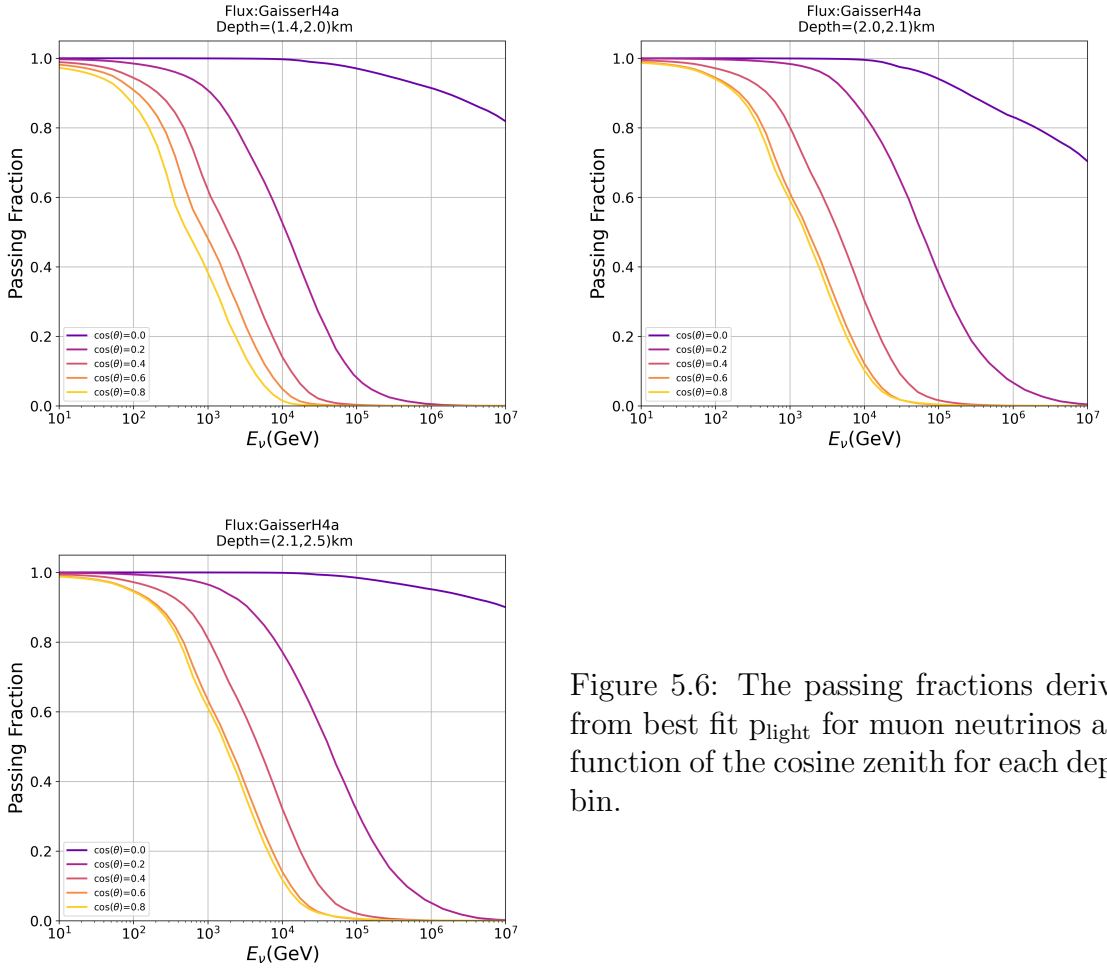

Figure 5.6: The passing fractions derived from best fit p_{light} for muon neutrinos as a function of the cosine zenith for each depth bin.

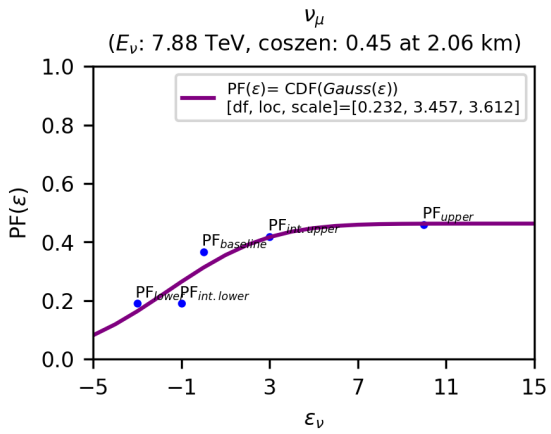

Figure 5.7: The effective veto nuisance parameter is used to parameterize the effect of the self-veto, and is obtained by fitting a χ^2 CDF to the best fit passing fraction along with the four passing fraction envelope values.

parameter. The nuisance parameter is then fit across all bins by the minimizer.

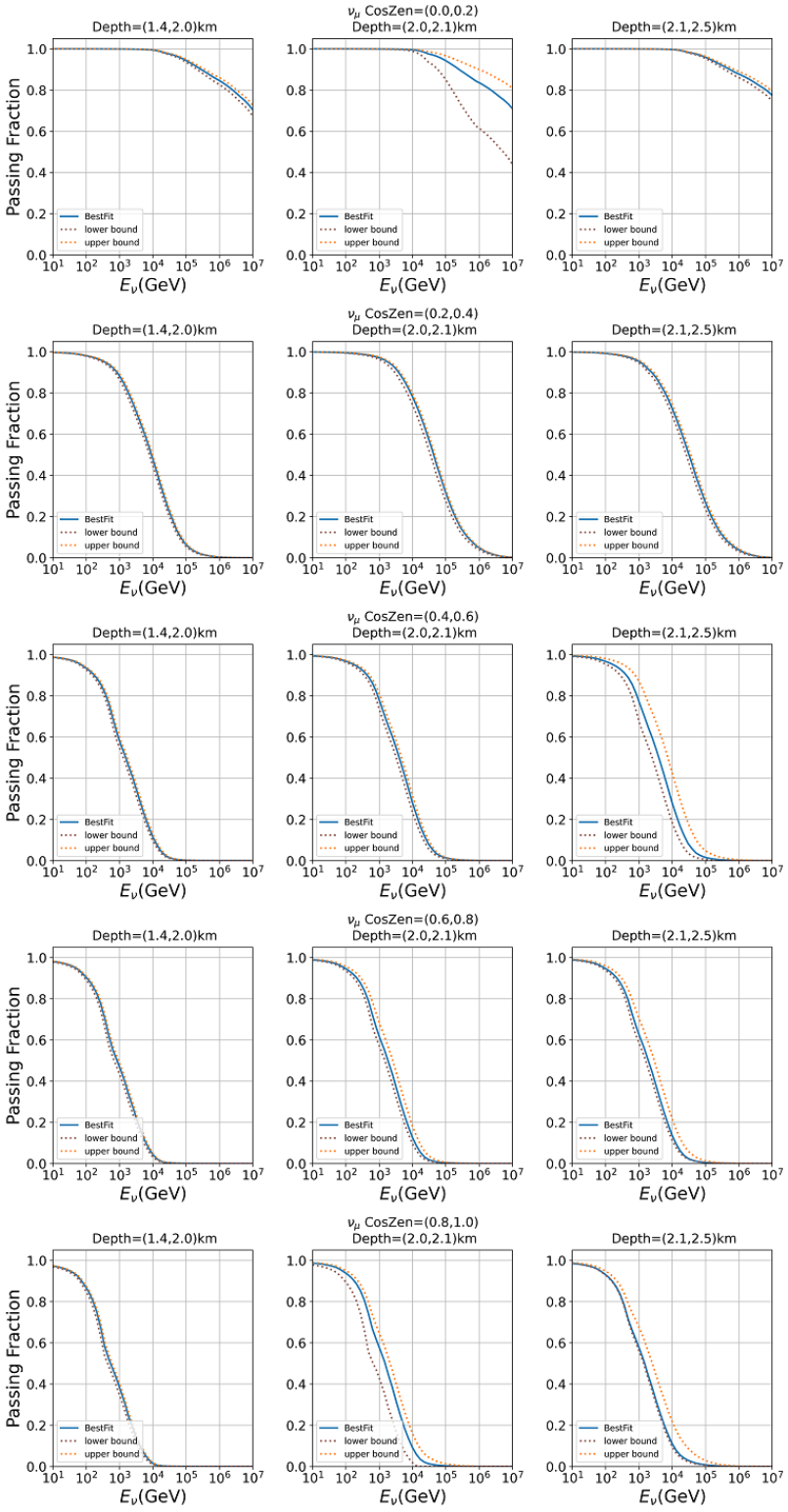

Figure 5.8: The upper and lower bound passing fraction envelopes for muon neutrinos in a specific cosine zenith and depth bin, along with the passing fractions derived from best fit p_{light}. The effective veto nuisance parameter is used to interpolate between these bounds to find the best fit to data

Chapter 6

Treatment of Systematic Uncertainties

The various uncertainties associated with the measurement of the astrophysical neutrino spectrum have been characterized using nuisance parameters. These parameters are allowed to vary while fitting the data, to account for variations beyond the change in the astrophysical flux parameters. This section will describe the treatment of the theoretical uncertainties associated with atmospheric cosmic ray air shower modelling, in particular the development of an improved technique to evaluate the effect of the atmospheric self-veto effect [73, 61]. The effects of uncertainties in the modelling of the IceCube detector and its response to neutrino events have been evaluated using the SnowStorm technique [80]. The fit of Monte Carlo simulation to data incorporates the signal astrophysical flux, along with various nuisance parameters to account for all of these effects.

6.1 Atmospheric Flux Uncertainties

We used the NuGen software [81] to simulate the DIS interactions of neutrinos in the detector volume. For the interactions, the Cooper-Sarkar-Mertsch-Sarkar (CSMS) model [36] for the neutrino-nucleon cross-sections is used with the Earth's density assumed to follow the Preliminary Reference Earth Model (PREM) model. The primary background to searches for TeV neutrinos arises from cosmic ray interactions in the atmosphere, creating showers of hadrons and leptons, resulting in a background of atmospheric muons and neutrinos at IceCube. The fluxes are computed using the MCEq cascade solver package [75], which evaluates the evolution of particle fluxes as they propagate through the atmosphere. The atmospheric flux is modelled using *H4a* [70] as the primary cosmic ray composition model, and *SIBYLL2.3c* as the baseline hadronic interaction model [71]. The flux of conventional atmospheric neutrinos, from the decay of pions and kaons created when cosmic rays interact with atmospheric nuclei, is fit by an overall normalization factor. The prompt atmospheric neutrino flux, from the decay of charmed hadrons created in cosmic ray interactions, is treated similarly.

In order to characterize variations from the baseline models, we incorporate a set of additional nuisance parameters. The Barr parameters are a set of nuisance parameters which allow for variations in the pion and kaon decays in cosmic-ray showers [82]. The MESE analysis uses four Barr parameters (*h, w, y, z*), which have been tested with simulation to have the greatest effect on our flux measurement. The baseline models assume that the primary cosmic ray spectrum follows a specific spectral index, and therefore variations in the atmospheric neutrino flux due to a change in the spectral index must also be accounted for with a nuisance parameter. Variations in the atmospheric neutrino spectrum due to the differences in the underlying cosmic

ray model are accounted for by interpolating between the *H4a* model and the *GST4* model [83]. This choice of models was based on the potential bias in the astrophysical model fit obtained, following the example of the ESTES analysis [57].

The overall atmospheric muon flux was simulated with the MuonGun package [84], which generates single muons based on simulations of cosmic ray air showers generated with CORSIKA [77], using the *SIBYLL2.1* [85] hadronic interaction model. The advantage of separating the neutrino and muon simulation in this manner is a significant reduction in computational cost, as compared to the full air shower simulation with CORSIKA. Due to the high purity of the final level event sample, after the selection cuts, the number of discrete MuonGun MC events is quite low. This results in statistical fluctuations and discontinuities in the expected muon flux in the reconstructed observable space. This led to the adoption of a smoothed template, generated from the MuonGun MC by a kernel density estimator (KDE). The template is generated by bootstrapping the MuonGun MC events to obtain the variation in the single muon distribution in observable space. This helps determine the variance on the template, which is then included in the fit with an overall normalization factor. A Gaussian prior is applied to the MuonGun normalization, derived from pre-final level comparisons of simulation to data. At the L4 stage, the data is still dominated by muon background, especially below 10 TeV. We therefore scale up the simulation to match the data in the energy range of 500 GeV to 1 TeV, as this is outside the MESE fit range for the astrophysical flux measurement, to avoid biasing the fit.

6.2 Detector Systematic Uncertainties

The detector systematics provide a handle on the effect that the ice modelling and detector simulation has on the events reconstructed by IceCube. The computational cost of modelling variations in the ice parameters or detector response can scale very quickly, especially when each set of parameters must be independently simulated. The SnowStorm method [80] was developed to tackle this limitation, requiring the simulation of a single set which can account for various parameter values.

The main factor of the SnowStorm method is the creation of an event ensemble, where each event is simulated with a different set of detector response parameters. These are chosen from individual sampling distributions to account for the model uncertainties. The method assumes the effects of systematic variations can be approximated by a linear perturbation, within a given range. This is performed by generating a gradient vector of nuisance parameters to calculate the expectation value for different detector response assumptions. Further details of the implementation may be found in [86]. The gradient vector is calculated assuming a nominal flux assumption, and applied to the weights of a simulation set of events assuming the various parameters fixed at their baseline values to evaluate the effect of changing the parameter values during the fit.

The systematic parameters that are treated with the SnowStorm method are:

- bulk-ice absorption
- bulk-ice scattering
- ice anisotropy
- hole ice angular acceptance parameters

- DOM efficiency

The bulk-ice at the South Pole is the Cherenkov medium for the photons emitted by charged secondary particles from a neutrino interaction. The photon travel paths through the ice vary with depth and also depend on the local absorption and scattering. The ice properties are parameterized by IceCube using studies with flashers onboard the DOMs, over multiple calibration campaigns. The non-isotropic angular photon acceptance of the downward-pointing PMTs inside DOMs, coupled with the effect of scattering from air bubbles in the refrozen holes, must also be accounted for. The variation in optical properties of the hole-ice compared to the bulk-ice is parameterized by two parameters p_0 and p_1, based on the parameterization used in [87]. The DOM efficiency uncertainty reflects the variation in converting photons incident at the PMT photocathode into an observed hit. The DOMs can have variable responses due to factors such as manufacturing tolerances, cable shadowing, and calibration uncertainties. This is modelled as a scaling factor applied globally to all DOMs. The measurement of the DOM efficiency was performed in a water tank with LED photon pulses [88], along with in-situ calibration using atmospheric muons. As the South Pole ice sheet has gradually evolved over millennia, there is also a variation due to the glacial flow direction, with light scattering more in one direction due to the orientation of dust grains. This results in a variation in refractive index along orthogonal directions, leading to a birefringence effect [89]. As the simulations used in the MESE analysis do not account for this anisotropic effect, a nuisance parameter has been added to the analysis to cover the expected variations.

6.3 Characterization

Various checks were performed on the systematic parameters to determine their relative importance to the fit, along with their effects on the physics parameters. Fig. 6.1 shows how the different systematic parameters affect each other, when evaluated from running fits to pseudo-data, having injected the best fit SPL flux from [13], with $\Phi_{\text{astro}} = 2.06$ and $\gamma_{\text{astro}} = 2.46$. We also verify the ability of the fitting tools (described in sec. 7.1) to recover the injected parameters, as observed in Fig. 6.2. A list of all the nuisance parameters and their priors when applicable is provided in Table. 6.1

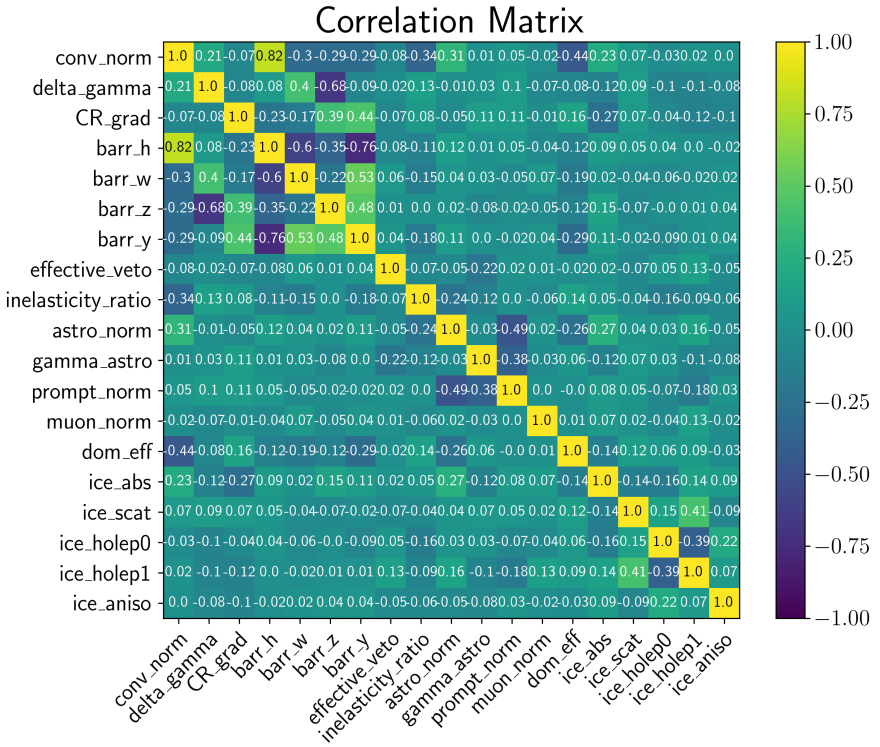

Figure 6.1: The correlation between various systematics, showing how they affect each other. We observe a high degree of correlation between the various parameters modelling the atmospheric flux.

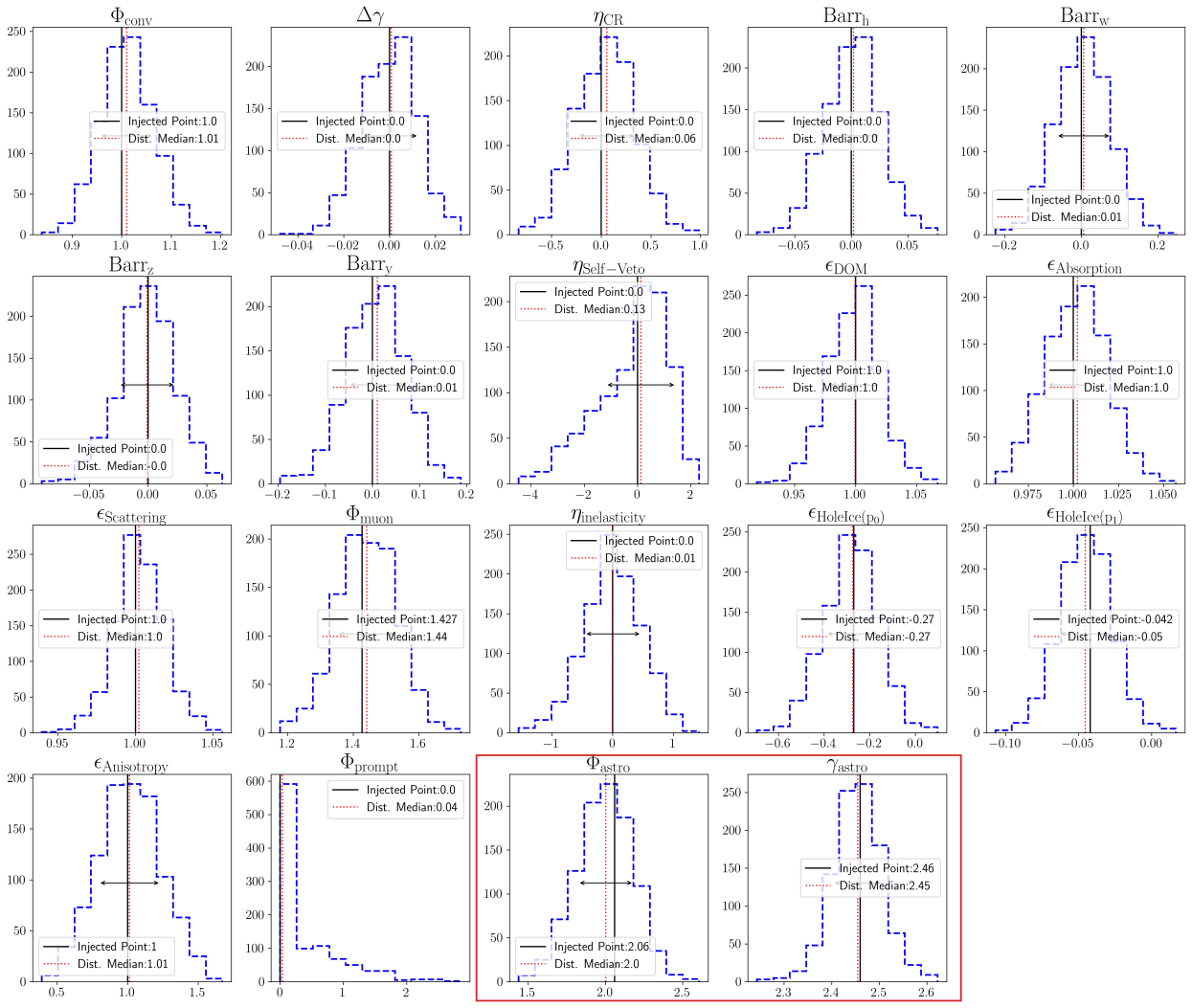

Figure 6.2: The distributions of fit parameters obtained from fits to pseudo-data generated from simulated inputs, with the 2-year MESE flux injected as the physics model.We show that we are able to recover the injected values. The physics parameters are outlined in red.

Parameter	Range	Prior	Nominal Value	Description
Atmospheric Flux Parameters				
Φ_{muon}	$[0, \infty)$	Gaussian	1.427 ± 0.75	Atmospheric muon flux normalization
Φ_{conv}	$[0, \infty)$	Gaussian	1.0 ± 0.25	Atmospheric conventional neutrino flux normalization
Φ_{prompt}	$[0, 4)$	-	-	Atmospheric prompt neutrino flux normalization
$\Delta\gamma$	$[-1, 1]$	Gaussian	0.0 ± 0.055	Variations in the spectral index of the primary cosmic-ray spectrum
η_{CR}	[-2,+1]	Gaussian	0 ± 1.0	H4a-GST cosmic ray flux model interpolation
Barr_{h}	[-0.8,0.8]	Gaussian	0 ± 0.15	Barr parameters
Barr_{w}	[-0.6,0.6]	Gaussian	0 ± 0.4	
Barr_{y}	[-0.6,0.6]	Gaussian	0 ± 0.3	
Barr_{z}	[-0.244,0.6]	Gaussian	0 ± 0.12	
$\eta_{\text{inelasticity}}$	[-2.0, 2.0]	Gaussian	0 ± 1.0	Variations of the inelasticity of neutrino interactions
$\eta_{\text{Self-Veto}}$	[-5, 15]	Gaussian	0 ± 3	Self-Veto interpolation
Detector Systematic Parameters				
$\epsilon_{\text{Scattering}}$	[0.9,1.1]	Gaussian	1 ± 0.05	Bulk-ice model scattering coefficient scaling
$\epsilon_{\text{Anisotropy}}$	[0.0,2.0]	Uniform	1.0 ± 1.0	Bulk-ice model anisotropy variation
$\epsilon_{\text{Absorption}}$	[0.9,1.1]	Gaussian	1 ± 0.05	Bulk-ice model absorption coefficient scaling
$\epsilon_{\text{HoleIce}(p_0)}$	[-0.84,0.3]	Uniform	-0.27	Hole ice angular acceptance parameter p0
$\epsilon_{\text{HoleIce}(p_1)}$	[-0.134,0.05]	Uniform	-0.042	Hole ice angular acceptance parameter p1
ϵ_{DOM}	[0.9,1.1]	Uniform	1	DOM efficiency

Table 6.1: Summary of all nuisance parameters used in the measurement of the astrophysical diffuse flux using MESE. All parameters are assumed to be independent.

Chapter 7

Measurement of the Diffuse Astrophysical Neutrino Flux

The following chapter elaborates on the techniques used to analyze the spectrum of diffuse astrophysical neutrinos, and then presents the results obtained. These results are intended to be published in [90] and [91]

7.1 Forward-folded Binned Likelihood Analyses

The measurement of the astrophysical neutrino flux is performed using a forward-folded binned likelihood analysis. The term forward folding refers to the processing of Monte Carlo generated events through the detector simulation, to obtain the fluxes predicted by a particular theoretical model. One can think of this as a convolution of expectations in the space of 'truth' quantities, such as true energy and true direction, with the detector response, to obtain expectations of reconstructed quantities, such as reconstructed energy and direction. As only reconstructed quantities are available for data, this enables the model predictions to be compared directly to data. This

is to be contrasted with an unfolding analysis, where one 'unfolds' the effects of the detector and selection effects to obtain the representation of the data in 'truth' space. A binned likelihood analysis is performed by constructing orthogonal bins in the reconstructed observables, which for MESE are the deposited energy and cosine zenith. Each simulated event is therefore placed in the corresponding 2-dimensional bin, after being processed through the event reconstructions as explained in Ch. 4. Upon applying the appropriate model-dependent weights to each event, this yields a bin-wise expectation value for each model flux. We then compare the observed number of events to the sum of the astrophysical neutrino flux, the conventional and prompt atmospheric neutrino fluxes, and the atmospheric muon flux. A Poissonian likelihood can be estimated for each bin using the MC sum as the expectation value λ, to be compared to the observed data k. The Poisson probabilities for each bin are then multiplied together. However, the Poissonian likelihood approach assumes the expectation value to be precisely evaluated for each bin, which is not possible when working with a finite simulation set, as there are insufficient statistics. The uncertainty in the expectation value is therefore comparable to the uncertainty in the observation, which may pull the fit parameters from their true values.

A modification of the Poissonian likelihood, known as the *effective likelihood* or $\mathcal{L}_{\text{eff}}$ [92], is used to mitigate the effect of limited simulation. In this approach, the weights of events in each bin is approximated by a scaled Poisson distribution. A measure for the simulation uncertainties is derived from the sum of the weights squared, and used in formulating $\mathcal{L}_{\text{eff}}$.

$$\sigma^2 = \sum_j w_j^2 \tag{7.1}$$

The $\mathcal{L}_{\text{eff}}$ results in widened contours for cases where the uncertainty in the simulation statistics is large, and converges to the Poissonian Likelihood when the uncertainties

are small.

The Gaussian priors ($\mathcal{N}$) on the nuisance parameters are incorporated as penalty terms to the likelihood, reducing the likelihood away from the prior value.

$$\mathcal{L}_{\text{eff}} = \prod_i \mathcal{L}_{\text{i}} \prod_j \mathcal{N}_j \tag{7.2}$$

7.2 Likelihood Minimization with NNMFit

The computation of the parameters which weight the MC to fit the data best is equivalent to evaluating the parameters which maximize the likelihood. This is an intensive computation, due to the large MC statistics required to accurately model the data. The diffuse analysis with the MESE sample was performed using the NNMFit toolkit to maximize the likelihood, or minimize the negative log-likelihood. It uses the aesara[93] library to perform large tensor operations efficiently. NNMFit is able to modify the eventwise weights based on changes in the fit parameters, reflected as a variation in the event counts in each bin. NNMFit then calculates a binwise and full likelihood under each set of parameters, and then minimizes the negative log likelihood using either the LBFGSB[94] or the MINUIT[95] minimization algorithm implemented in scipy.

7.3 Datasets

As explained, neutrino and muon events are simulated independently and weighted to account for the different fluxes. These signal and background simulation sets are used to develop the event selection before applying it to real data events, in addition to being used to perform the fits. A short overview of the different simulation sets used is provided in this section, with further details provided in Appendix A.

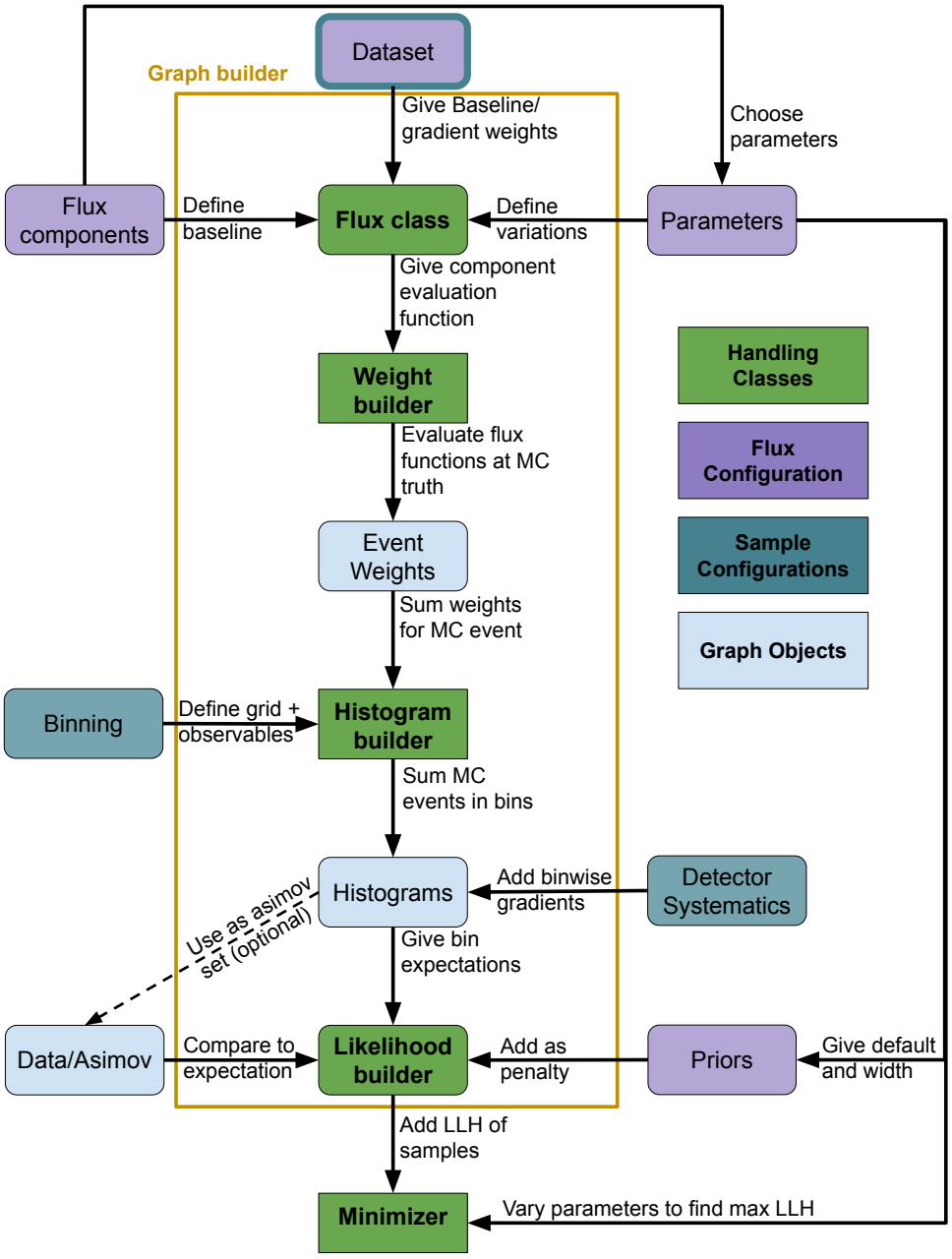

Figure 7.1: A diagram of the structure of the NNMFit Toolkit [96]

The first signal simulations used to refine the MESE event selection were the NuGen datasets of Table A and the MuonGun sets of Table A, which were generated by Dr. M. Silva. The MuonGun was also used to generate the KDE template used in the fits, necessary due to the low surviving statistics of the background simulation at final level. The low statistics could have affected the fit by modifying the uncertainties associated with the background predictions. The fit was performed using neutrino MC

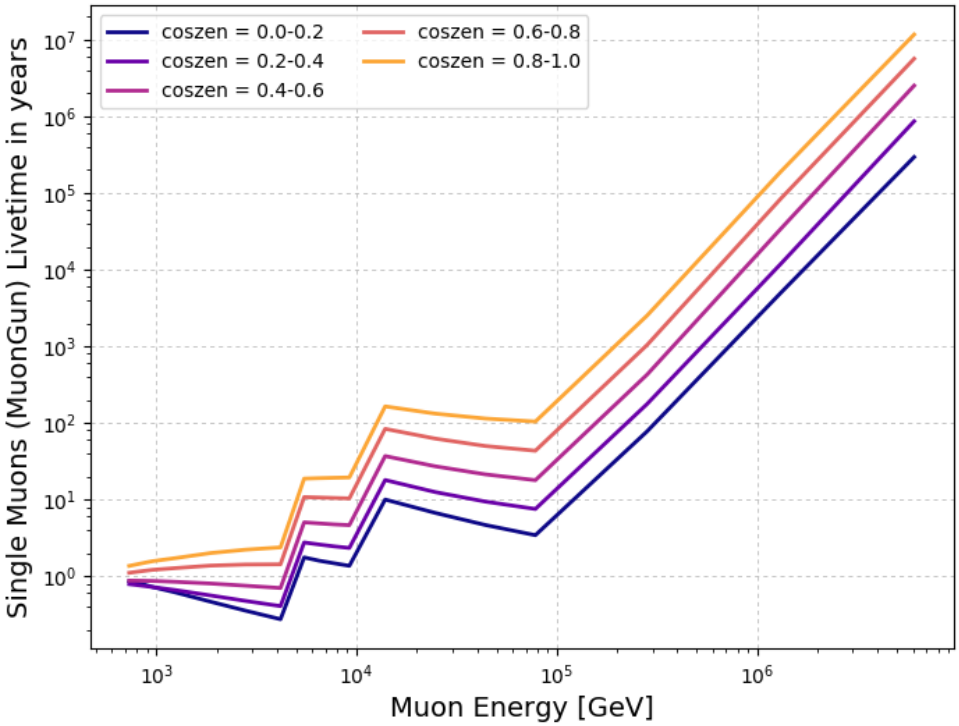

Figure 7.2: A plot of the livetime of simulated atmospheric muon background. simulated using the SnowStorm method, along with the KDE-derived muon template. The MC consists of both an ensemble dataset and a high statistics baseline set. The ensemble dataset (Table A) is used to derive the gradient vector used to evaluate the linear effects of systematic variations on the analysis bins. As this is a computationally intensive sample to simulate, this is a relative low statistics sample. There is therefore a high statistics sample (Table A) simulated which has all the parameters set to their nominal baseline. Only the gradients vary depending on the detector response, and can be iteratively recalculated as the fit varies from the nominal values.

7.4 Flux Models Tested

Various astrophysical flux models were tested. We assume the extragalactic neutrino flux to be isotropic, removing any dependence on the zenith bins. For each tested model, we fit nuisance parameters in addition to the model parameters. The models

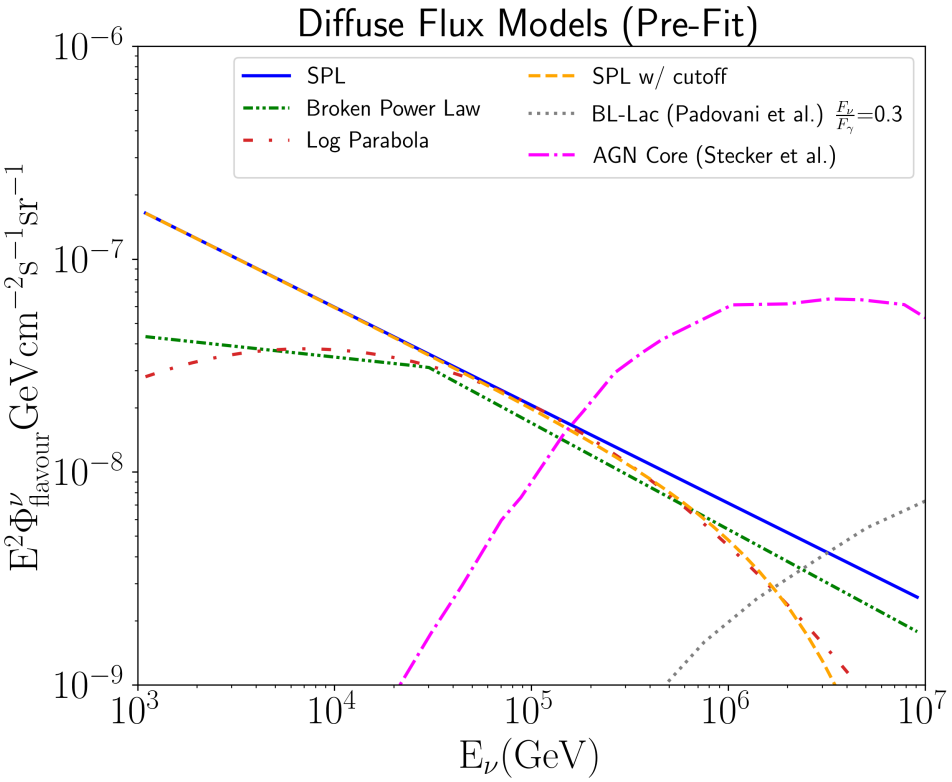

Figure 7.3: An illustration of the various astrophysical flux models tested in this analysis.

are tabulated in 7.2, in order of decreasing log likelihood, indicating a better fit. In addition to these fits using pre-defined spectral models, we conduct a model-independent fit of the normalization in 13 energy segments assuming a power law spectrum with index 2 in each segment, with each normalization being independently fit.

In additional to the single power law (SPL), we also fit modifications such as the SPL with an exponential cutoff (SPE), the SPL with a contribution from PeV-scale neutrinos from AGN cores [97], and the SPL with a contribution from neutrinos from BL Lacertae objects [98]. The broken power law (BPL) and log-parabolic (LP) flux models add curvature parameters to the spectrum across different energies, inspired by the steeper spectrum observed by HESE [12] at high energies. Another tested

Table 7.1: The various spectral models tested in the diffuse analysis. The flux normalization is evaluated per-flavour in units of $C = 10^{-18}/\mathrm{GeV}/\mathrm{cm}^2/\mathrm{s}/\mathrm{sr}$. All flux normalizations are at 100 TeV.

Flux Model	Flux Parameterisation
Single Power Law (SPL)	$\Phi^{\nu+\bar{\nu}}(\frac{\mathrm{E}_\nu}{100\mathrm{TeV}})^{-\gamma}$
SPL + AGN	$\Phi^{\nu+\bar{\nu}}(\frac{\mathrm{E}_\nu}{100\mathrm{TeV}})^{-\gamma} + \Phi_{\mathrm{AGN}}$
SPL + BLLac	$\Phi^{\nu+\bar{\nu}}(\frac{\mathrm{E}_\nu}{100\mathrm{TeV}})^{-\gamma} + \Phi_{\mathrm{BL-Lac}}$
SPL + Cutoff	$\Phi^{\nu+\bar{\nu}}(\Lambda)^{-\gamma} e^{\frac{-\mathrm{E}_\nu}{\mathrm{E}_{\mathrm{cutoff}}}}$ $\Lambda = \frac{\mathrm{E}_\nu}{100\mathrm{TeV}}$
SPL + Bump	$\Phi^{\nu+\bar{\nu}}(\frac{\mathrm{E}_\nu}{100\mathrm{TeV}})^{-\gamma} + \Phi_{\mathrm{bump}} e^{\frac{-(\mathrm{E}_\nu - \mathrm{E}_{\mathrm{bump}})^2}{2\sigma^2_{\mathrm{bump}}}}$
Log Parabola	$\Phi^{\nu+\bar{\nu}}(\frac{\mathrm{E}_\nu}{100\mathrm{TeV}})^{-\alpha_{\mathrm{LP}} - \beta_{\mathrm{LP}} \log_{10}(\frac{\mathrm{E}_\nu}{100\mathrm{TeV}})}$
Broken Power Law	$\Phi^{\nu+\bar{\nu}}(\frac{\mathrm{E}_\nu}{\mathrm{E}_{\mathrm{break}}})^{-\gamma_{\mathrm{BPL}}}(\frac{\mathrm{E}_{\mathrm{break}}}{100\mathrm{TeV}})^{-\gamma_1}$ $\gamma_{\mathrm{BPL}} = \begin{cases} \gamma_1 \, (\mathrm{E}_\nu < E_{\mathrm{break}}) \\ \gamma_2 \, (\mathrm{E}_\nu > E_{\mathrm{break}}) \end{cases}$

model is the SPL with a Gaussian bump, which was included because of an excess at 30 TeV observed by the 2 year MESE result [69].

We evaluate the sensitive energy range for each model by comparing the binwise likelihoods when comparing a background-only hypothesis (no astrophysical flux) to the signal hypothesis with the astrophysical flux component included. The difference in the binwise likelihoods shows the energy bins which have the most power to distinguish these two hypotheses.This distribution is integrated to yield a cumulative distribution, and the sensitive energy range is defined as the interval covering the 5%-95% region of this cumulative distribution.

7.5 Results

As tabulated in Table 7.2, the astrophysical flux model which fits the data best is the broken power law. This preference over the SPL hypotheses previously published by IceCube is primarily driven by an excess of events at 30 TeV, as visible in Fig. 7.5

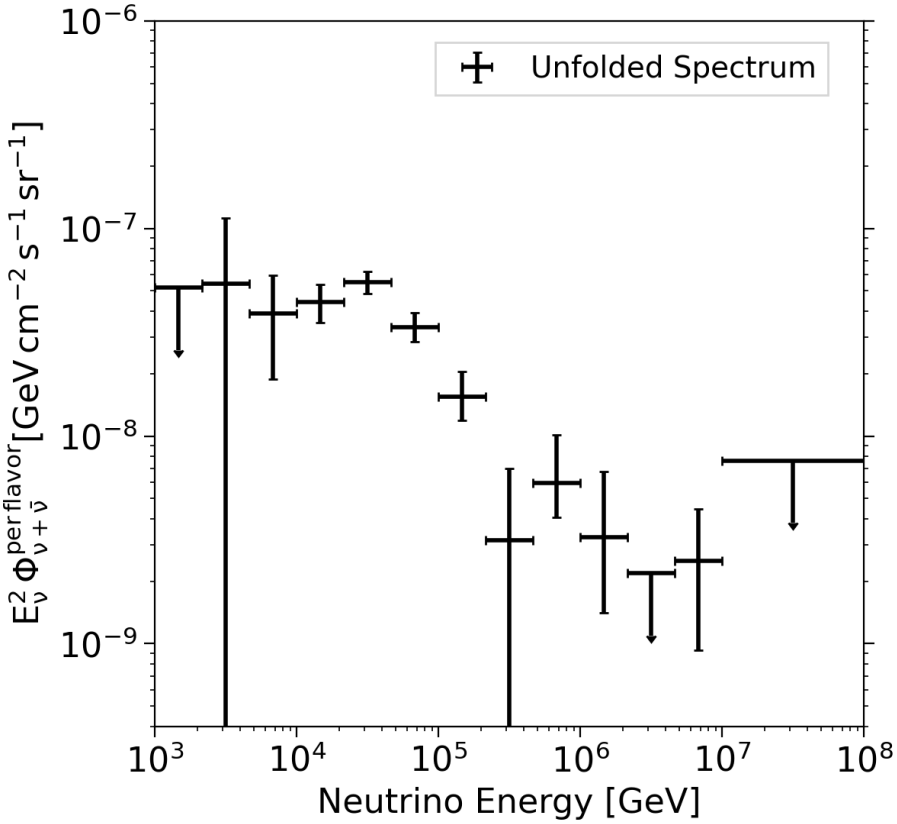

Figure 7.4: **Dataset Results**: Results of a fit of the astrophysical neutrino flux, assuming an E^{-2} flux in independent energy bands ranging from $10^3 - 10^8$ GeV. The energy range was divided into three bins per decade until 10^7 GeV, with events from $10^7 - 10^8$ GeV in a single bin. The uncertainties depicted are the 68% confidence intervals.

7.5.1 Single Power Law

The single power law (SPL) is the simplest flux model tested, and is motivated by models for cosmic ray acceleration by the Fermi mechanism. This is also the best fit model measured by analyses using the HESE [12] and ESTES [57] starting event samples.

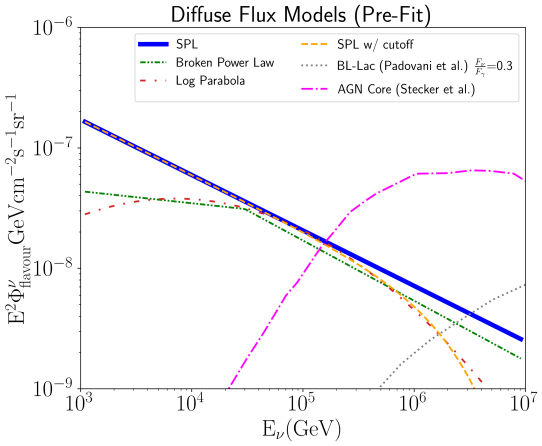

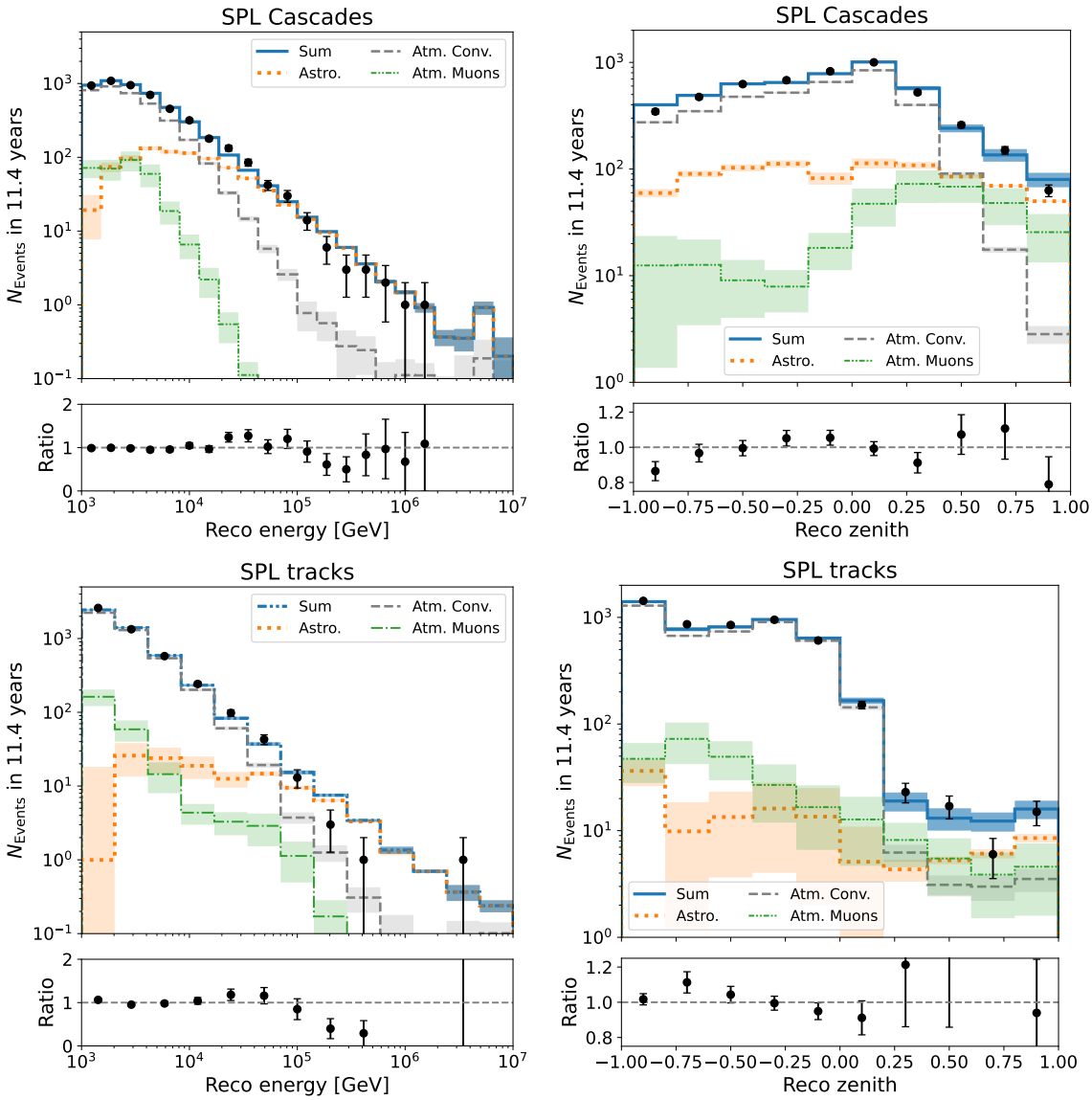

Figure 7.5: **MESE SPL Data MC**: Comparison of Data and MC simulation for the best-fit SPL model. Shown are reconstructed cascade energy (left), and reconstructed track energy (right). The atmospheric prompt neutrino flux normalization is a free parameter which fits to zero. The excess of data events at energies close to 30 TeV and the deficit of events above 100 TeV drive the preference for a BPL spectral model. The excess disappears for a fit with a BPL model (cf. figure 7.9).

The flux is given by the following model, where the free parameters are $\Phi^{\nu+\bar{\nu}}$, the flux normalization is evaluated per flavour in units of C =

10^{-18}/GeV/cm^2/s/sr, and the spectral index γ.

$$\Phi_{\text{astro}}(\mathrm{E}_\nu) = \Phi^{\nu+\bar{\nu}}(\frac{\mathrm{E}_\nu}{100\ \text{TeV}})^{-\gamma} \tag{7.3}$$

The best fit parameters obtained from the likelihood fit assuming the SPL flux model are

$$\Phi^{\nu+\bar{\nu}}/C = 2.13^{+0.18}_{-0.17}$$

$$\gamma = 2.55^{+0.04}_{-0.04}$$

We see, however, from Fig. 7.5 that the data indicates features in the spectrum which are not adequately modelled by a single power law. These include an excess at 30 TeV and a dip at a few hundred TeV. As the best fit prompt flux normalization we obtain is zero, we omit that flux component from our histograms. An important validity check is to see if the minimizer is stuck in a local minima, which would pull the fitter away from the best fit points. This is checked by performing 1-dimensional profile likelihood scans over each of the systematic or nuisance parameters, to see that the global minimum of this 1D likelihood is indeed the best fit point. This would obviate the issue of the physics parameters being pulled away from their actual values by a nuisance parameter which fits near the boundary or in a local minimum. We observe that the nuisance parameters fit well within their nominal bounds, as illustrated by Fig. 7.8.

In spite of the observations of structure beyond an SPL in our data, we perform a comparison of the MESE SPL result to previously published IceCube SPL measurements. In Fig. 7.6, we have performed a 2-dimensional profile likelihood scan over the physics parameters, and define the 68% and 95% confidence intervals around the best fit flux normalization and spectral index. We then compare the 68% confidence interval obtained by the MESE analysis to other IceCube SPL results in Fig. 7.7. We

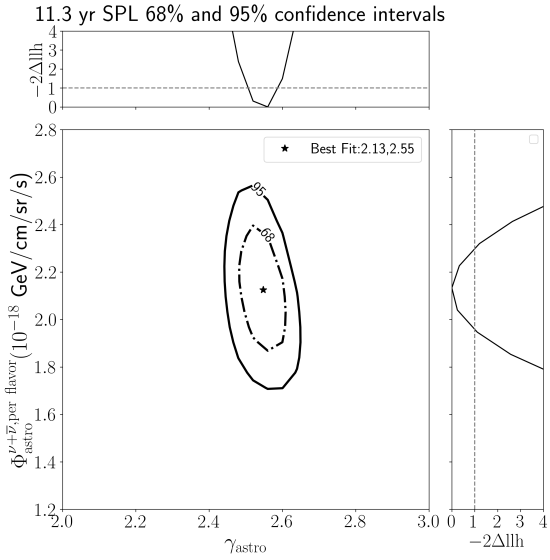

Figure 7.6: Two-dimensional profile likelihood scans of the physics parameters of the SPL flux model. Wilk's theorem is used to define the 68% and 95% confidence intervals.

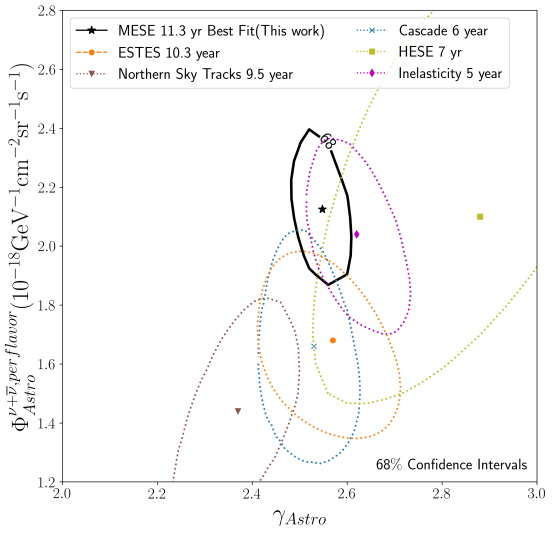

Figure 7.7: A comparison of the MESE measurement with published IceCube results.

observe that the MESE 68% contour overlaps with the results from the other measurements, notable HESE and ESTES, but is not consistent with the 9.5 yr Northern Sky Tracks result [99], which predicts a harder spectrum and a lower flux normalization. A feature worth noting in this plot is that the MESE selection, with $\sim 10^4$ events, constrains physics parameters more tightly compared to the other samples, such as Northern Tracks with $\mathcal{O}(10^6)$ events. This is an illustration of MESE's greater sensitivity to the astrophysical flux, especially at lower energies below 60 TeV. The greater sensitivity may be attributed to MESE's superior background rejection, in particular the implementation of the self-veto, along with improvements in energy resolution of reconstructed events.

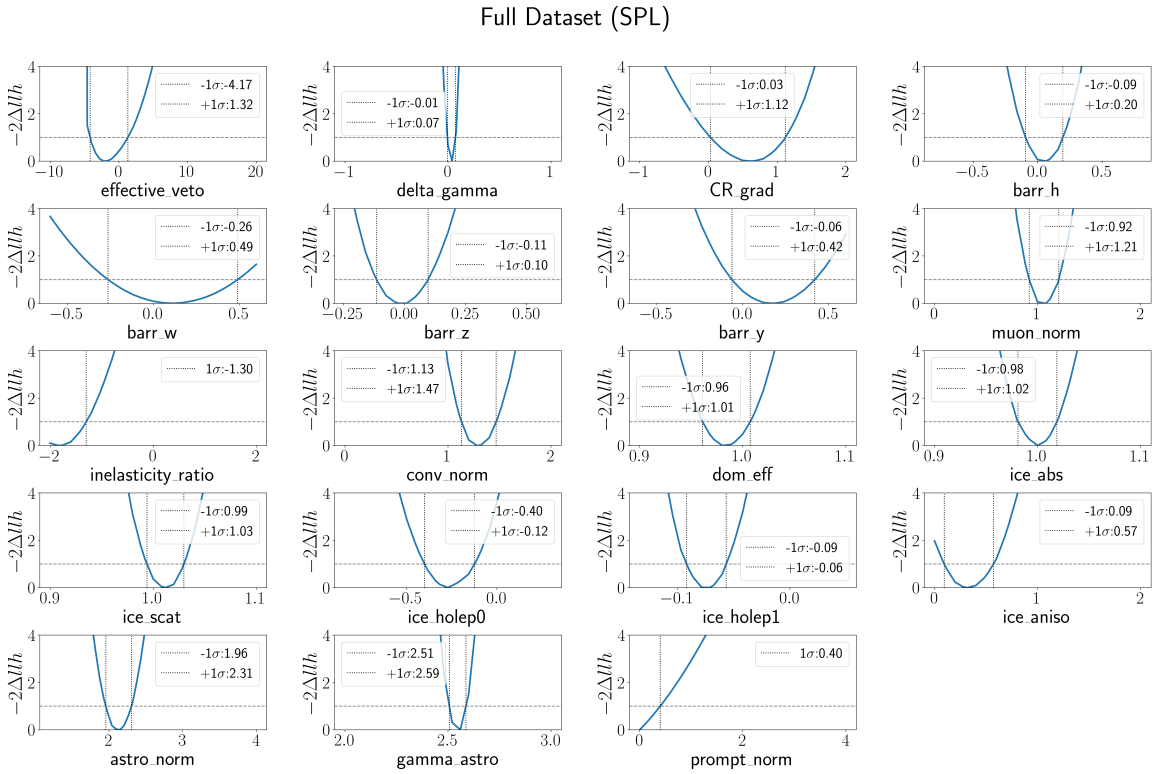

Figure 7.8: Profile likelihood scans of the various fit parameters assuming the SPL best fit parameters. We observe that the best fit parameters are well within the nominal bounds, and no local minima exist in the likelihood space

7.5.2 Broken Power Law

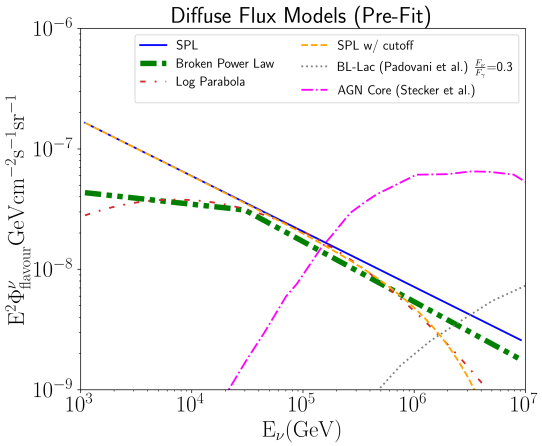

The broken power law (BPL) is a modification to the SPL, with additional physics parameters added to the fit. The flux is given by the following model, where the free parameters are $\Phi^{\nu+\bar{\nu}}$, the flux normalization in units of $C = 10^{-18}/\mathrm{GeV}/\mathrm{cm}^2/\mathrm{s}/\mathrm{sr}$, and the spectral indices γ_1 & γ_2, and the break energy E_{break}.

$$\Phi_{\mathrm{astro}}(\mathrm{E}_\nu) = \Phi^{\nu+\bar{\nu}}\left(\frac{\mathrm{E}_\nu}{\mathrm{E}_{\mathrm{break}}}\right)^{-\gamma_{\mathrm{BPL}}}\left(\frac{\mathrm{E}_{\mathrm{break}}}{100\mathrm{TeV}}\right)^{-\gamma_1} \tag{7.4}$$

$$\gamma_{\mathrm{BPL}} = \left\{ \begin{array}{l} \gamma_1\,(\mathrm{E}_\nu < E_{\mathrm{break}}) \\ \gamma_2\,(\mathrm{E}_\nu > E_{\mathrm{break}}) \end{array} \right\}. \tag{7.5}$$

The best fit values we obtain for the broken power law model are

$$\begin{aligned} \Phi^{\nu+\bar{\nu}}/C &= 2.28^{+0.22}_{-0.20} \\ \gamma_1 &= 1.72^{+0.26}_{-0.35} \\ \gamma_2 &= 2.84^{+0.11}_{-0.09} \\ \log_{10}\left(\frac{\mathrm{E}_{\mathrm{break}}}{\mathrm{GeV}}\right) &= 4.52^{+0.11}_{-0.09} \end{aligned}$$

The BPL is our best fit model, with the greatest $\Delta\log\mathcal{L} = 27.3$ relative to the SPL hypothesis. It provides a method to probe curvature in the astrophysical neutrino spectrum. The preference for the BPL over the SPL is primarily driven by the excess at 30 TeV observed in the SPL fit. The histograms comparing the data observations to the best fit Monte Carlo model (Fig. 7.9) show better agreement, indicating that

the BPL is a better model of the data than the SPL. We also observe that the nuisance parameters fit well within their nominal bounds, as illustrated by Fig. B.1. The physics parameters are also not correlated with the nuisance parameters to a significant degree, and are not pulled by the nuisance parameter fit values, as observed in Fig. B.2.

An important consequence of our results is that the extragalactic neutrino flux at $\mathcal{O}(10\,\mathrm{TeV})$ is lower compared to expectations from an SPL, favored by previous IceCube results. Various calculations hint towards the incompatibility of an SPL spectrum extrapolated to the 1-10 TeV energy range and the diffuse extragalactic gamma-ray spectrum [27, 100]. This is potentially alleviated by the BPL. This can also constrain the properties of extragalactic neutrino emitters (e.g., [32]). The MESE analysis prefers the BPL to the SPL by 4.7 σ, corresponding to a p-value of $1.2 \cdot 10^{-6}$, assuming Wilks' theorem is valid. As the SPL is nested within the BPL model, which means that the BPL can reduce to the SPL for a choice of physics parameters, this assumption is justified. We test the preference by injecting the best-fit SPL model and running pseudo-experiments fitting both the SPL and BPL fluxes, to obtain a test statistic (TS) distribution where the TS is defined as $TS = -2(LLh_{\mathrm{BPL}} - LLh_{\mathrm{SPL}})$. This is then compared to the TS obtained from the fits to data (Fig. B.3).

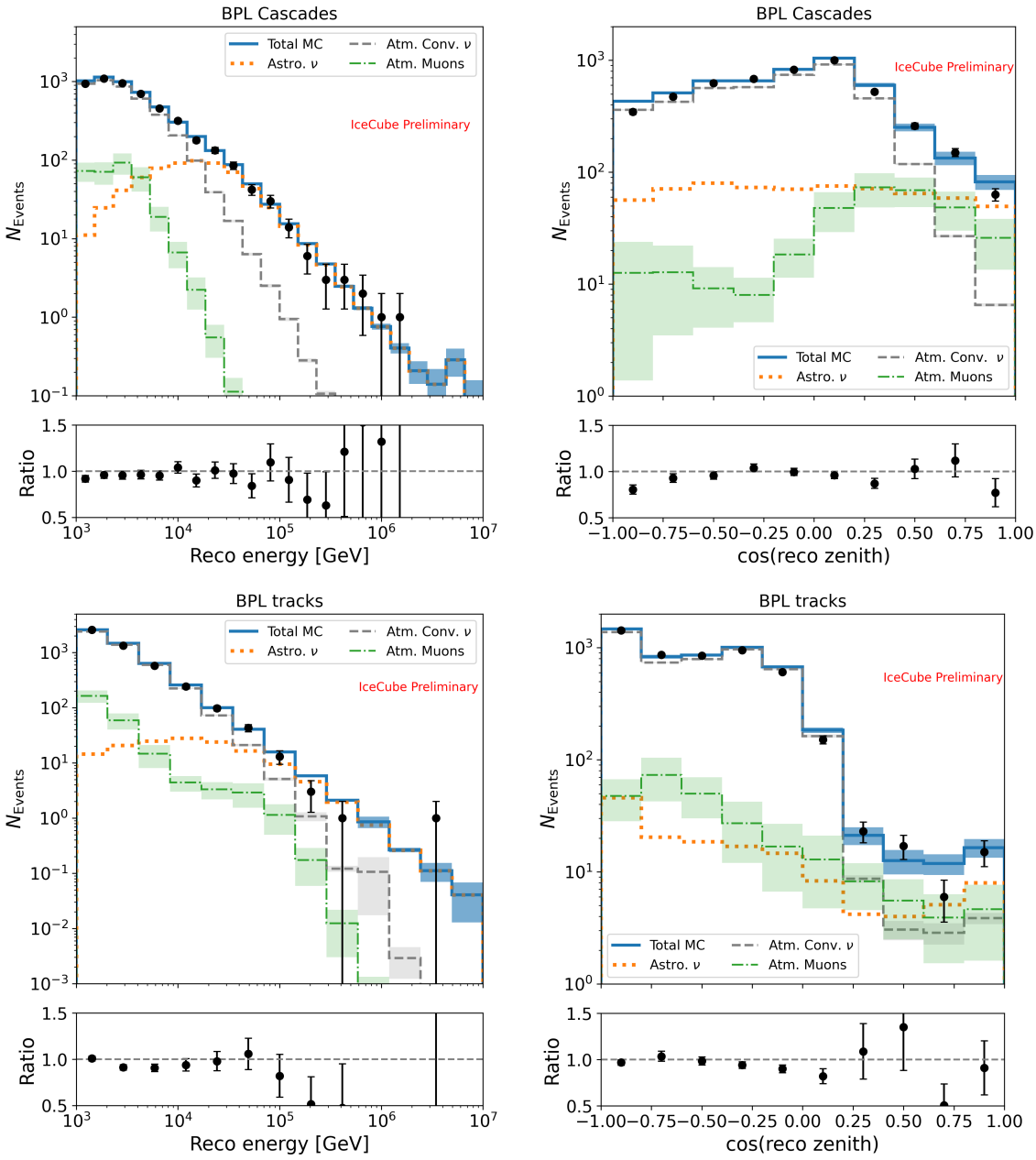

Figure 7.9: **MESE Broken Power Law Data/MC**: Comparison of data and MC simulation for the best fit Broken Power Law spectral model. Displayed are reconstructed cascade energy (upper left) , cos(zenith) (lower left), reconstructed track energy (upper right), and cos(zenith) (lower right). A DNN is used to classify tracks and cascades, and we use separate reconstructions for them. The atmospheric prompt neutrino flux normalization is a free parameter which fits to zero and is therefore not shown.

7.5.3 Log Parabola

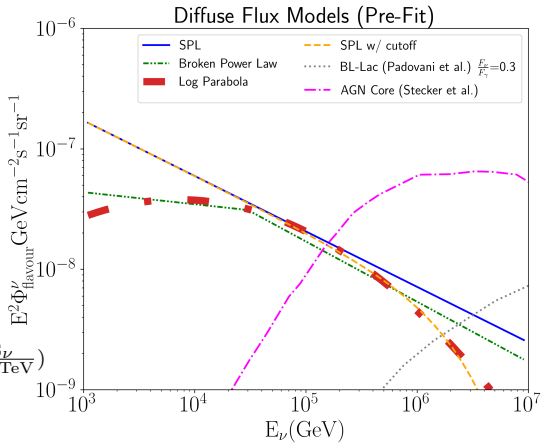

The Log Parabola is a model which adds a curvature parameter to the astrophysical neutrino spectrum The flux is given by

$$\Phi_{\text{astro}}(\text{E}_\nu) = \Phi^{\nu+\bar{\nu}}\left(\frac{\text{E}_\nu}{100\text{TeV}}\right)^{-\alpha_{\text{LP}}-\beta_{\text{LP}}\log_{10}\left(\frac{\text{E}_\nu}{100\text{TeV}}\right)} \tag{7.6}$$

where the free parameters are $\Phi^{\nu+\bar{\nu}}$, the flux normalization in units of $C = 10^{-18}/\text{GeV}/\text{cm}^2/\text{s}/\text{sr}$, and the spectral parameters α_{LP} & β_{LP}.

The best fit values obtained are

$$\Phi^{\nu+\bar{\nu}}/C = 2.58^{+0.26}_{-0.26}$$

$$\alpha_{\text{LP}} = 2.67^{+0.13}_{-0.06}$$

$$\beta_{\text{LP}} = 0.36^{+0.10}_{-0.08}$$

with the $\Delta\log\mathcal{L} = 18.84$ relative to the SPL hypothesis. We observe that the Log Parabola model is a better fit to the data, as illustrated by Fig. 7.10, than the SPL, with no excess observed at 30 TeV. The additional β_{LP} parameter adds curvature to the spectrum, with $\beta_{\text{LP}} = 0$ reducing to the SPL flux model. As this makes the SPL a nested submodel of the LP, Wilks' Theorem applies, and we find that MESE prefers the LP to the SPL by 4.18 σ. This corresponds to a p-value of $1.4 \cdot 10^{-5}$.

We evaluate this preference again by injecting the best-fit SPL model and running pseudo-experiments fitting both the SPL and LP fluxes, to obtain a test statistic (TS) distribution where the TS is defined as $TS = -2(LLh_{\text{LP}} - LLh_{\text{SPL}})$. This is then compared to the TS obtained from the fits to data (Fig. B.6).

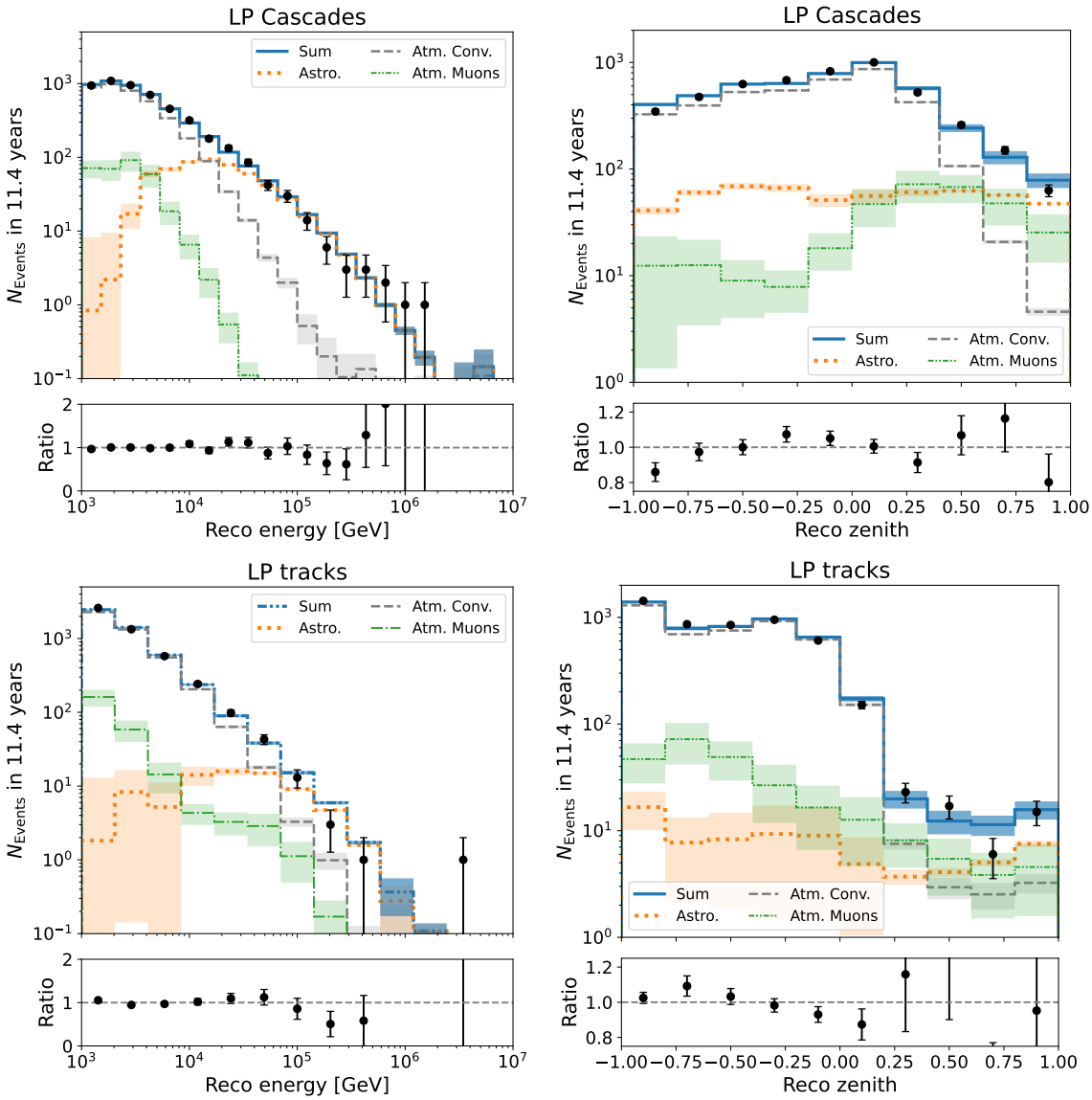

Figure 7.10: **MESE Log Parabola Data/MC**: Comparison of data and MC simulation for the best fit Log-Parabola spectral model. Displayed are reconstructed cascade energy (upper left) , cos(zenith) (lower left), reconstructed track energy (upper right), and cos(zenith) (lower right). A DNN is used to classify tracks and cascades, and we use separate reconstructions for them. The atmospheric prompt neutrino flux normalization is a free parameter which fits to zero and is therefore not shown.

We also perform a comparison between the LP and the BPL. As these models are not nested, however, Wilks' Theorem is not valid, and we must run multiple pseudoexperiments to obtain the underlying TS distribution. We obtain a preference for

the LP over the BPL by 0.9 σ when injecting the BPL best fit histogram (Fig. B.8) and a preference of 2.42 σ when injecting the LP best fit histogram (Fig. B.7) .

7.5.4 Single Power Law plus a Gaussian bump

The 2 year MESE analysis [69] found an excess in the Southern sky, at energy 30 TeV. With the increased statistics in the current analysis, the decision was made to fit an SPL + bump model, which would be able to determine if the excess was a statistical fluctuation. The flux is given by

$$\Phi_{\text{astro}}(\mathrm{E}_\nu) = \Phi^{\nu+\bar{\nu}}(\frac{\mathrm{E}_\nu}{100\ \text{TeV}})^{-\gamma} + \phi_{\text{bump}}(e^{-\frac{(E-E_{\text{bump}})^2}{2\sigma^2_{\text{bump}}}}) \tag{7.7}$$

where the normalization $\Phi^{\nu+\bar{\nu}}$, spectral index γ, bump normalization ϕ_{bump}, bump energy E_{bump}, and the spread of the bump σ_{bump} are free parameters in the fit.
The best fit values of this flux model are

$$\begin{aligned}
\Phi^{\nu+\bar{\nu}}\,/\,C &= 1.42^{+0.21}_{-0.20} \\
\gamma &= 2.51^{+0.05}_{-0.07} \\
\log_{10}(\frac{\mathrm{E}_{\text{bump}}}{\text{GeV}}) &= 4.30^{+0.13} \\
\log_{10}(\frac{\sigma_{\text{bump}}}{\text{GeV}}) &= 4.42^{+0.12}_{-0.13} \\
\Phi_{\text{bump}}\,/\,C &= 24.79^{+13.55}_{-7.95}
\end{aligned}$$

with the $\Delta\log\mathcal{L} = 22.3$ relative to the SPL hypothesis. Unfortunately, the likelihood space for the bump energy is quite flat outside the lower boundary, which results in the fit being forced to fit at the boundary value. With better conditioning of the fit parameters, it is possible this can be alleviated for the next analysis studying such a flux model. We observe that the SPL + Bump model is able to fit the structure observed in the data, as illustrated in Fig. 7.11. We therefore prefer it to the SPL model by 3.9 σ, corresponding to a p-value of $5.7\cdot10^{-5}$ [16], assuming Wilks' Theorem is valid.

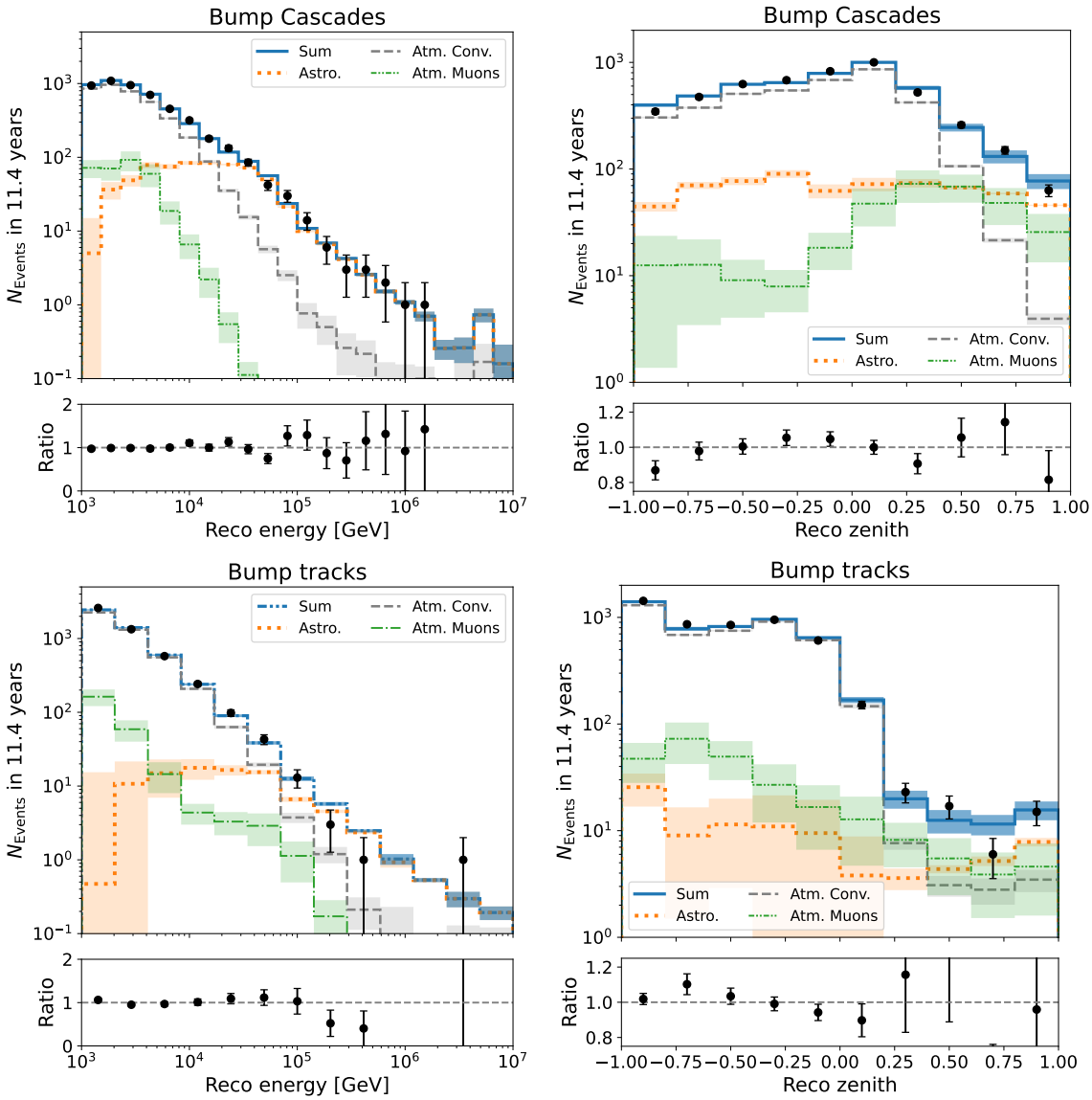

Figure 7.11: **MESE SPL + Bump Data/MC**: Comparison of data and MC simulation for the best fit of the SPL + Bump spectral model. Displayed are reconstructed cascade energy (upper left) , cos(zenith) (lower left), reconstructed track energy (upper right), and cos(zenith) (lower right). A DNN is used to classify tracks and cascades, and we use separate reconstructions for them. The atmospheric prompt neutrino flux normalization is a free parameter which fits to zero and is therefore not shown.

We perform a comparison between the SPL+ Bump and the BPL. As these models are not nested, however, Wilks' Theorem is not valid, and we must run multiple

pseudoexperiments to obtain the underlying TS distribution. We obtain a preference for the SPL +Bump over the BPL by 1.35 σ when injecting the SPL + Bump best fit histogram (Fig. B.11).

7.5.5 Single Power Law with exponential cutoff

Hints of a cutoff in the SPL spectrum were first noted in [76] The flux is given by the following model, where the per-flavour normalization ϕ_0, spectral index γ and the cut-off energy E_{cutoff} are free parameters.

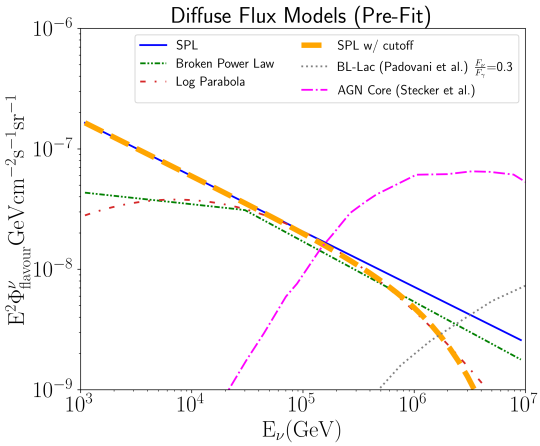

$$\Phi_{\text{astro}}(\mathrm{E}_\nu) = \Phi^{\nu+\bar{\nu}}\left(\frac{\mathrm{E}_\nu}{100\ \mathrm{TeV}}\right)^{-\gamma} e^{\frac{-E_\nu}{E_{\text{cutoff}}}} \tag{7.8}$$

The best fit parameters are

$$\Phi^{\nu+\bar{\nu}}/C = 3.975^{+1.14}_{-1.32}$$
$$\gamma = 2.16^{+0.23}_{-0.16}$$
$$\log_{10}\left(\frac{\mathrm{E}_{\text{cutoff}}}{\mathrm{GeV}}\right) = 5.40^{+0.51}_{-0.23}$$

, with the $\Delta\log\mathcal{L} = 1.8$ relative to the SPL. The cutoff does not greatly improve the fit to data, as can be evidenced by both the 30 TeV feature and the larger deviation in the reconstructed cosine zenith plots. The marginal improvement in $\Delta\log\mathcal{L}$ is therefore not entirely reflective of a better fit than the SPL, and may be attributed to the increase in the number of fit parameters, and the correspondingly greater degrees of freedom. The cutoff model is therefore only marginally preferred to the SPL, at 0.9 σ, which corresponds to a p-value of 0.18, assuming that Wilks' Theorem applies here.

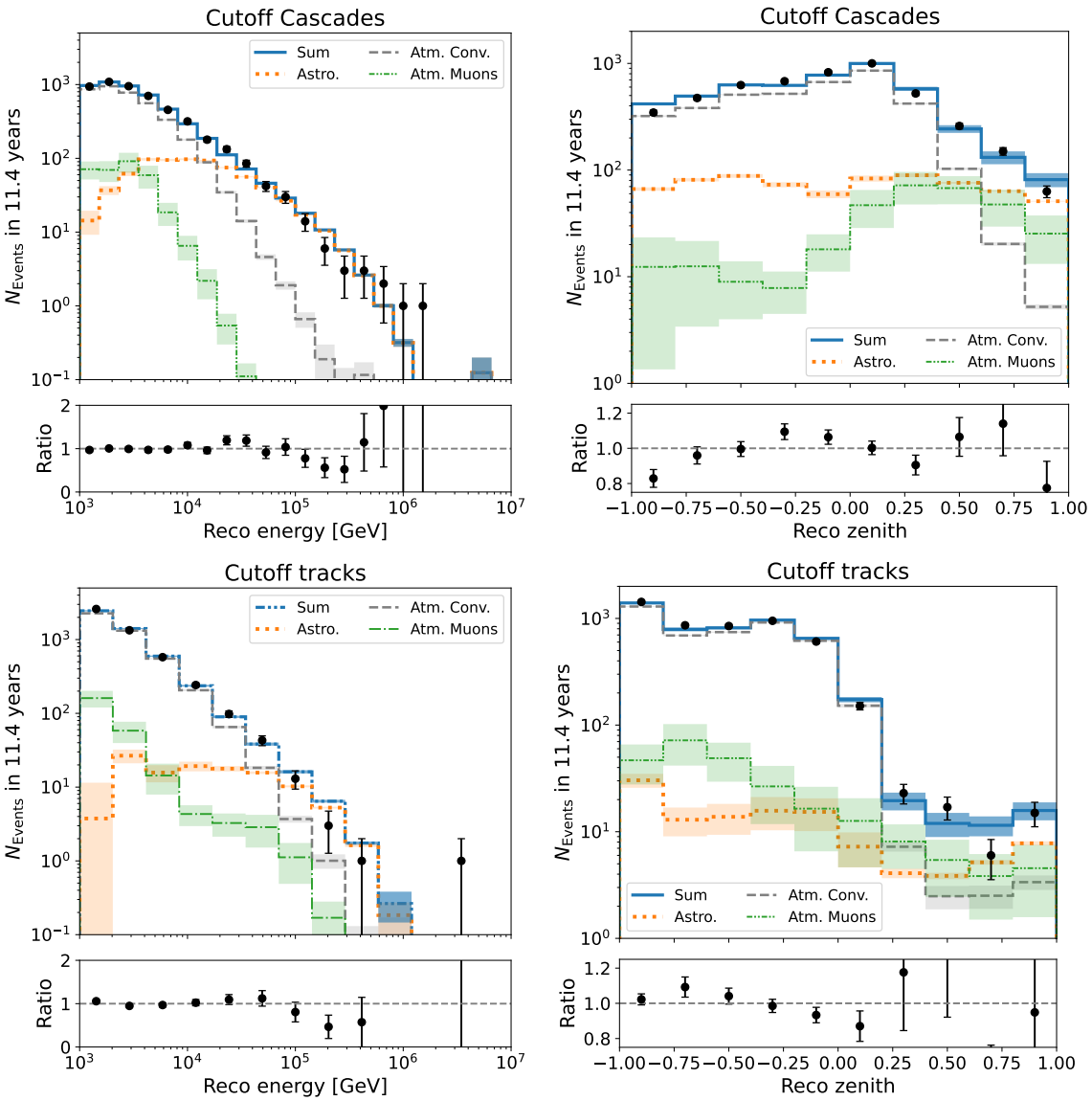

Figure 7.12: **MESE SPL + Cutoff Data/MC**: Comparison of data and MC simulation for the best fit of the SPL + Cutoff spectral model. Displayed are reconstructed cascade energy (upper left) , cos(zenith) (lower left), reconstructed track energy (upper right), and cos(zenith) (lower right). A DNN is used to classify tracks and cascades, and we use separate reconstructions for them. The atmospheric prompt neutrino flux normalization is a free parameter which fits to zero and is therefore not shown.

7.5.6 Single Power Law with neutrinos from Active Galactic Nuclei cores

We study a contribution to the PeV neutrino flux from AGN cores [97]. This is linked to the cosmic ray protons encountering photons at the accretion disk, with the resulting neutrino spectrum from the p-γ interactions. This would manifest as a peak in the neutrino spectrum at PeV energies. The flux is given by the following model, where the normalization ϕ_0, spectral index γ and the template normalization are free parameters.

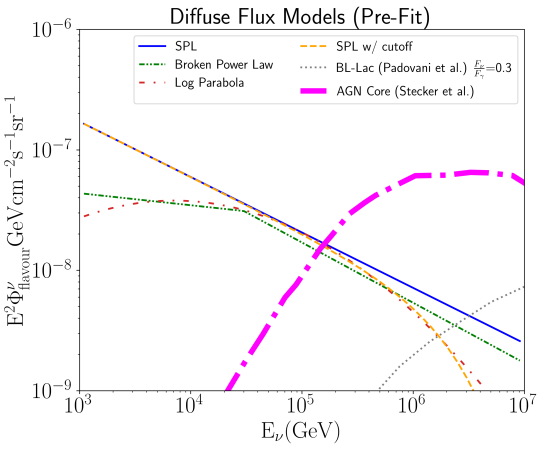

$$\Phi_{\text{astro}}(\mathrm{E}_\nu) = \Phi^{\nu+\bar{\nu}}\left(\frac{\mathrm{E}_\nu}{100\ \text{TeV}}\right)^{-\gamma} + \Phi_{\text{AGN}} \tag{7.9}$$

$$\Phi^{\nu+\bar{\nu}}/C = 2.13^{+0.18}_{-0.17}$$

$$\gamma = 2.55^{+0.04}_{-0.04}$$

$$\Phi_{\text{AGN}} = 0^{+0.002}$$

We fit a template normalization of zero, which means that the fit results are identical to the SPL fit. This results in a $\Delta\log\mathcal{L} = 0$.

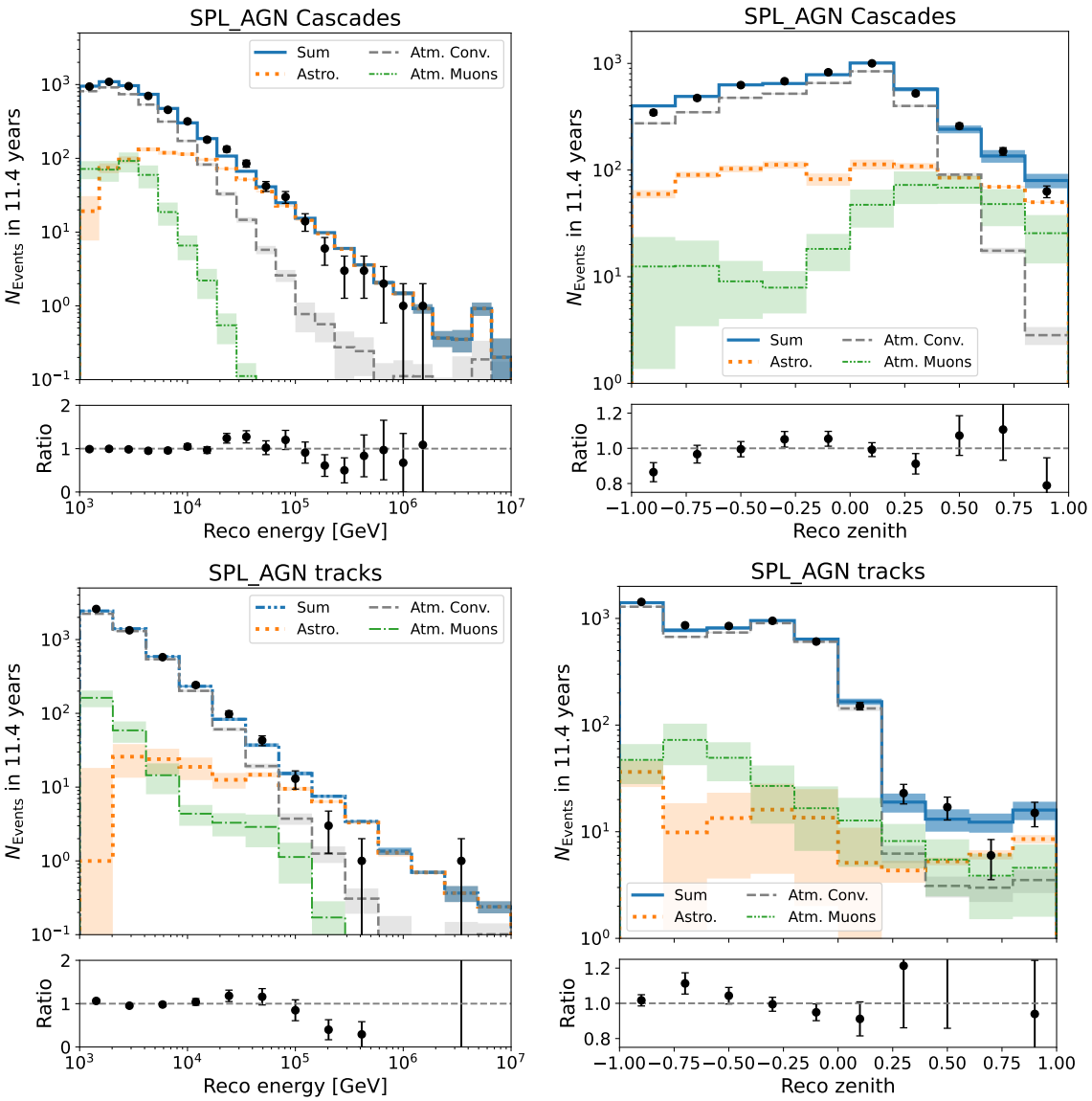

Figure 7.13: **MESE SPL + AGN core Data/MC**: Comparison of data and MC simulation for the best fit of the SPL + AGN core emission spectral model. Displayed are reconstructed cascade energy (upper left) , cos(zenith) (lower left), reconstructed track energy (upper right), and cos(zenith) (lower right). A DNN is used to classify tracks and cascades, and we use separate reconstructions for them. The atmospheric prompt neutrino flux normalization is a free parameter which fits to zero and is therefore not shown.

7.5.7 Single Power Law with neutrinos from BL Lac objects

We study a contribution to the PeV neutrino flux from BL Lac objects [98]. These are blazars (AGN which have a jet aligned along the line of sight) with strong broad emission lines in their optical spectra, and are theorized to dominate the neutrino flux above 0.5 PeV. The flux is modelled as the following, where the normalization ϕ_0, spectral index γ and the template normalization are free parameters.

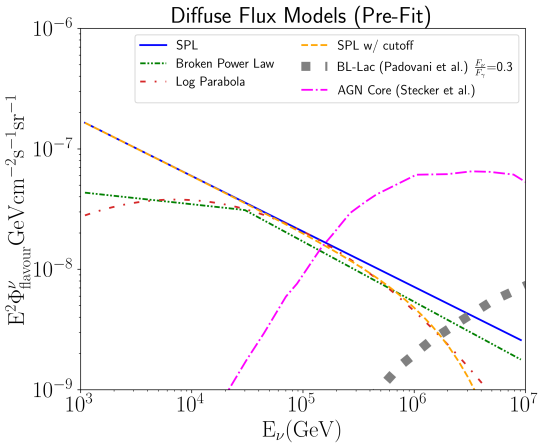

$$\Phi_{\text{astro}}(E_\nu) = \Phi^{\nu+\bar{\nu}}\left(\frac{E_\nu}{100\text{TeV}}\right)^{-\gamma} + \Phi_{\text{BLLac}} \tag{7.10}$$

The best fit parameters are

$$\Phi^{\nu+\bar{\nu}}/C = 2.13^{+0.18}_{-0.17}$$

$$\gamma = 2.55^{+0.04}_{-0.04}$$

$$\Phi_{\text{BLLac}} = 0^{+0.002}$$

We fit a template normalization of zero, which means that the fit results are identical to the SPL fit. This results in a $\Delta\log\mathcal{L} = 0$.

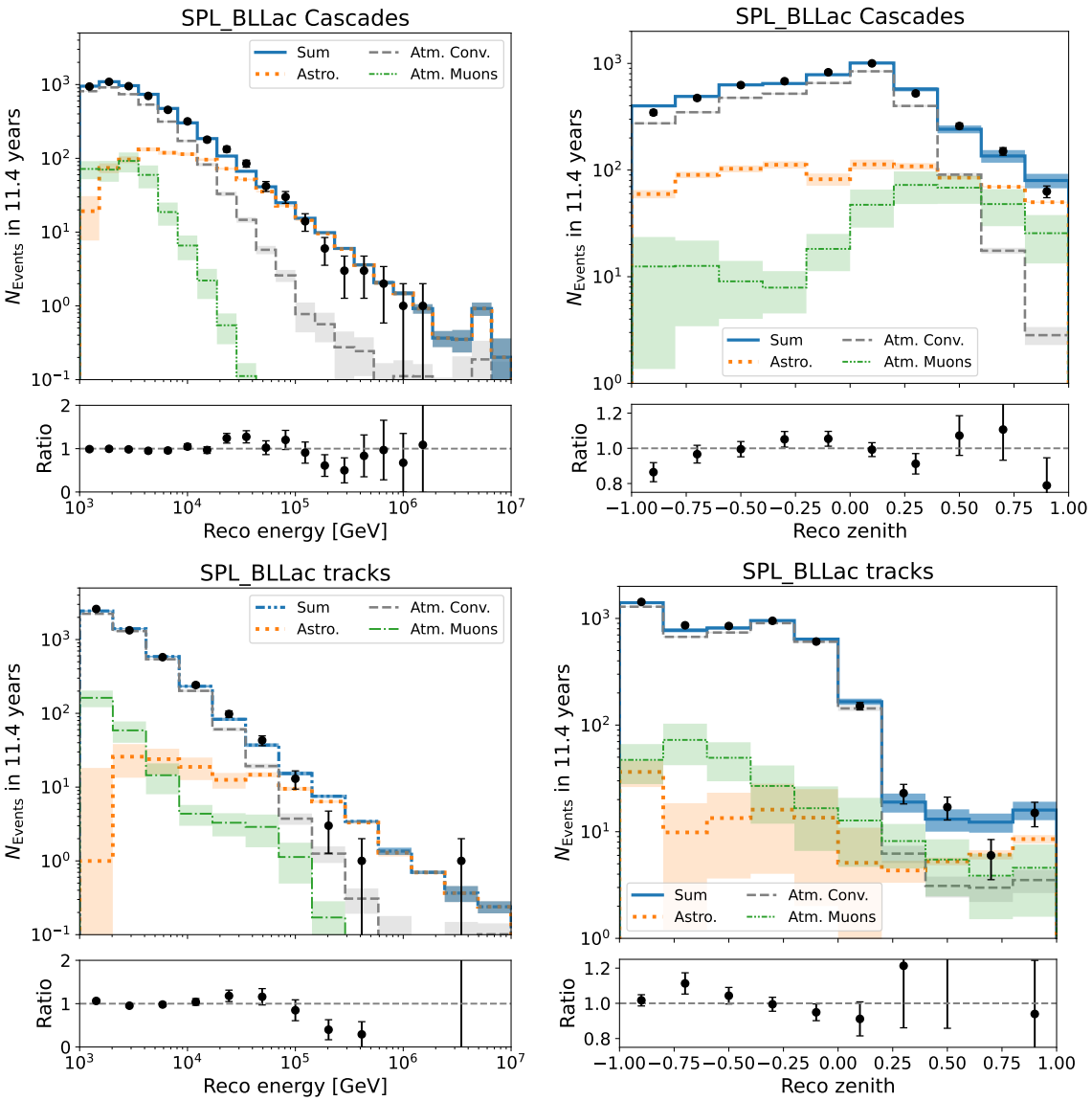

Figure 7.14: **MESE SPL + BL-Lac Data/MC**: Comparison of data and MC simulation for the best fit of the SPL + BLLac core emission spectral model. Displayed are reconstructed cascade energy (upper left) , cos(zenith) (lower left), reconstructed track energy (upper right), and cos(zenith) (lower right). A DNN is used to classify tracks and cascades, and we use separate reconstructions for them. The atmospheric prompt neutrino flux normalization is a free parameter which fits to zero and is therefore not shown.

7.5.8 Segmented Flux

To determine the energy spectrum without dependence on a particular flux model, we fit the normalization of the astrophysical neutrino flux independently in 13 energy segments of the total spectrum, assuming a power-law spectrum with index 2 in each segment. The energy bands and the normalization of the 'unfolded' flux measurement in each of them is listed in Table 7.3. It is instructive to dive deeper into the methodology of this fit, as the fit is performed in *true* neutrino energy space, and not reconstructed energy as the previous models were. The fit is performed by first binning the neutrino events by true energy, and then performing the fit in reconstructed energy space, as the sum of the astrophysical fluxes from each bin in true energy. Each flux contribution corresponds to a certain range in true energy, and is therefore orthogonal to other ranges. The normalization obtained for each flux is the result of the fit tabulated in Table 7.3.

Table 7.2: Results for the spectral models tested in the diffuse analysis. The uncertainties are derived from 1D profile likelihood scans, assuming Wilks' theorem applies. We show the preference over the single power-law hypothesis in terms of $-2\Delta\log\mathcal{L}$. The flux normalization is quoted per-flavour in units of $C = 10^{-18}/\mathrm{GeV}/\mathrm{cm}^2/\mathrm{s}/\mathrm{sr}$. All flux normalizations are at 100 TeV.

Flux Model	Fit Parameters	$-2\Delta\log\mathcal{L}$ (compared to SPL)
Single Power Law (SPL) $\left[\Phi^{\nu+\bar{\nu}}(\frac{\mathrm{E}_\nu}{100\mathrm{TeV}})^{-\gamma}\right]$	$\Phi^{\nu+\bar{\nu}}/C = 2.13^{+0.18}_{-0.17}$ $\gamma = 2.55^{+0.04}_{-0.04}$	0
SPL + AGN $\left[\Phi^{\nu+\bar{\nu}}(\frac{\mathrm{E}_\nu}{100\mathrm{TeV}})^{-\gamma} + \Phi_{\mathrm{model}}\right]$	$\Phi^{\nu+\bar{\nu}}/C = 2.13^{+0.18}_{-0.17}$ $\gamma = 2.55^{+0.04}_{-0.04}$ $\Phi_{\mathrm{model}} = 0^{+0.002}$	0
SPL + BLLac $\left[\Phi^{\nu+\bar{\nu}}(\frac{\mathrm{E}_\nu}{100\mathrm{TeV}})^{-\gamma}\right]$	$\Phi^{\nu+\bar{\nu}}/C = 2.13^{+0.18}_{-0.17}$ $\gamma = 2.55^{+0.04}_{-0.04}$ $\Phi_{\mathrm{model}} = 0^{+0.002}$	0
SPL + Cutoff $\left[\Phi^{\nu+\bar{\nu}}(\Lambda)^{-\gamma} e^{\frac{-\mathrm{E}_\nu}{\mathrm{E}_{\mathrm{cutoff}}}}\right]$ $\Lambda = \frac{\mathrm{E}_\nu}{100\mathrm{TeV}}$	$\Phi^{\nu+\bar{\nu}}/C = 3.975^{+1.14}_{-1.32}$ $\gamma = 2.16^{+0.23}_{-0.16}$ $\log_{10}(\frac{\mathrm{E}_{\mathrm{cutoff}}}{\mathrm{GeV}}) = 5.40^{+0.51}_{-0.23}$	1.8 $p = 0.18$ $(0.9\,\sigma)$
Log Parabola $\left[\Phi^{\nu+\bar{\nu}}(\frac{\mathrm{E}_\nu}{100\mathrm{TeV}})^{-\alpha_{\mathrm{LP}}-\beta_{\mathrm{LP}}\log_{10}(\frac{\mathrm{E}_\nu}{100\mathrm{TeV}})}\right]$	$\Phi^{\nu+\bar{\nu}}/C = 2.58^{+0.26}_{-0.26}$ $\alpha_{\mathrm{LP}} = 2.67^{+0.13}_{-0.06}$ $\beta_{\mathrm{LP}} = 0.36^{+0.10}_{-0.08}$	18.84 $p = 1.42 \cdot 10^{-5}$ $(4.2\,\sigma)$
SPL + Bump $\left[\Phi^{\nu+\bar{\nu}}(\frac{\mathrm{E}_\nu}{100\mathrm{TeV}})^{-\gamma} + \Phi_{\mathrm{bump}} e^{\frac{-(\mathrm{E}_\nu-\mathrm{E}_{\mathrm{bump}})^2}{2\sigma^2_{\mathrm{bump}}}}\right]$	$\Phi^{\nu+\bar{\nu}}$ / C $= 1.42^{+0.21}_{-0.20}$ $\gamma = 2.51^{+0.05}_{-0.07}$ $\log_{10}(\frac{\mathrm{E}_{\mathrm{bump}}}{\mathrm{GeV}}) = 4.30^{+0.13}$ $\log_{10}(\frac{\sigma_{\mathrm{bump}}}{\mathrm{GeV}}) = 4.42^{+0.12}_{-0.13}$ Φ_{bump} / C $= 24.79^{+13.55}_{-7.95}$	22.3 $p = 5.65 \cdot 10^{-5}$ $(3.9\,\sigma)$
Broken Power Law $\left[\Phi^{\nu+\bar{\nu}}(\frac{\mathrm{E}_\nu}{\mathrm{E}_{\mathrm{break}}})^{-\gamma_{\mathrm{BPL}}}(\frac{\mathrm{E}_{\mathrm{break}}}{100\mathrm{TeV}})^{-\gamma_1}\right]$ $\gamma_{\mathrm{BPL}} = \begin{cases} \gamma_1\,(\mathrm{E}_\nu < E_{\mathrm{break}}) \\ \gamma_2\,(\mathrm{E}_\nu > E_{\mathrm{break}}) \end{cases}$	$\Phi^{\nu+\bar{\nu}}/C = 2.28^{+0.22}_{-0.20}$ $\gamma_1 = 1.72^{+0.26}_{-0.35}$ $\gamma_2 = 2.84^{+0.11}_{-0.09}$ $\log_{10}(\frac{\mathrm{E}_{\mathrm{break}}}{\mathrm{GeV}}) = 4.52^{+0.11}_{-0.09}$	27.3 $p = 1.2 \cdot 10^{-6}$ $(4.7\,\sigma)$

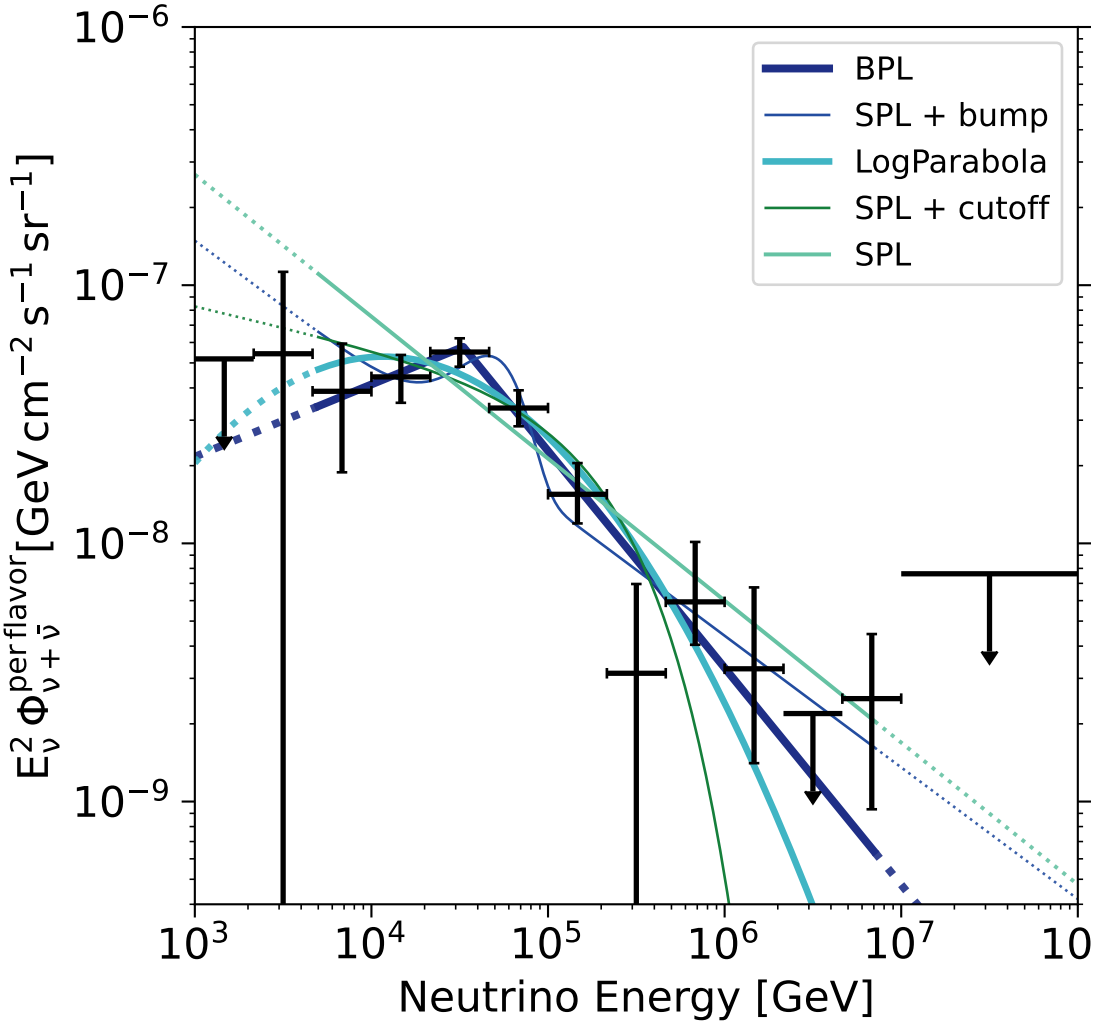

Figure 7.15: **MESE Fit Results**: Results of a fit of the astrophysical neutrino flux in independent energy bands. The results are compared to the models fitted in the analysis. The legend is ordered according to the likelihood obtained for each model. The solid lines show the energy range where the dataset is sensitive to the respective model, and the dotted lines show the energy range over which the fit is performed [16].

Table 7.3: Results for the segmented power law tested in the analysis. The uncertainties are derived from 1D profile likelihood scans, assuming Wilks' theorem applies. The flux is measured per-flavour in units of $C = 10^{-18}/\mathrm{GeV}/\mathrm{cm}^2/\mathrm{s}/\mathrm{sr}$ and all normalization components are fit simultaneously, assuming a power-law spectrum with index 2 in each neutrino energy band.

Energy Bins (TeV)	Fit result
(1.0, 2.15)	$0^{+5.2}$
(2.15, 4.64)	$5.4^{+5.8}_{-5.4}$
(4.64, 10.0)	$3.9^{+2.1}_{-2.0}$
(10.0, 21.5)	$4.41^{+0.93}_{-0.90}$
(21.5, 46.4)	$5.51^{+0.72}_{-0.66}$
(46.4, 100)	$3.34^{+0.63}_{-0.52}$
(100, 215)	$1.55^{+0.50}_{-0.35}$
(215, 464)	$0.31^{+0.33}_{-0.31}$
(464, 1000)	$0.59^{+0.42}_{-0.23}$
(1000, 2154)	$0.327^{+0.32}_{-0.059}$
(2154, 4642)	$0.0^{+0.19}$
(4642, 10000)	$0.25^{+0.24}_{-0.16}$
(10000, 100000)	$0^{+0.76}$

Chapter 8

Validity and Robustness Checks

The robustness of the analysis results was validated with numerous checks, both before and after the dataset was unblinded. This ensured that the data was accurately modelled by the simulations and no biases are introduced by unaccounted or mismodelled systematic uncertainties. As the analysis must be blinded to the physics parameters following IceCube policy, numerous validation checks were performed on the fit before the physics parameters were unveiled. These served as stopping conditions in the unblinding procedure, enabling the discovery and remediation of any inconsistencies between data and simulation without potential bias from knowledge of the analysis results. We begin by presenting these pre-unblinding checks, and then present the results of other 'post-unblinding' validation tests, performed after the fit results had been derived. This chapter follows [16] closely.

8.1 Pre-Unblinding Checks

8.1.1 Muon Background Simulation (MuonGun) Statistics

As shown in Fig. 7.2, we have $\sim$ 10 years of simulated livetime of background muon events in the 10-50 TeV range, critical for our analysis. Due to the stringent cuts applied to suppress the background, the surviving simulated background statistics at final level were quite low, and may not accurately reflect the uncertainties associated with the background for $>$ 10 years of data. Therefore, to reduce the fluctuations associated with the limited statistics, a kernel density estimator (KDE) is used to create a smoothed template approximating the true muon distribution. The analysis was therefore run with the KDE smoothed template in place of the original MuonGun histogram, resulting in minimal changes in the physics parameter best fit values, with the values within the 68% uncertainty of the fit with the original MuonGun histogram.

8.1.2 Uncertainties in the mean inelasticity

The MESE analysis includes a scale parameter for uncertainties on the mean inelasticity as a fit parameter in the baseline fit. Any change in this parameter introduces changes in the cross section.We observe that the best-fit value for this nuisance parameter pulls away from the baseline prediction from CSMS. The best-fit value is $\sim$11% lower for the BPL fit and $\sim$18% for the SPL fit when compared to the baseline value from CSMS, across all energies. This deviation from the baseline model can potentially arise from several channels. It is unclear if this is attributed to an actual change in the neutrino DIS modeling, or if this parameter is absorbing some unknown systematic. A reduction in the average inelasticity (while holding the other

parameters fixed) results in lesser number of observed events in both the cascades and tracks channels. This can be attributed to the dimming of the energy deposit from the initial interaction point of the neutrino events, which results in less events depositing enough energy in the detector to cross the charge threshold of the MESE event selection. This deviation is larger than the uncertainties typically quoted for the mean inelasticities in theoretical calculations. However, it is also possible that this parameter is absorbing some unmodelled systematic effect. A reduction in the scale parameter for the mean inelasticity (while holding all other parameters fixed) results in a lower number of observed events in both the cascades and tracks channels, as fewer events pass the charge threshold of the MESE event selection. The inelasticity scaling parameter is not correlated to the astrophysical flux parameters. Hence the astrophysical flux measurement is robust against the observed deviation.

8.1.3 Dataset splits

Several dataset split tests were performed where the dataset was divided into complementary subsamples, with the fits rerun on each subsample. These fits were then compared to the results obtained with the full dataset. The datasets were separated based on event metrics such as

- Events occurring during the Antarctic summer vs the winter, testing for seasonal variations in the data
- Events from the southern sky vs the northern sky, since we have different background rates in the two hemispheres
- Events with interaction vertices above and below the dust band (2000-2100m below the surface, refer sec. 3.3.2), as the ice below the dust band shows on

average less absorption and scattering than that above; There is also a factor of 3x suppression in the muon background in the deepest part of the detector.

- Events from the first chronological half of the sample (2011-2017) to the second half (2017-2022)

The compatibility of these splits was checked by comparing the 1D profile likelihood scans of the nuisance parameters and requiring that at least 7 out of the 15 nuisance parameters fit within the 1σ regions of the full dataset fit, to proceed with unblinding. All observed variations of the physics parameters are within 3σ of the best fit with the full dataset, as evidenced in Table C.1. As we passed the unblinding criteria, the same was also done subsequently for the astrophysical parameters.

8.2 Post-Unblinding Checks

8.2.1 Neutrinos from the Galactic plane

Table 8.1: A comparison of the BPL fit result with a model incorporating a non-isotropic neutrino flux contribution from the plane of the Milky Way galaxy. The uncertainties are derived from 1D profile likelihood scans, assuming Wilks' theorem applies. The per-flavour flux normalization is measured in units of $C = 10^{-18}/\mathrm{GeV}/\mathrm{cm}^2/\mathrm{s}/\mathrm{sr}$. All flux normalizations are at 100 TeV.

Flux Model Parameters	Unblinded fit (Physics result)	Fit with Galactic plane flux
$\phi^{\nu+\bar{\nu}}/C$	$2.28^{+0.22}_{-0.20}$	$2.28^{+0.28}_{-0.52}$
γ_1	$1.72^{+0.26}_{-0.35}$	$1.72^{+0.34}_{-0.72}$
γ_2	$2.84^{+0.11}_{-0.09}$	$2.84^{+0.19}_{-0.11}$
$\log_{10}(\frac{\mathrm{E_{break}}}{\mathrm{GeV}})$	$4.52^{+0.11}_{-0.09}$	$4.52^{+0.17}_{-0.11}$
ϕ^{GP}/C	NA	$0.0^{+7.04}$

IceCube has recently detected a flux of neutrinos from the plane of the Milky Way [54], which contributes to the diffuse neutrino spectrum measured by the analysis. The anisotropy of the Galactic plane neutrino flux could affect the fitted parameters of the spectral models used to describe the diffuse neutrino flux, which is assumed to be isotropic. Quoting the MESE publication [16], currently under review:

> The impact on the spectral fits is tested by adding a Galactic component to our spectral model, using the emission template from [54] that showed the best agreement with IceCube data ("Fermi-π^0"). The normalization of the Galactic-emission flux template becomes an additional free parameter in the fit to data. We find that the spectral parameters for the diffuse astrophysical neutrino flux remain stable at their baseline best-fit values, and that our best fit of the Galactic plane flux normalization is zero.

8.2.2 Atmospheric neutrino flux modelling

Table 8.2: A comparison of the BPL fit result with a model incorporating the DaemonFlux atmospheric flux model. The uncertainties are derived from 1D profile likelihood scans, assuming Wilks' theorem applies. The per-flavour flux normalization is measured in units of $C = 10^{-18}/\mathrm{GeV}/\mathrm{cm}^2/\mathrm{s}/\mathrm{sr}$. All flux normalizations are at 100 TeV.

Flux Model Parameters	Unblinded fit (Physics result)	Fit with DaemonFlux
$\phi^{\nu+\bar{\nu}}/C$	$2.28^{+0.22}_{-0.20}$	$= 2.22^{+0.33}_{-0.27}$
γ_1	$1.72^{+0.26}_{-0.35}$	$= 1.88^{+0.31}_{-0.48}$
γ_2	$2.84^{+0.11}_{-0.09}$	$= 2.84^{+0.15}_{-0.15}$
$\log_{10}(\frac{\mathrm{E_{break}}}{\mathrm{GeV}})$	$4.52^{+0.11}_{-0.09}$	$= 4.55^{+0.18}_{-0.13}$

A set of fits was performed with updated parametrizations of the atmospheric neutrino spectrum [101], using the DAta-drivEn MuOn-calibrated Neutrino Flux model

(DaemonFlux). The fits using the flux predictions from DaemonFlux, were compared to the baseline (*H4a*+SIBYLL2.3c) fits. Quoting the MESE publication [16], currently under review:

> DaemonFlux uses data-driven models of the cosmic ray composition [102] and the secondary particle yields [103] as inputs to the MCEq code [75], to produce an atmospheric neutrino flux model with the lowest uncertainties to date. We perform the spectral model fits assuming DaemonFlux to be our model for the atmospheric neutrino flux and evaluate the effect on the physics parameters. We observe that the physics parameters do not vary significantly compared to the baseline, while the nuisance parameters describing the uncertainties in the DaemonFlux predictions fit well within their expected ranges. This test confirms that our results do not depend significantly on the detailed CR composition and hadronic interaction models.

8.2.3 Prompt atmospheric neutrinos

The prompt atmospheric neutrino flux is the predicted flux from the decay of charmed mesons created in cosmic ray interactions in the atmosphere. As the best-fit value for the normalization of the prompt atmospheric neutrino flux is zero in this analysis, a check was performed to ensure that the prompt normalization hitting the boundary was not pulling the fit away from the true minima of the likelihood space. The fit was therefore re-run with the prompt flux normalization left unbounded. The best fit prompt normalization for the unbounded fit was at -1.1, which is less than 1σ away from zero, the result of the baseline fit. We also note that the unbounded prompt flux fit resulted in no significant bias in any of the other physics parameters.

Table 8.3: A comparison of the BPL fit result with a model incorporating an unbounded prompt atmospheric neutrino flux normalization. The uncertainties are derived from 1D profile likelihood scans, assuming Wilks' theorem applies. The per-flavour flux normalization is measured in units of $C = 10^{-18}/\text{GeV}/\text{cm}^2/\text{s}/\text{sr}$. All flux normalizations are at 100 TeV.

Flux Model Parameters	Unblinded fit (Physics result)	Fit with DaemonFlux
$\phi^{\nu+\bar{\nu}}/C$	$2.28^{+0.22}_{-0.20}$	$2.38^{+0.25}_{-0.21}$
γ_1	$1.72^{+0.26}_{-0.35}$	$1.88^{+0.23}_{-0.33}$
γ_2	$2.84^{+0.11}_{-0.09}$	$2.86^{+0.13}_{-0.09}$
$\log_{10}(\frac{\text{E}_{\text{break}}}{\text{GeV}})$	$4.52^{+0.11}_{-0.09}$	$4.55^{+0.10}_{-0.10}$
ϕ_{prompt}/C	$0.0^{+0.49}$	$-1.18^{+1.68}_{-3.08}$

8.2.4 Model Crossfits

Cross-model fits were performed on the MESE samples, where we inject the best fit flux of one model and attempt to fit a different flux parameterization model. This enables the evaluation of how well different spectral models fit an idealized 'Asimov' data set, derived purely from simulated fluxes, when the best fit was derived from data under the assumption of another model. The test statistics obtained are illustrated in Fig. 8.1, where we see that the BPL and LP models do not exhibit a great variation in the test statistic difference when injecting each other as the alternate best fit. As there is a significant test statistic difference compared to the SPL hypothesis, similar to what we observe in data.

8.2.5 Check on γ_1 envelope

Two-dimensional profile likelihood scans were performed to test the ability of MESE to constrain the best fit BPL parameters, as illustrated in Fig. 10.2. The closing of the MESE γ_1-γ_2 contour along the γ_1 axis illustrates that MESE is sensitive to the

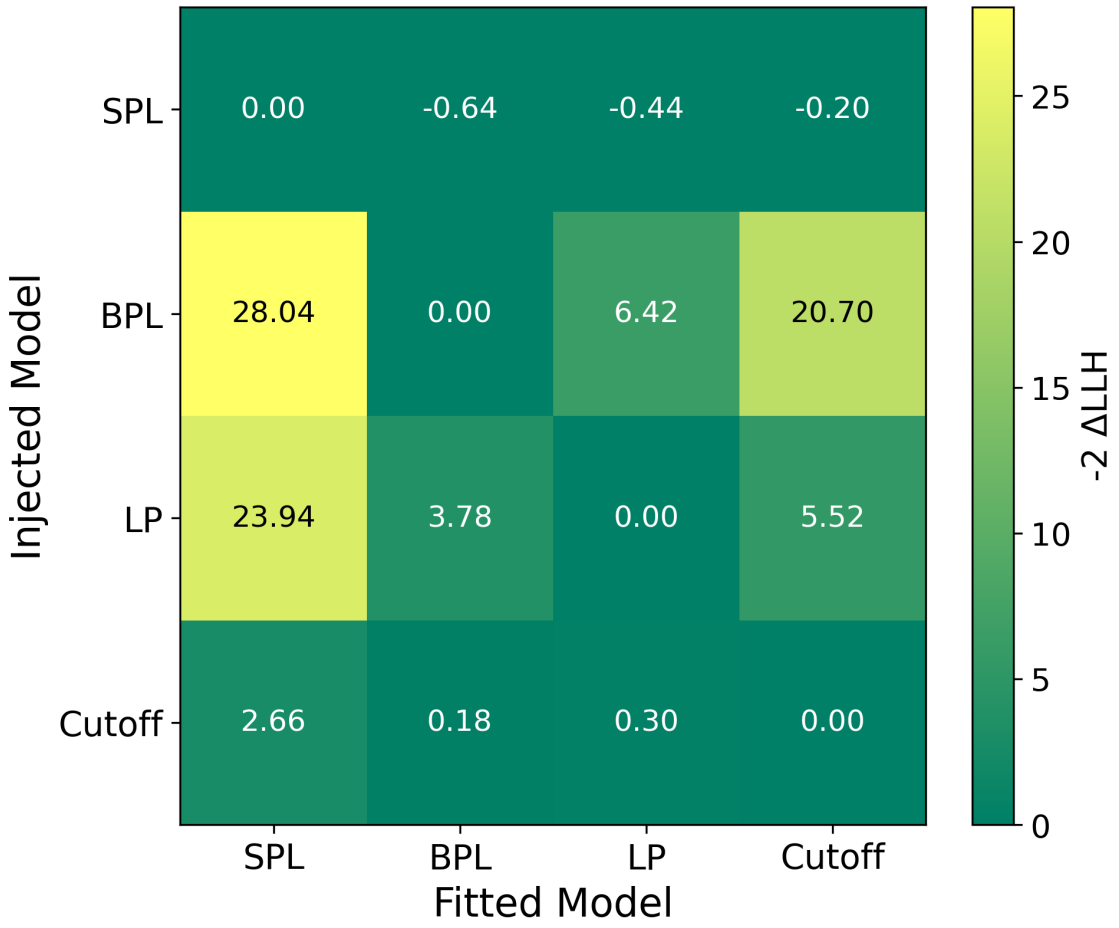

Figure 8.1: **Cross-fit test statistic for the MESE analysis**: The best fit for a given spectral model is injected and subsequently fitted with another spectral model. The TS for these fits are shown in the color scale where the LLH of the fitted model is compared to the LLH of the fit from the injected model. The TS values indicate the power of the analysis to distinguish between different underlying models [16].

low energy astrophysical neutrino flux, especially compared to the complementary Combined Fit analysis [16], discussed later in Ch. 10. A validation check was performed on the error envelope of γ_1 using the MESE dataset. The test aimed to check how likely it was to obtain a constraint on γ_1 similar to that observed with the fit to data. A sample of pseudo data was generated from simulation assuming the best fit astrophysical flux model, and a sub-sample of events whose best-fit parameters

are close to the data fit were selected, as we expected their likelihood profiles and error envelopes to be similar with that obtained by directly fitting to the data. For these pseudo data, we further fixed the γ_1 parameter to the $\pm 95\%$ values in the data contour and evaluate the likelihood value while allowing the remaining parameters to fit freely. The ΔLLH distributions, where $\Delta\text{LLH} = \text{LLH}_{\text{fixed}\,\gamma_1} - \text{LLH}_{\text{free fit}}$, were determined for these realizations of pseudo data and were compared to the ΔLLH from observed data. Again quoting the MESE publication [16]:

> A substantial fraction of the pseudo data had ΔLLH greater than that of the observed data, indicating that if the observed data follows those realizations, the likelihood contour would close for them as well. This gives us confidence that the closed contour is not the effect of unmodeled systematics that artificially force the data fit to exclude zero.

8.3 Summary

We have presented various tests which were performed on the fit results, both before and after unblinding the spectral parameters. This allowed us to ascertain whether the data was accurately modelled, or whether the results were unduly influenced by mismodelled or unaccounted effects. Profile likelihood scans of the physics parameters were used to ensure that the best fit values were not at the boundaries or in unphysical regions of the parameter space.

These included splitting the dataset based on numerous event metrics, and examining the fit results. We observed that none of the parameters were biased more than 3σ away from the best fit with the full dataset, as evidenced in Tab. C.1. The effects of the atmospheric flux model and additional non-isotropic fluxes from the Galactic plane were also tested, and were found to have minimal effects on the astrophysical

flux parameters. The effect of the prompt atmospheric flux hitting the boundary was also studied and was determined to be consistent within 1σ to the minimum of the unbounded likelihood space, while not biasing the physics parameters beyond 1σ. Post-unblinding checks were also carried out to validate the low-energy sensitivity of the MESE analysis, and on the degree of bias introduced into the fitted physics parameters if a different flux hypothesis was injected. We determined that the analysis was robust to these modifications and checks, and thus validated the results of the analysis.

Chapter 9

IceCube's Highest Energy Event

The MESE dataset contains the highest energy event recorded by IceCube to date. It was observed on March 31 2019, and is identified as a starting track from the Southern Sky. A General Coordinates Network (GCN) alert was sent to the multi-messenger community using an erroneous direction obtained from the LineFit reconstruction [64] performed 'online' at the South Pole, later corrected using the offline Millipede reconstruction [67]. A more detailed discussion of the event in a multi-messenger context will follow in sec. 9.2.

9.1 Reconstruction with the DirectFit algorithm

In this section we study this event from the context of the MESE analysis, demonstrating the wide energy range spanned by the event sample. The event was tagged as a HESE event [104], allowing it to proceed through the stages of the MESE analysis without further cuts. It has a reconstructed deposited energy of $\sim$ 3.7 PeV using the reconstruction algorithms introduced in Ch. 4. A subsequent reconstruction of

the event was conducted using the latest DirectFit algorithm [104]. DirectFit is an event reconstruction, which resimulates events similar to the observed neutrino event many times, and compares the distribution of observables to arrive at the most probable neutrino parameters. DirectFit simulates a large number of iterations similar to the given event ($\sim$ 10000 for determining the solution and another $\sim$ 10000 to calculate the uncertainties), exploring its allowed parameter space, and further propagating the event through ice to obtain the deposited light in the DOMs. This procedure enables accurate modeling of the reconstructed event, however at very high computational costs, and is therefore not performed for every event in the MESE sample. All events released in [104] and additional interesting events such as the multi-PeV track-like event in [105] and [106] have been reconstructed using DirectFit. DirectFit uses the most recent ice models, including details of ice layer undulations and ice model anisotropy [104], not otherwise used in the standard simulations generated for the measurement of the spectrum presented in this paper. The deposited or 'visible' energy was reconstructed using these updates as a part of the HESE data release [104] as 4.4 PeV, if one assumes the initial cascade is electromagnetic (EM), and scales up to 4.6 PeV if we assume that the initial cascade is hadronic. The reconstruction of the track segment gives an estimate of its average $\mathrm{d}E/\mathrm{d}x$ as 1.125 TeV m^{-1} in the last 400 m before leaving the detector. This means that 450 TeV, or 10% of the visible energy, is deposited in the track section of the starting track event.

We draw samples from an energy distribution from $\sim$ 5 PeV to 100 PeV, assuming a neutrino spectrum that follows a broken power law with the parameters obtained as our best fit, and perform resimulations. The lower limit of this sampled energy distribution arises from the reconstructed energy loss. These resimulations are performed under the constraint that the event deposits 450 TeV in these 400 m. The muon en-

Table 9.1: A table summarizing the various observables and reconstructed parameters of the high energy starting track observed in the MESE sample [16]

Event Metrics	Values
Zenith angle (IceCube coordinates)	68°
Declination (J2000 coordinates, 90% PSF containment)	$-20.70^\circ\,^{+0.30^\circ}_{-0.48^\circ}$
Right Ascension (J2000 coordinates, 90% PSF containment)	$337.68^\circ\,^{+0.23^\circ}_{-0.34^\circ}$
Initial Cascade $E_{\mathrm{vis,EM}}$	4.4 PeV
Initial Cascade $E_{\mathrm{vis,hadronic}}$	4.6 PeV
Avg. $\mathrm{d}E/\mathrm{d}x$	1.125 TeV m^{-1}
E_μ range estimate	4.3-9.3 PeV
E_ν range estimate (BPL flux hypothesis)	$8.9 - 13.9$ PeV (68% CL)
most probable E_ν (BPL flux hypothesis)	11.4 PeV

ergy distribution is further constrained by the inelasticity relationship (neutrino cross section), assuming the first interaction is a hadronic cascade with an equivalent EM energy of 4.6 PeV. This results in an initial muon energy between $4.3-9.3$ PeV, which corresponds to a total neutrino energy of $8.9-13.9$ PeV (68% CL), assuming the flux follows the BPL flux hypothesis. The most probable neutrino energy is 11.4 PeV. If we assume that the spectrum, instead, follows a SPL, the estimated neutrino energy lies within $9.0-14.1$ PeV. Fig. 9.1 provides a visualisation of this event, along with the energy estimate obtained from DirectFit.

9.2 Multi-messenger followup campaign

The high energy event was identified in 2019 by the High Energy Starting Event (HESE) track selection as very likely to be an astrophysical muon neutrino [109], and an alert was sent out to the multi-messenger community. An initial automated alert had incorrect reconstructed values for the direction, and was followed by a cor-

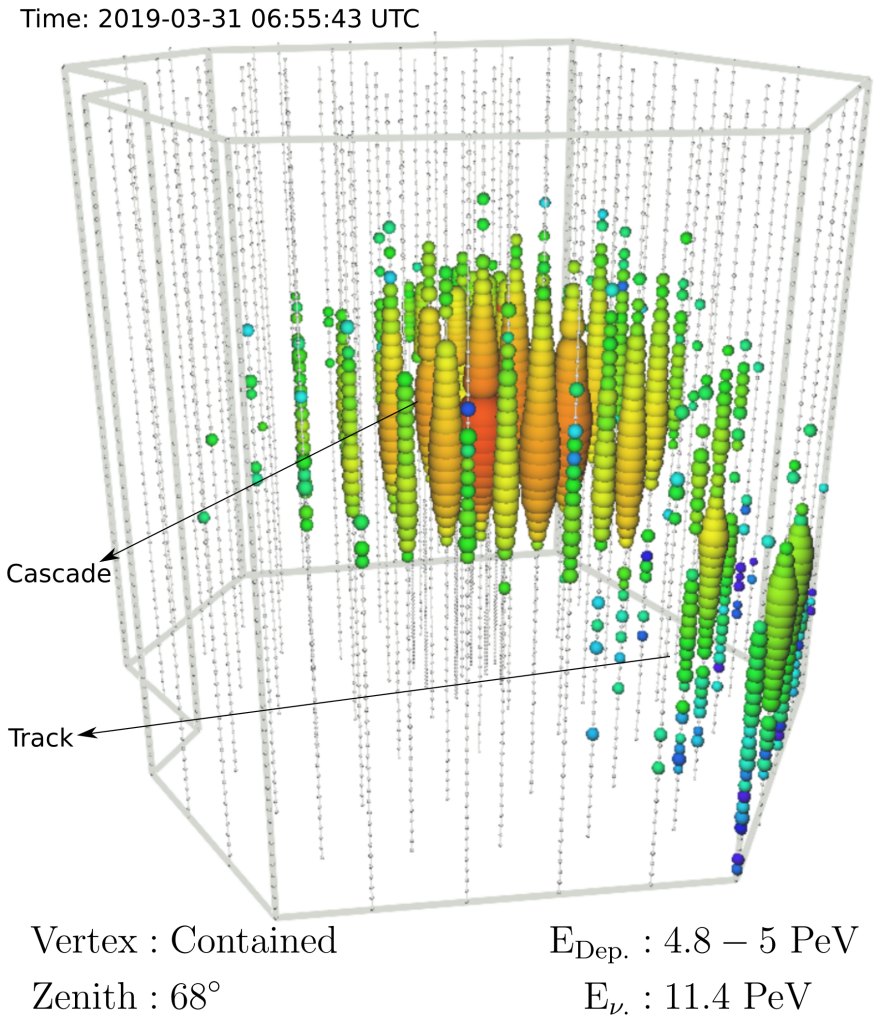

Figure 9.1: **The Highest Energy IceCube Neutrino**: the event view of the highest neutrino energy event recorded to date by IceCube [104, 16]

rection after offline Millipede reconstruction was performed. The corrected direction coordinates were, in the J2000 coordinate system, a declination of $-20.70^{\circ}{}^{+0.30^{\circ}}_{-0.48^{\circ}}$ and a right ascension of $337.68^{\circ}{}^{+0.23^{\circ}}_{-0.34^{\circ}}$, with the error values representing the 90% Point Spread Function (PSF) containment. The Millipede reconstructed direction reported in [109] had a very tight 90% confidence region, due to a scaling relation extrapolated from lower energy modelling, which was only corrected in subsequent software releases. Reconstruction with DirectFit yielded a more accurate evaluation of the

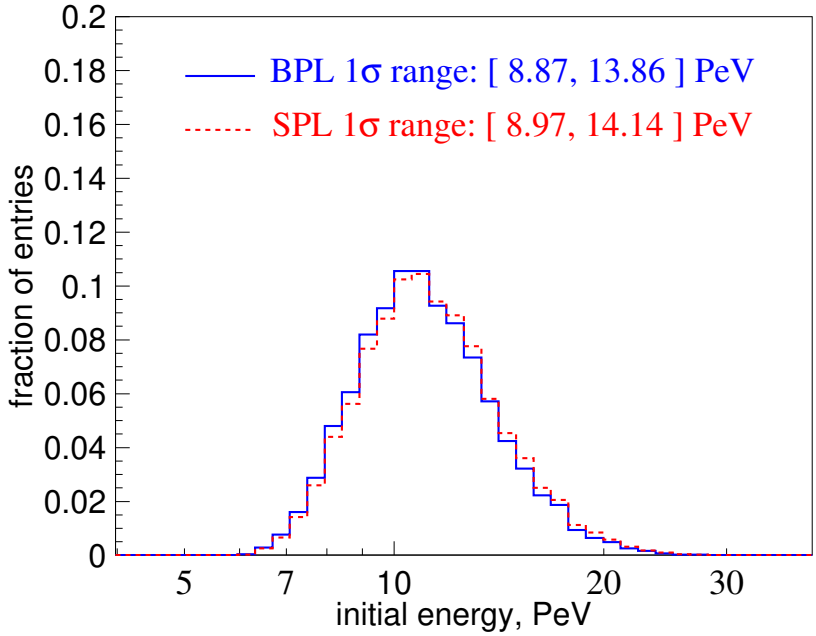

Figure 9.2: **DirectFit energy reconstruction**: the posterior distribution of the reconstructed neutrino energy of the highest neutrino energy event recorded to date by IceCube. The median neutrino energy is 11.4 PeV assuming the best fit broken power law spectral model for the astrophysical neutrino flux. Figure from D. Chirkin [16]

Table 9.2: A list of neutrino events observed with energy above 1 PeV

Event	MJD	Most probable E_ν	RA	Dec.
IceCube HESE [51] 'Bert'	55782.5	1.1 PeV	268.5°	-25.3°
IceCube HESE [51] 'Ernie'	55929.4	1.2 PeV	37.0°	-66.1°
IceCube HESE [51] 'Big Bird'	56265.1	2.1 PeV	245.83°	-51.7°
IceCube Northern Tracks [99, 107] 'Kloppo'	56819.2	8.7 PeV	110.7°	11.5°
IceCube Glashow Resonance 'Hydrangea' [39, 107]	57730.1	6.3 PeV	192.7°	15.9°
IceCube Northern Tracks [99]	58063.8	NA ($E_{\mu,\text{proxy}} = 1.2$ PeV)[1]	340.1°	7.44°
IceCube HESE [16, 104] (**This Event**)	58573.3	11.4 PeV	337.8°	-21.99°
KM3NeT[108] 'KM3-230213A'	59988.1	220 PeV	94.3°	-7.8°

[1]If one assumes a scaling relationship between E_ν and $E_{\mu,\text{proxy}}$ like that observed in 'Kloppo', due to the similar declination, the best estimate for $E_\nu = 2.4$ PeV

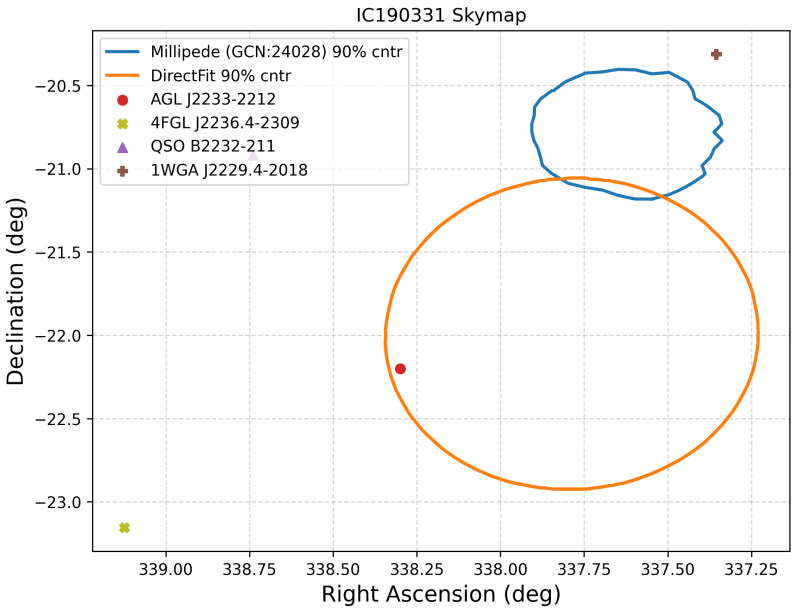

Figure 9.3: **IC190331 skymap**: An illustration of a few possible sources in the vicinity of the PeV neutrino IC190331. Contours from T. Yuan [104]

90% confidence region (Fig. 9.3).

Followup searches for additional track events from the same direction in a 2 day time window found no astrophysical event candidates, as did a subsequent search using the month of data preceding the alert event [110]. No gamma ray sources listed in the Fermi 4FGL catalog were in the 90% region, and subsequent searches for transient sources indicated no significant ($> 5\sigma$) emission from any sources in the vicinity [111]. The MASTER-OAFA optical telescope, however, observed NGC 7293 (the Helix Nebula) inside the error region provided in the IceCube alert [112]. The Neil Gehrels Swift Observatory, an X-ray satellite telescope, found four X-ray sources in a circular region centered around the best fit IceCube declination and right ascension, with a radius of 33 arcmin. From the GCN Circular from the Swift-XRT collaboration [113], the highest-significance X-ray source was located at right ascension 337.35513°, and declination -20.31324° (J2000), within the IceCube 90%-containment region, matching the known X-ray source 1WGA J2229.4-2018 from ROSAT/WGACAT within (15.37

arcsec distance). Further details of possible counterparts are provided in [114].

The AGILE satellite observed transient gamma ray emission above 100 MeV at a preliminary significance level of 4σ from the source AGL J2233-2212 [115]. This was the first significant emission observed from this source, which was not observed by other instruments at the time.

Chapter 10

Discussion of Spectral Measurement

Among all the tested astrophysical flux hypotheses, we find that the obtained likelihood is minimal for a broken power law (BPL) model, with an improvement of TS $= -2\Delta\log\mathcal{L} = 27.3$ when compared to the likelihood obtained for a single power law (SPL) model. We infer therefore that the BPL hypothesis provides the best characterisation of the observed data. The TS for the BPL model tested against the SPL corresponds to a p-value of $1.2 \cdot 10^{-6}$ or 4.7 σ, meaning that for the first time IceCube is able to reject the SPL hypothesis to a significant degree, and resolve structure in the neutrino spectrum below 30 TeV.

The SPL is often seen as the baseline model for astrophysical fits for a few reasons. These include the fact that it is the simplest flux model and has previously been a good description of observed data, and a power law spectrum is also predicted by the Fermi model for cosmic acceleration (refer sec. 2.1.1). Two features in the observed data presented in this analysis drive the preference for the change in the spectral shape, the excess at $\sim$ 30 TeV and a deficit at a few hundred TeV, when compared

to the baseline SPL model. Fig. 7.5 shows the distribution of the energy proxy for cascades and tracks in the MESE analysis, where the simulation for the best-fit SPL model is compared to observed data. There is a visible excess of data compared to this simulation around 30 TeV energy. This is more prominent in the cascades channel, and is also visible within $1\,\sigma$ errors for the MESE tracks sample, as illustrated in Fig. 10.1.

This preference for the BPL could imply a more complex origin for the observed astrophysical neutrinos than described by the Fermi model. One possible explanation could be a departure from the assumptions of the Fermi model, such as inelastic collisions with the shock front [116, 117], or lower acceleration efficiency [118, 119]. The observed spectrum could also be a feature of interactions of the accelerated particles with the source environment, such as an effectively energy-dependent attenuation. This may be a consequence of neutrino production in cosmic ray reservoirs, discussed in sec. 2.1.2.2, with the escape or 'leakage' rate of cosmic rays depending on their energies.

Fig. 10.2 shows the 2D profile likelihood scans of the parameters of the BPL spectral model ($\phi^{\nu+\bar{\nu}}$: the astrophysical flux normalization at 100 TeV, γ_1: the low energy spectral index, γ_2: the high energy spectral index, and E_{break}: the break energy) for the analysis presented here. In addition to the preference for the BPL model, we also obtain a significant improvement of the fit when we compare a log-parabola (LP) model to an SPL spectrum (TS = $18.8 \rightarrow 4.2\,\sigma$). The assumed spectral shape of SPL + Gaussian bump also provides a significant deviation from an SPL with a TS of 22.3 ($3.9\,\sigma$). We again determine the chances of mis-identifying a true SPL + bump model as a BPL model from pseudo experiments. Here, we inject the SPL + bump best fit and calculate $\text{TS} = -2\,\Delta\text{LLH} = \text{LLH}_{\text{BPL}} - \text{LLH}_{\text{SPL+bump}}$ to compare the two model fits. Obtaining a p-value of 0.09 for this test, we are not able to distinguish

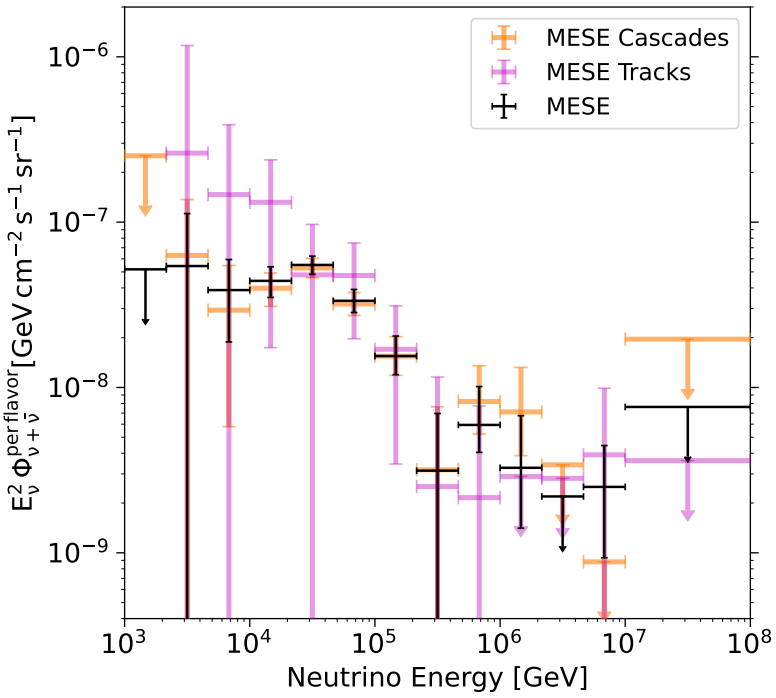

Figure 10.1: MESE segmented fits with only MESE cascades and only MESE tracks compared to the segmented fit including both detection channels.

this model from the best-fit model of a BPL.

Fig. 10.3 compares the 2D profile likelihood scans for the parameters of the LP model (ϕ_{astro}: the astrophysical flux normalization at 100 TeV, α: the parameter describing the spectral index, and β: the curvature parameter).

10.1 Comparison to previous IceCube measurements

The results of the MESE analysis indicate the presence of structure in the diffuse astrophysical neutrino spectrum beyond a single power law. The techniques presented in this thesis yield improved sensitivity to the neutrino flux down to $\mathcal{O}$(TeV) scales,

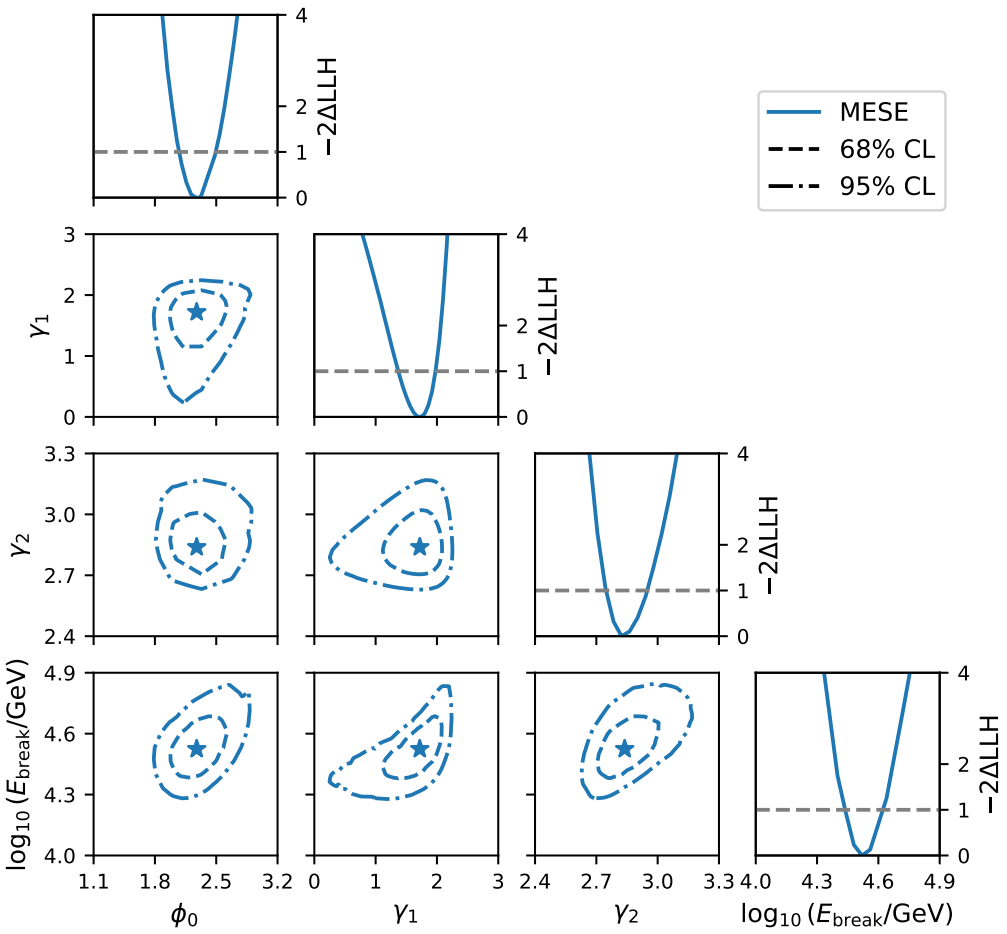

Figure 10.2: **Broken Power Law spectral parameters**: Two-dimensional profile likelihood scans of all physics parameters in the BPL model fit. The star markers indicate the best fit parameter values with ϕ_{astro} =2.28, γ_1 = 1.72, γ_2 = 2.84, and $\log_{10}(\mathrm{E_{break}}/\mathrm{GeV})$ = 4.52. The contours represent the 68% and 95% confidence regions for the parameters based on Wilks' theorem.

where the deviation from a single power law is most pronounced. The excess of events at 30 TeV and a dip at a few hundred TeV are the clearest manifestations of features that cannot be explained by a single power law. As illustrated in Fig. 10.4, the spectral hardening observed by this analysis represents a departure from IceCube's previously published observations. The three most recent analyses, which reflect the 'state of the art' of diffuse measurements are the:

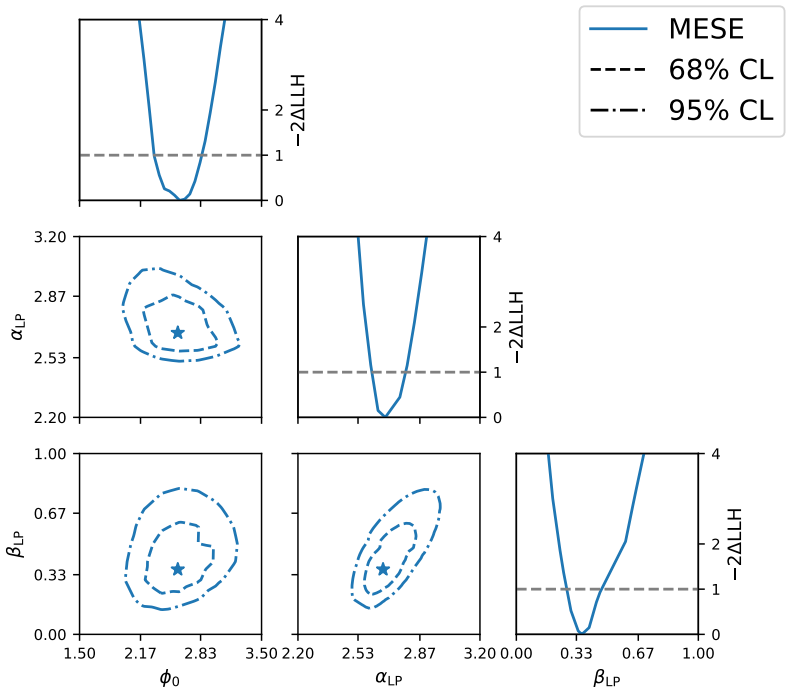

Figure 10.3: **Log Parabola physics parameters**: Two-dimensional profile likelihood scans of all physics parameters in the LP model fit. The star markers indicate the best fit parameter values with ϕ_0 =2.58, α_{LP} = 2.67, and β_{LP} = 0.36. The contours represent the 68% and 95% confidence regions based on Wilks' theorem.

- **MESE analysis**: The subject of this thesis, MESE is focused on starting events. The event selection consistently selects cascade and starting track events through the same background suppression veto techniques. MESE's sensitive energy range is calculated to extend from 5 TeV to 7.5 PeV

- **'Combined Fit' analysis**: This combines a sample of contained cascade events [76], extended with five additional years of data, and a sample of through-going tracks from the Northern sky [99]. While these were previously used independently to measure the astrophysical neutrino flux, visible in 'Cascades SPL (2020)' and 'Tracks SPL (2022)' in Fig. 10.4, the 'Combined Fit' aims to perform a joint fit with both samples. This leverages the high statistics of the tracks sample and the neutrino-purity of the cascades sample as complementary

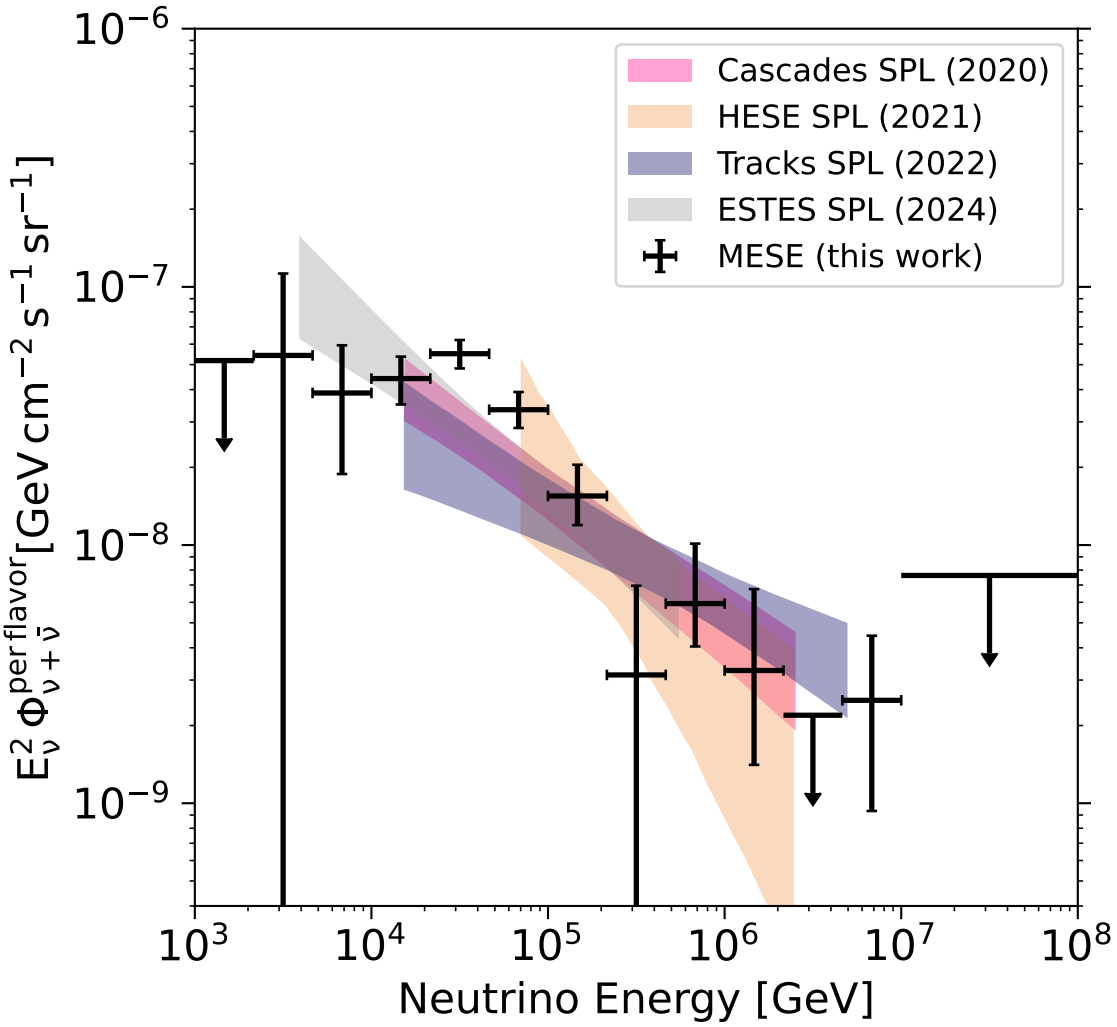

Figure 10.4: **MESE Segmented Flux Comparison**: Results of a fit of the astrophysical neutrino flux in independent energy bands. The segmented fit is compared to previous measurements from IceCube, all of which measured the best fit flux hypothesis to be an SPL. The uncertainties on the previous results are the 68% CL envelopes [16].

advantages. The energy range of the 'Combined Fit' extends from 13 TeV to 10 PeV.

- **ESTES**: The ESTES analysis uses a high-purity sample of starting tracks to measure the neutrino spectrum. As discussed in sec. 3.4.2, starting track events inherit the excellent angular resolution of track events while the contained neu-

trino interaction vertex allows accurate energy estimation. ESTES, like MESE, is sensitive to neutrinos from the entire sky, and in particular also benefits from the Self-Veto effect's enhancement of the astrophysical neutrino sensitivity from the Southern sky. The sensitive energy range of ESTES is from 3 TeV to 550 TeV. As visible in Fig. 10.4, the ESTES result is compatible with a single power law, even below 10 TeV.

While ESTES favours the SPL model, both MESE and 'Combined Fit' prefer the BPL model [15, 16, 120, 86]. The ESTES analysis also used a different treatment of systematic uncertainties, and used a different parameterization of the atmospheric and self-veto uncertainties when compared to both MESE and the 'Combined Fit' analysis.

It is noteworthy that the ESTES measurements are compatible with the differential fit using only starting tracks from the MESE selection, shown in Fig. 10.1. The preference for the BPL is most prominent in MESE's cascades subsample, which is also more sensitive to the (< 60 TeV) astrophysical neutrino flux than the tracks channel, as evidenced by the wide error bars on the tracks result in Fig. 10.1. The 'Combined Fit' also finds that its cascade subsample is driving the preference for the BPL, although a caveat is that the 'Northern Tracks' component is heavily dominated by atmospheric neutrinos until $\sim \mathcal{O}(100$ TeV), and is therefore less sensitive to the astrophysical flux below that threshold. One point worth noting is that the 'Combined Fit' predicts a bigger deviation from the ESTES result than MESE does. This may be due to MESE's incorporation of starting track events

This difference between the results is under active investigation by IceCube. It is implausible for different neutrino flavours (which, after all, is what the cascade and track morphologies indicate) to have differing spectra at lower energies. At present, no models predict an astrophysical origin for this observation, and the cross-checks

performed in Ch. 8 indicate that the MESE result is robust. Efforts are underway to unify the different samples with an identical treatment of systematic uncertainties and updated simulations, and thus obtain a more complete picture.

10.2 Implications for neutrino source models

This harder flux at $\mathcal{O}(10$ TeV) guides one towards specific models of neutrino emission in a multi-messenger context. The extrapolation of the prior SPL results to lower energies leads to tensions with the *Fermi*-LAT observations of the extragalactic gamma-ray flux at GeV energies. This tension can be alleviated by positing that the bulk of neutrino sources are opaque to GeV gamma rays [27, 100]. In fact, the spectral hardening observed by MESE is anticipated by the minimal p-γ model of Fig. 2.9 which assumes a break in the neutrino spectrum at 25 TeV. Explicitly constructed to be more consistent with limits on the extragalactic gamma-ray flux, a similar model of neutrino emission could help illuminate the connection between sources of neutrinos and gamma rays. In the case of neutrino sources opaque to gamma rays, which are favoured due to their consistency with existing GeV gamma-ray flux measurements, we can also study the mechanism by which the gamma-ray flux is attenuated.

Various models for neutrino spectra from sources both transparent and opaque to gamma rays are discussed in [32], as illustrated in Fig. 10.5. These gamma rays interact with the radiation field surrounding the source, as discussed in sec. 2.3, and cascade down to lower energies via pair production. The cascaded flux is strongly dependent on the source radiation field, and particularly the upper bound of the energy of the field photons. As observed in the right panel of Fig. 10.5, the break energy of the neutrino spectrum is negatively correlated with the peak photon energy which is required to ensure consistency with the isotropic gamma ray background from *Fermi*-

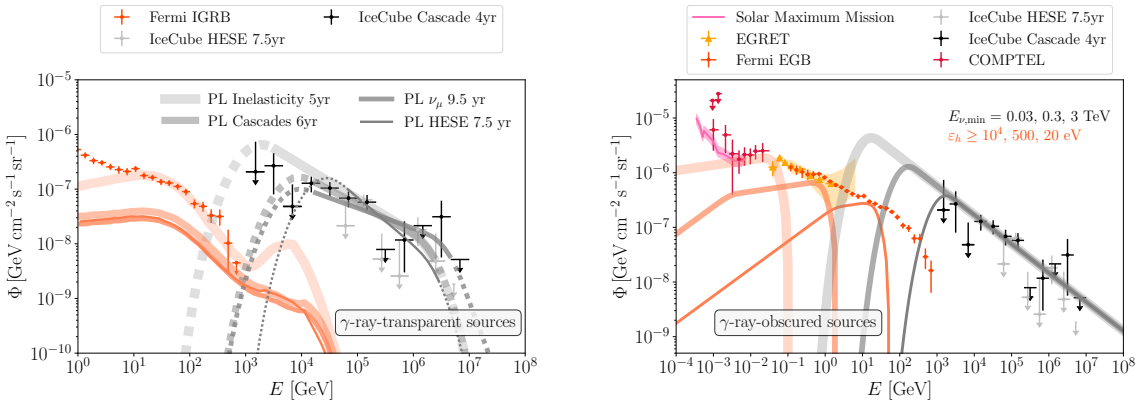

Figure 10.5: **Cosmic Neutrino and Gamma Ray Spectra** [32]: *Left*: A comparison of neutrino spectra and the isotropic gamma ray fluxes assuming the sources of neutrinos are transparent to gamma rays. *Right*: Spectra from gamma-ray obscured sources, where a source radiation field at X-ray or UV regimes is necessary to initiate pair production cascades and suppress the gamma ray flux.

LAT. We note that the sensitivity of MESE to the $\mathcal{O}$(10 TeV) neutrino spectrum can therefore provide a means of studying the source radiation field. The suppression of GeV gamma rays from neutrino emitters also motivates complementary analyses of these sources in the X-ray or MeV gamma ray energy band.

10.3 p-p vs p-γ hadronic interactions

As discussed in sec. 2.3, the neutrino spectrum typically obtained from p-p hadronic interactions follows the primary spectrum as a power law. The p-γ scenario, on the other hand, involves structure in the neutrino spectrum, due to the resonant production of the Δ^+ baryon. This resonance gives a characteristic peaked structure to the neutrino spectrum, along with a low energy cutoff depending on the surrounding photon field. The transition in the spectral index observed at 30 TeV by MESE indicates a preference for p-γ origins for the $\mathcal{O}$(10 TeV) diffuse neutrino flux. From the resonance condition, we have the center of mass energy $s \sim m^2_{\Delta^+} = E_p.\epsilon_\gamma$, with the primary proton energy E_p constraining the energy of the required photon field

ϵ_γ. The results obtained here may indicate the presence of X-ray photon fields in the surrounding environment. Further observation and analysis would be required before a definitive resolution can be obtained.

10.4 Future spectral analyses

Various efforts are underway to improve the understanding of the astrophysical neutrino spectrum. Improvements in ice modelling which account for anisotropy and birefringence [121] in the detector medium will lead to more robust event reconstructions, improving the resolution of fine spectral features. The upcoming IceCube Upgrade [122, 89] plans to carry out fine measurements of the South Pole ice, among its other science goals, which will further improve our understanding of systematic uncertainties related to the ice.

Event selections too are utilizing the latest machine learning techniques, with a neural net based cascade selection developed from the selection described here [54] to capture partially contained events. This would greatly boost the effective area at low energies, better resolving the spectrum below 10 TeV. Further investigations into the nature of the observed dip at $\sim$ 100 TeV would also shed light on the dynamics of high energy neutrino sources.

10.5 The PeV neutrino flux

The high energy neutrino flux is also being studied with updated versions of IceCube's Extremely High Energy (EHE) event selections [123]. In addition to the three events above 5 PeV observed by IceCube, including the high energy event seen by MESE (IC190331) with a reconstructed event of $\mathcal{O}$(10 PeV), the KM3NeT collaboration

recently announced the observation of a neutrino with energy an order of magnitude higher, at the $\mathcal{O}$(100 PeV) scale [108]. These neutrinos imply the production of neutrinos via the interaction of UHECRs with the extragalactic background light (EBL). These observations bode well for the future of ultra high energy neutrino astronomy, and a future expansion of IceCube, IceCube-Gen2 is poised to lead the next generation of experiments studying the neutrino flux at PeV scales and beyond.

Chapter 11

Outlook for Future Measurements

IceCube has been taking data since 2011, and future expansions of the detector are already underway, illustrated in Fig. 11.1. The IceCube Upgrade aims to study neutrino oscillations at GeV energies, and also enhance our understanding of the properties of the South Pole ice. It is scheduled for deployment during the austral summer from 2025-2026. The upcoming IceCube Upgrade will consist of nearly 800 new optical modules on 7 strings. There are two main optical module designs for the Upgrade: the mDOM [124] (Figure 11.2), featuring 24 PMTs of 3" diameter, yielding an almost homogeneous angular coverage, and the DEgg [125] (Figure 11.3), with two 8" PMTs opposite each other. The Upgrade also provides an opportunity to test the instrumentation designed for Gen2, based on multi-PMT pixelated detectors.

On the other hand, IceCube-Gen2 is a planned expansion of the IceCube Neutrino Observatory aimed at increasing sensitivity to PeV neutrinos. In addition to an optical array, IceCube-Gen2 will have a scintillator array mounted on the surface, along with radio antennae to study cosmic ray air showers. IceCube-Gen2 will also have a radio array for the detection of EeV neutrinos, using a cluster of both surface and buried radio antennas.

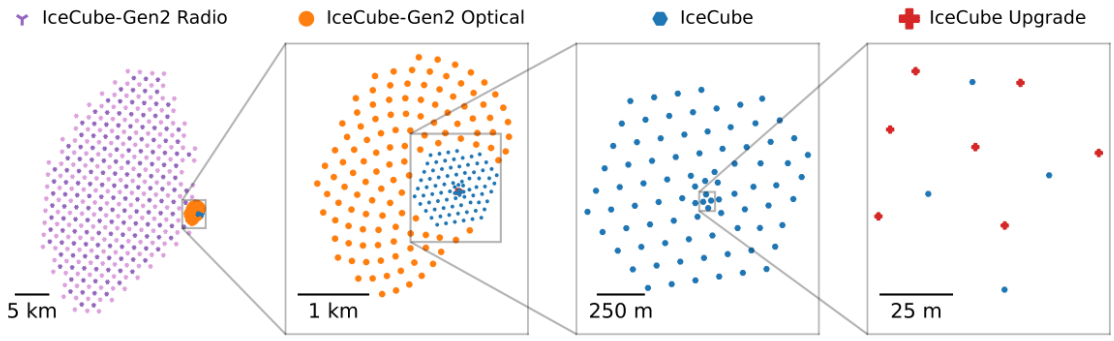

Figure 11.1: The IceCube Upgrade aims to increase IceCube's sensitivity to GeV neutrinos, while IceCube-Gen2 is focused on events at PeV energies and higher [46].

Figure 11.2: The multi-PMT Digital Optical Module (mDOM). Picture courtesy L. Classen

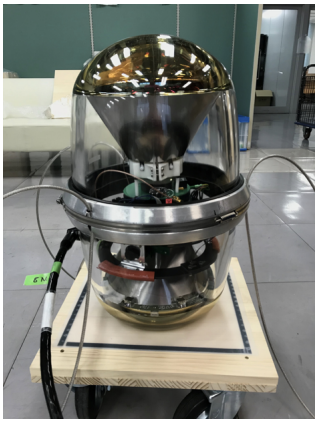

Figure 11.3: The D-Egg, an acronym for Dual optical sensors in an Ellipsoid Glass for Gen2. Picture courtesy N. Shimizu

11.1 IceCube-Gen2 Instrumentation Development

The optical array design for IceCube-Gen2 will instrument an 8 km^3 volume with advanced optical detectors, arranged in strings spaced 240 meters apart in a 'sunflower' pattern. This layout is optimized to prevent any gaps or "corridors" that could allow muons to pass undetected. Each string will contain 80 optical modules,

vertically spaced 17 meters apart. My contributions to this project included the design, prototyping, and integration of a multi-pixel digital optical module (DOM) for IceCube-Gen2 [126], referred to here as the Long Optical Module (LOM).

The LOM, developed from the multi-PMT Upgrade modules, has a reduced diameter (12.5") to enable the module to fit in a narrower hole, saving time and fuel costs for drilling. Multiple 4" PMTs have been used to maximize effective area with fewer channels. The LOM is designed to be sensitive to the brightest PeV neutrino events, with a linear response across a wide dynamic range upto a signal of 5000 photoelectrons (PE) in 25 ns. The waveform processing has been shifted to the PMT base, integrating digitization and high voltage (HV) generation, and reducing power consumption to a target of 4 W per module. Two variations of this design are currently

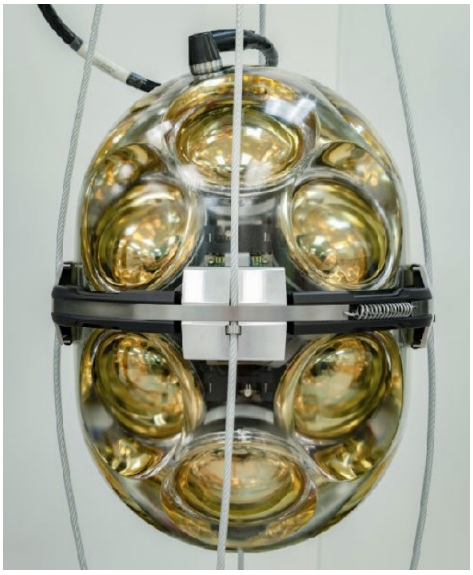

Figure 11.4: The 16 PMT Long Optical Module (LOM) design. Picture courtesy Y. Makino

Figure 11.5: The 18 PMT Long Optical Module (LOM) design. Picture courtesy N. Shimizu

under development (Fig. 11.4 & 11.5), with 16 and 18 PMTs, at UW Physical Sciences Lab (PSL) and Chiba University respectively. My work has focused primarily

on the development of the 16 PMT design as part of the Wisconsin IceCube Particle Astrophysics Center (WIPAC) and PSL team, further details of which are provided in Appendix D. In the near term, the goal is to build ten modules of each type, and deploy 12 modules for testing during the Upgrade. These will be developed into a single baseline design for Gen2, which will have 9600 modules distributed across 120 strings [127]. IceCube-Gen2 is estimated to increase the cascade fiducial volume

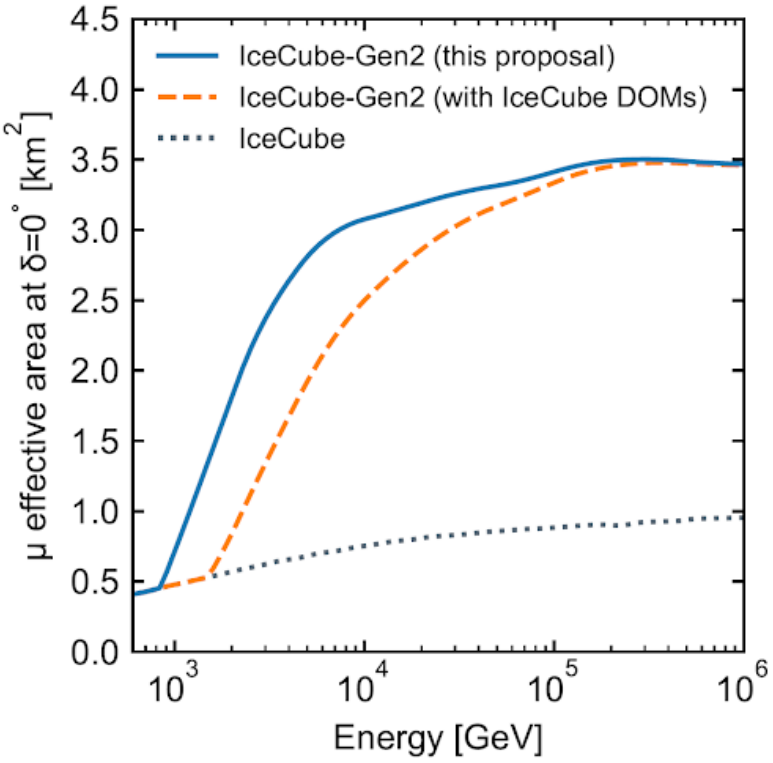

Figure 11.6: Effective area for detection of horizontal muons [46]. The higher sensitivity of the Gen2-DOMs lowers the detection threshold for throughgoing muons by >2x at string spacing 240 m.

roughly ten-fold, enabling better characterization of the cosmic neutrino flux above 100 TeV. It also improves sensitivity to point sources, with the median angular error of upgoing tracks improved two-fold, with a 5x increase in the detector effective area. This grants sensitivity to both transient and steady sources of neutrinos, enabling the observation of many more neutrino emitters relative to IceCube.

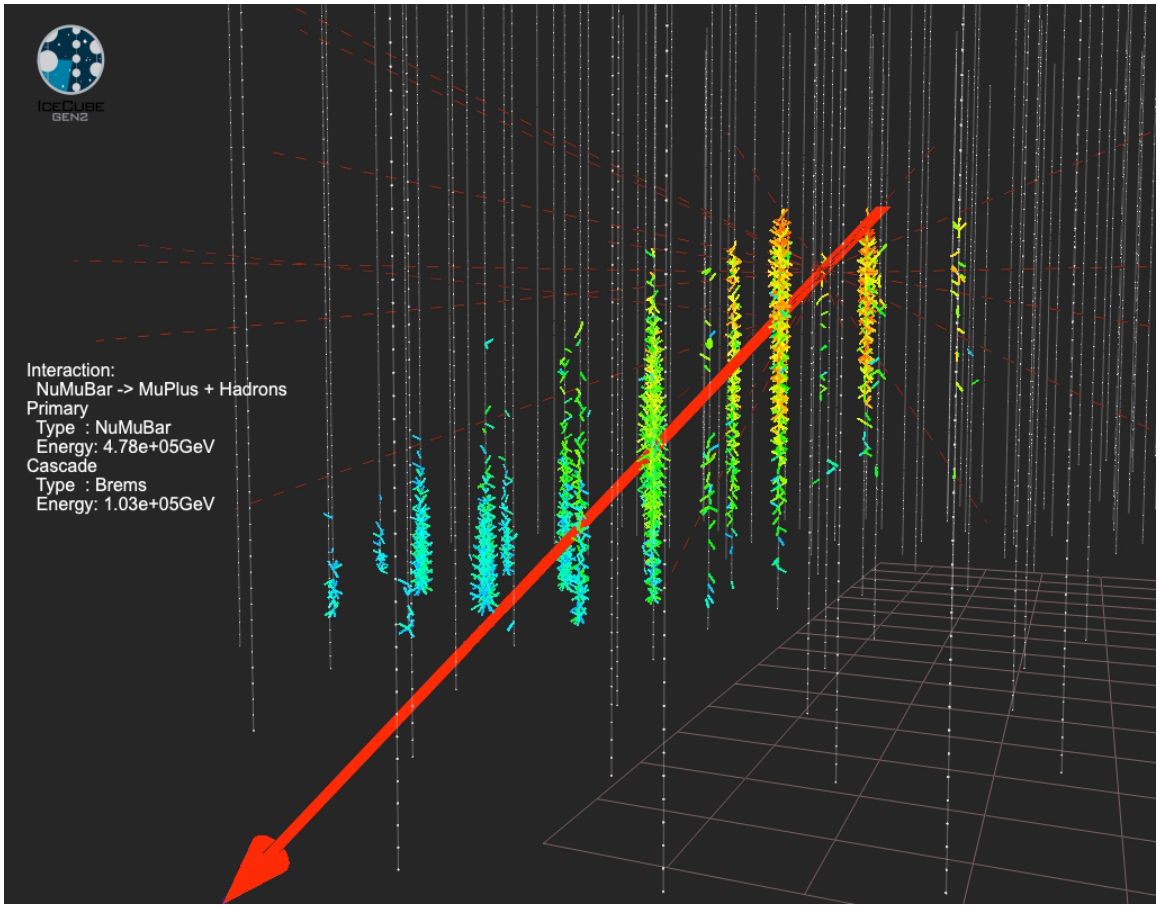

Figure 11.7: An event view of a simulated 100 TeV ν_μ CC starting track event with the IceCube-Gen2 optical modules. The response of individual PMTs can be resolved due to the multi-pixel readout. Image courtesy J. Vara

11.2 Neutrino spectral measurements with IceCube-Gen2

Efforts are currently underway to simulate neutrino events with the geometry used for IceCube-Gen2, and incorporate the response of the new optical modules. This is a complex undertaking, requiring a deep knowledge of the current IceCube software along with the tools required for Gen2. A projected measurement of the astrophysical neutrino spectrum for IceCube-Gen2 is shown in Fig. 11.8, extrapolating currently published IceCube results at 10 PeV upto the EeV energies of extragalactic cosmic

rays (CRs). IceCube-Gen2's sensitivity to the neutrino spectrum in this energy gap allows for the validation of different model predictions for the neutrino flux beyond 10 PeV. This could more thoroughly explore the connection between the origins of neutrinos and CRs in extragalactic cosmic accelerators. The increase in statistics with more years of observation will also enable for more specialized studies of the composition of astrophysical neutrinos, including searches for energy dependence of the flavour ratio.

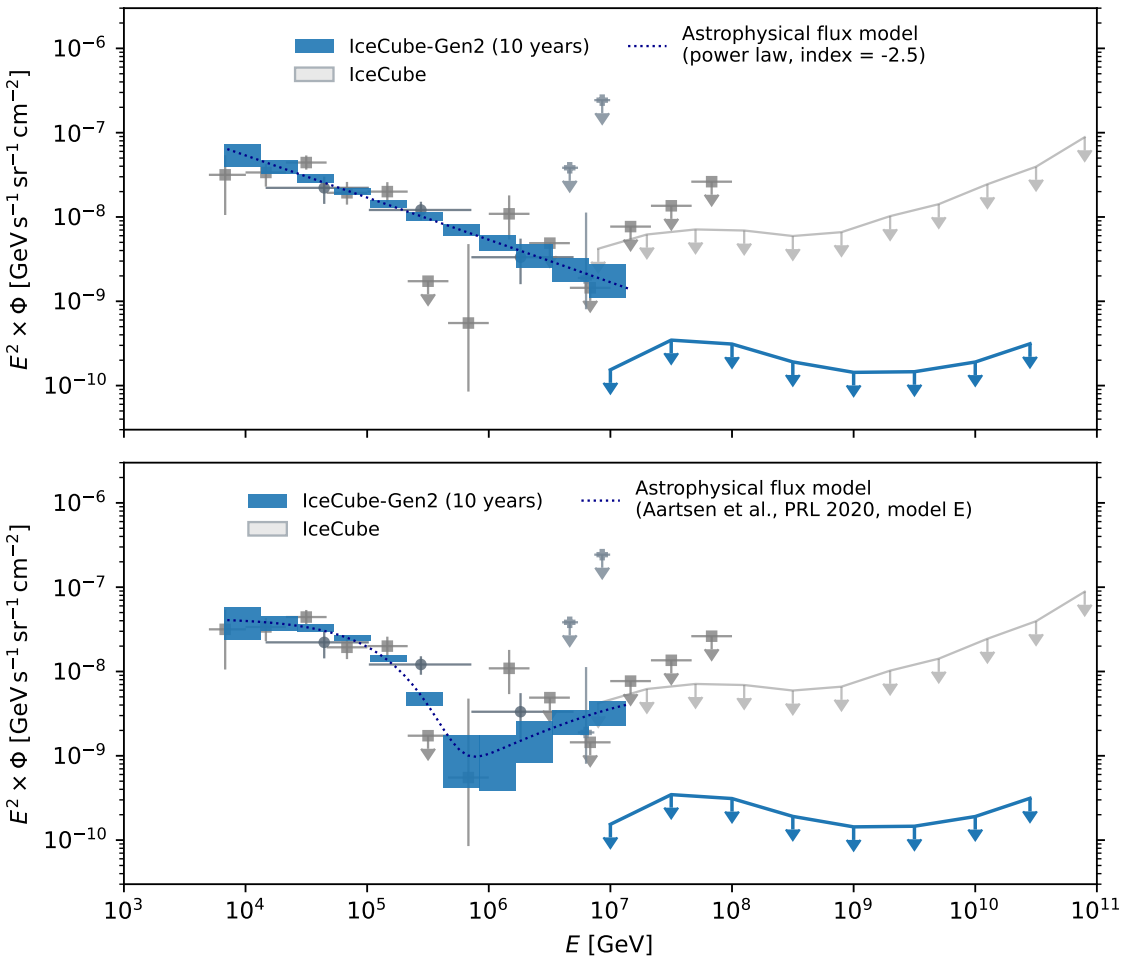

Figure 11.8: Projections of the sensitivity of IceCube-Gen2 [46], compared to predictions from published IceCube diffuse measurements using the cascades [76] and tracks [99] results. In addition, observations of extremely high energy (EHE) events [128] and a Glashow resonance event [39]. The upper panel assumes a uniform SPL flux, while the lower panel assumes an exponential cutoff near 100 TeV, along with a high energy contribution at tens of PeV from BLLac sources[98]. These hypotheses cannot be distinguished with IceCube's data samples, but will benefit from measurements with IceCube-Gen2 (here assuming a 10-year livetime).

Chapter 12

Conclusion

This work presents the development of an event selection to find neutrino events with contained vertices ("starting events") from 11.4 years of IceCube data. This sample was used to analyze the diffuse astrophysical neutrino spectrum from 1 TeV-10 PeV, using the NNMFit software package to perform a forward-folded binned likelihood analysis. The SnowStorm simulation method was used to account for the effect of detector systematic uncertainties on the flux measurement. A new technique was used to model the atmospheric neutrino self-veto effect, where neutrino events are rejected due to the presence of accompanying atmospheric muons from the same air shower, which cause the veto to reject the entire event. We use tables of atmospheric muon multiplicities and energies, derived from CORSIKA simulations of cosmic ray air showers, to inject muon bundles into neutrino signal events. As we know these neutrino signal events in isolation are not rejected, the response of the event selection when these are combined with muon bundles serves to measure the effect of the self-veto phenomena. These modeling techniques, along with improved veto strategies compared to older versions of MESE, are tailored to boost low energy sensitivity.

Previously published measurements of astrophysical neutrinos, using event samples

such as ESTES [57] and HESE [12], found that a single power law was sufficient to explain the spectral shape. The Cascades [76] measurement, while favoring a single power law, saw traces of spectral structure beyond the SPL at a level below the significance threshold for evidence. The spectral measurement presented in this thesis finds evidence of structure in the astrophysical neutrino spectrum, rejecting the null hypothesis of a single power law (SPL) by $> 4\ \sigma$ for the first time with IceCube data. In parallel, an analysis performed by IceCube collaborators at RWTH Aachen, DESY Zeuthen, and Stony Brook University, combining the Cascades and Northern Tracks samples, referred to as "CombinedFit", observed similar features in their spectral measurement, and also rejected the SPL by $> 4\ \sigma$. The results of these analyses will be published as a paired publication in the Physical Review Letters and Physical Review D journals.

Other features of the MESE diffuse measurement which invite further study with future samples include the presence of a dip at $\mathcal{O}(100$ TeV). We also find no contribution from the predicted prompt atmospheric flux to our measurement of the neutrino spectrum above 1 TeV, in line with previous measurements. In Ch.10, we go over our results in detail, along with their implications. The presence of the highest energy neutrino event measured by IceCube to date in the MESE sample motivates further searches for ultra high energy (>10 PeV) neutrinos, with IceCube-Gen2. In addition, numerous checks were performed to quantify the effects of various flux and model uncertainties on the measured results. These included the incorporation of a non-isotropic flux to model the effects of neutrinos from the Galactic Plane, which was shown not to have an effect on the measured flux parameters. The Daemon-Flux atmospheric model was also tested, to measure the effect of the atmospheric flux model on the measured astrophysical flux. Once again, the measured spectral parameters did not vary to a significant extent. The full details of the numerous

validation checks carried out are provided in sec. 8.

In summary, this thesis presents the development of a new event selection with contained vertices in 11.4 years of IceCube data, covering the largest energy range yet in IceCube, and an analysis to measure the diffuse astrophysical neutrino spectrum above 1 TeV using this sample. Updated veto strategies have been used to boost sensitivity to TeV neutrinos, and a new technique has been implemented to characterize the effect of the neutrino self-veto effect on the atmospheric neutrino spectrum in the Southern Sky. We find evidence for structure beyond the single power law, with a spectral hardening observed below 30 TeV.This result has significant implications in searches for neutrino sources, theorized to be pion-producing cosmic accelerators. As neutral pions produce gamma rays, the flux of diffuse neutrinos is expected to be compatible with Fermi's measurement of the GeV gamma-ray flux. Previous studies have shown that extrapolations of IceCube's previous SPL measurements were incompatible with Fermi's results [27, 100], which could be reconciled by the MESE measurement. This constrains population models for cosmic accelerators, particularly gamma-opaque sources, as a complement to gamma-ray surveys.

Appendix A

Simulation Datasets Used

Table A.1: ESTES NuGen MC Sample

	Neutrino Flavor	**Energy Range**	**Cross Section**	**Spectral Index**	**Bulk Ice Model**
21217**	NuMu	100 GeV - 100 PeV	CSMS	-1.5	Spice 3.2.1: scat=+0%, abs=+0%
21218**	NuE	100 GeV - 100 PeV	CSMS	-1.5	Spice 3.2.1: scat=+0%, abs=+0%
21219**	NuTau	100 GeV - 100 PeV	CSMS	-1.5	Spice 3.2.1: scat=+0%, abs=+0%

Table A.2: MuonGun MC Sample

did	**21319****	**21318****	**21317****	**21316****	**21315****
Energy Range	700 GeV - 1 TeV	1 TeV - 5 TeV	5 TeV - 10 TeV	10 TeV - 100 TeV	100 TeV - 1 EeV

Table A.3: SnowStorm Ensemble MC Sample

Dataset ID	**Flavor**	**Energy Range [GeV]**	**Spectrum**
22010	NuMu	$10^2 - 10^4$	-1.5
22011	NuMu	$10^4 - 10^6$	-1.5
22012	NuMu	$10^6 - 10^8$	-1.0
22013	NuE	$10^2 - 10^4$	-1.5
22014	NuE	$10^4 - 10^6$	-1.5
22015	NuE	$10^6 - 10^8$	-1.0
22016	NuTau	$10^2 - 10^4$	-1.5
22017	NuTau	$10^4 - 10^6$	-1.5
22018	NuTau	$10^6 - 10^8$	-1.0

Table A.4: SnowStorm Baseline MC Sample

Dataset ID	**Flavor**	**Energy Range [GeV]**	**Spectrum**
22042 & 22078	NuMu	$10^2 - 10^4$	-1.5
22043 & 22079	NuMu	$10^4 - 10^6$	-1.5
22044 & 22080	NuMu	$10^6 - 10^8$	-1.0
22045 & 22081	NuE	$10^2 - 10^4$	-1.5
22046 & 22082	NuE	$10^4 - 10^6$	-1.5
22047 & 22083	NuE	$10^6 - 10^8$	-1.0
22048 & 22084	NuTau	$10^2 - 10^4$	-1.5
22049 & 22085	NuTau	$10^4 - 10^6$	-1.5
22050 & 22086	NuTau	$10^6 - 10^8$	-1.0

Appendix B

Additional results for different astrophysical flux models

B.1 Broken Power Law

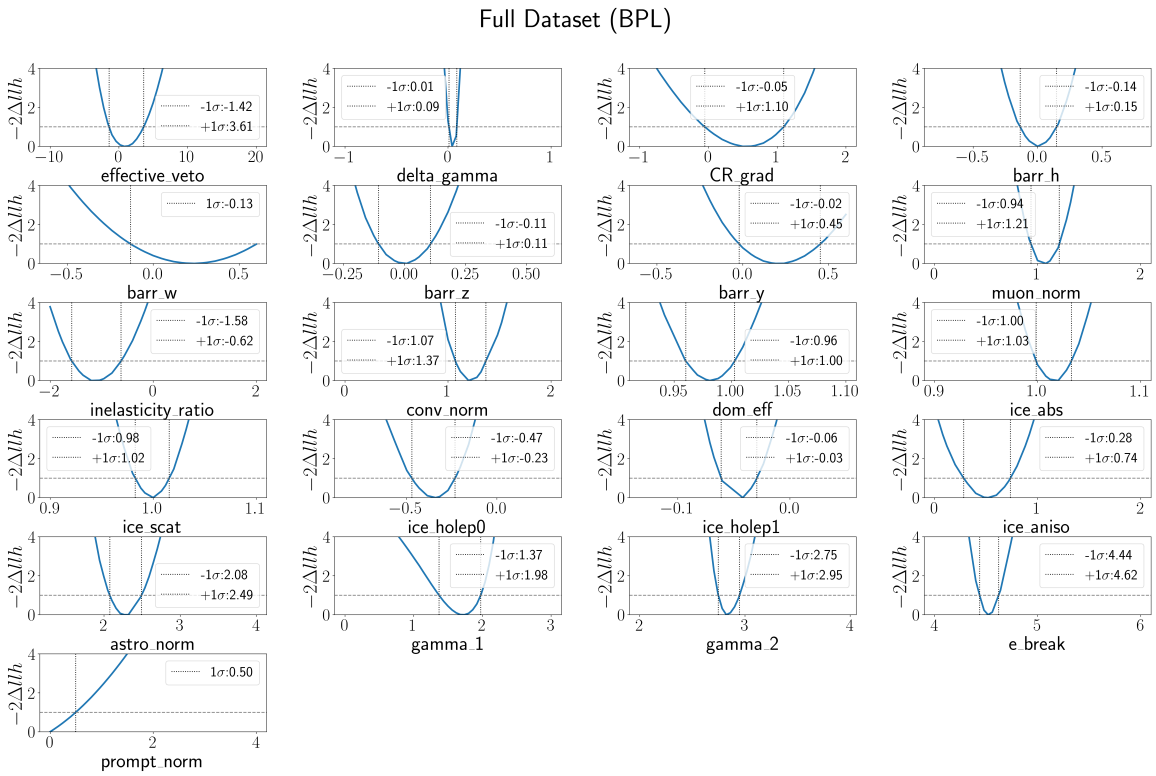

Figure B.1: Profile likelihood scans of the various fit parameters assuming the BPL best fit parameters. We observe that the best fit parameters are well within the nominal bounds, and no local minima exist in the likelihood space

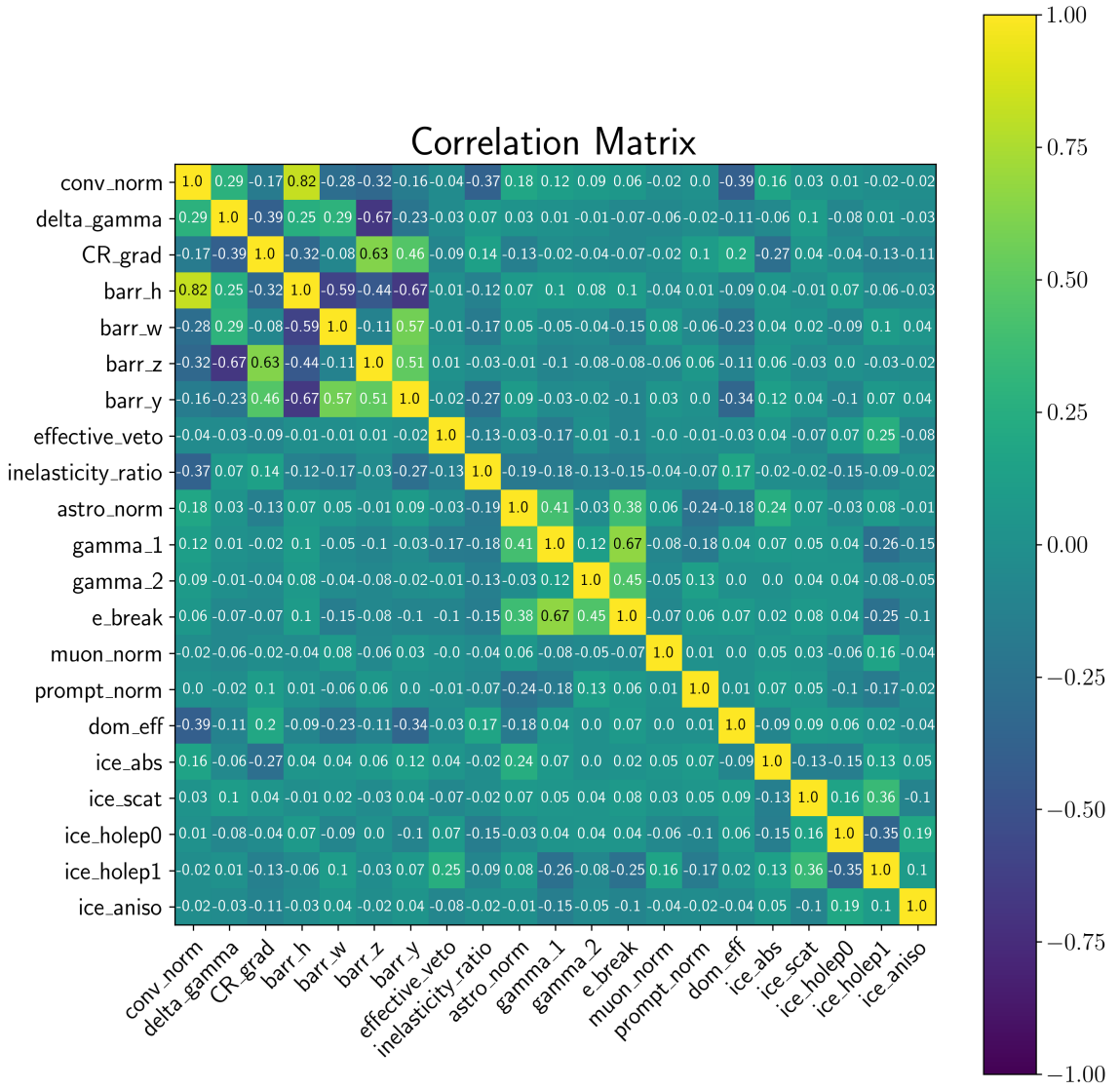

Figure B.2: Correlations between the various parameters used in the broken power law flux measurement, calculated using 1k pseudo-experiments

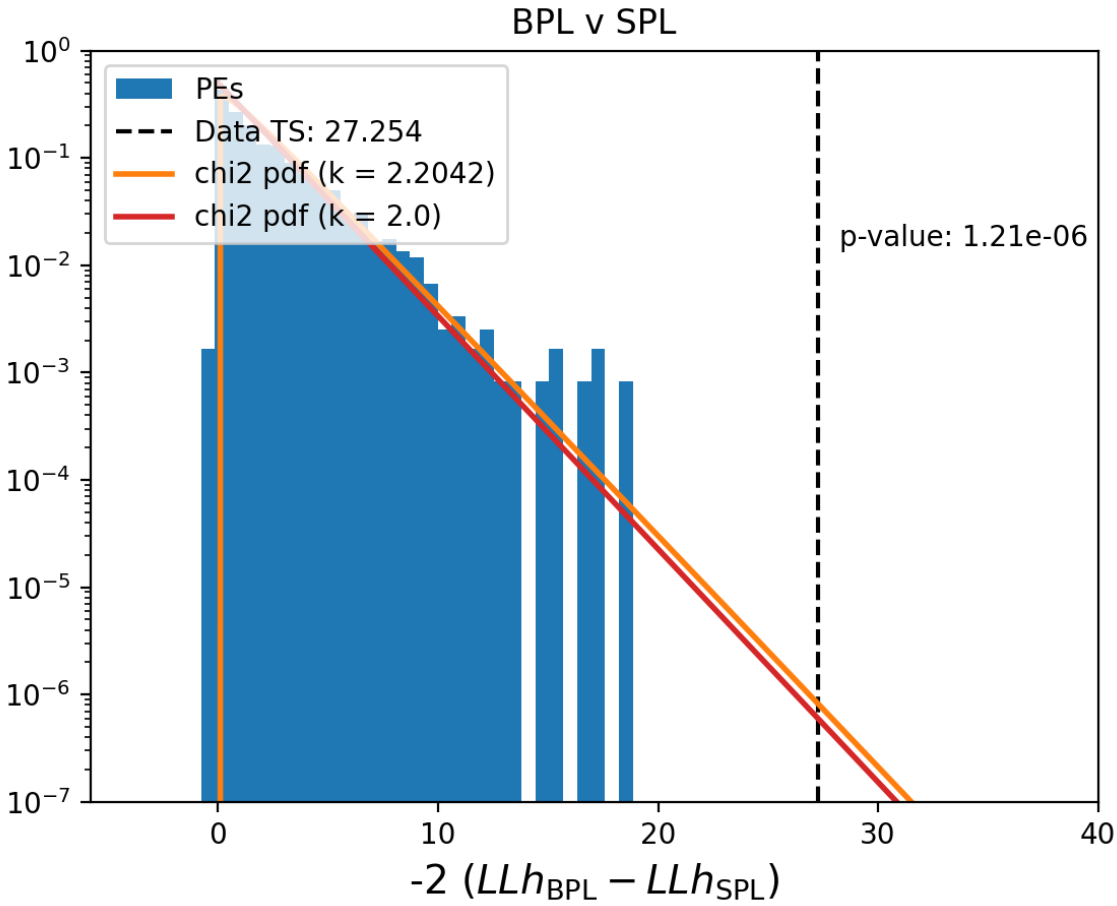

Figure B.3: The TS distribution for the BPL compared to the SPL flux model. As these are nested flux models, we assume Wilks' Theorem holds, and determine the significance assuming a χ^2 distribution

B.2 Log Parabola

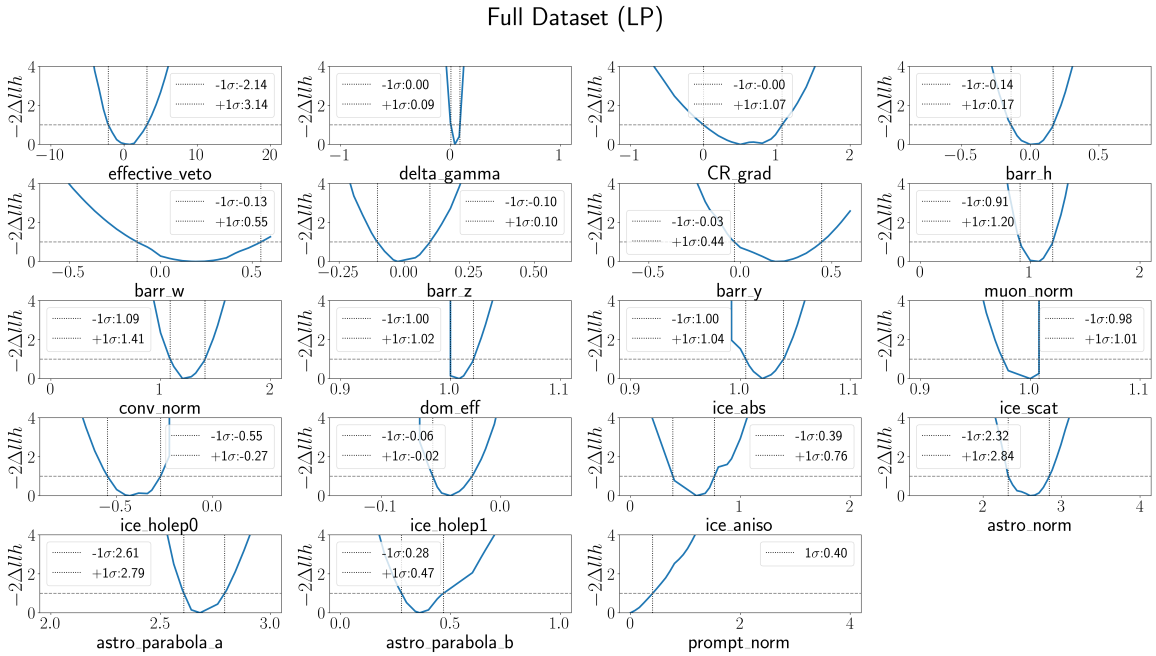

Figure B.4: Profile likelihood scans of the various fit parameters assuming the LP best fit parameters. We observe that the best fit parameters are well within the nominal bounds, and no local minima exist in the likelihood space

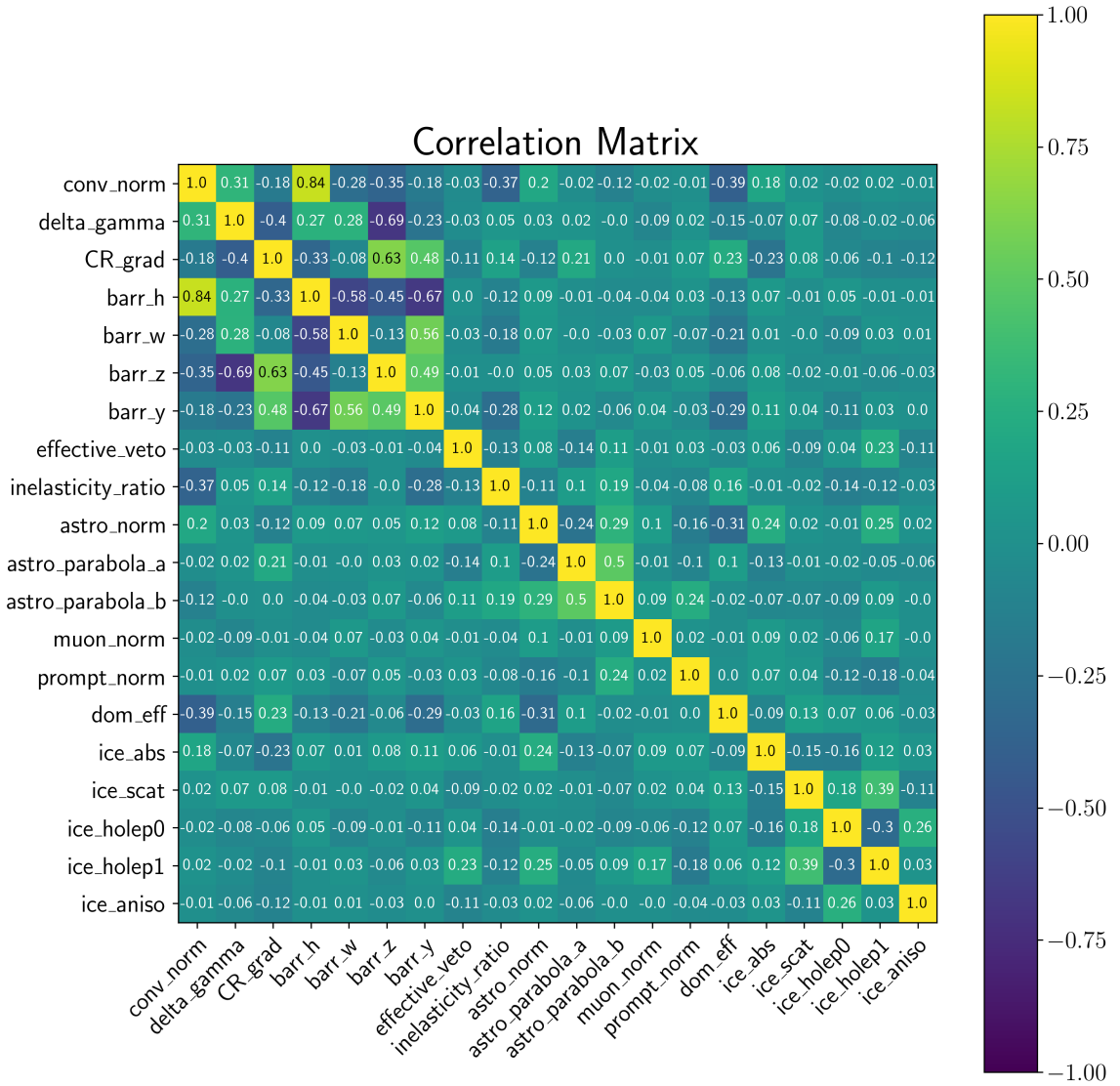

Figure B.5: Correlations between the various parameters used in the log parabola flux measurement, calculated using 1k pseudo-experiments

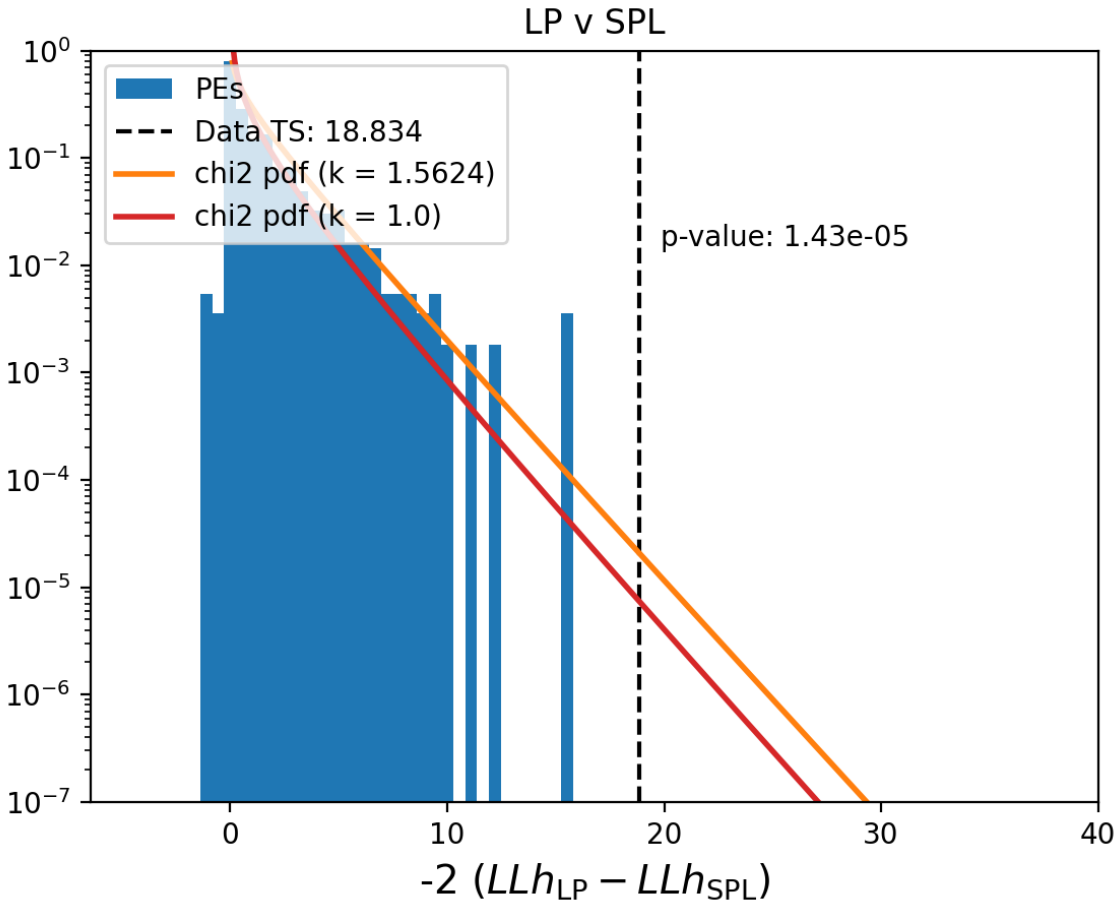

Figure B.6: The TS distribution for the LP compared to the SPL flux model. As these are nested flux models, we assume Wilks' Theorem holds, and determine the significance assuming a χ^2 distribution

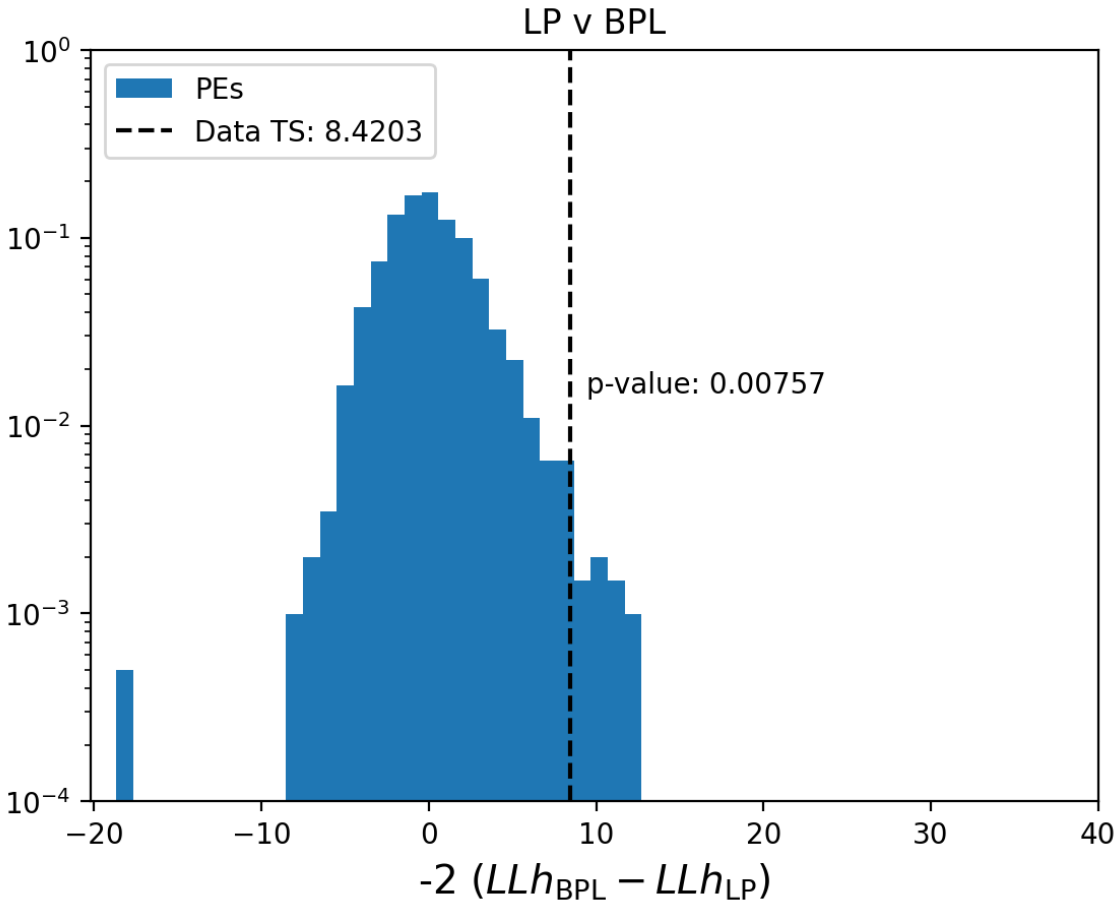

Figure B.7: The TS distribution for the BPL compared to the LP flux model. As these are not nested flux models, Wilks' Theorem does not hold, and we determine the significance directly by running pseudoexperiments

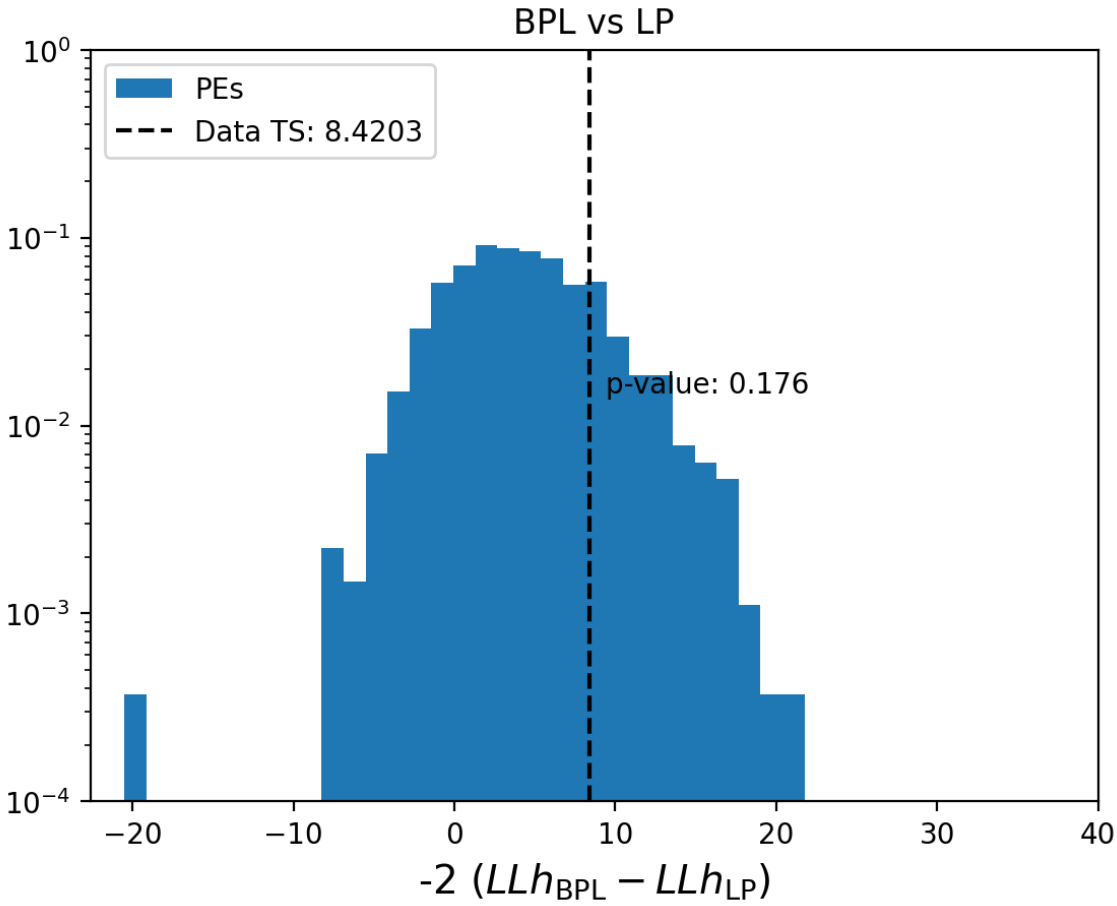

Figure B.8: The TS distribution for the LP compared to the BPL flux model. As these are not nested flux models, Wilks' Theorem does not hold, and we determine the significance directly by running pseudoexperiments

B.3 Single Power Law with Gaussian Bump

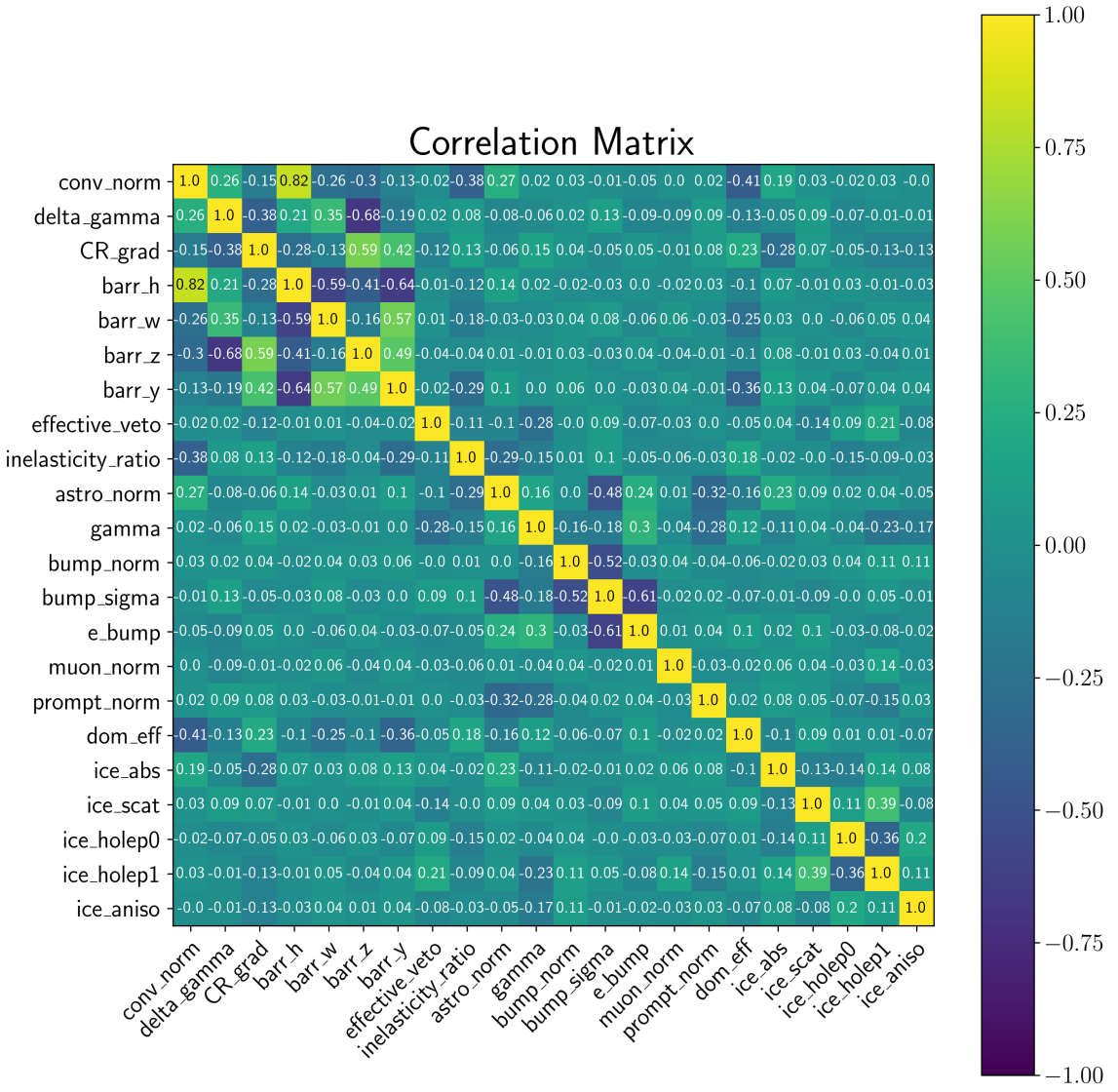

Figure B.9: Correlations between the various parameters used in the SPL + bump flux measurement, calculated using 1k pseudo-experiments

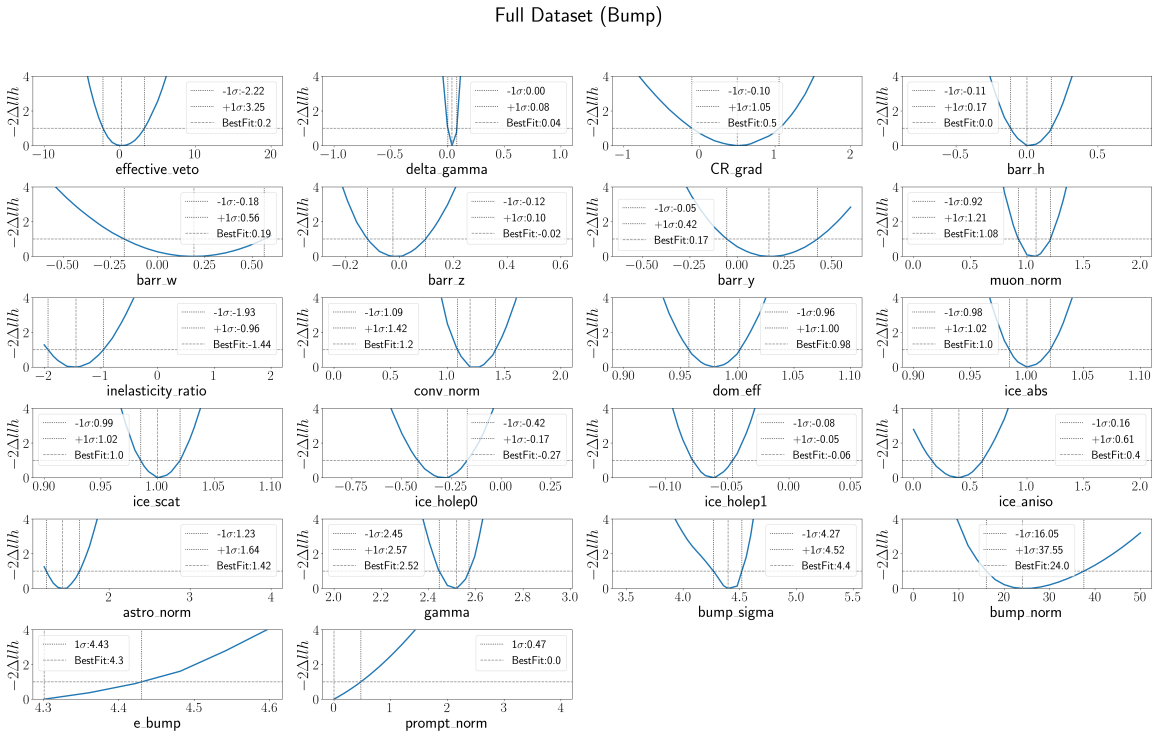

Figure B.10: Profile likelihood scans of the various fit parameters assuming the Bump best fit parameters. We observe that the best fit parameters are well within the nominal bounds, and no local minima exist in the likelihood space

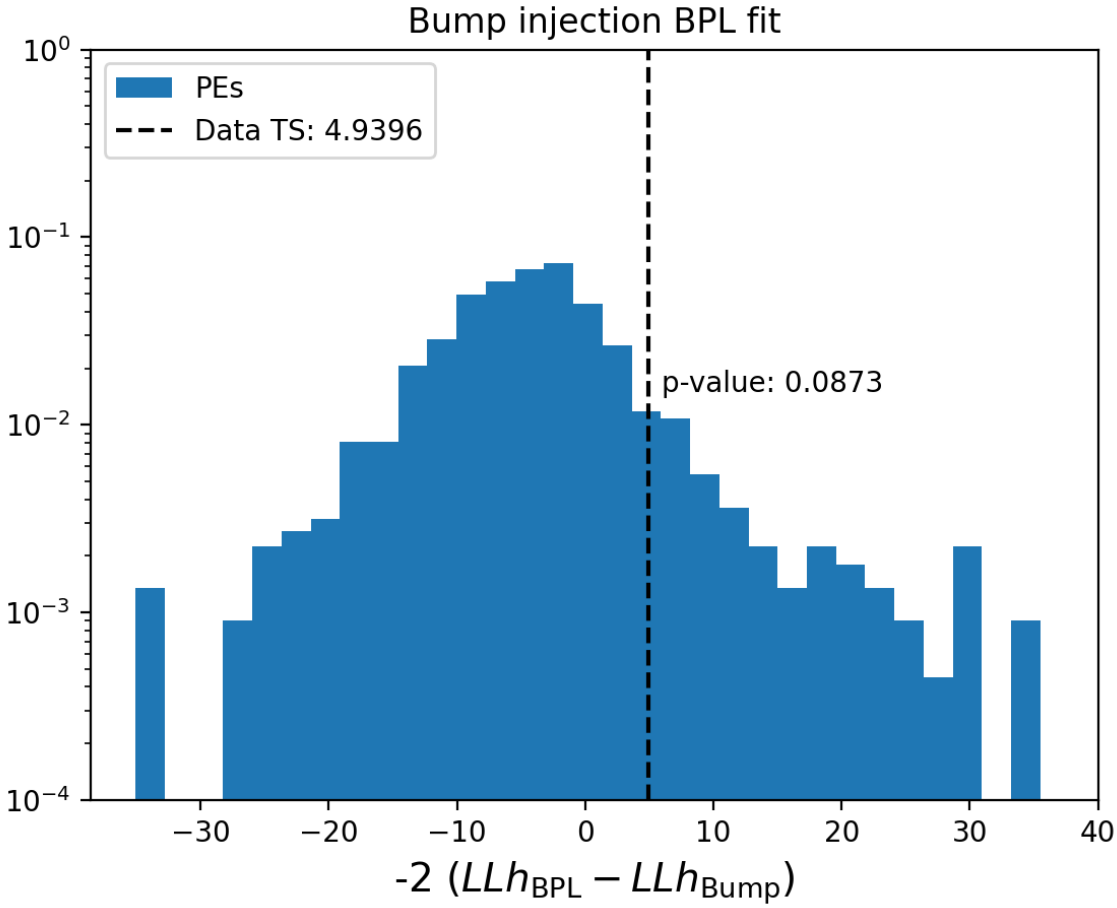

Figure B.11: The TS distribution for the SPL + Bump compared to the BPL flux model. As these are not nested flux models, Wilks' Theorem does not hold, and we determine the significance directly by running pseudoexperiments

B.4 Single Power Law with exponential Cutoff

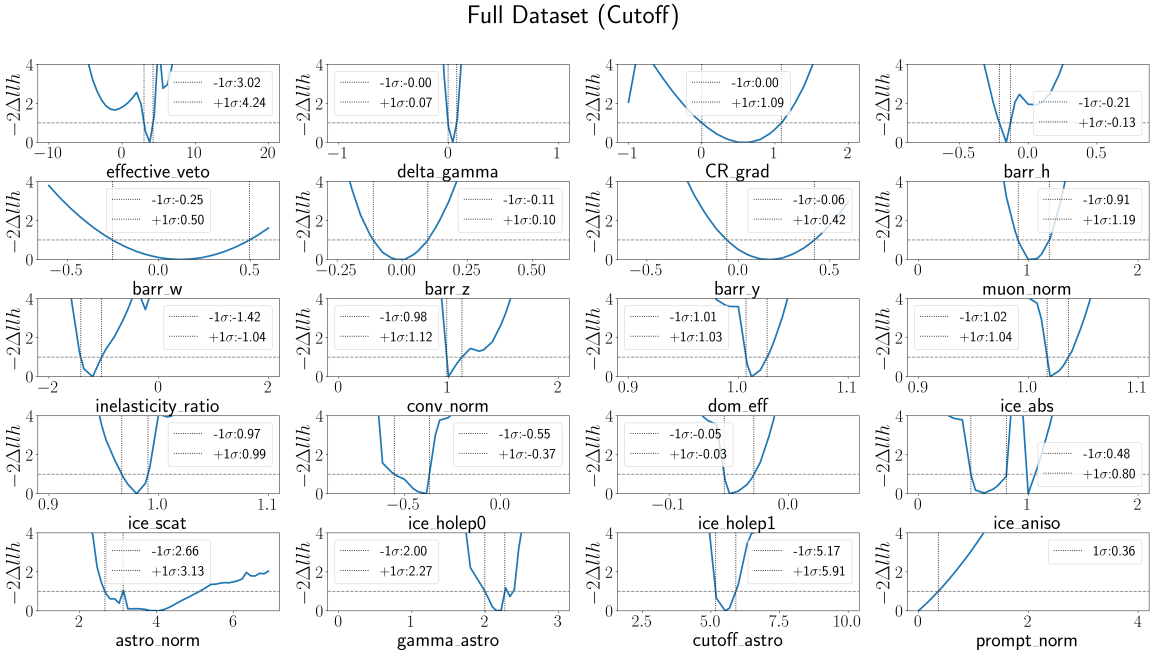

Figure B.12: Profile likelihood scans of the various fit parameters assuming the SPL + exponential cutoff best fit parameters. We observe that the best fit parameters are well within the nominal bounds, and no local minima exist in the likelihood space

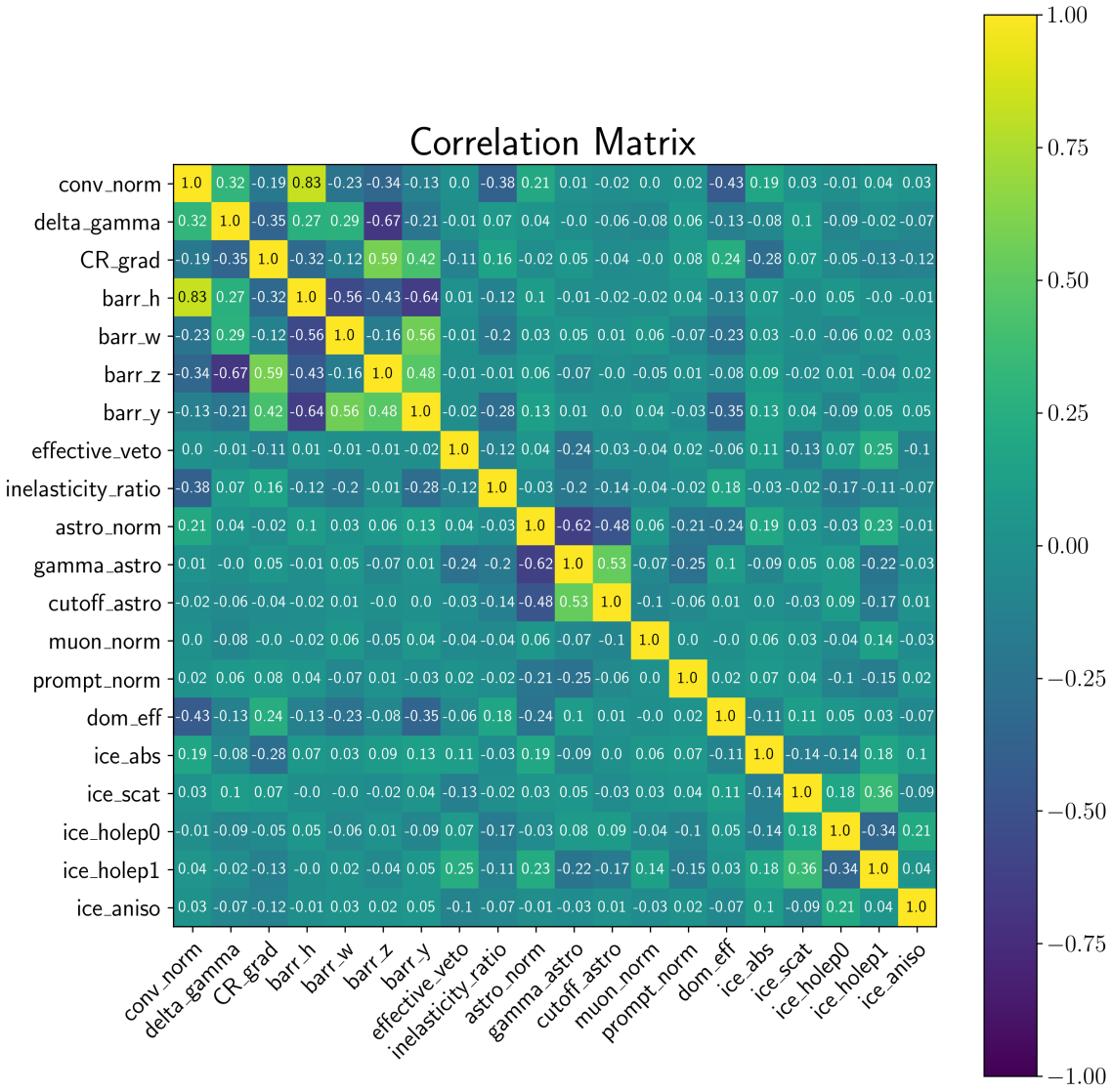

Figure B.13: Correlations between the various parameters used in the SPL + exponential cutoff flux measurement, calculated using 1k pseudo-experiments

B.5 Single Power Law with neutrinos from Active Galactic Nuclei cores

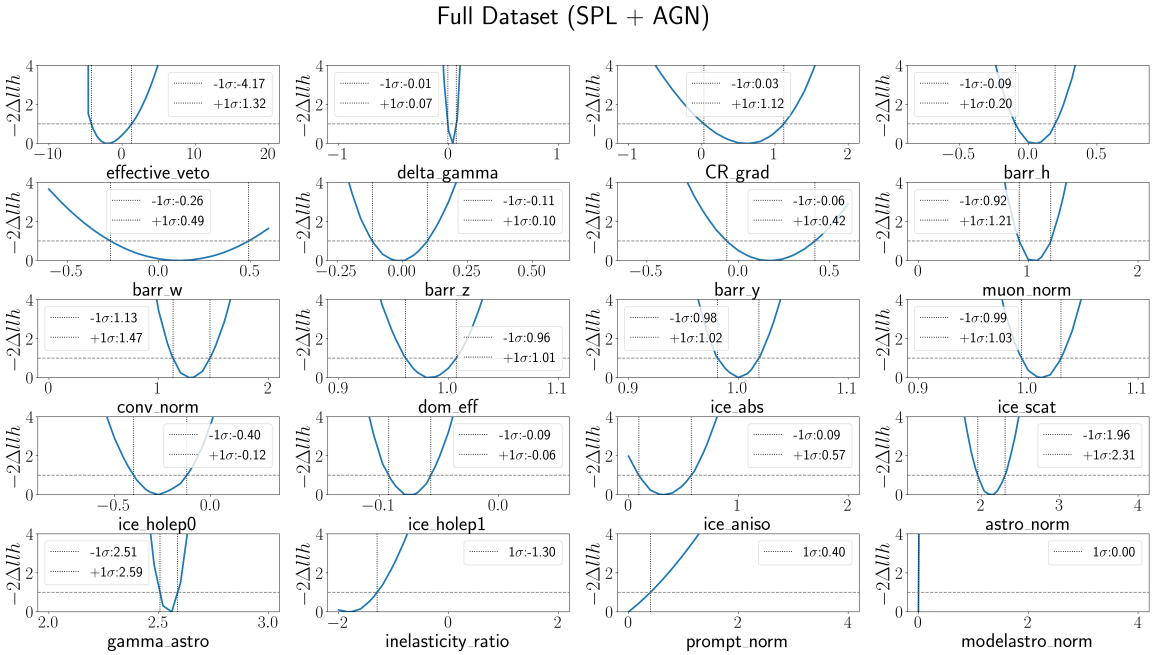

Figure B.14: Profile likelihood scans of the various fit parameters assuming the SPL + AGN core emission best fit parameters. We observe that the best fit parameters are well within the nominal bounds, and no local minima exist in the likelihood space

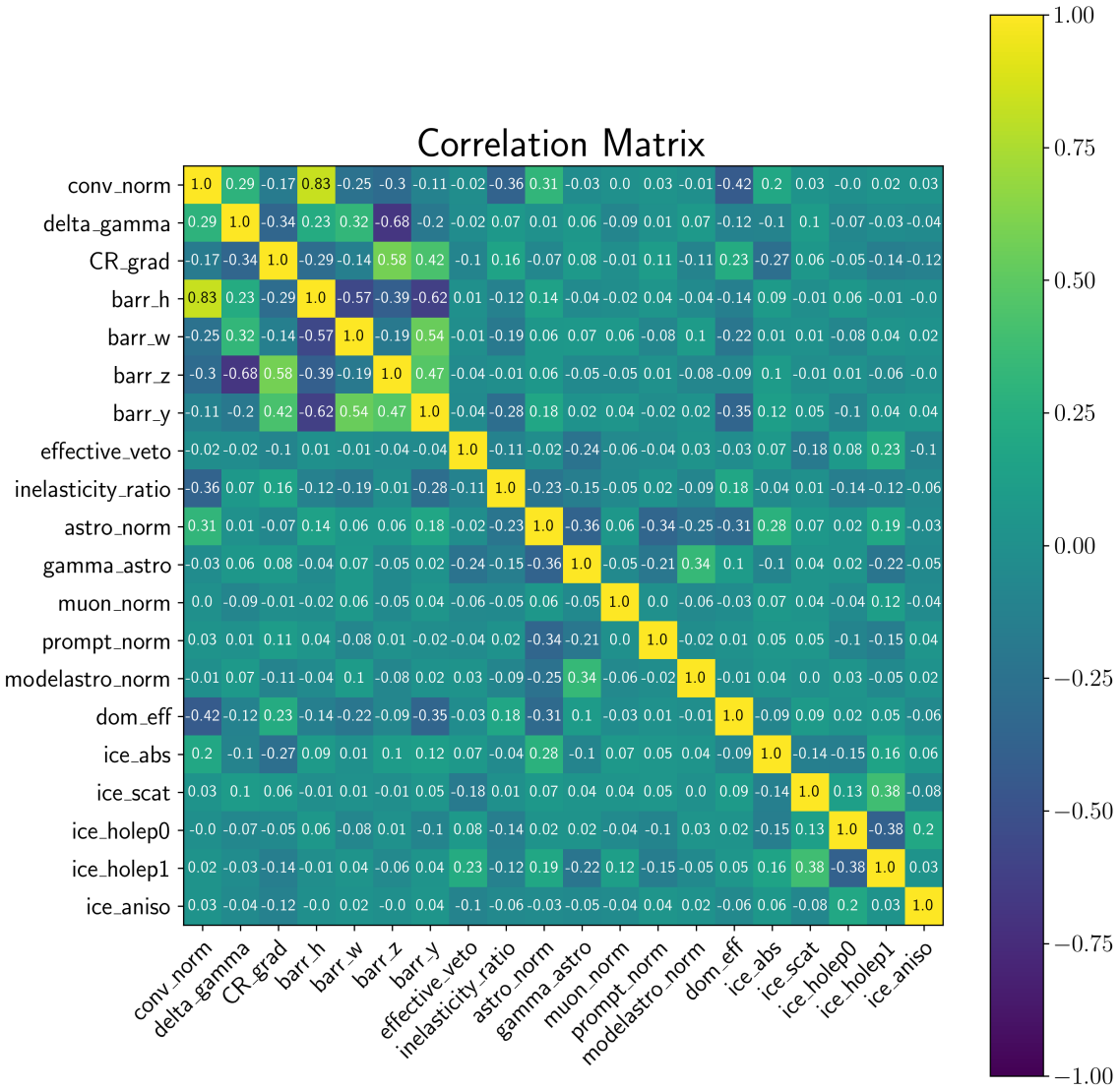

Figure B.15: Correlations between the various parameters used in the SPL + AGN core emission flux measurement, calculated using 1 k pseudo-experiments

B.6 Single Power Law with neutrinos from BL Lacertae objects

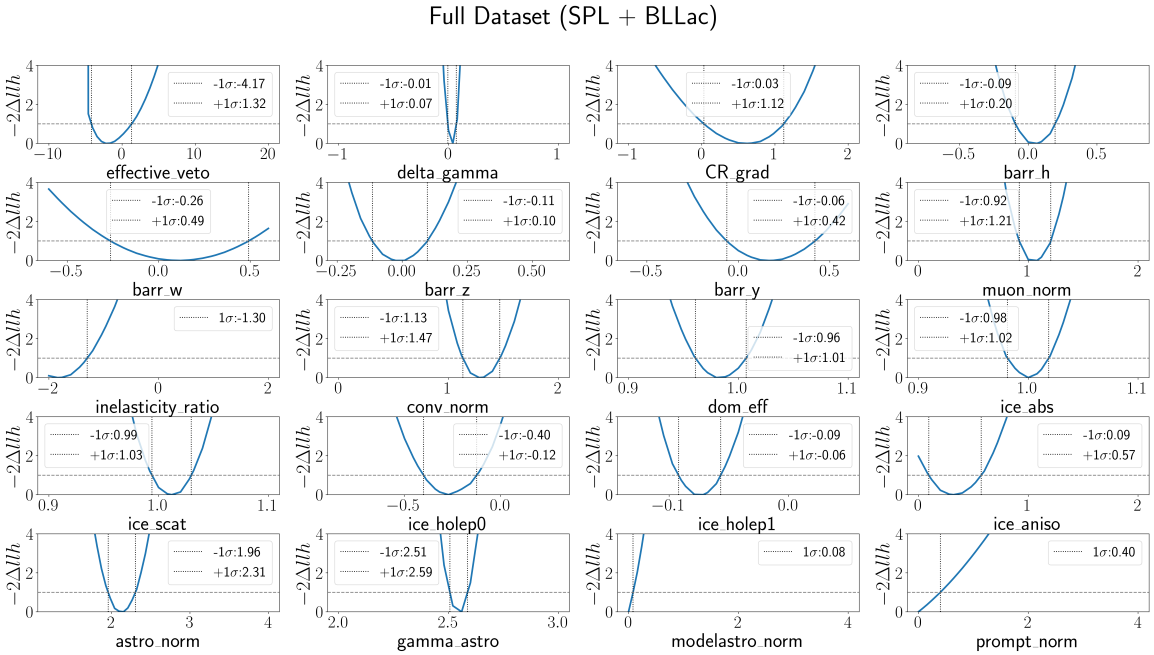

Figure B.16: Profile likelihood scans of the various fit parameters assuming the SPL + BLLac emission best fit parameters. We observe that the best fit parameters are well within the nominal bounds, and no local minima exist in the likelihood space

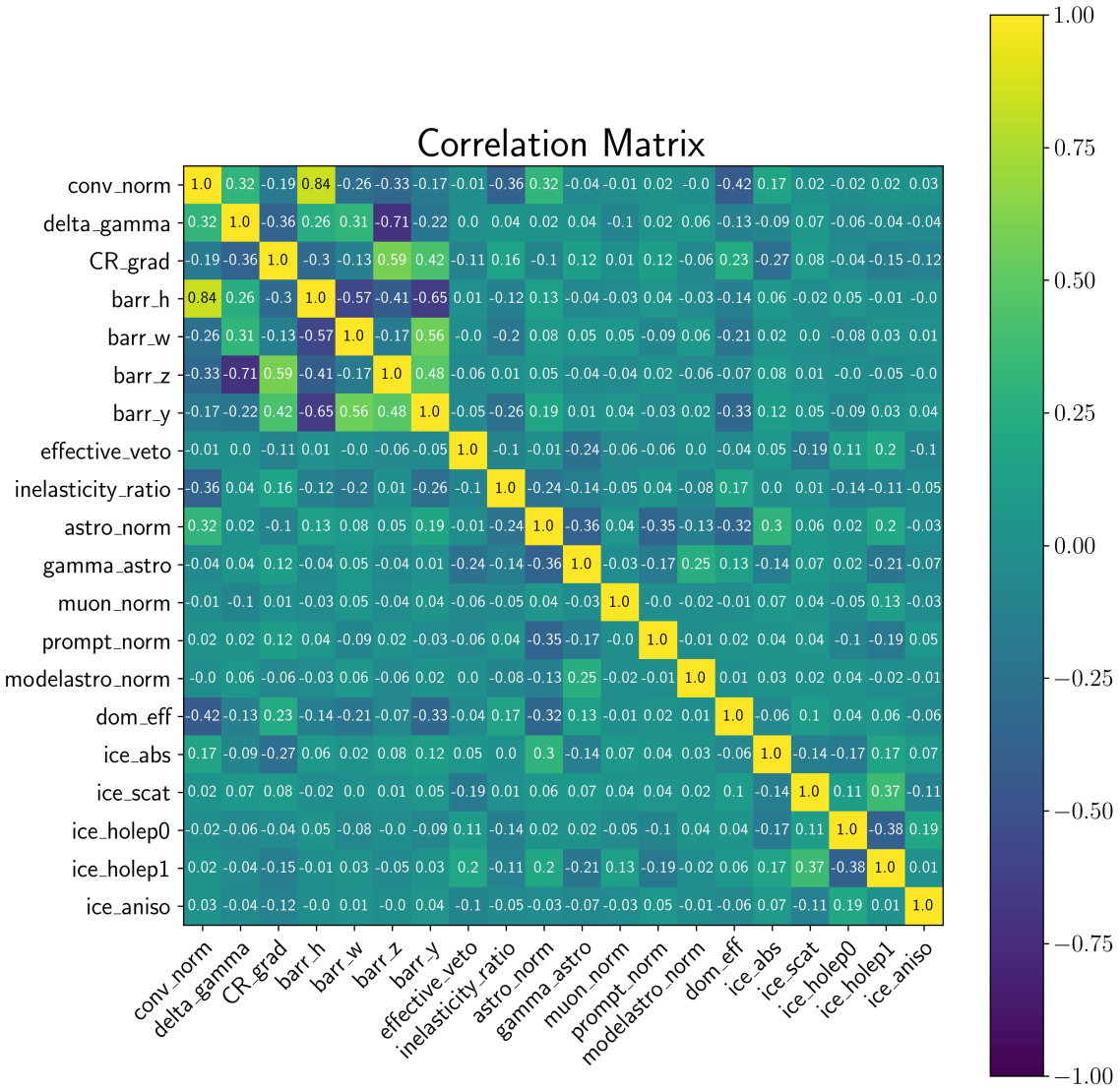

Figure B.17: Correlations between the various parameters used in the SPL + BLLac emission flux measurement, calculated using 1 k pseudo-experiments

Appendix C

Results from fits with dataset subsamples

Table C.1: Results for the fits with dataset splits in the MESE analysis. The uncertainties are derived from 1D profile likelihood scans, assuming Wilks' theorem applies. The per-flavour flux normalization is measured in units of $C = 10^{-18}/\mathrm{GeV}/\mathrm{cm}^2/\mathrm{s}/\mathrm{sr}$. All flux normalizations are at 100 TeV.

		Full Data	Deep (below dust band)	Shallow (above dust band)	Upgoing	Downgoing	Early (2011-June 2017)	Late (June 2017-2022)	Summer	Winter
SPL	$\phi^{\nu+\bar{\nu}}/C$	$2.13^{+0.18}_{-0.17}$	$2.18^{+0.25}_{-0.28}$	$1.78^{+0.23}_{-0.19}$	$2.06^{+0.51}_{-0.81}$	$2.12^{+0.20}_{-0.26}$	$2.22^{+0.25}_{-0.23}$	$1.89^{+0.23}_{-0.22}$	$2.09^{+0.29}_{-0.19}$	$2.08^{+0.27}_{-0.18}$
	γ	$2.55^{+0.04}_{-0.04}$	$2.50^{+0.05}_{-0.08}$	$2.59^{+0.07}_{-0.03}$	$2.46^{+0.07}_{-0.18}$	$2.65^{+0.08}_{-0.05}$	$2.55^{+0.03}_{-0.07}$	$2.54^{+0.08}_{-0.04}$	$2.52^{+0.06}_{-0.05}$	$2.52^{+0.07}_{-0.04}$
SPE	$\phi^{\nu+\bar{\nu}}/C$	$3.975^{+1.14}_{-1.32}$	$9.31^{+5.91}_{-1.60}$	$5.88^{+0.88}_{-2.18}$	$2.23^{+0.31}_{-1.01}$	$2.57^{+0.38}_{-0.34}$	$2.86^{+0.51}_{-0.39}$	$7.12^{+5.91}_{-1.48}$	$7.63^{+1.28}_{-2.34}$	$3.33^{+1.09}_{-1.38}$
	γ	$2.16^{+0.23}_{-0.16}$	$1.73^{+0.22}_{-0.18}$	$1.94^{+0.18}_{-0.22}$	$2.44^{+0.14}_{-0.32}$	$2.52^{+0.09}_{-0.12}$	$2.51^{+0.09}_{-0.10}$	$1.84^{+0.21}_{-0.05}$	$1.76^{+0.09}_{-0.13}$	$2.28^{+0.09}_{-0.13}$
	$\log_{10}(\frac{\mathrm{E_{cutoff}}}{\mathrm{GeV}})$	$5.40^{+0.51}_{-0.23}$	$5.00^{+0.07}_{-0.33}$	$5^{+0.36}_{-0.27}$	$10^{+4.73}_{-4.87}$	$6.0^{+0.55}_{-0.19}$	$6^{+0.41}_{-0.14}$	$5^{+0.30}_{-0.09}$	$5.0^{+0.22}_{-0.27}$	$5.68^{+0.22}_{-0.27}$
BPL	$\phi^{\nu+\bar{\nu}}/C$	$2.28^{+0.22}_{-0.20}$	$4.12^{+1.04}_{-0.34}$	$1.71^{+0.26}_{-0.30}$	$2.26^{+0.35}_{-0.62}$	$2.33^{+0.33}_{-0.34}$	$2.38^{+0.26}_{-0.33}$	$1.98^{+0.35}_{-0.33}$	$2.25^{+0.28}_{-0.29}$	$2.21^{+0.30}_{-0.26}$
	γ_1	$1.72^{+0.26}_{-0.35}$	$2.07^{+0.17}_{-0.14}$	$1.59^{+0.6}_{-0.41}$	$1.81^{+0.8}_{-0.36}$	$1.99^{+0.29}_{-0.44}$	$1.72^{+0.37}_{-0.64}$	$1.69^{+0.31}_{-0.45}$	$1.22^{+0.55}_{-0.98}$	$1.98^{+0.23}_{-1.98}$
	γ_2	$2.84^{+0.11}_{-0.09}$	$3.94^{+2.96}_{-0.35}$	$3.09^{+0.27}_{-0.08}$	$2.66^{+0.10}_{-0.21}$	$2.98^{+1.96}_{-0.12}$	$2.8^{+0.11}_{-0.14}$	$3.14^{+0.73}_{-0.17}$	$2.88^{+1.88}_{-0.1}$	$2.79^{+0.13}_{-0.18}$
	$\log_{10}(\frac{\mathrm{E_{break}}}{\mathrm{GeV}})$	$4.52^{+0.11}_{-0.09}$	$5.07^{+0.12}_{-0.15}$	$4.53^{+0.12}_{-0.16}$	$4.39^{+0.14}_{-0.13}$	$4.65^{+0.18}_{-0.1}$	$4.48^{+0.16}_{-0.16}$	$4.61^{+0.14}_{-0.15}$	$4.47^{+0.11}_{-0.09}$	$4.54^{+0.19}_{-0.52}$
LP	$\phi^{\nu+\bar{\nu}}/C$	$2.58^{+0.26}_{-0.26}$	$2.90^{+0.46}_{-0.37}$	$2.02^{+0.30}_{-0.21}$	$2.44^{+0.39}_{-0.37}$	$2.48^{+0.30}_{-0.29}$	$2.68^{+0.35}_{-0.31}$	$2.34^{+0.36}_{-0.28}$	$2.66^{+0.36}_{-0.32}$	$2.43^{+0.31}_{-0.29}$
	α_{LP}	$2.67^{+0.13}_{-0.06}$	$2.91^{+0.12}_{-0.21}$	$3.0^{+0.15}_{-0.28}$	$2.80^{+0.17}_{-0.51}$	$2.70^{+0.07}_{-0.08}$	$2.66^{+0.06}_{-0.15}$	$3.00^{+0.38}_{-0.13}$	$2.63^{+0.30}_{-0.04}$	$2.70^{+0.13}_{-0.13}$
	β_{LP}	$0.36^{+0.10}_{-0.08}$	$0.82^{+0.26}_{-0.20}$	$0.69^{+0.27}_{-0.19}$	$0.50^{+0.29}_{-0.47}$	$0.31^{+0.15}_{-0.13}$	$0.31^{+0.09}_{-0.09}$	$0.78^{+0.16}_{-0.22}$	$0.38^{+0.33}_{-0.20}$	$0.35^{+0.20}_{-0.15}$
SPL + Bump	$\phi^{\nu+\bar{\nu}}/C$	$1.42^{+0.21}_{-0.20}$	$1.34^{+0.37}_{-0.38}$	$1.00^{+0.34}_{-0.18}$	$1.67^{+0.47}_{-0.87}$	$1.48^{+0.24}_{-0.26}$	$1.58^{+0.31}_{-0.23}$	$1.09^{+0.20}_{-0.23}$	$1.28^{+0.30}_{-0.29}$	$1.51^{+0.31}_{-0.25}$
	γ	$2.51^{+0.05}_{-0.07}$	$2.58^{+0.10}_{-0.07}$	$2.55^{+0.12}_{-0.07}$	$2.42^{+0.08}_{-0.24}$	$2.65^{+0.08}_{-0.09}$	$2.52^{+0.07}_{-0.09}$	$2.55^{+0.08}_{-0.11}$	$2.48^{+0.02}_{-0.06}$	$2.53^{+0.09}_{-0.08}$
	$\log_{10}(\frac{\mathrm{E_{bump}}}{\mathrm{GeV}})$	$4.30^{+1.3}$	$4.60^{+0.04}_{-0.04}$	$4.45^{+0.11}_{-0.08}$	$4.30^{+0.50}$	$4.33^{+0.37}$	$4.30^{+0.1}_{-0.12}$	$4.48^{+0.10}_{-0.12}$	$4.30^{+0.05}$	$4.30^{+0.2}$
	$\log_{10}(\frac{\sigma_{\mathrm{bump}}}{\mathrm{GeV}})$	$4.42^{+0.12}_{-0.13}$	$4.48^{+0.02}_{-0.06}$	$4.37^{+0.09}_{-0.26}$	$4.14^{+1.11}_{-0.27}$	$4.48^{+0.07}_{-0.23}$	$4.35^{+0.13}_{-0.32}$	$4.46^{+0.04}_{-0.16}$	$4.37^{+0.27}_{-0.19}$	$4.47^{+0.08}_{-0.26}$
	ϕ^{bump}/C	$24.44^{+13.55}_{-7.95}$	$28.0^{+17.84}_{-14.79}$	$34^{+11.64}_{-14.34}$	$42.77^{+29.49}_{-22.14}$	$17.11^{+13.16}_{-5.03}$	$28.72^{+9.88}_{-19.95}$	$24.33^{+16.78}_{-11.19}$	$34.55^{+20.34}_{-13.61}$	$16.82^{+14.23}_{-9.51}$

Appendix D

Instrumentation Development

The development of new instrumentation, both to increase sensitivity to PeV-scale neutrino events and to improve directional reconstruction resolution, requires a departure from the concept behind the currently operational IceCube DOMs. In place of a single large photomultiplier tube (PMT), newer designs have converged towards multiple smaller PMTs for a segmented design.

D.1 Mechanical Structure

My work on the LOM began with CAD modelling of the internal layout, and devising a way to place multiple PMTs inside a glass vessel while minimizing the diameter. The earliest iterations of the LOM, an inline design, used a narrow cylindrical pressure vessel, with a single PMT in each layer pointing in different directions, to cover 2π in azimuth. Multiple PMT diameters were also tested, from the existing 3" designs used in the mDOM to larger PMTs which would need to be custom made. This design was later abandoned due to concerns about the economical manufacture of the pressure vessel, along with the implementation of the electronics in the confined spaces. It

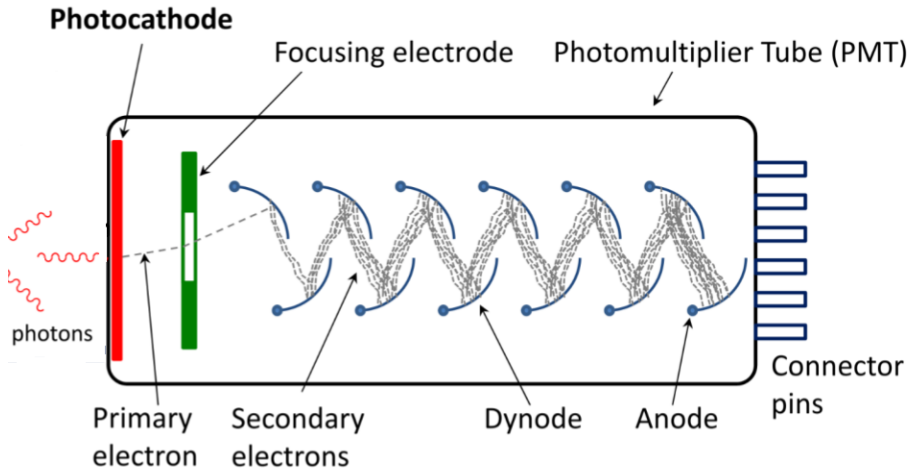

Figure D.1: A schematic of a photomultiplier tube [129], illustrating the amplification of the electron signal at each dynode stage

was also noted that such a narrow design, under 20 cm diameter, was unnecessary as there would be limited economic benefit to designing a correspondingly narrow drill. The design then pivoted to a wider pressure vessel, using the DEgg as a modelling tool, and using multiple 4" PMTs to optimize getting a large geometric photocathode area while still fitting into the vessel. A benefit of using larger PMTs is a reduced number of data acquisition channels for a given photocathode area, which reduces the power consumption of the module. The design later evolved to using a bespoke pressure vessel, with two parallel designs being developed. These used 16 and 18 4" PMTs respectively, with the extra pair of PMTs being aligned along the module axis.

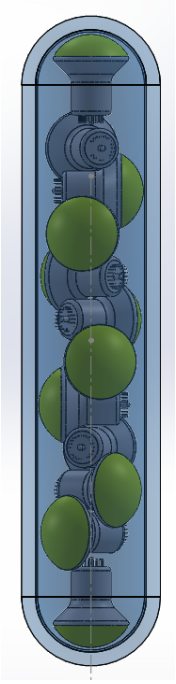

Figure D.2: The inline design with 4” PMTs.

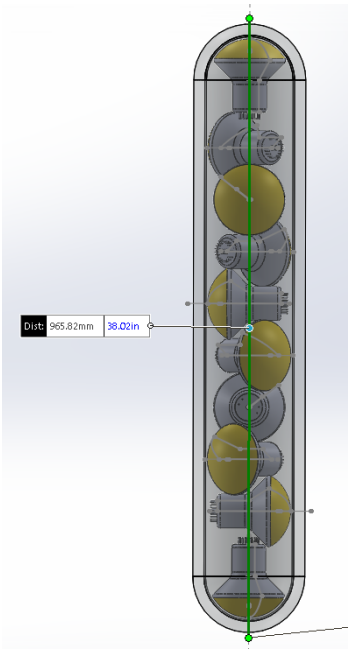

Figure D.3: The inline design with 4.5” PMTs.

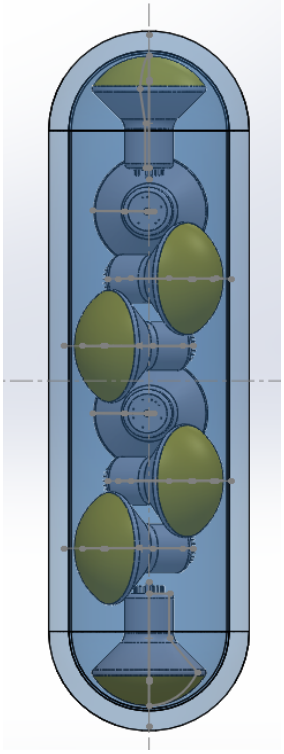

Figure D.4: The inline design with 5” PMTs.

D.1.1 Gel Pads

As the Cherenkov photons enter the LOM from the surrounding bulk ice, they must travel through the glass pressure vessel to the PMT photocathodes. If there is a layer of air between the PMT face and the pressure vessel, a large fraction of these photons will be totally internally reflected back into the ice at the interface between the vessel wall and the air in the interior. The PMTs therefore need to be optically coupled to the glass with an optically dense medium to minimize reflective losses. This medium is usually a silicone gel, which is transparent and cures when mixing a resin and hardener component. In prior IceCube optical modules, the silicone was poured around the PMTs to cover the entire photocathode. As the LOM consists of PMTs pointing in multiple directions, this approach would be very expensive, while

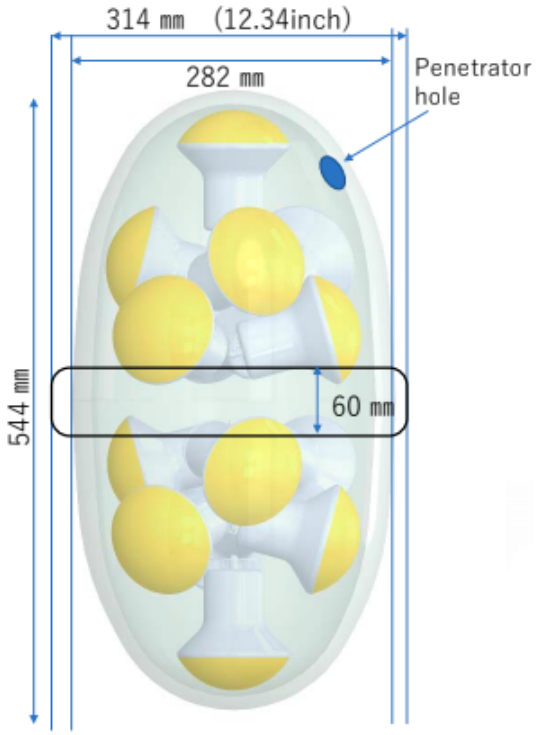

Figure D.5: A design using the DEgg pressure vessel, containing 14 4" PMTs for 4π angular coverage.

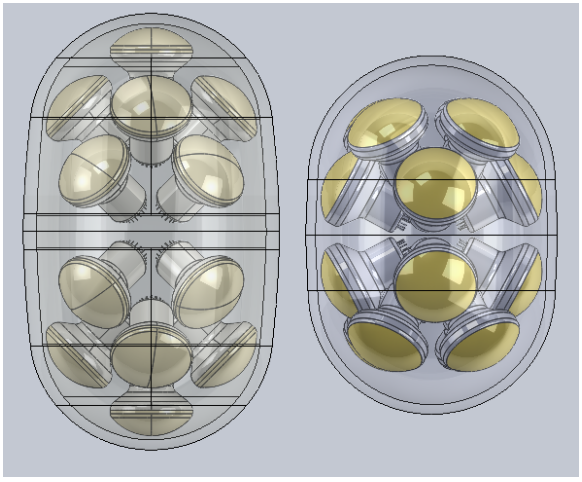

Figure D.6: The two LOM designs.

also increasing the weight of each module with the vast quantity of gel required. An alternative approach was thus taken, to mould gel onto the PMT photocathode as conical 'pads', which are then coupled to the vessel. In addition to being far more

economical, due to the reduced quantity of gel required, this approach also improves the photon capture efficiency due to the gel pad walls acting to collimate photons into the PMT via total internal reflection.

Initial attempts at casting these gel pads studied moulding these onto the PMT while the PMT was mounted in its final orientation within the LOM, using 3D printed 'shells' to be filled with liquid gel in-situ. Another attempt was to smear a layer of liquid gel onto the face of a gel pad and then press it against the pressure vessel to cure, which would bond the pad to the glass. Numerous practical difficulties led to the

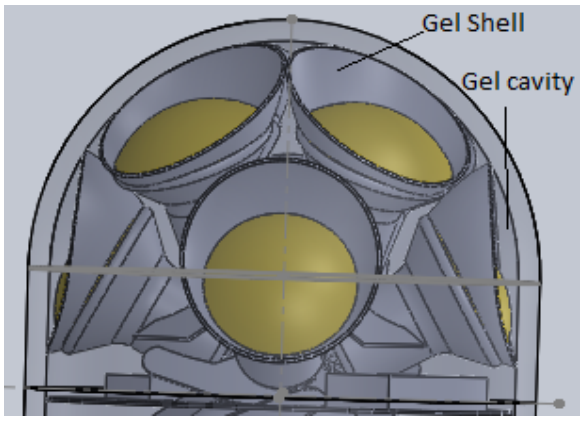

Figure D.7: Plastic gel 'shells' to be filled with liquid gel in-situ.

Figure D.8: A gel pad coupled to a PMT

abandonment of these methods, such as the lack of a suitable cold-resistant material for the shells, and the leakage of liquid gel at the pad-vessel interface when the pads were pressed against the vessel. These problems were solved by using a cavity seal approach. This involves creating an empty cavity between the pad and the pressure vessel, which is then filled with gel. The advantage of this approach is that it can conform to almost any surface as long as the cavity rim is properly sealed to the vessel, to prevent leakage of liquid gel. This necessitates the development of multiple gel pad moulds, for PMTs closer to the equator compared to PMTs closer to the poles of the pressure vessel, where the geometry changes. A slight complication of this method

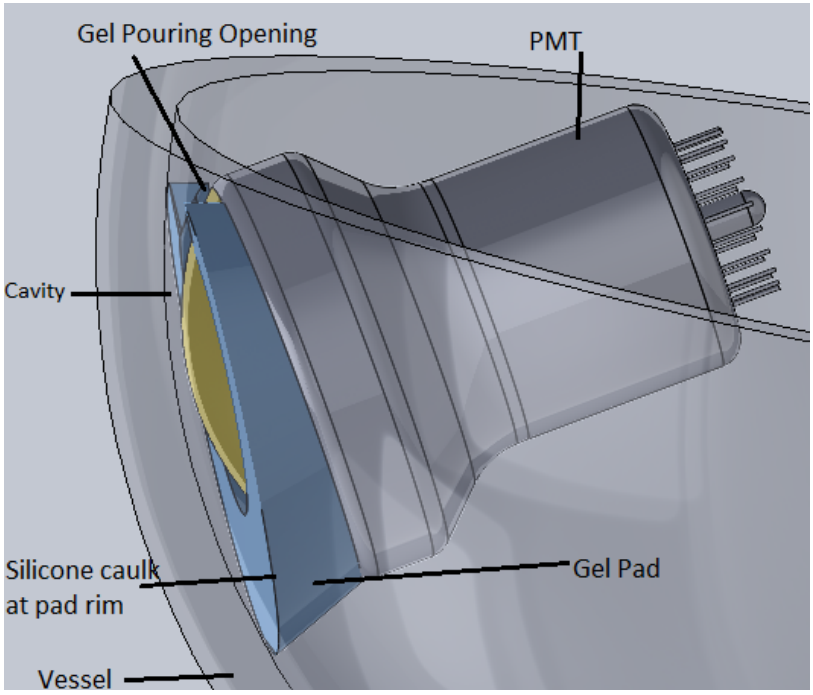

Figure D.9: A cavity is created between the pressure vessel and the gel pad, which is sealed around the rims.

is that the silicone gel poured into the cavity must be degassed in a vacuum after pouring, to remove bubbles entrained during mixing the gel and during the pouring process. As the Shin-Etsu OSN-3547 gel used spontaneously evolves bubbles under pressures below 0.2 atm, this degassing must be very carefully controlled to remove entrained bubbles without evolving more. The gel nominally requires 72 hours to cure at room temperature, which is reduced to 16 hours at the increased temperature of 40°C

The quality of the gel pad finish is crucial to the success of this method, as even minor surface imperfections can cause leaks in the cavity. The pad casting process underwent a series of refinements, leading to the use of vacuum formed PETG moulds, which provide the best surface finish for our gel pads

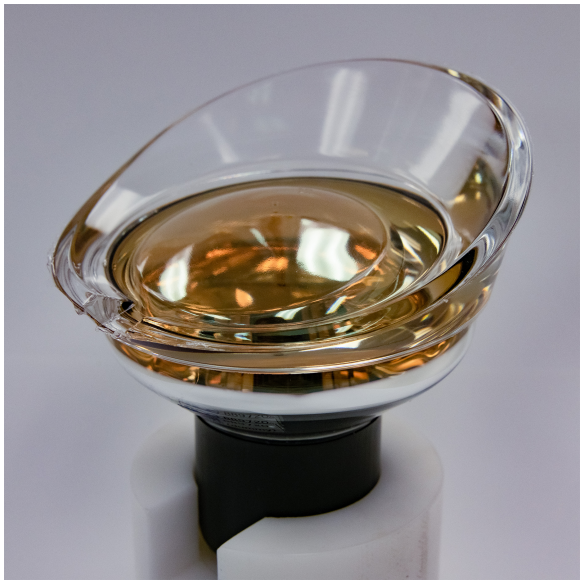

Figure D.10: The gel pads cast onto the PMT face within their moulds

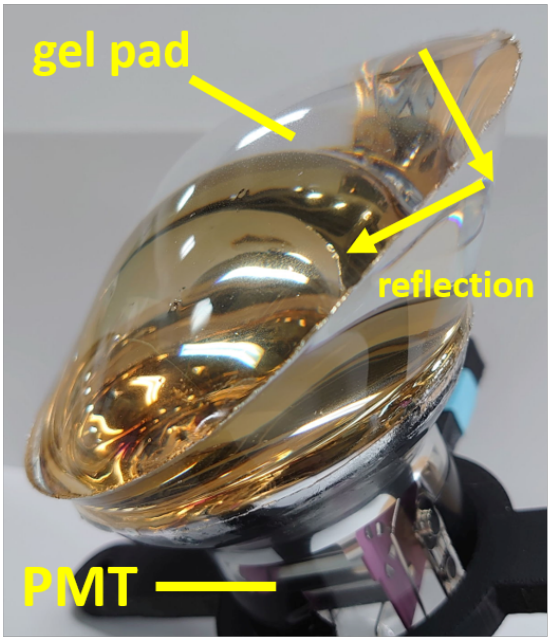

Figure D.11: Fully shaped gel pads cast onto PMTs

D.1.2 PMT Support Structures

As the gel pad integration procedure requires the gel pad to be pressed against the pressure vessel, the support structure must be designed to be able to push the PMT and gel pad 'subassembly' radially outward. This ensures that the pad rim makes contact with the pressure vessel, sealing the cavity well, and also acts as insurance against the gel pad delaminating over the course of its lifetime. It must also accommodate the shrinkage (around 4 mm in diameter) of the pressure vessel under the 70 kPa stresses encountered as the water in the holes freezes around the module.

Achieving these design goals led to the development of a sheet metal support structure, with each PMT supported by a bushing to constraint the PMT orientation, along with foam collars to help absorb the stresses on the PMT. These bushings have features which connect to the support bracket and constrain the clocking of the PMT, ensuring the boards cannot rotate from their nominal position around the

PMT axis. The outward motion of the gel pads is achieved by using an inflatable

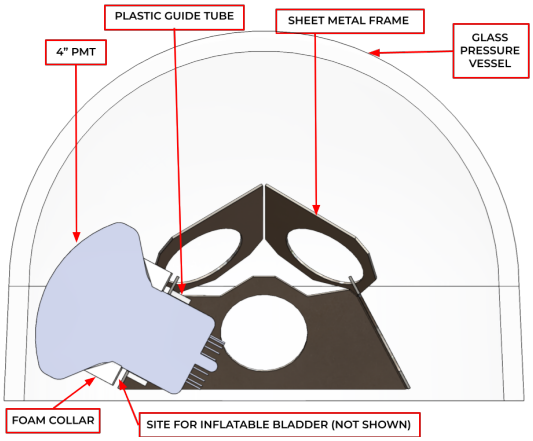

Figure D.12: Each PMT has an inflatable bladder which is filled with a silicone epoxy, pushing the PMT axially outward by ∼5mm. Figure from J. Cherwinka.

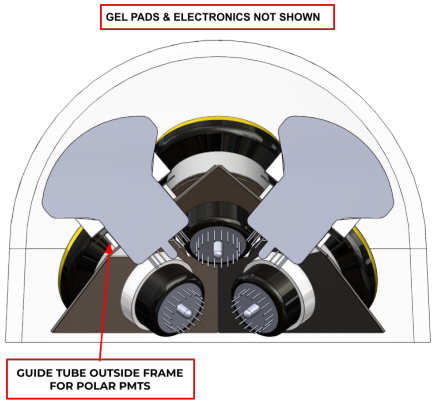

Figure D.13: The PMT has a support bushing to constrain the axis of motion. Figure from J. Cherwinka.

'bladder', which moves the PMT forward by 5 mm when full. We fill the bladder with a silicone epoxy, chosen to cure in 24 hours so that any leaks due to bladder degradation would not prevent the pushing of the PMT. Together with the gel pad, and a foam collar around the bulb of the PMT, the bladder acts as a spring to cushion the PMT from compressive forces during hole freeze-in. It is important to note that the bladder inflation technique is unique to the LOM-16, while the LOM-18 uses a system of springs which are used to push the PMTs against the pressure vessel.

The support structures in each hemisphere interface with each other through multiple wave springs, ensuring the two opposing frames push off each other, ensuring the gel pads remain under compression during the lifetime of the LOM and mitigating the possibility of gel pad delamination. These wavesprings are mounted to a stainless steel ring at the equator. The ring was made of sheet metal to ensure it would not flex or crack under spring compression, and also because the properties at low temperatures were well understood. The concerns about conductive materials in the

vicinity of high voltage circuits were mitigated by the semi circular bends, necessary to maintain the minimum spacing to prevent sparking discharges.

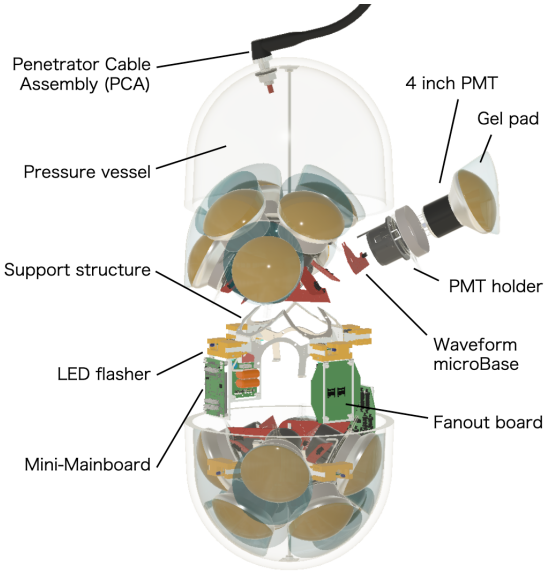

Figure D.14: An exploded diagram of the LOM-16, showing the various elements interfacing together [46]

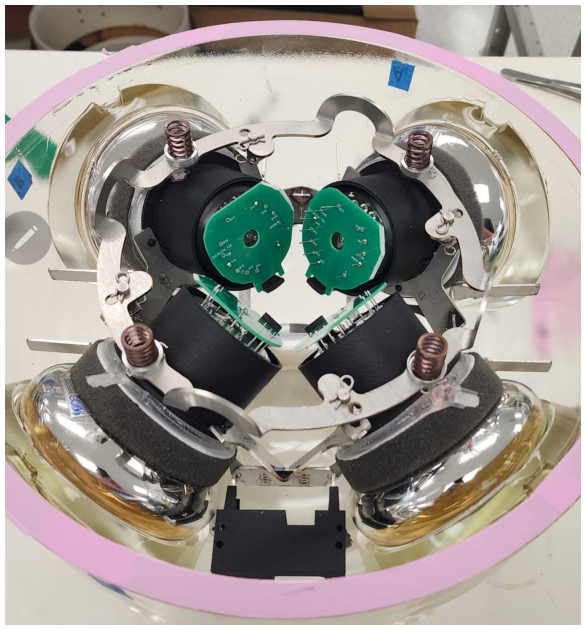

Figure D.15: A close up of the equatorial ring used to interface the two hemispheres together.

D.1.3 Module Integration

The stages of integrating the LOM after production of the PMT+gel pad subassemblies are geared towards ensuring the structural integrity of the gel pads. The first step in the process involves peeling the casting moulds off the gel pads, which are then covered with a protective wrap to prevent damage. The PMTs are then mounted onto the sheet metal support bracket, which is held in place by a custom designed jig. The next step of integration involves mounting the mini Mainboard (MMB) and fanouts at the sites on the support frame, around the equator. At this stage, the wuBases are connected to the fanout boards using ribbon cables of specific lengths, and the tubing for the inflatable bladders is connected to the diagonally opposite bladder with

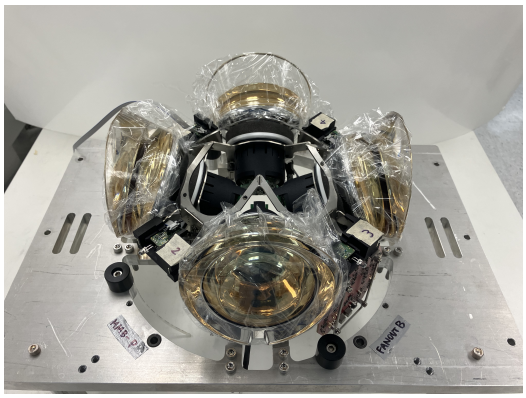

Figure D.16: The equatorial PMT Subassemblies mounted onto the support bracket, on the assembly jig.

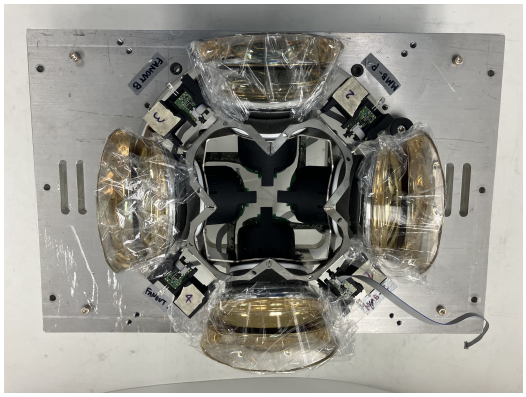

Figure D.17: A top down view showing the clearance between components, particularly the PMT bushings (in black).

a T-junction to ensure that forces are applied to the pressure vessel in balanced pairs during inflation. The bladders are filled with the EcoFlex ™ 00-30 addition curing silicone rubber [130], which was chosen for its ability to withstand low temperatures tested upto $-40°$C, as well as a serviceable work time of 45 minutes before it cured. We use a compressed air pump to inject the epoxy through the tubing at 30 PSI, to ensure the gel pads were fully inflated. Any air bubbles in the bladders would expand under the degassing vacuum, squeezing the gel cavity and causing overflow or leakage. To prevent this, we evacuate the bladder tubes with a vacuum pump before injecting the silicone epoxy, ensuring no air enters the lines. Once the PMTs are mounted, the protective wrap is peeled off, and a layer of liquid gel is smeared onto the pad rims to ensure that there are no bubbles during sealing. A crane is used to lower the pressure vessel onto the jig, taking care not to make contact with the pads to avoid an uneven rim contact. Due to the shape of the equatorial pads, they need to be forcibly retracted to compress the gel pad enough to avoid interfering with the vessel. Once in position, the vessel is secured to the jig with a ratchet strap, to prevent it shifting under the upward compressive force exerted by the gel pads

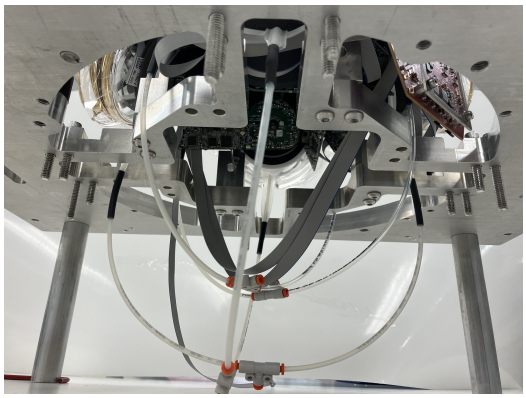

Figure D.18: The bladders are connected with T-junctions during inflation with epoxy, which prevents loss of compressive pressure in case of leaks developing in the bladder

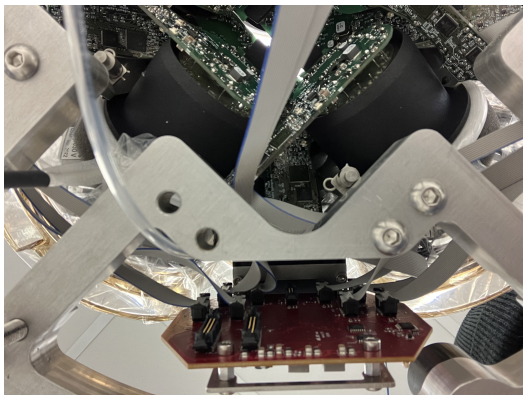

Figure D.19: The wuBase ribbon cables are routed around the equatorial spaces to connect to the fanout boards.

during bladder inflation. Once the bladders are inflated, the pad rims are visually

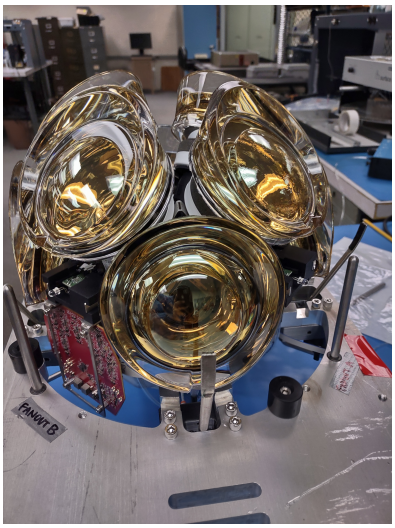

Figure D.20: The metal arms in front of the equatorial gel pads are used to push them away from the pressure vessel

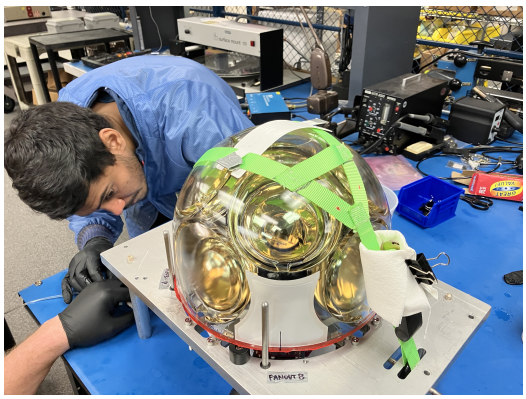

Figure D.21: A compressed air pump is used to inject the EcoFlex silicone epoxy into the bladders, which have a capacity of about 10-15 cc each. The pressure vessel is restrained by a ratchet strap to prevent it shifting.

inspected to ensure a good seal. The assembly is then placed in a vacuum chamber to remove rim bubbles, and allowed to rest overnight for the rim gel to cure. The next stage of integration involves backfilling the gel cavities with Shin-Etsu silicone.

This is performed at the prototyping using an electric caulking gun to inject the gel using 200 cc syringes, but will use a specialized gel dispenser for efficient mixing and backfilling. Metal tubes are inserted into the cavity openings, and connected to the syringe with luer-lock tubing for a secure connection. We take care to ensure the gel drips down along the walls of the pressure vessel as a smooth flow, to avoid entraining bubbles during pouring. With the syringe+caulking gun mechanism, backfilling

Figure D.22: With the prototype jig used for the Upgrade module production, we are able to fill four pads simultaneously.

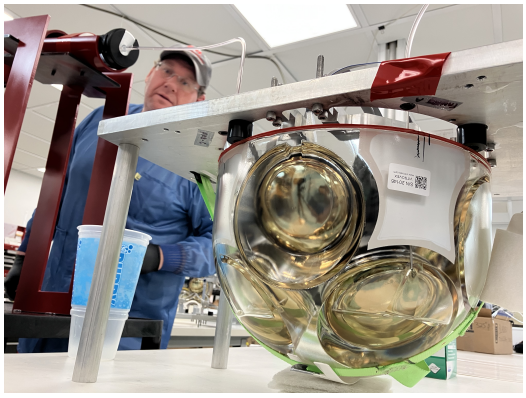

Figure D.23: A view of the pads midway through backfilling. The white cutout observed protects the vessel from gel dripped accidentally, and is peeled off after backfilling

takes 10-20 minutes per pad. This rate is constrained by the need to ensure a smooth laminar gel flow, without trapping or adding bubbles into the gel, and the maximum pressure tolerance of the syringes used. Once completed, the jig is transferred into a vacuum chamber for pad degassing. This consists of reducing the pressure down to 0.27 atm in stages, allowing the system to equilibrate at each vacuum setting for 3-5 minutes before further reduction. This procedure has been verified to remove all the entrained air bubbles while avoiding the spontaneous bubbling inherent to the Shin-Etsu compound. Once degassing is complete, the hemisphere is placed in an oven at 40°C, enabling the gel to cure at an accelerated rate.

Once both lower and upper hemispheres have been installed, they must be inte-

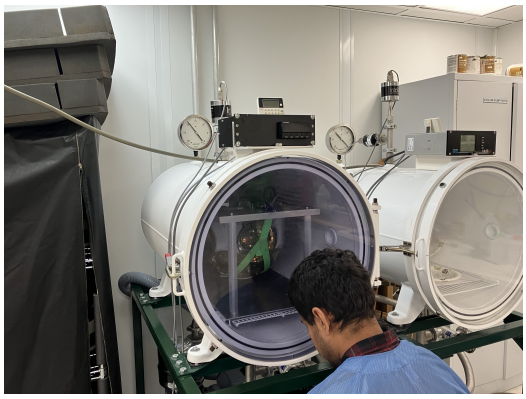

Figure D.24: The assembly jig is placed inside a vacuum chamber after all 8 PMTs are backfilled, to remove any entrained bubbles prior to curing

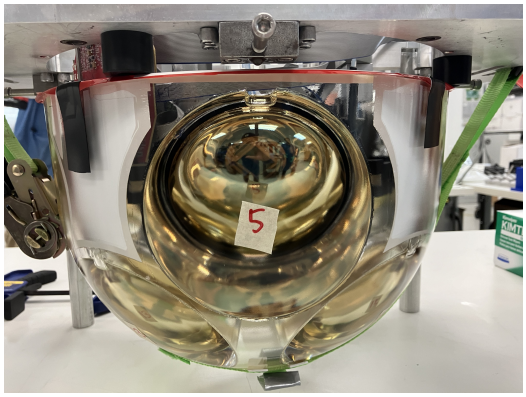

Figure D.25: A view of the pads after degassing. No bubbles are visible, and the meniscus visible at the filling port at the top is filled by a few drops of gel

grated together.Care must be taken while mating the two halves of the vessel, as any scratches or damage at the interface can cause catastrophic failure of the vessel under freeze-in pressure. The upper hemisphere is inverted on a crane-mounted jig, and lowered onto the lower hemisphere. The fanout boards in the two hemispheres, Fanout-A in the upper hemisphere and Fanout-B in the lower hemisphere, are connected with ribbon cables at this stage, providing power and communications to the lower hemisphere. The electronics are described in greater detail in the next section. The next step in the integration procedure is the evacuation and sealing of the pressure vessel, and the replacement of the interior atmosphere with nitrogen at 0.5 atm. This is performed by first applying a layer of butyl rubber sealant around the equatorial seam, leaving a brass shim in place for the nitrogen flushing. The flushing is performed by alternating a vacuum with injections of nitrogen gas in a pressure chamber. The final stage of integration involves taping the butyl with a protective layer of black Scotchrap tape.

Figure D.26: A. Arbuckle of PSL operating the pressure chamber to flush the LOM atmosphere with nitrogen.

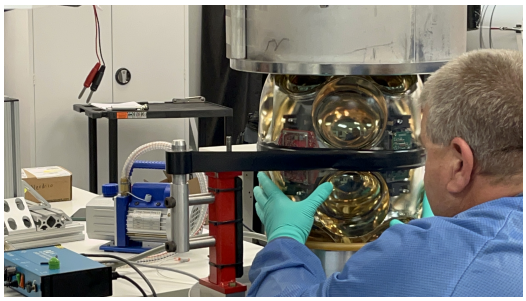

Figure D.27: Following the nitrogen flush, the evacuated LOM is sealed at the equator with a layer of tape, protecting the butyl which helps maintain the 0.5atm pressure inside.

Figure D.28: The team with the first complete LOM-16 prototype.

D.2 Electronics Design

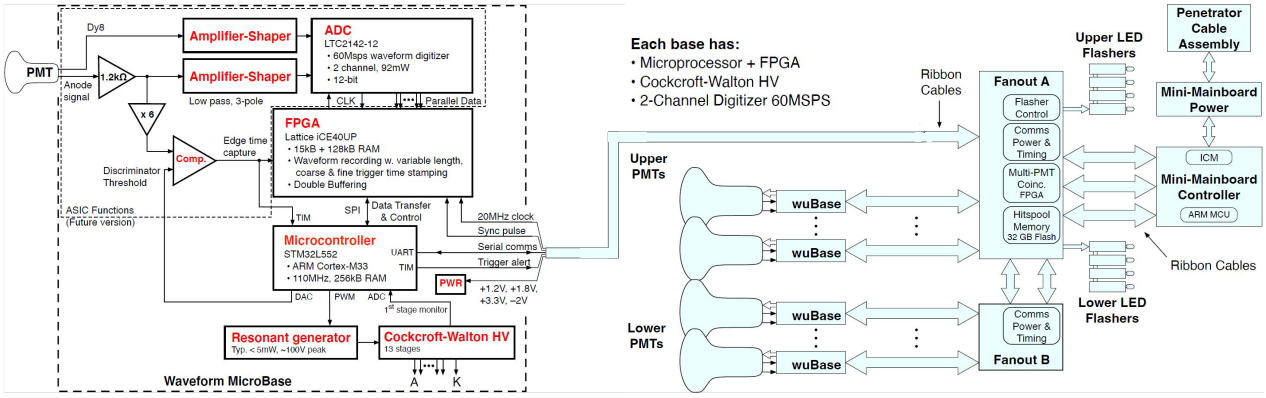

Figure D.29: A schematic diagram of the electronics design for the LOM. Figure from C. Wendt.

The LOM is a multi-pixel detector, and as such follows a distributed philosophy in the design of its readout electronics. Each PMT is soldered to a Waveform MicroBase (wuBase) which is responsible for both generating the high PMT bias voltage required for operation, and for readout and data acquisition (DAQ). As the LOM was designed to capture PeV-scale neutrino events without saturating, each wuBase has two digitization channels, a high-gain channel for dim events and a low-gain channel which remains linear even for bright signals. An on-board Lattice field programmable gate array (FPGA) is used for recording waveforms and timing information. An STM32 microcontroller (MCU) handles communications and timing for the board, while also controlling the FPGA. A 13 stage Cockcroft-Walton generator is used to generate the high voltage required for PMT biasing.

Each hemisphere has a fanout board to interface with all the PMT wuBases in that hemisphere, with Fanout-A mounted in the upper hemisphere and Fanout-B handling the lower hemisphere. The fanouts are responsible for multiplexing the PMT readout channels, and contain SD cards for hitspool storage. In addition to distributing power

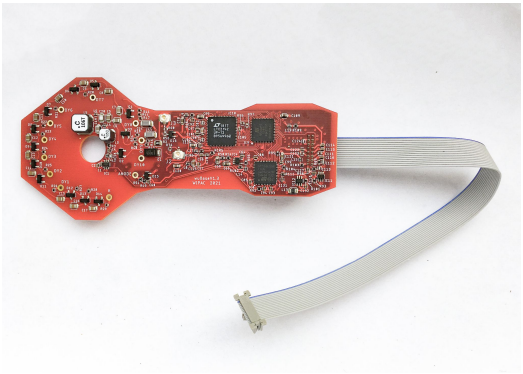

Figure D.30: wuBases are shaped to fit around closely packed PMTs. This is the design selected for the polar PMTs.

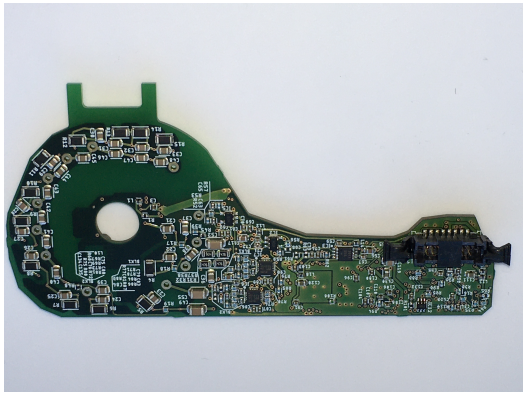

Figure D.31: The equatorial wuBase design

and communications channels to the various wuBases, an FPGA on the fanout board is responsible for triggering on multi-PMT coincidences. The fanout boards are also connected to LED flasher boards used for in-ice calibration studies.

The fanouts connect to the Mini MainBoard (MMB), responsible for surface communications and power distribution across all the devices planned for the IceCube Upgrade. The MMB is split into the MMB-Power board, which connects directly to the Penetrator Cable Assembly (PCA) that interfaces with the main cable to the surface, and the MMB-Communication board, responsible for in-ice communications. The MMBs and Fanout-A are mounted in the equatorial gaps in the upper hemisphere, while Fanout-B is mounted in the same space in the lower hemisphere.

D.3 Module Performance

One of my projects was to verify the functionality of the LOM, measuring performance characteristics such as the dark noise rate. Another important task was to calibrate the operational parameters for the module, such as the discriminator threshold and

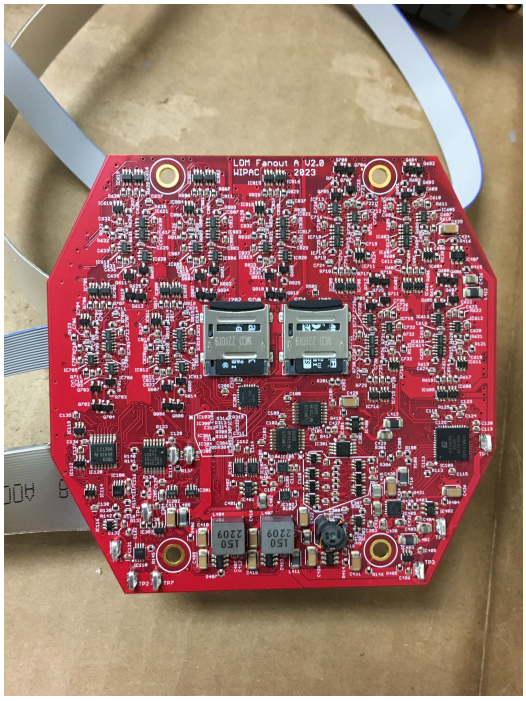

Figure D.32: The SD cards are mounted onto Fanout-A, which is mounted on the upper hemisphere

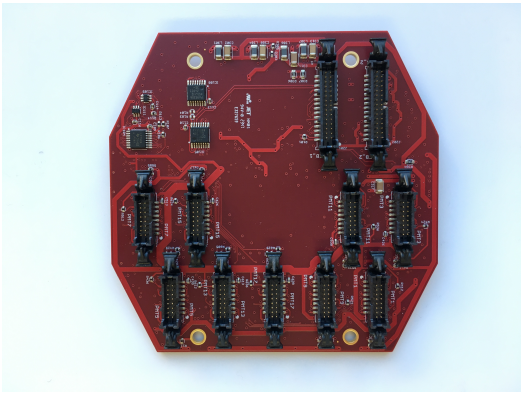

Figure D.33: The 16-pin connectors on Fanout-B for the various wuBases in the lower hemisphere, along with the 30-pin connectors to connect to Fanout-A

gain. The LOM's response to photon signals was also measured, to ensure that it would be able to record both single photoelectron (SPE) events, and bright multiple photoelectron (MPE) signals. These measurements were carried out both on the integrated module and also on the PMT subassemblies prior to integration. The purpose of testing the subassemblies was to ensure that only known good hardware was integrated and deployed, as, once installed, it is not possible to replace any parts. I developed a suite of testing and analysis tools based on software developed by C. Wendt, S. Griffin, J. Braun and others at IceCube for Upgrade devices. I also worked on developing a testbench where one could inject photon signals from LED sources, to mimic real physics signals, and measure the PMT response. The tests performed will be explained in further detail in the following sections

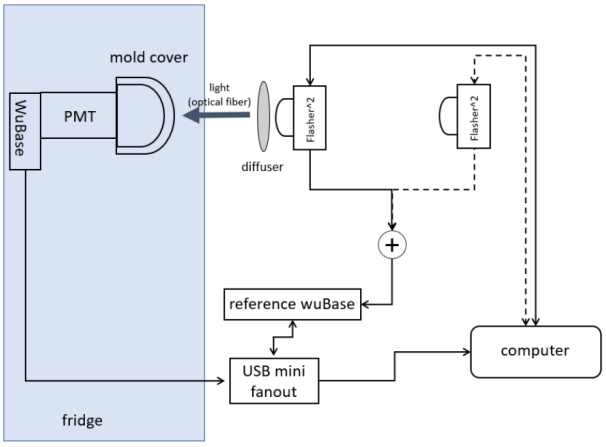

Figure D.34: A diagram of the PMT subassembly testbench.

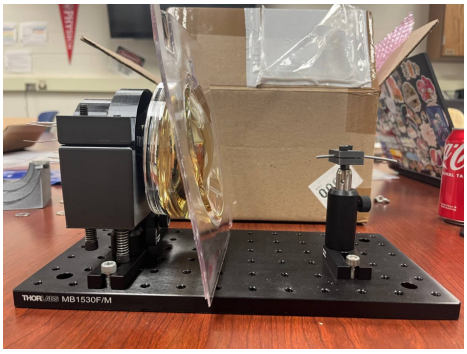

Figure D.35: The PMT subassemblies are mounted onto custom 3D printed holders, with optic fibers opposite to inject signals from LED flasher boards.

D.3.1 Dark Noise Measurements

As the dark noise of a PMT varies greatly with temperature, these measurements must be performed in a controlled environment, with minimal light leakage. At $-40°$C, where LOMs are expected to operate, the dominant source of inherent dark noise occurs from radioactive decays in the glass of the PMTs and the pressure vessel. To get a handle on the true dark rate of a PMT, therefore, we set a chest freezer to operate at $-40°$C, and covered it with blackout cloth to prevent the PMTs from being affected by ambient light. A group of ribbon cables are fed through to the freezer to communicate with the PMTs, as are optic fibers from light sources.

As the dark rate increases with temperature, we perform two sets of tests. One measurement is taken at $-40°$C over a 12 hour period, to verify the stability of the dark rate. Another measurement is taken with the freezer warming up to room temperature, to verify the dark rate rises uniformly with temperature.

Another important measurement performed was the measurement of the dark rate in the integrated module, to capture the contribution from radioactive decays in the pressure vessel glass. For the Upgrade modules, the pressure vessels are manufactured

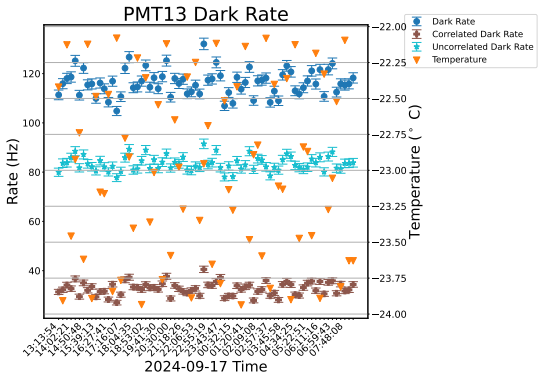

Figure D.36: Cold Dark Rate.

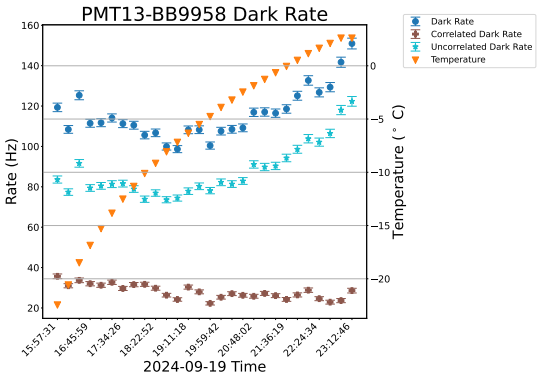

Figure D.37: Rampup Dark Rate.

by Nautilus Marine Service GmbH for the LOM-16 and Okamoto Glass Co. Ltd for the LOM-18. At time of writing, the Nautilus pressure vessel had a higher dark noise rate compared to the Okamoto Glass, as visible in Figs. D.38 and D.39.

D.3.2 Gain and Discriminator calibration

Each PMT is biased to a specific voltage, which is responsible for setting the gain of that channel. A discriminator threshold must also be set so that the PMT does not trigger on the noise floor, using up all the data bandwidth for pedestal hits. For the LOM, the gain was chosen to be 5e6, which means that a single photoelectron (SPE) would be amplified to 0.8 pC (1.6e$-$19 $\frac{\mathrm{C}}{\mathrm{e}^-} \times$ 5e6). The discriminator threshold was selected to be 0.2 SPE, to ensure that even dim events were captured to enhance low energy sensitivity. At the target gain, 0.2 SPE evaluates to 0.16 pC of charge.

To identify the target voltage and discriminator settings for each PMT, we take multiple runs of dark noise data, scanning over different settings. We then fit the resulting charge distribution with the sum of a decaying exponential function and a Gaussian curve, multiplied by a sigmoid function. The exponential models the pedestal feature in the charge distribution, while the Gaussian models the peak of the SPE distribution. The sigmoid function is responsible for modelling the threshold, which

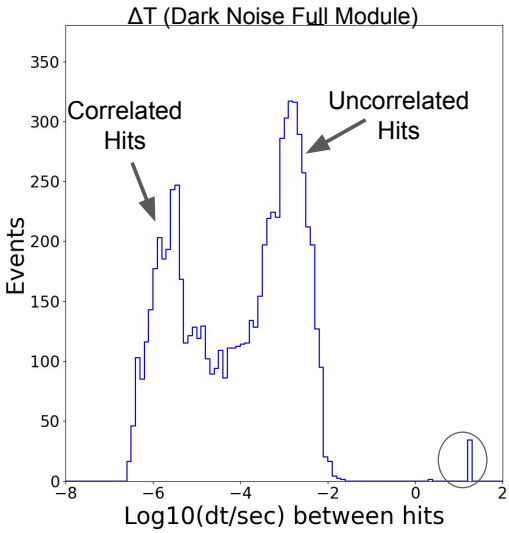

Figure D.38: Dark rate for a Hamamatsu PMT integrated into a LOM-16 pressure vessel, expressed in terms of the time difference between hits. The right peak should peak at the time difference between uncorrelated dark noise hits, which is the reciprocal of the dark noise rate. At time of writing, the DAQ firmware used to analyze this data had a large deadtime, visible as a small peak of time differences above 1 s, which will be eliminated in production modules.

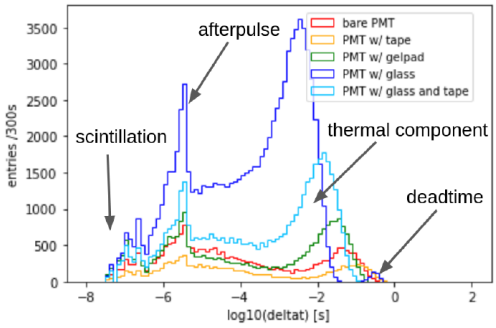

Figure D.39: Dark rate for a Hamamatsu PMT integrated into a LOM-18 pressure vessel, expressed in terms of the time difference between hits.

eliminates hits below a certain charge. The fitting procedure follows the equation:

$$\mathcal{N}_{\mathrm{Q_{pC}}} = \frac{1}{1. + e^{-a(log(\mathrm{Q}) - log(\mathrm{Thresh}))}} \left(b * e^{-\frac{(log(\mathrm{Q}) - log(\mathrm{Peak}))^2}{2\sigma^2}} + c * e^{-d*\mathrm{Q}} \right) \tag{D.1}$$

We first scan over different discriminator DAC setting values holding the voltage constant, to obtain a linear curve relating the charge threshold to the DAC value (Fig. D.40). Once the target discriminator DAC setting is obtained, we run over multiple voltage settings holding the discriminator constant, fitting the SPE peak at each gain. We then plot the gain against the voltage setting on a log-log plot, taking care to keep the voltage from getting too high and into the non-linear region. We

then identify the voltage at which the target gain is attained, and thus we obtain our operating parameters for each PMT

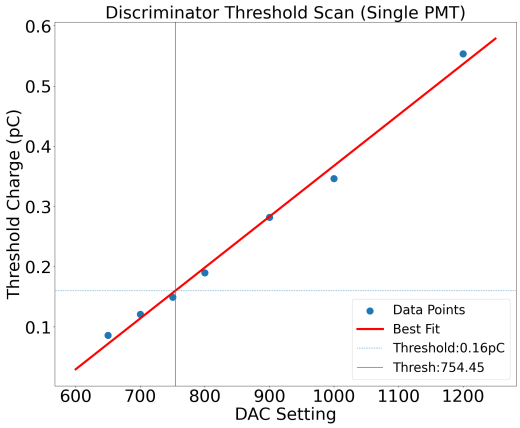

Figure D.40: A plot of the thresholds obtained by fitting the charge distributions at different settings of the Discriminator DAC. We fit a straight line and select the DAC setting which gives us a threshold of 0.16pC

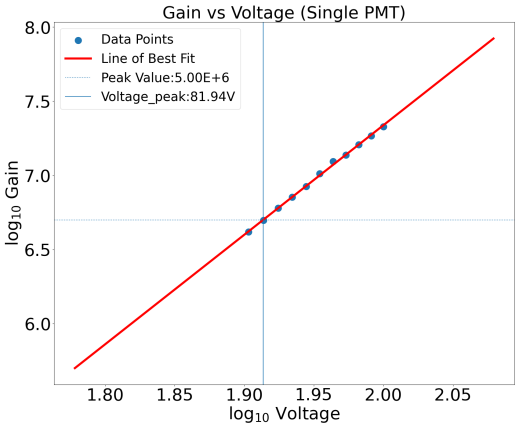

Figure D.41: A plot of the gains obtained by fitting the charge distributions at different settings of the applied voltage. We fit a straight line on a log-log plot and select the voltage setting which gives us a gain of 5e6

D.3.3 SPE timing resolution

A very important performance metric for optical modules is the timing resolution for SPE pulses. Being able to resolve the timing of different photon pulses to the order of a few ns is essential to the performance of IceCube-Gen2, in particular the angular resolution of reconstructed events. We measure the timing resolution using SPE-level photon pulses from an LED flasher (Fig. D.43), injected using an optic fibre to the PMT photocathode. A secondary timing wuBase is used to clock the intervals at which pulses are injected, and we compare this to the time at which the PMT receives the pulse. The spread of the distribution of the timing difference is a measure of the timing resolution. As the PMT waveform is digitized at 60 MSPS, nominally it would not be possible to resolve signals below the 16.67 ns sampling

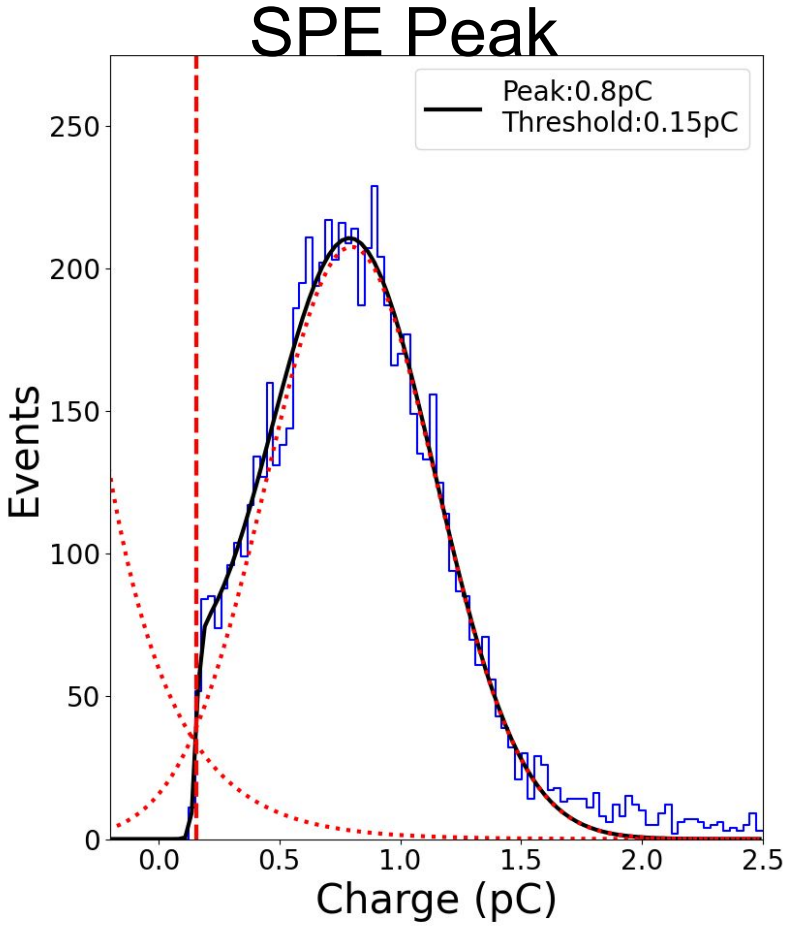

Figure D.42: A charge distribution plot of dark noise for a PMT. The gain and threshold are at or close to the target values, with the red dotted lines indicating the fitted exponential and Gaussian functions, and the red dashed line indicating the position of the sigmoid threshold.

time window. However, by fitting a template to the SPE waveforms, we are able to resolve signals down to 3 ns. This template was created by Y. Makino, taking the functional form

$$\mathrm{F(t)} = A\left(ce^{e^{\frac{-(x-x_0)}{b1}}} + e^{\frac{(x-x_0)}{b2}}\right)^p \tag{D.2}$$

where $c = 0.7$ and $p = -8$ while $b1$ and $b2$ are fit parameters. The fit encompasses the 5 points before and the 7 points after the peak point.

For the SPE time resolution measurements, it is very important to know which wave-

forms correspond to the flasher pulses and which are merely dark noise. This winnowing of the noise pulses is even more important due to the issues with the DAQ deadtime, which means that pulses may get missed. The first stage in cleaning out the noise pulses, therefore, is to obtain the offset between the clock on the timing wuBase, and the clock on the wuBase mounted to the test PMT. As this offset is expected to remain constant over the duration of a run, it is possible to search for PMT signals within a certain window after the time recorded by the timing wuBase. This offset calculation is performed by sending a series of bright pulses to the PMT, which is operated in a mode which triggers off the low gain channel. This has the advantage of greatly suppressing the dark noise hits, making it easier to isolate true LED signal waveforms. Once the hits are acquired, we use our knowledge of the signal injection frequency (set to be 1 Hz for convenience and to avoid filling up the data buffer with the preliminary DAQ) to eliminate spurious hits received at the wrong intervals to neighbouring hits, as these are likely to arise from dark noise. With a cleaned set of hits, we compare the times recorded by the PMT wuBase to the times recorded by the timing wuBase, and obtain the relative time offsets for each signal channel. These time offsets are verified to stay constant over periods of time extending to a few days, as long as the wuBases haven't been rebooted.

Once we have the timing offsets for each channel, we take data with the flasher LED brightness lowered to the SPE level. This necessitates triggering on the high gain channel, with the dark rate subsequently rising. As this high dark rate causes a loss of hits to deadtime with the preliminary DAQ used at the time of writing, it was necessary to extend this data taking run for a 12 hour period to ensure a reasonable number of signal hits were obtained. The data then undergoes cleaning to remove dark noise hits by comparing the offset times to the times recorded by the flasher LEDs. The cleaned subset of signal hits is used to study metrics such as the

Figure D.43: The Flasher LEDs used for injecting pulses for PMT testing. There are two Flasher[2] boards used for generating the LED signal, and sending a trigger signal to the timing wuBases in the lower half of the image, to register as waveforms. The leftmost board is used for dim SPE signal studies, with the ground glass diffuser between the LED and the optical fibers. The centre board is used for bright narrow pulses, as part of the tests of the low gain channel readout. This board is connected to a separate timing base, and also sends a trigger signal to a function generator. This function generator is used to generate bright wide and double pulses, injected into the PMTs using the LED on the right

Figure D.44: A view of the PMT testbench in the freezer dark box, with three optic fibers mounted in front of each PMT. These fibers bring in the photon signal from the three sources visible in Fig. D.43

Peak/Valley ratio of the charge distribution, and the time resolution.

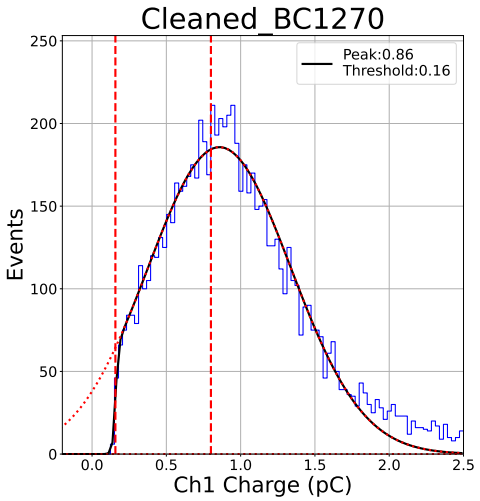

Figure D.45: The SPE charge distribution from flasher LED pulses. As visible, the peak is close to the target of 0.8 pC (possibly off due to fluctuations in the fit, or due to rounding errors while setting the bias voltage), while the threshold has fit at the target value of 0.2 SPE. One important performance metric is the Peak to Valley ratio, evaluated as the ratio of the height of the SPE peak to the valley between the peak and the pedestal. This quantity is a measure of the ability to resolve the SPE peak, the charge resolution of the detector. We require the P/V ratio to be greater than 2

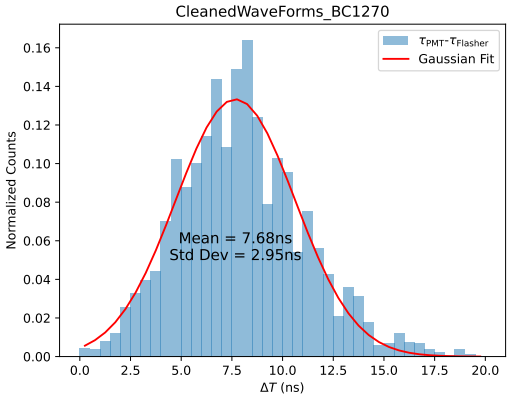

Figure D.46: The distributions of the time difference between the time measured at the PMT and the time recorded by the flasher for the SPE photon pulses. The distribution is fit by a Gaussian, with the standard deviation of the Gaussian a measure of the time resolution, required to be below 5ns

D.3.4 PMT Response to Bright Pulses

As mentioned earlier, the LOM utilizes two readout channels on the wuBase for the digitization of photon signals to extend neutrino spectral measurements to PeV scales. These are named "channel-1", a high gain channel for dim SPE-level signals, and "channel-2", a channel with lower gain, to be able to digitize bright signals without saturating. Studies performed by Y. Makino during the development of the wuBase mapped out the dynamic range of the sensor, as illustrated in Fig. D.47. To

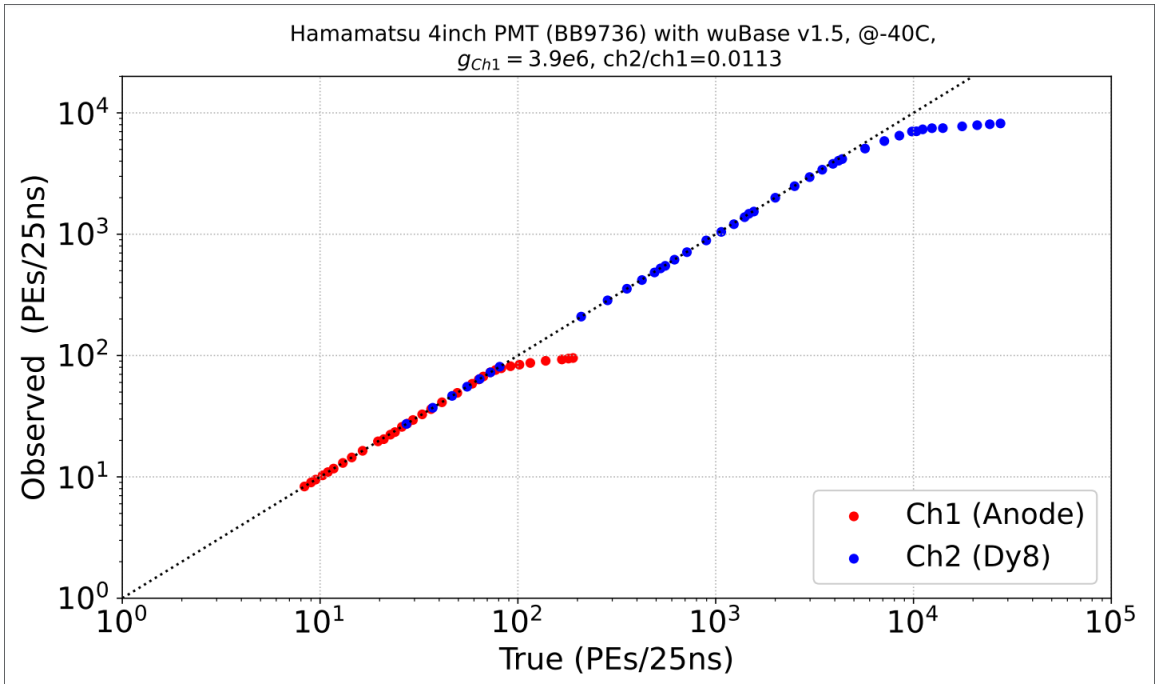

Figure D.47: A comparison of the linear dynamic range of the two channel readout. The input of channel 1 is the PMT anode, while channel 2 reads the signal from Dynode 8, which is at a lower amplification stage within the PMT. As illustrated, there is good overlap in linear response ranges of both channels. We begin to see signs of bias in the observed charge due to PMT saturation beyond 2000 PE/25 ns, although Ch2 is able to digitize waveforms upto 7,800 PE/25 ns at 5e6 gain (wuBase V1.5 Final Version-Extended Dynamic Range design)

verify the performance of the response to bright pulses, which saturate channel-1 but are linearly digitized by channel-2, a series of photon signals are injected, using a

similar apparatus to the SPE signals used for timing resolution measurements. This serves to characterize the PMT response to multiple photoelectron (MPE) signals. The first of the MPE tests involve using fast pulses, with a width of approximately 100 ns, of varying intensities. At each photon intensity, we validate the linearity of the response by testing the shape of the waveform in both channels. If the measured shape follows the SPE template (Eq.D.2), we infer that the response is still linear. Beyond a certain brightness threshold, the channel-1 waveform saturates, while the channel-2 response is still linear. We also evaluate the residual differences between the fit waveform and the sampled points, looking for systematic under or overshoots which may hint towards faults in the wuBase manufacture.

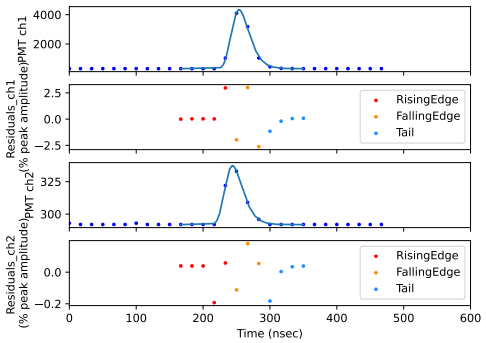

Figure D.48: Signal waveforms at a brightness where both channels are linear, demonstrating the overlap in the channels' dynamic ranges

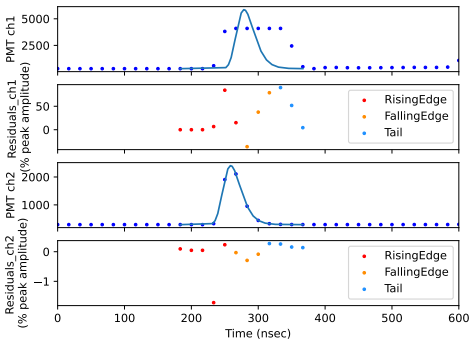

Figure D.49: Signal waveforms at a much higher brightness, where channel-1 is saturated. Channel-2, however, remains linear.

D.3.5 PMT Response to Wide Pulses

In addition to characterizing the input from pulses of varying intensities, we also require the sensor to be able to digitize long waveforms with widths of the order of 1 μs. We inject these pulses using a function generator set to trigger on a pulse

from our external LED flasher, as the external flasher board is unable to provide the waveforms itself.

D.3.6 PMT Response to Double Pulses

The double pulse signature of a tau neutrino CC interaction is modelled by two bright pulses separated by 60 ns. Once again we inject this signal using a function generator, and the recorded waveform shows that we are indeed able to capture and resolve this waveform.

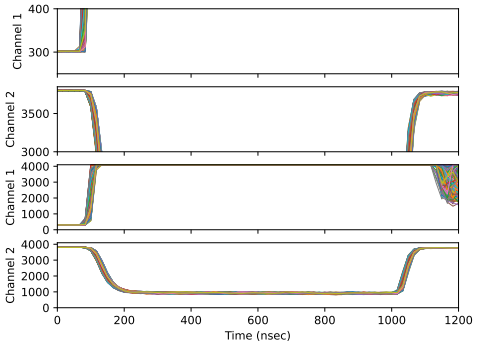

Figure D.50: Waveforms from the bright wide pulse studies

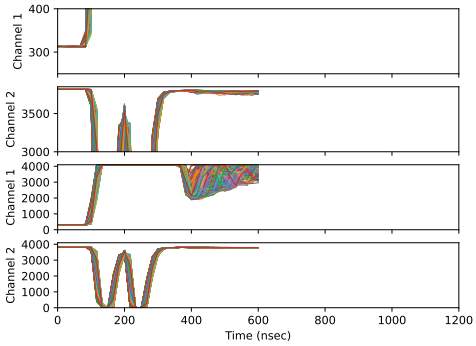

Figure D.51: Waveforms from the Double pulse studies

Bibliography

[1] Donald H Perkins. *Particle Astrophysics*. Number 10. Oxford University Press, 2009.

[2] David Griffiths. *Introduction to elementary particles*. John Wiley & Sons, 2020.

[3] Bartoszek, Larry and Barnes, E and Miller, JP and Mott, J and Palladino, A and Quirk, J and Roberts, BL and Crnkovic, J and Polychronakos, V and Tishchenko, V and others. Mu2e technical design report. Technical report, eScholarship, University of California, 2015.

[4] K Zuber, Y Zhang, J Zhang, MV Zdorovets, Yu V Yudin, Y Yuan, T Yoshioka, M Yoshida, H Yoshida, B Yeo, et al. COMET Phase-I technical design report. *Progress of Theoretical and Experimental Physics*, 2020(3), 2020.

[5] KATRIN Collaboration*. Direct neutrino-mass measurement with sub-electronvolt sensitivity. *Nature Physics*, 18(2):160–166, 2022.

[6] Eleonora Di Valentino and Alessandro Melchiorri. Neutrino Mass Bounds in the Era of Tension Cosmology. *The Astrophysical Journal Letters*, 931(2):L18, 2022.

[7] Christian Spiering. Towards High-Energy Neutrino Astronomy: A Historical Review. *The European Physical Journal H*, 37(3):515–565, 2012.

[8] Robert E Lopez, Scott Dodelson, Andrew Heckler, and Michael S Turner. Precision Detection of the Cosmic Neutrino Background. *Physical Review Letters*, 82(20):3952, 1999.

[9] IceCube Collaboration*. Evidence for high-energy extraterrestrial neutrinos at the IceCube detector. *Science*, 342(6161):1242856, 2013.

[10] IceCube Collaboration, Mark Aartsen, Markus Ackermann, Jenni Adams, Juan Antonio Aguilar, Markus Ahlers, Maryon Ahrens, Imen Al Samarai, David Altmann, Karen Andeen, et al. Neutrino emission from the direction of the blazar TXS 0506+ 056 prior to the IceCube-170922A alert. *Science*, 361(6398):147–151, 2018.

[11] IceCube Collaboration*†, R Abbasi, M Ackermann, J Adams, JA Aguilar, M Ahlers, M Ahrens, JM Alameddine, C Alispach, AA Alves Jr, et al. Evidence for neutrino emission from the nearby active galaxy NGC 1068. *Science*, 378(6619):538–543, 2022.

[12] R. Abbasi et al. IceCube high-energy starting event sample: Description and flux characterization with 7.5 years of data. *Phys. Rev. D*, 104:022002, Jul 2021.

[13] M. G. Aartsen et al. Atmospheric and astrophysical neutrinos above 1 TeV interacting in IceCube. *Phys. Rev. D*, 91(2):022001, 2015.

[14] IceCube Collaboration. Characterization of the three-flavor composition of cosmic neutrinos with IceCube. *Physical Review Letters*, In Preparation.

[15] IceCube Collaboration. Evidence for Spectral Break or Curvature in the Spectrum of Astrophysical Neutrinos from 5TeV - 10PeV. *Physical Review Letters*, In Preparation.

[16] IceCube Collaboration. Improved measurements of the TeV- PeV extragalactic neutrino spectrum from joint analyses of IceCube tracks and cascades. *Physical Review D*, In Preparation.

[17] Carmelo Evoli. The Cosmic-Ray Energy Spectrum, December 2020.

[18] Thomas K Gaisser, Ralph Engel, and Elisa Resconi. *Cosmic rays and particle physics*. Cambridge University Press, 2016.

[19] Rafael Alves Batista, Jonathan Biteau, Mauricio Bustamante, Klaus Dolag, Ralph Engel, Ke Fang, Karl-Heinz Kampert, Dmitriy Kostunin, Miguel Mostafa, Kohta Murase, et al. Open questions in cosmic-ray research at ultrahigh energies. *Frontiers in Astronomy and Space Sciences*, 6:23, 2019.

[20] Naoko Kurahashi, Kohta Murase, and Marcos Santander. High-energy extragalactic neutrino astrophysics. *Ann. Rev. Nucl. Part. Sci. 2022*, 2022.

[21] Volker Beckmann and Chris Shrader. *Active Galactic Nuclei*. John Wiley & Sons, 2012.

[22] Mark G Aartsen, M Ackermann, J Adams, JA Aguilar, M Ahlers, M Ahrens, D Altmann, T Anderson, M Archinger, C Arguelles, et al. Measurement of the atmospheric ν e spectrum with icecube. *Physical Review D*, 91(12):122004, 2015.

[23] MG Aartsen, K Abraham, M Ackermann, J Adams, JA Aguilar, M Ahlers, M Ahrens, D Altmann, T Anderson, M Archinger, et al. Characterization of the atmospheric muon flux in icecube. *Astroparticle physics*, 78:1–27, 2016.

[24] Esteban Roulet. On the relation between the astrophysical neutrino fluxes and the cosmic ray fluxes. *Journal of Cosmology and Astroparticle Physics*, 2021(08):009, 2021.

[25] Markus Böttcher. Progress in multi-wavelength and multi-messenger observations of blazars and theoretical challenges. *Galaxies*, 7(1):20, 2019.

[26] Damiano FG Fiorillo and Mauricio Bustamante. Bump hunting in the diffuse flux of high-energy cosmic neutrinos. *Physical Review D*, 107(8):083008, 2023.

[27] Kohta Murase, Dafne Guetta, and Markus Ahlers. Hidden Cosmic-Ray Accelerators as an Origin of TeV-PeV Cosmic Neutrinos. *Phys. Rev. Lett.*, 116(7):071101, 2016.

[28] Ke Fang and Kohta Murase. Linking high-energy cosmic particles by black-hole jets embedded in large-scale structures. *Nature Physics*, 14(4):396–398, 2018.

[29] Markus Ackermann, M Ajello, Andrea Albert, WB Atwood, Luca Baldini, J Ballet, G Barbiellini, Denis Bastieri, K Bechtol, R Bellazzini, et al. The spectrum of isotropic diffuse gamma-ray emission between 100 mev and 820 gev. *The Astrophysical Journal*, 799(1):86, 2015.

[30] Markus Ahlers and Francis Halzen. Opening a new window onto the universe with icecube. *Progress in Particle and Nuclear Physics*, 102:73–88, 2018.

[31] Antonio Capanema, Arman Esmaili, and Kohta Murase. New constraints on the origin of medium-energy neutrinos observed by icecube. *Physical Review D*, 101(10):103012, 2020.

[32] Ke Fang, John S. Gallagher, and Francis Halzen. The TeV Diffuse Cosmic Neutrino Spectrum and the Nature of Astrophysical Neutrino Sources. *Astrophys. J.*, 933(2):190, 2022.

[33] Stefaan Tavernier. *Experimental Techniques in Nuclear and Particle Physics*. Springer Nature, 2010.

[34] Joseph A. Formaggio and G. Zeller. From eV to EeV: Neutrino Cross Sections Across Energy Scales. *Reviews of Modern Physics*, 84:1307–1341, 2012.

[35] G. P. Zeller. Neutrino cross section measurements. *Particle Data Group*, 2023.

[36] Amanda Cooper-Sarkar, Philipp Mertsch, and Subir Sarkar. The high energy neutrino cross-section in the standard model and its uncertainty. *Journal of High Energy Physics*, 2011(8):1–20, 2011.

[37] R Abbasi, M Ackermann, J Adams, JA Aguilar, M Ahlers, M Ahrens, C Alispach, AA Alves Jr, NM Amin, K Andeen, et al. Measurement of the high-energy all-flavor neutrino-nucleon cross section with icecube. *Physical Review D*, 104(2):022001, 2021.

[38] IceCube Collaboration*. Detection of a particle shower at the Glashow resonance with IceCube. *Nature*, 591(7849):220–224, 2021.

[39] Sheldon L Glashow. Resonant scattering of antineutrinos. *Physical Review*, 118(1):316, 1960.

[40] Jan-Hendrik Koehne, Katharina Frantzen, Martin Schmitz, Tomasz Fuchs, Wolfgang Rhode, Dmitry Chirkin, and J Becker Tjus. Proposal: A tool for propagation of charged leptons. *Computer Physics Communications*, 184(9):2070–2090, 2013.

[41] Dmitry Chirkin and Wolfgang Rhode. Propagating leptons through matter with muon monte carlo (mmc). *arXiv preprint hep-ph/0407075*, 2004.

[42] Sw. Banerjee and A. Lusiani. τ branching fractions. *Particle Data Group*, 2019.

[43] William R Leo. *Techniques for nuclear and particle physics experiments: a how-to approach*. Springer Science & Business Media, 1994.

[44] IceCube Collaboration. IceCubeWiki:Gallery. Creative Commons Attribution-Share Alike 3.0.

[45] M. G. Aartsen et al. The IceCube Neutrino Observatory: Instrumentation and Online Systems. *JINST*, 12(03):P03012, 2017.

[46] IceCube-Gen2 Technical Design Report. 7 2023. IceCube-Gen2 Technical Design Report, link.

[47] IceCube Collaboration. IceCubeWiki:CoordinateSystem. Creative Commons Attribution-Share Alike 3.0.

[48] Rasha Abbasi, Yasser Abdou, T Abu-Zayyad, J Adams, JA Aguilar, M Ahlers, K Andeen, J Auffenberg, X Bai, M Baker, et al. Calibration and characterization of the IceCube photomultiplier tube. *Nuclear Instruments and Methods in Physics Research Section A: Accelerators, Spectrometers, Detectors and Associated Equipment*, 618(1-3):139–152, 2010.

[49] DF Cowen, forthe IceCube Collaboration, et al. Tau neutrinos in IceCube. In *Journal of Physics: Conference Series*, volume 60, page 227. IOP Publishing, 2007.

[50] T. Glauch. Application of Deep Neural Networks to Event Type Classification in IceCube. *PoS*, ICRC2019:937, 2019.

[51] IceCube Collaboration*. Evidence for high-energy extraterrestrial neutrinos at the IceCube detector. *Science*, 342(6161):1242856, 2013.

[52] MG Aartsen, M Ackermann, J Adams, JA Aguilar, M Ahlers, M Ahrens, C Alispach, K Andeen, T Anderson, I Ansseau, et al. Search for sources of astrophysical neutrinos using seven years of IceCube cascade events. *The Astrophysical Journal*, 886(1):12, 2019.

[53] Sarah Mancina. *Astrophysical Neutrino Source Searches Using IceCube Starting Tracks*. PhD thesis, University of Wisconsin-Madison, 2022.

[54] IceCube Collaboration*†, R Abbasi, M Ackermann, J Adams, JA Aguilar, M Ahlers, M Ahrens, JM Alameddine, AA Alves Jr, NM Amin, et al. Observation of high-energy neutrinos from the Galactic plane. *Science*, 380(6652):1338–1343, 2023.

[55] R Abbasi, M Ackermann, J Adams, SK Agarwalla, JA Aguilar, M Ahlers, JM Alameddine, NM Amin, K Andeen, G Anton, et al. Improved modeling of in-ice particle showers for icecube event reconstruction. *Journal of Instrumentation*, 19(06):P06026, 2024.

[56] Manuel Silva. *Measurement of the Astrophysical Diffuse Neutrino Flux using Starting Track Events in IceCube*. PhD thesis, University of Wisconsin-Madison, 2023.

[57] R Abbasi, M Ackermann, J Adams, SK Agarwalla, JA Aguilar, M Ahlers, JM Alameddine, NM Amin, K Andeen, G Anton, et al. Characterization of the astrophysical diffuse neutrino flux using starting track events in icecube. *Phys. Rev. D*, 110:022001, Jul 2024.

[58] Aswathi Balagopal V and Vedant Basu. Diffuse Astrophysical Neutrino Measurements With IceCube All Flavor Starting Events. *Bulletin of the American Physical Society*, 2024.

[59] Marcel Usner. *Search for astrophysical tau-neutrinos in six years of high-energy starting events in the icecube detector*. PhD thesis, Humboldt-Universität zu Berlin, 2018.

[60] Juliana Stachurska. *Astrophysical Tau Neutrinos in IceCube*. PhD thesis, Humboldt-Universität zu Berlin, 2020.

[61] Jakob Van Santen. *Neutrino Interactions in IceCube above 1 TeV Constraints on Atmospheric Charmed-Meson Production and Investigation of the Astrophysical Neutrino Flux with 2 Years of IceCube Data taken 2010-2012*. PhD thesis, University of Wisconsin-Madison, 2014.

[62] Albrecht Karle and Dmitry Chirkin. Enhanced energy reach of IceCube.

[63] MG Aartsen, R Abbasi, Y Abdou, M Ackermann, J Adams, JA Aguilar, M Ahlers, D Altmann, J Auffenberg, X Bai, et al. The IceCube neutrino observatory part VI: ice properties, reconstruction and future developments. *arXiv preprint arXiv:1309.7010*, 2013.

[64] IceCube Collaboration. IceCubeWiki:LineFit. Creative Commons Attribution-Share Alike 3.0.

[65] IceCube Collaboration. IceCubeWiki:Lilliput. Creative Commons Attribution-Share Alike 3.0.

[66] Kai Schatto. *Stacked searches for high-energy neutrinos from blazars with IceCube*. PhD thesis, Mainz, Univ., Diss., 2014, 2014.

[67] Alexander Lyle Wallace. *Direction reconstruction of IceCube neutrino events with millipede*. PhD thesis, 2016.

[68] Theo Glauch. i3deepice. `https://github.com/tglauch/i3deepice`, 2021.

[69] M. G. Aartsen et al. Atmospheric and astrophysical neutrinos above 1 TeV interacting in IceCube. *Phys. Rev. D*, 91(2):022001, 2015.

[70] Thomas K. Gaisser. Spectrum of cosmic-ray nucleons, kaon production, and the atmospheric muon charge ratio. *Astropart. Phys.*, 35:801–806, 2012.

[71] Felix Riehn, Hans P. Dembinski, Ralph Engel, Anatoli Fedynitch, Thomas K. Gaisser, and Todor Stanev. The hadronic interaction model SIBYLL 2.3c and Feynman scaling. *PoS*, ICRC2017:301, 2018.

[72] Alexa Nelson. WIPAC Graphic Design. Creative Commons Attribution-Share Alike 3.0.

[73] Carlos A. Argüelles, Sergio Palomares-Ruiz, Austin Schneider, Logan Wille, and Tianlu Yuan. Unified atmospheric neutrino passing fractions for large-scale neutrino telescopes. *JCAP*, 2018(7):047, July 2018.

[74] Carlos A. Argüelles, Sergio Palomares-Ruiz, Austin Schneider, Logan Wille, and Tianlu Yuan. Unified atmospheric neutrino passing fractions for large-scale neutrino telescopes. *JCAP*, 2018(7):047, July 2018.

[75] Anatoli Fedynitch and Hans Dembinski. MCEq. mceq-project, July 2022.

[76] M. G Aartsen et al. *Phys. Rev. Lett.*, 125:121104, Sep 2020.

[77] Dieter Heck, Johannes Knapp, JN Capdevielle, G Schatz, T Thouw, et al. CORSIKA: A Monte Carlo code to simulate extensive air showers. 1998.

[78] Hans Dembinski, Ariel Bridgeman, Benjamin Fuchs, Detlef Maurel, Daniela Mockler, Alexander Schulz, and Felix Werner. PyIK - The Python Instrument Kit. `https://github.com/HDembinski/pyik`, 2021.

[79] Edwin B Wilson. Probable inference, the law of succession, and statistical inference. *Journal of the American Statistical Association*, 22(158):209–212, 1927.

[80] M. G. Aartsen et al. Efficient propagation of systematic uncertainties from calibration to analysis with the SnowStorm method in IceCube. *JCAP*, 10:048, 2019.

[81] IceCube Collaboration. IceCubeWiki:NuGen. Creative Commons Attribution-Share Alike 3.0.

[82] G. D. Barr, T. K. Gaisser, S. Robbins, and Todor Stanev. Uncertainties in Atmospheric Neutrino Fluxes. *Phys. Rev. D*, 74:094009, 2006.

[83] Thomas K. Gaisser, Todor Stanev, and Serap Tilav. Cosmic Ray Energy Spectrum from Measurements of Air Showers. *Front. Phys. (Beijing)*, 8:748–758, 2013.

[84] Jakob van Santen. *Neutrino Interactions in IceCube above 1 TeV Constraints on Atmospheric Charmed-Meson Production and Investigation of the Astrophysical Neutrino Flux with 2 Years of IceCube Data taken 2010–2012*. PhD thesis, University of Wisconsin, Madison, 2014.

[85] Eun-Joo Ahn, Ralph Engel, Thomas K Gaisser, Paolo Lipari, and Todor Stanev. Cosmic ray interaction event generator SIBYLL 2.1. *Physical Review D—Particles, Fields, Gravitation, and Cosmology*, 80(9):094003, 2009.

[86] Richard Naab. *Evidence for a break in the difuse extragalactic neutrino spectrum*. PhD thesis, Humboldt-Universität zu Berlin, 2024.

[87] R Abbasi, M Ackermann, J Adams, SK Agarwalla, JA Aguilar, M Ahlers, JM Alameddine, NM Amin, K Andeen, G Anton, et al. Measurement of atmospheric neutrino mixing with improved IceCube DeepCore calibration and data processing. *Physical Review D*, 108(1):012014, 2023.

[88] D. Tosi and C. Wendt. Calibrating photon detection efficiency in IceCube. *PoS*, TIPP2014:157, 2014.

[89] Martin Rongen, Dmitry Chirkin, IceCube Collaboration, et al. Advances in icecube ice modelling & what to expect from the upgrade. *Journal of Instrumentation*, 16(09):C09014, 2021.

[90] IceCube Collaboration. Evidence for Spectral Break or Curvature in the Spectrum of Astrophysical Neutrinos from 5TeV - 10PeV. Creative Commons Attribution-Share Alike 3.0.

[91] IceCube Collaboration. Improved measurements of the TeV- PeV extragalactic neutrino spectrum from joint analyses of IceCube tracks and cascades. Creative Commons Attribution-Share Alike 3.0.

[92] Carlos A Argüelles, Austin Schneider, and Tianlu Yuan. A binned likelihood for stochastic models. *Journal of High Energy Physics*, 2019(6):1–18, 2019.

[93] W. Brandon et al. Aesara. doi: 10.5281/zenodo.8365100.

[94] Ciyou Zhu, Richard H Byrd, Peihuang Lu, and Jorge Nocedal. Algorithm 778: L-bfgs-b: Fortran subroutines for large-scale bound-constrained optimization. *ACM Transactions on mathematical software (TOMS)*, 23(4):550–560, 1997.

[95] Fred James et al. Minuit. *CERN Program Library Long Writeup D*, 506:1993, 1994.

[96] IceCube Collaboration. NNMFit – A Forward-Folding Likelihood Framework for Neutrino Telescopes. *Journal of Open Source Software*, In Preparation.

[97] Floyd W. Stecker. PeV neutrinos observed by IceCube from cores of active galactic nuclei. *Physical Review D—Particles, Fields, Gravitation, and Cosmology*, 88(4):047301, August 2013.

[98] P. Padovani, M. Petropoulou, P. Giommi, and E. Resconi. A simplified view of blazars: the neutrino background. *MNRAS*, 452(2):1877–1887, September 2015.

[99] Rasha Abbasi, M Ackermann, J Adams, JA Aguilar, M Ahlers, M Ahrens, JM Alameddine, C Alispach, AA Alves Jr, NM Amin, et al. Improved characterization of the astrophysical muon–neutrino flux with 9.5 years of icecube data. *The Astrophysical Journal*, 928(1):50, 2022.

[100] Antonio Capanema, Arman Esmaili, and Kohta Murase. New constraints on the origin of medium-energy neutrinos observed by IceCube. *Phys. Rev. D*, 101(10):103012, 2020.

[101] Juan Pablo Yañez and Anatoli Fedynitch. DAEMONFLUX: DAta-drivEn MuOn-calibrated atmospheric Neutrino Flux. *arXiv preprint arXiv:2303.00022*, 2023.

[102] Hans Dembinski, Ralph Engel, Anatoli Fedynitch, Thomas Gaisser, Felix Riehn, and Todor Stanev. Data-driven model of the cosmic-ray flux and mass composition from 10 gev to 10^{11} gev. *arXiv preprint arXiv:1711.11432*, 2017.

[103] Anatoli Fedynitch and Matthias Huber. Data-driven hadronic interaction model for atmospheric lepton flux calculations. *Physical Review D*, 106(8):083018, 2022.

[104] D Chirkin, T Yuan, R Abbasi, M Ackermann, J Adams, SK Agarwalla, J Aguilar, M Ahlers, JM Alameddine, NMB Amin, et al. Updated directions of icecube hese events with the latest ice model using directfit. In *38th International Cosmic Ray Conference*, page 1030, 2024.

[105] M. G. Aartsen et al. Observation and Characterization of a Cosmic Muon Neutrino Flux from the Northern Hemisphere using six years of IceCube data. *Astrophys. J.*, 833(1):3, 2016.

[106] M. G. Aartsen et al. Detection of a particle shower at the Glashow resonance with IceCube. *Nature*, 591(7849):220–224, 2021. [Erratum: Nature 592, E11 (2021)].

[107] Marco S Muzio, Tianlu Yuan, and Lu Lu. Emergence of a neutrino flux above 5 pev and implications for ultrahigh energy cosmic rays. *arXiv preprint arXiv:2502.06944*, 2025.

[108] KM3NeT Collaboration. Observation of an ultra-high-energy cosmic neutrino with KM3NeT. *Nature*, 638(8050):376–382, 2025.

[109] Icecube Collaboration. IceCube-190331A - IceCube observation of a high-energy neutrino candidate event. *General Coordinates Network*, 24028:1, January 2019.

[110] Icecube Collaboration. Search for additional neutrino events from the direction of IceCube-190331A with IceCube. *General Coordinates Network*, 24039:1, January 2019.

[111] S. Buson and S. Garrappa. Fermi-LAT Gamma-ray Observations of IceCube-190331A. *General Coordinates Network*, 24040:1, January 2019.

[112] V. Lipunov, E. Gorbovskoy, N. Tyurina, V. Kornilov, D. Vlasenko, V. Vladimirov, D. Zimnukhov, A. Kuznetsov, P. Balanutsa, A. Chasovnikov, V. Topolev, F. Balakin, K. Zhirkov, D. Kuvshinov, R. Podesta, C. Lopez, C. Francile, F. Podesta, H. Levato, R. Rebolo, M. Serra, N. Lodieu, G. Israelian, L. Suarez-Andres, D. Buckley, O. Gress, N. M. Budnev, O. Ershova, S. Yazev, V. Yurkov, A. Gabovich, Y. Sergienko, D. Kobcev, A. Tlatov, V. Senik, A. V. Parhomenko, and D. Dormidontov. IceCube-190331A: MASTER optical follow-up observations. *General Coordinates Network*, 24034:1, January 2019.

[113] A. Keivani, M. Santander, J. A. Kennea, P. A. Evans, D. B. Fox, and F. Krauss. IceCube-190331A: Swift-XRT Follow-up Observations. *General Coordinates Network*, 24094:1, January 2019.

[114] Felicia Krauß, Emily Calamari, Azadeh Keivani, Alexis Coleiro, Phil A Evans, Derek B Fox, Jamie A Kennea, Peter Mészáros, Kohta Murase, Thomas D Russell, et al. Multimessenger observations of counterparts to icecube-190331a. *Monthly Notices of the Royal Astronomical Society*, 497(3):2553–2561, 2020.

[115] F. Lucarelli, M. Cardillo, M. Tavani, C. Pittori, F. Verrecchia, A. Bulgarelli, N. Parmiggiani, V. Fioretti, C. Casentini, G. Piano, A. Ursi, I. Donnarumma, S. Vercellone, F. Gianotti, M. Trifoglio, A. Giuliani, S. Mereghetti, P. Caraveo, F. Perotti, A. Chen, A. Argan, E. Costa, E. Del Monte, Y. Evangelista, M. Feroci, L. Pacciani, P. Soffitta, V. Vittorini, G. Di Cocco, F. Fuschino, M. Galli, C. Labanti, M. Marisaldi, A. Pellizzoni, M. Pilia, A. Trois, G. Barbiellini, E. Vallazza, F. Longo, A. Morselli, P. Picozza, M. Prest, P. Lipari, D. Zanello, P. W. Cattaneo, A. Rappoldi, A. Ferrari, F. Paoletti, L. A. Antonelli, P. Giommi, L. Salotti, G. Valentini, and F. D'Amico. AGILE detection of the source AGL J2233-2212 in temporal and space closeness to the IceCube-190331A neutrino event. *The Astronomer's Telegram*, 12623:1, April 2019.

[116] Edson D Leonel. Breaking down the fermi acceleration with inelastic collisions. *Journal of Physics A: Mathematical and Theoretical*, 40(50):F1077, 2007.

[117] Diego FM Oliveira, Jürgen Vollmer, and Edson D Leonel. Fermi acceleration and its suppression in a time-dependent lorentz gas. *Physica D: Nonlinear Phenomena*, 240(4-5):389–396, 2011.

[118] Donald C Ellison, Donald C Warren, and Andrei M Bykov. Monte carlo simulations of nonlinear particle acceleration in parallel trans-relativistic shocks. *The Astrophysical Journal*, 776(1):46, 2013.

[119] Donald C Ellison, Donald C Warren, and Andrei M Bykov. Particle spectra and efficiency in nonlinear relativistic shock acceleration–survey of scattering models. *Monthly Notices of the Royal Astronomical Society*, 456(3):3090–3099, 2016.

[120] Erik Ganster. *Evidence for a break in the difuse extragalactic neutrino spectrum.* PhD thesis, Humboldt-Universität zu Berlin, 2024.

[121] Rasha Abbasi, Markus Ackermann, Jenni Adams, Sanjib Kumar Agarwalla, Juanan Aguilar, Markus Ahlers, Jean-Marco Alameddine, Najia_Moureen Binte Amin, Karen Andeen, Gisela Anton, et al. Approximating new ice models with b-splines for improved icecube event reconstruction: application to cascades and tracks. 2023.

[122] Aya Ishihara. The IceCube Upgrade - Design and Science Goals. *PoS*, ICRC2019:1031, 2021.

[123] Maximilian Meier. Recent cosmogenic neutrino search results with icecube and prospects with icecube-gen2. *arXiv preprint arXiv:2409.01740*, 2024.

[124] Lew Classen et al. Design and performance of the multi-PMT optical module for IceCube Upgrade. *PoS*, ICRC2021:1070, these proceedings.

[125] Yuya Makino. D-egg: A next-generation optical module for icecube. In *EPJ Web of Conferences*, volume 207, page 06005. EDP Sciences, 2019.

[126] V. Basu. A long multi-PMT optical sensor for IceCube-Gen2. *JINST*, VLVnT21, these proceedings.

[127] **IceCube** Collaboration, Mark G Aartsen, et al. *J. Phys. G*, 48(6):060501, 2021.

[128] Rasha Abbasi, Markus Ackermann, Jenni Adams, Sanjib Agarwalla, Juanan Aguilar, Markus Ahlers, Jean-Marco Alameddine, Najia Moureen Binte Amin, Karen Andeen, and Gisela Anton. Search for Extremely High Energy Neutrinos with IceCube. Technical report, 2023.

[129] Qwerty123uiop. PhotoMultiplierTubeAndScintillator. Available at Link (2024/04/14). Creative Commons Attribution-Share Alike 3.0.

[130] *Ecoflex™ Series Super-Soft, Addition Cure Silicone Rubbers.*